Systematic Studies of an On-Off-Analysis of H.E.S.S. data in Search for a Signal from the Dark Matter Halo of the Milky Way

Systematische Studien einer On-Off-Analyse mit
H.E.S.S. Daten
zur Suche nach einem Signal
vom Dunkle Materie Halo in der Milchstraße

Der Naturwissenschaftlichen Fakultät
der Friedrich-Alexander-Universität Erlangen-Nürnberg
zur Erlangung des Doktorgrades Dr. rer. nat.

vorgelegt von
Constanze Verena Jahn
aus Stuttgart

Als Dissertation genehmigt von der Naturwissenschaftlichen Fakultät der Friedrich-Alexander-Universität Erlangen-Nürnberg

Tag der mündlichen Prüfung:	27.09.2013
Vorsitzender des Promotionsorgans:	Prof. Dr. Johannes Barth
Gutachter/in:	Prof. Dr. Gisela Anton
	Prof. Dr. Christian Stegmann

Abstract

The search for dark matter forms one of the key scientific goals in contemporary particle and astroparticle physics. The distribution of dark matter in the Milky Way is thought to be radially symmetric and to peak at the Galactic Centre, which makes the latter a very interesting target for the search for dark matter. Models predict the annihilation or decay of dark matter into standard model particles, among them gamma rays with potentially very high energies (VHE, $E \geq 100\,\mathrm{GeV}$). In this energy regime the High Energy Stereoscopic System (H.E.S.S.) operates, which is an array of four imaging atmospheric Cherenkov telescopes (IACT) situated in the Khomas highland in Namibia. H.E.S.S. detects gamma rays with energies between about 100 GeV and up to several tens of TeV. Furthermore it has observed the Galactic Centre for over 100 hours. In this thesis an on-off-analysis method based on the Model++ reconstruction, a new and very sensitive reconstruction method, is developed. Detailed systematic studies are presented and used to quantify the uncertainty of the developed analysis method. The on-off-analysis method is then applied to the data taken on the Galactic Centre region and upper limits on the velocity-averaged dark matter annihilation cross-section are derived.

Zusammenfassung

Die Suche nach Dunkler Materie ist eines der wichtigsten wissenschaftlichen Ziele der modernen Teilchen- und Astroteilchenphysik. Die Verteilung der Dunklen Materie (DM) in der Milchstraße wird als radialsymmetrisch angenommen und hat den höchsten Wert im Galaktischen Zentrum. Deshalb ist das Galaktische Zentrum eine spannende Region im Hinblick auf die Suche nach Dunkler Materie. Modelle sagen die Annihilation bzw. den Zerfall von DM-Partikeln in Teilchen des Standardmodells, darunter auch Photonen mit sehr hohen Energien ($E \geq 100\,\mathrm{GeV}$), voraus. In diesem Energiebereich arbeitet das High Energy Stereoscopic System (H.E.S.S.), das ein Teleskopsystem bestehend aus vier abbildenden atmosphärischen Cherenkovteleskopen ist und sich im Khomas Hochland in Namibia befindet. H.E.S.S. weist Gammastrahlen mit Energien zwischen ungefähr 100 GeV und etwa 50 TeV nach. H.E.S.S. hat das Zentrum unserer Galaxie länger als 100 Stunden beobachtet. In der vorliegenden Arbeit wird eine On-Off-Analyse basierend auf der Model++ Rekonstruktion, einer neuen und sehr sensitiven Rekonstruktionsmethode, entwickelt. Desweiteren werden detailierte systematische Studien präsentiert und verwendet um die Unsicherheiten der entwickelten Methode zu quantifizieren. Die On-Off-Analyse wird dann angewandt um die Daten vom Galaktische Zentrum zu analysieren und obere Grenzen an den Wirkungsquerschnitt der Annihilation der Dunklen Materie zu bestimmen.

Contents

Introduction

The search for dark matter forms one of the key scientific goals in contemporary particle and astroparticle physics. Measurements of the cosmic microwave background (CMB) with the WMAP (Wilkinson Microwave Anisotropy Probe) satellite agree well with a cosmology model containing $\sim 5\%$ baryonic (ordinary) matter, $\sim 70\%$ dark energy and $\sim 25\%$ dark matter (Bennett et al., 2012). Common baryonic matter interacts electromagnetically and can therefore be observed relatively easily. Dark matter, however, only interacts weakly and through gravitation, therefore it is very difficult to obtain information about the nature of dark matter.
Nevertheless, many experiments search for evidence of dark matter. These efforts include direct searches for signals from collisions of dark matter particles with ordinary matter particles as well as indirect searches for secondary particles originating from decaying or annihilating dark matter in the Universe. Among those secondary particles are also gamma rays. Theories predict gamma rays from dark matter annihilation up to the energy of the dark matter particle mass, which could be as high as TeV energies.
An experiment searching for such very high energy (VHE, $E \geq 100\,\mathrm{GeV}$) gamma rays is the H.E.S.S. (High Energy Stereoscopic System) experiment. H.E.S.S. is the most successful ground based VHE gamma-ray experiment. So far, it has observed many regions of interest inside and outside our Galaxy. Furthermore it identified over 50 gamma-ray sources consisting mostly of pulsar wind nebulae, active galactic nuclei and supernova remnants. The H.E.S.S. experiment has also observed regions, where an enhanced dark matter density is predicted, and set upper limits on the velocity-averaged cross section of dark matter annihilation (e.g. Abramowski et al. 2011b). In the last years a new reconstruction technique (Model++, de Naurois and Rolland 2009) has been developed, which results in higher sensitivity and better gamma-hadron separation.
One of the most promising regions for the search for dark matter with H.E.S.S. is certainly the dynamical centre of our Galaxy. The Galactic Centre region is expected to host the highest dark matter density in the Milky Way. The Galactic Centre region also contains a lot of other interesting astrophysical objects, such as the super-massive back hole Sgr A*. Therefore H.E.S.S. obtained deep observations of the Galactic Centre region consisting of over 100 hours of data. In this work these data are carefully analysed using the Model++ reconstruction in order to derive new upper limits on the velocity-averaged cross-section of the dark matter particles.

This thesis is structured as follows:

- The first Chapter reviews the subject of dark matter and motivates the analysis of the Galactic Centre region carried out in this thesis.
- The second Chapter briefly introduces gamma-ray astronomy and then focuses on the H.E.S.S. experiment and the reconstruction and analysis technique used by the H.E.S.S. collabration.
- The third Chapter describes comprehensive systematic studies, which are conducted in order to develop a so-called On-Off-analysis method, which is well suited for the search for a signal from the dark matter halo of our Milky Way. This On-Off-analysis method and its uncertainties are then also explained.
- The fourth Chapter presents the results of applying the analysis to the dark matter search in the H.E.S.S. observations of the Galactic Centre region.
- The last Chapter summarises the results and gives a brief outlook.

1. Dark Matter Halo Signal from the Milky Way

The aim of this work is to search for a gamma-ray signal from the dark matter halo in the Milky Way. The following Chapter introduces dark matter and its properties and sheds light on previous searches for dark matter. Furthermore the Galactic Centre region is described as a target region for dark matter search.

1.1. Dark Matter

This Section provides an overview and introduction to dark matter. The name dark matter was introduced to account for matter in the Universe that is non-luminous and therefore not directly visible in observations. The existence of dark matter was claimed as an explanation for observed gravitational effects, such as stellar velocities, that contradict Newtonian dynamics. Besides resolving these contradictions dark matter also nicely fits in the prevailing theory of the evolution of the Universe, the Big Bang theory. Measurements agree quite well with the predictions of the Big Bang theory assuming a Lambda Cold Dark Matter (ΛCDM) cosmology. These two main motivations for the existence of dark matter are described in more detail in the following two Sections. In the third Section the properties required for a particle to be a dark matter candidate are discussed and candidates arising from theoretical models are introduced. Estimates for the dark matter density distribution (halo) of the Milky Way are given in the fourth Section. Eventually in the last two Sections the different searching techniques for dark matter are listed and the searches performed by the H.E.S.S. experiment are described.

1.1.1. Evidence for Dark Matter through Gravitational Interaction

In the 17th century the Newton's law of gravitation was introduced (Newton, 1687). The law describes the attractive force that acts between any two point masses. In terms of a vector field it can be described as follows:

$$\mathbf{F}_{\text{grav}} = G \cdot m_1 \cdot m_2 \cdot \frac{\mathbf{r}_1 - \mathbf{r}_2}{|\mathbf{r}_1 - \mathbf{r}_2|^3}. \tag{1.1}$$

Here m_1 and m_2 are the two point masses, $\mathbf{r}_1$ and $\mathbf{r}_2$ are the coordinates of the two masses and G is the gravitational constant. Later, in the early 20th century, Einstein found a more general formulation in his theory of General Relativity (Einstein, 1916). He postulated a connection between space-time and the gravitational field. This is summed up in Einstein's equations

$$R_{\mu\nu} - \frac{1}{2} g_{\mu\nu} R + g_{\mu\nu}\Lambda = \frac{8\pi G}{c^4} T_{\mu\nu}. \tag{1.2}$$

$R_{\mu\nu}$ is the Ricci curvature tensor, R the scalar curvature and $g_{\mu\nu}$ the metric tensor. Λ is called cosmological constant. G is the gravitational constant and c the speed of light in vacuum. Lastly $T_{\mu\nu}$ is the energy-stress tensor.
In most cases the Newtonian law is a perfectly good approximation. Only if a system is very massive or dense, moving at a speed close to the speed of light or if very precise measurements are required, General Relativity needs to be taken into account. The Newtonian law is the low-gravity limit of General Relativity.
Under the assumption that General Relativity and Newtonian gravity hold, the first hints of dark matter were discovered in the early 1930s. Further evidence was then brought up in the 1970s and even today more precise measurements of gravitational effects continue to reveal even more evidence for dark matter. These historic steps are outlined in the following.

Missing Mass

In astronomy it is common to estimate the mass of an object through its mass-to-luminosity ratio M/L. The total luminosity can be estimated via the so-called apparent magnitude and the distance of the object. The magnitude m is a measure for the brightness of a stellar object as seen from Earth. The brighter an object appears the lower its magnitude. The exact distance of a stellar object is difficult to determine but there are several methods which can be used to estimate it. An example is a method which uses a relation between the period and the absolute brightness of Cepheids. Cepheids are stars with variable luminosities. Getting the absolute brightness from the relation and knowing the apparent brightness one can then immediately estimate the distance. Another way to estimate the distance is the cosmological redshift, which results from the expansion of the Universe. The different methods of distance estimation are valid at different distance regimes, adjacent and partly overlapping, such as to form the so-called cosmic distance ladder. Beside the mass and the distance also velocities of stellar objects can be determined. This is done via the Doppler effect, i.e. with the local[1] redshift or blueshift of the objects.
With these techniques in 1932 J.H. Oort determined the velocities and the masses of stars moving near the Galactic Plane (Oort, 1932). When inserting his results into the laws of gravity he found a marked discrepancy between the depth of the gravitational potential arising from the mass of the luminous objects and the proper motion of the individual stars: their velocities were too high for the stars to actually be gravitationally bound.

[1] "Local" in contrast to the global cosmological redshift.

Hence the stars should escape the system. However, no stars escaping the Milky Way were observed and Oort concluded that there might be more mass than that of the luminous objects. But he also strongly attenuated this statement by suggesting alternative solutions, namely an 85% absorption of the light from the Galactic Centre due to dust or other matter in between or an error in the velocity measurements. In the following year, though, F. Zwicky made similar observations on a much larger scale (Zwicky, 1933). He was analysing observations of extragalactic objects in order to study their redshift – not the redshift due to the Doppler effect but the cosmological redshift which has its origin in the expansion of space. Zwicky described different implications of the redshift in his paper (Zwicky, 1933) in 1933. In Section 5 he focuses on the Coma cluster and its velocities. In the Coma cluster he noticed a large scatter in the values determined for the velocities of the different galaxies in the cluster. He therefore made an Ansatz calculating the mass of the cluster with the virial theorem assuming the system being in a stationary state. Using the mean kinetic and the mean potential energy, $\langle E_{\mathrm{kin}} \rangle$ and $\langle E_{\mathrm{pot}} \rangle$ respectively, the virial theorem states the following:

$$\langle E_{\mathrm{kin}} \rangle = -\frac{1}{2} \langle E_{\mathrm{pot}} \rangle. \tag{1.3}$$

Zwicky assumed that the mass in the cluster is distributed homogeneously and set the radius of the cluster to approximately $R = 1.0 \cdot 10^6\,\mathrm{ly} = 10^{24}\,\mathrm{cm}$. Then the cluster contains 800 galaxies each with a mass of about $10^9\,\mathrm{M}_\odot$. This yields a total mass of $M = 1.6 \cdot 10^{45}\,\mathrm{g}$. Inserting this into the gravitational potential Zwicky found the potential energy

$$\langle E_{\mathrm{pot}} \rangle = -\frac{3}{5}\, G \cdot \frac{M^2}{R} \tag{1.4}$$

with G being the gravitational constant. Inserting this into Eq. 1.3 and solving for the mean velocity $\overline{v}$ he obtained

$$\overline{v} = 80\,\mathrm{km\,s^{-1}}. \tag{1.5}$$

This is in contrast with the measurement, where a mean velocity of $1000\,\mathrm{km\,s^{-1}}$ was determined. In order to get the measured velocity the mass on the right hand side of Eq. 1.3 has to be about 400 times larger than the total mass assumed above. Zwicky concluded that this clearly indicates the existence of a large fraction of dark matter in the cluster. He emphasised that even in the case of non-equilibrium dark matter is needed. Otherwise taking the laws of gravity the galaxies in the cluster would fly apart with high velocities, because of the missing gravitational pull to hold them together. But he dismissed this suggestion because no single galaxy with such a high speed is observed. A few years later in 1937 F. Zwicky published a paper dedicated to the derivation of the mass of clusters (Zwicky, 1937b). There he demonstrated two more techniques besides the virial theorem to determine the mass. He stated again that the mass-to-luminosity ratio can only give a lower limit on the absolute cluster mass and only with other techniques the missing mass due to dark matter is revealed.

Summarising, already in the early 1930s it became clear that there are large discrepancies between the results of the different mass determination techniques of gravitationally bound

objects. The mass derived via the luminosity is lower than the mass expected due to the motion in gravitational potentials. A potential solution to this problem is the existence of so-called dark matter, which is not visible in optical astronomy. During the 20th century a lot more wavelengths became accessible to us, but dark matter is still not visible in any of them. Hence dark matter is assumed not to interact electromagnetically but only weakly.

Rotation curves

Although the results from the 1930s indicated that dark matter might exist, it was not until the 1970s that measurements provided new hints. It was at this time when the accuracy in the measurement of spectra from stars and other objects increased sufficiently to be able to derive the rotation curves of galaxies. This was shown by V. Rubin and colleagues for the Andromeda Nebula (Rubin and Ford, 1970). Later they went on to publish results on 21 different galaxies (Rubin et al., 1980):
They used the Doppler effect on the Hα line of the observed spectra to determine the radial velocities of stars in the galaxies. From this they inferred, under the assumption of circular orbits around the centre of the galaxy, the rotational velocity of the stars. Since individual stars are indeed too faint, regions of hot gas were chosen. In Fig. 1.1 the rotation curves for the 21 galaxies are shown (Rubin et al., 1980). Due to gravitation and the Keplerian laws the stars and the gas in the galaxies are expected to be on Keplerian orbits around the centre of the galaxy. The velocity of the objects should then fall off as $\sim \sqrt{\frac{1}{r}}$ with the distance r to the centre of the galaxy. This follows directly from the assumption that the centripetal force related to the rotational velocity equals the gravitational force related to the masses of the objects:

$$v\,(r) = \sqrt{\frac{GM}{r}}. \tag{1.6}$$

v is the rotational velocity, G the gravitational constant, M the mass within a certain radius ($\leq r$) around the centre and r the distance to the centre. For the motion of the planets around the Sun in our solar system this $\sqrt{\frac{1}{r}}$-dependence of the velocity is observed. The green dashed line A in Fig. 1.1 shows this dependence. The rotational velocities of regions further away from the galaxy centres should decrease with $\sqrt{\frac{1}{r}}$. But this behaviour is not visible in the data, as shown in Fig. 1.1. This led V. Rubin to the interpretation that the mass distribution in the galaxies must be different from the distribution of the luminous material. The flat or even rising rotation curves can be explained by requiring more mass also in the outer parts of the galaxies. As such masses are not seen in any observations the rotation curves are considered a further evidence for dark matter.

Gravitational lensing

Already in Einstein's publication on General Relativity (Einstein, 1916) a further effect, namely the deflection of light by a gravitational potential, was predicted. The deflection

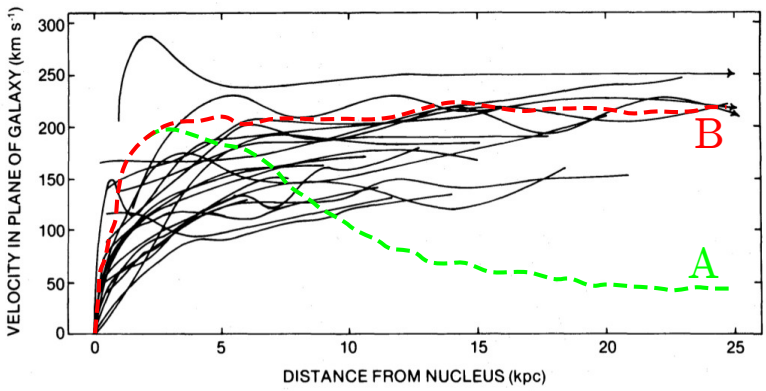

Figure 1.1.: Rotation curves for 21 different galaxies as taken from Rubin et al. (1980). Overlaid are the expected behaviour of a rotation curve as a green dashed line (A) and the trend as obtained from the combined measurements as a red dashed line (B).

angle of light coming from the general direction of the Sun was measured shortly after during a solar eclipse in 1919 (Dyson et al., 1920). The measurement agreed well with the value that Einstein had predicted. Therefore the measurement of this deflection angle was a first validation of General Relativity. After this the effect of the deflection of light – or gravitational lensing, as it is also called – was further studied in theory. Many different phenomena were predicted, among them image distortions, such as Einstein Rings, arcs or multiple images (for an introduction to gravitational lensing the reader may consult, e.g., Narayan and Bartelmann (1996)). The basic principle of gravitational lensing is illustrated in Fig. 1.2. There the deflection of light rays from a distant galaxy by a massive galaxy cluster is shown.

Even though many theoretical predictions of gravitational lensing existed, only in 1979 a lensed astronomical object was identified for the first time (Walsh et al., 1979). The object observed was a quasar (Q0957+561). It appeared as two spatially separated quasars in the observation. But the spectra of both objects were remarkably similar. That is why discoverer D. Walsh proposed the two quasars might just be the same object gravitationally lensed and multiplied. Later the almost identical lightcurves (corrected for offsets in time and magnitude) of the two quasar images showed beyond a doubt that they were the first detected gravitationally lensed image. From then on gravitational lensing became an observational science. One example for luminous arcs and arclets also due to gravitational lensing is shown in Fig. 1.3. There a Hubble Space Telescope (HST) image of the Abell cluster is visible. All the phenomena described so far are due to so called *strong lensing*. Of course light is also deflected when passing through inhomogeneous mass distributions. The effects are similar to the ones described above but are manifested on a much smaller scale.

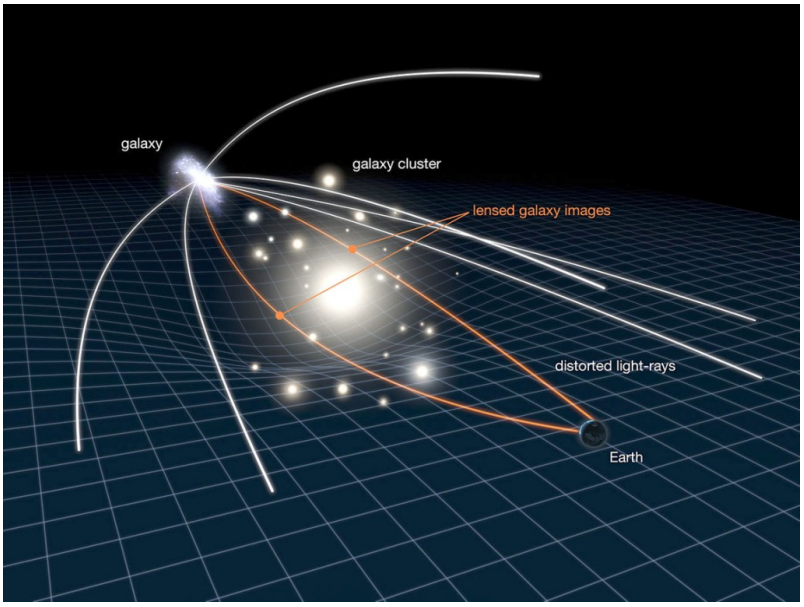

Figure 1.2.: Illustration of gravitational lensing. All the indicated light paths represent deflections by the massive galaxy cluster in the centre of the image. The orange light paths are the ones detected on Earth and lead to the observation of two images of the lensed galaxy. Image credit: NASA, ESA, L. Calcada

Measurements are not detailed enough to see this effect in individual images. Nevertheless, with statistical methods it is possible to determine such effects. This is called *weak lensing*. In between *strong* and *weak lensing* there is also *microlensing*, which is mostly used to search for localised clumps of matter, such as MACHOS (massive compact halo objects) like faint stars or planets or dark matter clumps.
The important point in all the lensing scenarios is that from a lensed image properties of the lens can be obtained, especially the mass distribution of the lens. Therefore lensing surveys are used to search for non-luminous matter, like planets or dark matter. A special case that promotes dark matter very nicely is the so-called Bullet Cluster (Clowe et al., 2006). This cluster actually contains two clusters which collided some time ago. With observations in the optical, radio and X-ray band it was possible to locate the luminous parts, like gas and molecular clouds that had interacted in the collision. At the same time lensing studies of objects behind the cluster were able to determine the distribution of the significant amounts of mass in the collided system. A combination of the two results is shown in Fig. 1.4. The red regions in the image indicate the luminous material seen in X-rays and the blue regions are the regions where according to the lensing most of the mass should be located. It is obvious that the different coloured regions are well separated. This is attributed to the fact that the visible matter interacts and therefore stays near the collision site, while the dark matter only interacts weakly and therefore flies just through. Hence also for the separation of matter in the Bullet Cluster dark matter offers a straightforward explanation.

Figure 1.3.: Hubble Space Telescope image of the Abell 2218 cluster of galaxies. Lensing effects such as aclets are visible. Image credit: NASA/ESA.

1.1.2. Cosmological Evidence

We have already seen that many observations of gravitational effects show that there might be a non-luminous (not electromagnetically interacting) kind of matter, namely dark matter. Additionally it turns out that also in cosmology dark matter fits in nicely. A promising and simple model of cosmology is the Lambda Cold Dark Matter (ΛCDM) cosmology model. The ΛCDM cosmology model is a parametrisation of the Big Bang model. Λ here stands for a cosmological constant – frequently attributed to so-called dark energy – and cold dark matter is dark matter with certain properties. The ΛCDM cosmology model describes the evolution of the Universe from the Big Bang until today. There are several measurements testing the parameters of cosmological models. The results of these measurements are well described by the ΛCDM cosmology model where non-baryonic dark matter plays a significant role. This is further described in the following.

Introducing Cosmological Parameters

A key element of the Big Bang theory is General Relativity, which was already mentioned in Section 1.1.1. The other important concept for the Big Bang theory is the Cosmological Principle. It assumes that the Universe is homogeneous and isotropic. A homogeneous Universe looks the same from anywhere and an isotropic Universe looks the same in any direction. Thus, no location in the Universe is in any way special. These two assumptions have been tested with experiments by making large surveys of the visible Universe. In

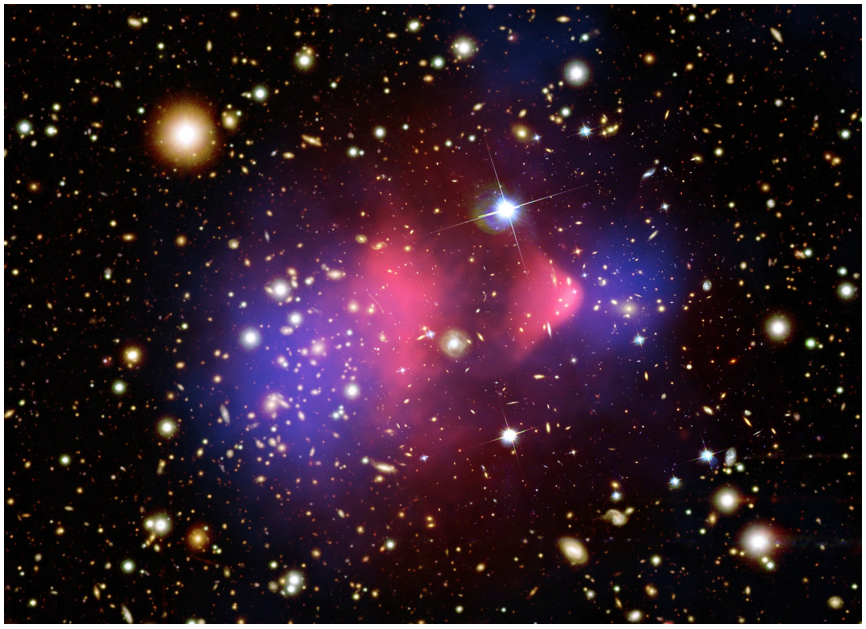

Figure 1.4.: Optical image of the Bullet Cluster. The X-ray signal is overlaid in red and the mass located via lensing is overlaid in blue. Image Composite Credit: X-ray: NASA/CXC/CfA/ (Markevitch, 2006), Lensing Map: NASA/STScI; ESO WFI; Magellan/U.Arizona/ (Clowe et al., 2006), Optical: NASA/STScI; Magellan/U.Arizona/D.Clowe et al.;

Fig. 1.5 the results of such a survey, namely the 2dF Galaxy Redshift Survey (Colless et al., 2001) are shown. There the positions of 62559 galaxies and their redshift are plotted. According to these measurements the assumption of homogeneity is valid on large scales. The best evidence for the isotropy of the Universe is probably the measurement of the cosmic microwave background (CMB) which was first measured by the COBE (Cosmic Background Explorer) satellite (Smoot et al., 1992). The CMB is uniform down to a scale of 10^{-5} K. The CMB is also important for constraining other parameters from the Big Bang theory as will be described later.
The Cosmological Principle and General Relativity are the pillars on which the Big Bang theory rests. Furthermore Hubble's discovery, dating from the late 1920s, that the Universe is expanding (Hubble, 1929) is taken into account by the theory. A metric complying with all these conditions is the Friedmann-Lemaître-Robertson-Walker (FLRW) metric, which was described mathematically by Robertson and Walker in the 1930s (Robertson, 1935), (Robertson, 1936a), (Robertson, 1936b) but also derived from Einstein's equations by Friedmann (Friedman, 1922), (Friedmann, 1924) and independently by Lemaître around 1927 (English translation published some years later, (Lemaître, 1931))[2]. The metric solves Einstein's equations 1.2 and allows for a homogeneous and isotropic expansion of the

[2]The metric is sometimes also called Robertson-Walker or Friedmann-Lemaître metric, but in the following the democratic name FLRW metric is used.

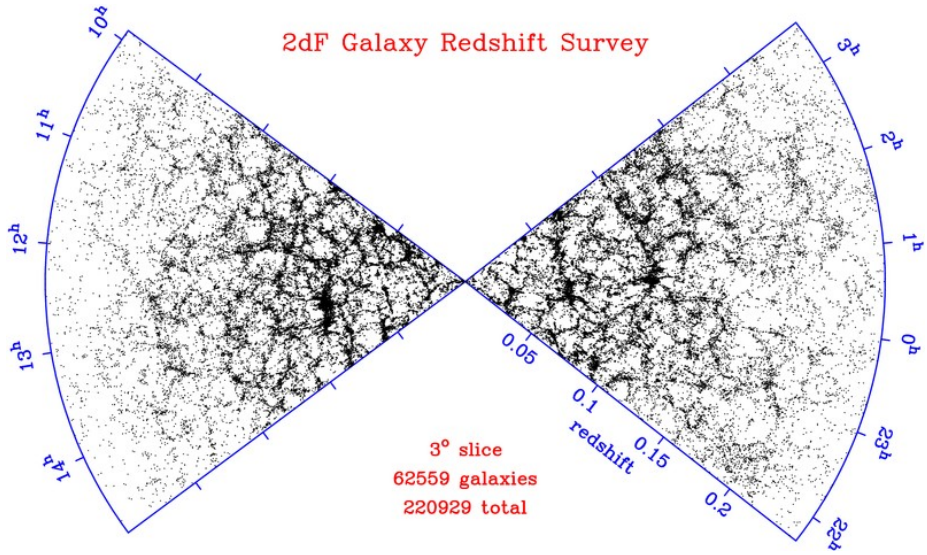

Figure 1.5.: Results of the 2dF galaxy redshift survey (Colless et al., 2001). Image taken from `http://magnum.anu.edu.au/~TDFgg/`.

Universe. From now on $c = 1$ will be used. The metric reads

$$ds^2 = dt^2 - a^2(t)d\Sigma, \qquad d\Sigma = \frac{dr^2}{1-kr^2} + r^2 d\psi^2, \tag{1.7}$$

with scale factor $a\,(t) = R(t)/R_0$ and k being an integer defining the curvature. The solutions one obtains from inserting the FLRW metric into the Einstein equations (Eqn. 1.2) are called the Friedmann equations (Friedman, 1922). One of these equations relates the Hubble parameter $H = \frac{\dot{a}}{a} = \frac{\dot{R}}{R}$ to the curvature k (not an integer here) and the density ρ_{M} of the Universe.

$$H^2 \equiv \left(\frac{\dot{R}}{R}\right)^2 = \frac{8\pi G}{3}\rho_{\mathrm{M}} + \frac{\Lambda}{3} - \frac{k}{R^2} \tag{1.8}$$

The parameter Λ can be interpreted as a vacuum energy or – as Einstein phrased it – a cosmological constant. Now the critical density ρ_{crit}, which is the density at which the curvature of the Universe is zero ($k = 0$) when $\Lambda = 0$, is defined as

$$\rho_{\mathrm{crit}} = \frac{3H^2}{8\pi G}. \tag{1.9}$$

With the critical density a further density parameter Ω is defined.

$$\Omega = \frac{\rho}{\rho_{\mathrm{crit}}}, \tag{1.10}$$

where ρ is the total density. With these definitions it follows that for

$$\Omega > 1 \quad \Rightarrow \quad k > 0 \tag{1.11}$$
$$\Omega = 1 \quad \Rightarrow \quad k = 0 \tag{1.12}$$
$$\Omega < 1 \quad \Rightarrow \quad k < 0. \tag{1.13}$$

The different values of the curvature correspond to an open ($k > 0$), closed ($k < 0$) or flat ($k = 0$) Universe. Splitting Ω into individual components arising from matter (Ω_{M}), curvature (Ω_{k}) and vacuum energy (Ω_{Λ}) and taking Eq. 1.8 at $t = t_0$ (today) gives

$$1 = \Omega_{\mathrm{M}} + \Omega_{\Lambda} + \Omega_{\mathrm{k}}. \tag{1.14}$$

One of the key questions in cosmology today concerns deriving the values of these different density parameters. The ΛCDM cosmology model requires non-baryonic dark matter and the matter density Ω_{M} can be further divided into the baryonic matter density Ω_{B} and the dark matter density Ω_{DM}. Therefore measuring these parameters reveals information about the composition of the Universe. In the following the results of several experiments which help to constrain the density parameters are given.

Constraints from CMB, BAO and Type Ia Supernovae

The Wilkinson Microwave Anisotropy Probe (WMAP) measured the changes in the CMB in the range of μK, see Fig. 1.6(a). Recently the full WMAP data set comprising 9 years of data has been analysed and the results are summarised in Bennett et al. (2012) and Hinshaw et al. (2012). In Fig. 1.6(b) the temperature angular power spectrum (TT) is shown. The red curve is a fit of a ΛCDM cosmology model to the data. From this fit the values of the density parameters can be determined. The results for the density parameters obtained in Hinshaw et al. (2012) are listed in Table 1.1. The results show that the contribution of dark matter to the total density is in the order of 24%, whereas the baryonic matter only accounts for about 5%. [3]

Other constraints on the density parameters come from the measurements of type Ia supernovae. The type Ia supernovae serve as "standard candles" for the determination of the distance in astronomy. With measuring the redshift and the luminosity of the supernovae limits on Ω_{Λ} and Ω_{M} can be derived. In 1999 measurements of supernovae type Ia gave evidence that the expansion of the Universe is accelerating (Perlmutter et al., 1999). This corresponds to a positive Λ term in Eq. 1.8 or a positive Ω_{Λ}. This density is associated with the so-called dark energy. In Kowalski et al. (2008) a large set of type Ia supernovae was analysed. The results for the limits of Ω_{Λ} and Ω_{M} are shown in Fig. 1.7 in blue.

[3] In early 2013 also the first results of the *Planck* satellite, which also measures the CMB, were published (Planck Collaboration et al., 2013). There "with respect to pre-*Planck* values" they "find a weaker cosmological constant (by 2%), more baryons (by 3%) and more cold dark matter (by 5%)".

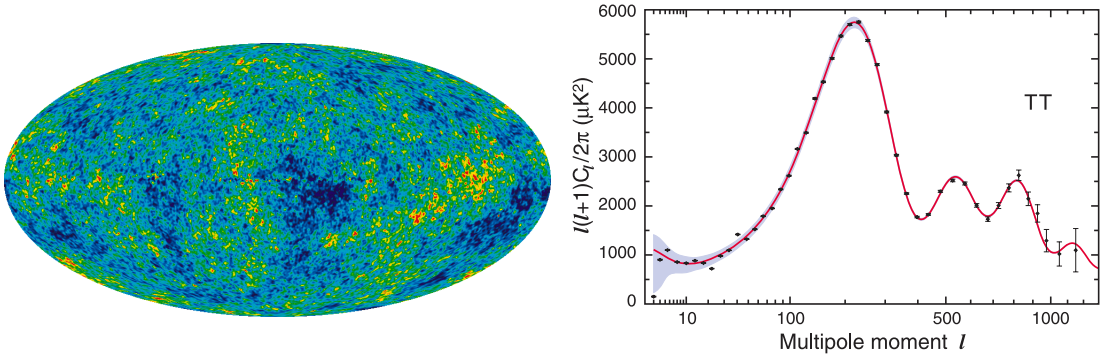

(a) (b)

Figure 1.6.: (a) The results of nine years of WMAP data. Image taken from `http://map.gsfc.nasa.gov/media/121238/index.html`. (b) The nine-year temperature angular (TT) power spectrum taken from Bennett et al. (2012).

Table 1.1.: Results from the fit of a 6 parameter ΛCDM cosmology model to the nine-year WMAP angular power spectrum data. Values taken from Table 3 and for Ω_k from Section 4.5 in Hinshaw et al. (2012).

density parameter	9-year WMAP
Ω_B	0.0463 ± 0.0024
Ω_{DM}	0.233 ± 0.023
Ω_Λ	0.721 ± 0.025
Ω_k	$-0.037^{+0.044}_{-0.042}$

Additionally constraints derived with other techniques are included in Fig. 1.7. In orange the constraints from the WMAP measurements, though just for the seven year data set, are shown, whereas in green the constraints from measurements of baryon acoustic oscillations (BAO) are shown. BAO are periodic density variations in the baryonic matter density, which are due to acoustic waves existing in the early Universe. The BAO can be determined when studying large scale structures, an example is given in Eisenstein et al. (2005). In Kowalski et al. (2008) the combined constraints (visible in Fig. 1.7) show that the Universe is probably flat ($\Omega_k = 0.010^{+0.010+0.006}_{-0.011-0.004}$) with a matter density of $\Omega_M = 0.285^{+0.020+0.011}_{-0.019-0.011}$.

Constraints from Big Bang Nucleosynthesis

Very shortly after the Big Bang the Universe was very hot. It was too hot for atoms to form. But as the Universe expands it also becomes cooler and protons and neutrons started to form deuterium nuclei and after that also helium-3, helium-4, lithium, and beryllium nuclei.

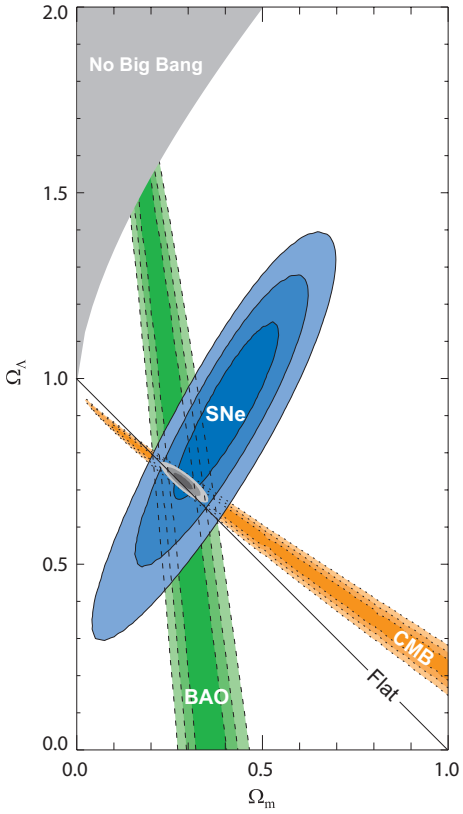

Figure 1.7.: Combined constraints on the density parameters Ω_Λ and Ω_M from CMB, BAO and type Ia supernovae measurements. Image taken from Kowalski et al. (2008).

This process of the formation of elements, which took place in the very first minutes after the Big Bang, is called nucleosynthesis. It was first discussed in Gamow (1946), Alpher (1948) and inAlpher et al. (1948). For a recent review of Big Bang nucleosynthesis see Section 22 in Beringer et al. (2012a). The rate at which the elements are formed depends on the baryon density of the Universe. With the baryon density decreasing due to the expansion of the Universe the formation process slows down. Finally after some minutes no more free neutrons are available for nucleosynthesis, because the lifetime of the neutron is only about 15 minutes and the formation of the elements stops. The amount of the light elements, which are formed in the early Universe, depends on the expansion rate of the Universe, which depends on the overall matter density Ω_M, and the baryonic density Ω_B of protons and neutrons. Today it is possible to measure the abundances of these light elements. The measurements agree well with the predictions from ΛCDM cosmology models, see Fig. 1.8. The ΛCDM cosmology model predicting the measured abundances has a much smaller baryonic density Ω_B than total matter density Ω_M. This further promotes the existence of dark matter and also that it is non baryonic.

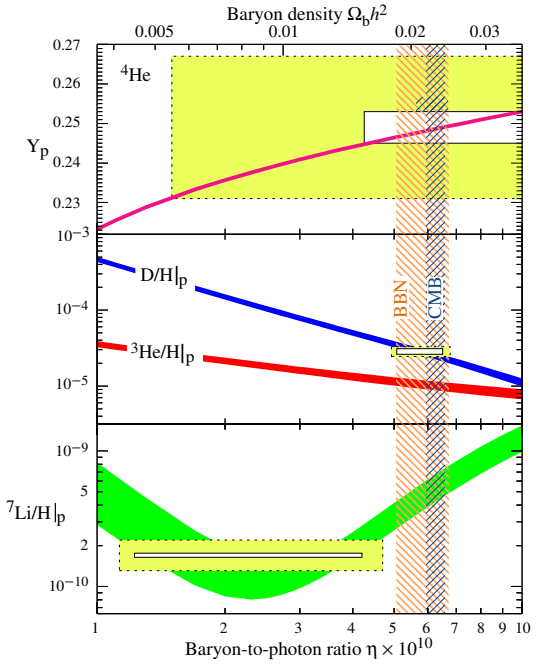

Figure 1.8.: The predicted and measured abundances for the light elements. The baryon density is given on the top axis. The coloured lines are the model predictions and the rectangular boxes are the measurements (white) with errors (yellow). Image taken from `http://pdg.lbl.gov/2012/figures/bbn_11.eps`.

Structure Formation

In Fig. 1.5 the positions of many galaxies according to their redshift are shown and they appear homogeneous on large scales. However, when taking a closer look the galaxies are arranged in some kind of filament structure. How this structure and the structure of the galaxies evolved from the Big Bang is studied in large N-body simulations. It is assumed that the structure seen today is due to quantum fluctuations in the dark matter density in the early Universe. These fluctuations are then blown up in scale by inflation (for a review see Linde (2008)), a rapid expansion of the Universe. The structure forms around the gravitational potentials of the perturbations. The N-body simulations take some simple initial conditions and evolve them to today's complex structure. One of the largest simulations so far is the Millennium simulation (Springel et al., 2005). There a ΛCDM model is assumed and 10 billion dark matter particles, each with a mass of about $10^9\,M_\odot$, are simulated. How well this simulation works is shown in Fig. 1.9(a). The results of the Millennium simulation are compared to measurements from the 2dF galaxy redshift survey (Springel et al., 2006). In Fig. 1.9(b) a result of the Millenium simulation for the structure of dark matter galaxies, which correspond to visible galaxies, is shown. The simulation agrees very well with the measured structure, which further supports the ΛCDM model and the existence of dark matter. Another even more recent simulation is the Aquarius

simulation, see Springel et al. (2008a) and Springel et al. (2008b). From the simulations also information about the distribution of the dark matter today can be gained, which will be discussed later in Section 1.1.4.

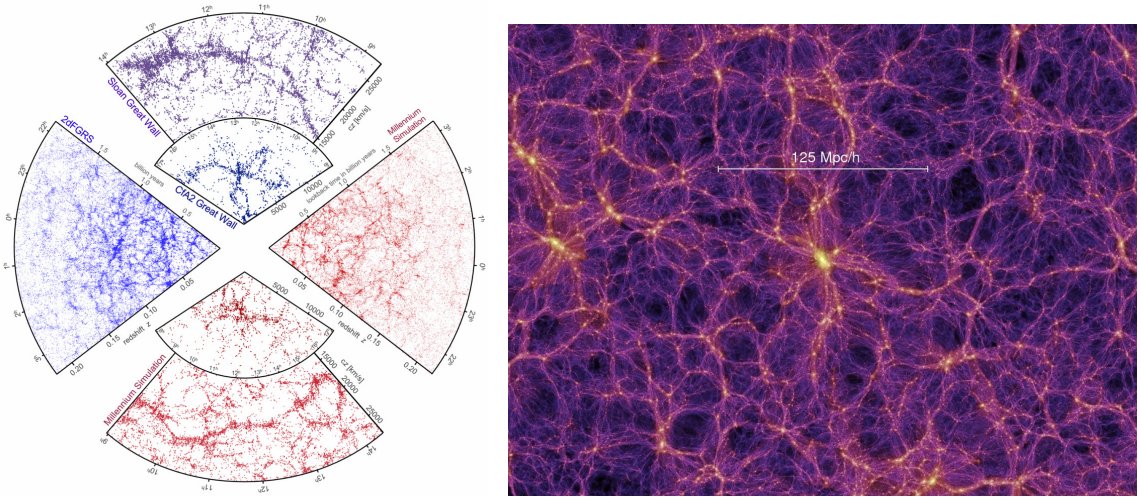

(a) (b)

Figure 1.9.: (a) The results from the Millennium N-body simulation in red and measured results in blue for the 2dF galaxy survey. Image taken from Springel et al. (2006). In (b) the distribution of galaxies over their redshift resulting from the simulation is visible, taken from `http://www.mpa-garching.mpg.de/galform/virgo/millennium/seqD_063a_half.jpg`

1.1.3. Dark Matter Candidates

The measurements and models, described in the Sections before, not only nicely motivate the existence of a dark matter particle, they also already imply most of the properties a dark matter particle candidate must have. Combining the different assumptions and results from above it is clear that the following must hold for a particle to be a dark matter candidate:

- Most essentially the particle must not interact electromagnetically or strongly but only weakly,
- and it must be stable in order to provide the right matter density today.

Further requirements of the dark matter particle candidate are that

- it should be rather massive, otherwise it might have been discovered already,
- and it should be cold or cool, i.e. moving non-relativistically ($v \ll c$) in order to allow for structure formation.

A specific kind of particles that fulfil all of the four criteria are called WIMPs (weakly interacting massive particles) and are among the most promising candidates for dark matter. In the following it is shortly discussed why dark matter candidates in the standard model are not sufficient to describe all the phenomena of the previous Section. After that dark matter candidates beyond the standard model are introduced with focus on WIMPs in supersymmetric theories.

In the Standard Model of Particle Physics

The standard model of particle physics consists of 18 particles and their antiparticles. These are divided into three generations or families of quarks and leptons, plus the force carrier particles (the gauge bosons) and the Higgs particle. The names of the standard model particles and their spin are listed in Table 1.2 on the left. A short look at the conditions above (only the first two) immediately shows that only the neutrinos are viable dark matter candidates. They are neutral and only interact weakly with a very small cross section. Indeed the standard model neutrinos do contribute to the non-baryonic dark matter. Their masses are not precisely known and found to be much smaller than those of any other standard model particle (e.g. Beringer et al. (2012b)), and hence also their contribution to the dark matter density Ω_{DM} is limited. Furthermore because of their low mass neutrinos may travel relativistically, almost with the speed of light. Such fast moving dark matter particles, so-called hot dark matter (HDM), are difficult to include into the structure formation process because they erase structures at small scales.
Other candidates are the massive compact halo objects (MACHOS) already mentioned before. However, they can not account for the dark matter required to coincide with the results described above, see, e.g., Tisserand et al. (2007).
Nevertheless in models beyond the standard model various dark matter candidates exist. Why such extensions of the standard model are needed in general, not only to come up with dark matter candidates, is shortly motivated at the beginning of the next Section. Then models beyond the standard model and the dark matter candidates arising from these are introduced.

Beyond the Standard Model

Despite the fact that the standard model of particle physics agrees very well with the results of many experiments, there are also problems which the standard model cannot fully address. Next to the need for a dark matter candidate there are, e.g., also the hierarchy problem, the strong CP problem and the unification with gravity (for a short description of these problems the reader may consult e.g. Langacker (2003)).
The hierarchy problem can be solved elegantly by introducing of a new symmetry between fermions and bosons – the so-called "supersymmetry". In supersymmetry also a dark matter candidate arises quite naturally. Therefore the next Section is devoted to the concept of supersymmetry (the description follows the first Sections of Martin (1998)).

Supersymmetry and Supergravity

Supersymmetry is a theory based on a hypothetical new symmetry between fermions and bosons. For each fermion the theory supposes the existence of a bosonic partner, and vice versa. The so-called "superpartners" are connected via a supersymmetric transformation. This can be expressed in terms of an operator Q acting either on a fermionic or bosonic particle:

$$Q|\text{Boson}\rangle = |\text{Fermion}\rangle, \qquad Q|\text{Fermion}\rangle = |\text{Boson}\rangle \tag{1.15}$$

Since standard model particles cannot be superpartners to any other standard model particle, the number of particles doubles with the introduction of supersymmetry. The superpartners of the standard model particles are listed in Table 1.2. The naming convention is the following: bosonic partners get an additional 's' at the beginning of the name (e.g. electron – selectron), fermionic partners get the suffix 'ino' appended to the name (e.g. photon – photino).

Table 1.2.: The standard model particles and their superpartners in case of the minimal extension of the standard model.

Standard model	Name	Spin	Superpartner	Name	Spin
ν_e, ν_μ, ν_τ	Neutrinos	$\frac{1}{2}$	$\tilde{\nu_e}$, $\tilde{\nu_\mu}$, $\tilde{\nu_\tau}$	Sneutrinos	1
e	Electron	$\frac{1}{2}$	$\tilde{e}$	Selectron	1
μ	Muon	$\frac{1}{2}$	$\tilde{\mu}$	Smuon	1
τ	Tauon	$\frac{1}{2}$	$\tilde{\tau}$	STauon	1
u,d,s,c,t,b	Quarks	$\frac{1}{2}$	$\tilde{u}$,$\tilde{d}$,$\tilde{s}$,$\tilde{c}$,$\tilde{t}$,$\tilde{b}$	Squarks	1
γ	Photons	1	$\tilde{\gamma}$	Photino	$\frac{1}{2}$
Z	Z-Boson	1	$\tilde{Z}$	Zino	$\frac{1}{2}$
W^+,W^-	W bosons	1	$\tilde{W^+}$,$\tilde{W^-}$	Winos	$\frac{1}{2}$
g	Gluons	1	$\tilde{g}$	Gluinos	$\frac{1}{2}$
H_2^+,H_1^-,H_2^0,H_1^0	Higgs	1	$\tilde{H_2^+}$,$\tilde{H_1^-}$,$\tilde{H_2^0}$,$\tilde{H_1^0}$	Higgsinos	$\frac{1}{2}$

Without further requirements the masses of the supersymmetric partner particles would be degenerate with those of the standard model particles. However, such particles have not been found experimentally and therefore the masses of the superpartners must be different from the standard model masses, i.e. supersymmetry has to be broken. This can be achieved by adding a soft breaking term $\mathcal{L}_{\text{soft}}$ to the supersymmetry Lagrangian $\mathcal{L}_{\text{susy}}$ (for details the reader may consult Martin (1998)). The soft breaking leads to masses of the superpartners heavier than the standard model masses.

Another problem, though, is that with supersymmetry, as defined so far, proton decay becomes possible with a lifetime inconsistent with lower limits from experiments (e.g. Nishino et al. (2009)). A solution is provided by introducing a new quantum number called R-parity and imposing its conservation. The R-parity is defined as

$$R = (-1)^{3\cdot(B-L)+2S} \tag{1.16}$$

where B is the baryon number, L the lepton number and S the spin of the particle. With this definition every supersymmetric particle automatically has $R = -1$ and every standard model particle $R = 1$. The conservation of R-parity then implies that the product of R-parities R_i at each vertex of a Feynman diagram equals 1: $\prod R_\mathrm{i} = +1$. With this condition the decay of the proton mediated by a supersymmetric particle is forbidden.
With this the lightest supersymmetric particle (LSP) naturally emerges as dark matter candidate. In the following only the case where the LSP is the so-called neutralino is considered. The term neutralino denotes a linear mixture of the eigenstates of the Bino $\tilde{B}$, the Wino $\tilde{W}_3$ and the neutral Higgsinos $\tilde{H}_1^0$, $\tilde{H}_2^0$. Due to R-parity and energy conservation the neutralino is stable. Furthermore it is neutral and only weakly interacting. While it is stable, the neutralino can annihilate, because it is a Majorana particle, i.e. its own antiparticle. This makes the neutralino a perfect dark matter candidate and the products of the annihilation process can be searched for in experiments.
In order to obtain predictions for the properties and signals from the annihilation of supersymmetric dark matter one can use elaborated software (e.g. the darkSUSY package (Gondolo et al., 2004)). The predictions are mostly obtained for the minimal supersymmetric and the minimal supergravity model (MSSM and mSUGRA, respectivly). The MSSM is a model where the overall number of parameters (105) in supersymmetry is reduced to seven parameters. mSUGRA is a further extension of supersymmetry including gravity. It also contains the neutralino as dark matter candidate. mSUGRA only takes five parameters. Nevertheless also for mSUGRA many different potential models exist and predictions can again be obtained with darkSUSY (Gondolo et al., 2004). In the following Sections the focus will lie on supersymmetric (neutralino) dark matter, but for completeness some alternative models and dark matter candidates are listed, as well.

Other extensions to the standard model

Besides supersymmetry many other ways to extend the standard model of particle physics exist. A lot of these extensions also contain potential dark matter candidates. In the following two other dark matter candidates apart from the supersymmetric neutralino are introduced.

- In the Kaluza-Klein theory (first discussed by Kaluza (Kaluza, 1921) and Klein (Klein, 1926)) the existence of universal extra dimensions (UED) is assumed. The underlying idea was to unify gravity with electromagnetism. Again, similar to supersymmetry,

the lightest Kaluza-Klein particle (LKP) serves as a good dark matter candidate. Searches for supersymmetric dark matter are often also sensitive to Kaluza-Klein dark matter, because the products from the decay or annihilation of Kaluza-Klein dark matter are essentially the same as from supersymmetry.

- Another dark matter candidate are axions. Axions are particles postulated by a theory from Peccei and Quinn (1977) invented in order to solve the strong CP problem. In contrast to the LSP and the LKP the axion is lighter than all standard model particles. It is supposed to exist in a so called hidden sector of the standard model, which only very weakly interacts with the standard model particles. The axion can be included in the standard model and could also have a massive supersymmetric partner. So far no signal of axions has been found.

No dark matter

A completely different approach to the problem of dark matter independent of the standard model of particle physics is the MOND (modified Newtonian dynamics) theory (Milgrom, 1983). There Newtonian gravity is altered in such a way that it can account for the observations of rotation curves of galaxies without the need of additional mass. Hence in MOND theories no dark matter at all is needed.

1.1.4. Dark Matter Halo

In the previous Sections the existence of dark matter was motivated and potential dark matter candidates were introduced. Now the question arises how the dark matter is distributed in the Universe. In the following two formulas for the dark matter density in galaxies are introduced.
Usually the dark matter forms a halo around the centre of a galaxy. Several observational but also theoretical methods enable us to estimate the distribution of dark matter. Measurements of rotation curves of galaxies can be used to infer the characteristics of the dark matter halo. A phenomenological shape of dark matter halos that agrees with many observations is

$$\rho(r) \propto \frac{\rho_0}{\left(\frac{r}{a}\right)^{\gamma}\left[1+\left(\frac{r}{a}\right)^{\alpha}\right]^{\frac{\beta-\gamma}{\alpha}}} \tag{1.17}$$

with r being the radial distance to the centre of the galaxy and a a scale parameter. ρ_0 is a normalisation and in case of the Milky Way is chosen such that the density at Earth is $\rho(r = 8.5\,\mathrm{kpc}) = 0.39\,\frac{\mathrm{GeV}}{\mathrm{cm}^3}$). For $\alpha = 1.0$, $\beta = 3.0$ and $\gamma = 1.0$ the Navarro-Frenk-White profile (NFW profile (Navarro et al., 1996)) is obtained. This profile has a scale factor of $20\,\mathrm{kpc} \leqslant a \leqslant 30\,\mathrm{kpc}$ for a galaxy of similar size as the Milky Way. The NFW profile was derived from N-body simulations (Navarro et al., 1996).

The most recent N-body simulations of structure formation are the Aquarius (Springel et al., 2008a) and the Via Lactea II project (Diemand et al., 2008). For Milky Way like galaxies the Via Lactea project found a halo comparable with the NFW profile, but the results from the Aquaruis project favoured a different shape: The Einasto profile (Einasto, 1965). It is defined as

$$\rho(r) = \rho_0 \exp\left[-\frac{2}{\alpha}\left(\left(\frac{r}{r_\mathrm{s}}\right)^{\alpha} - 1\right)\right]. \tag{1.18}$$

In the Aquarius simulation a value of $\alpha = 0.17$ was found. The normalisation ρ_0 is chosen in the same way as above.
Compared to the NFW profile the Einasto profile is less steep towards the centre of the galaxy, see Fig. 1.10(b). Nevertheless the density is highest in the galaxy centre also for the Einasto profile. In the simulations by Springel et al. (2008a) and Diemand et al. (2008) especially the influence of subhalos, i.e. smaller local halos inside the galaxy, on the overall halo was studied, but found to be very small (Pieri et al., 2011). The shape of the density distribution is determined by the main halo around the centre. An example of such a main halo for a Milky Way like galaxy as it results from the Aquarius project (Springel et al., 2008b) is displayed in Fig. 1.10(a).
There are also other dark matter halo profiles, e.g. the Moore profile (Moore et al., 1998), which corresponds to $\alpha = 1.5$, $\beta = 3.0$ and $\gamma = 1.5$ in Eq. 1.17. Essentially the profiles all agree well with the general shape of Eq. 1.17. In the following only the profiles fitting the recent results by Springel et al. (2008a) and Diemand et al. (2008) are used.

1.1.5. Dark Matter Searches

So far no dark matter particle has been identified but there are many experiments searching for dark matter. Two different approaches are used to search for hints of dark matter particles. One way is to search for dark matter dierctly. The method is called direct because the primary interaction between dark matter particles and other particles is studied. In contrast to this indirect searches for dark matter focus on the detection of secondary particles from the annihilation or decay of dark matter. These two methods are described further in the following.

Direct Detection

In direct dark matter searches it is tried to measure the recoil energy of a target nucleus which was hit by a dark matter particle. This is a very difficult task because of the extreme level of background rejection typically required in such experiments. Therefore these experiments are usually conducted deep underground and further use elaborate shielding techniques to reduce the background. The target material of the experiments varies from crystals to cyroliquids, common choices are Germanium and/or Silicon (EDELWEISS (EDELWEISS, 2013), CoGeNT (COGENT, 2013), CDMS (CDMS, 2013)), (thallium-doped) sodium

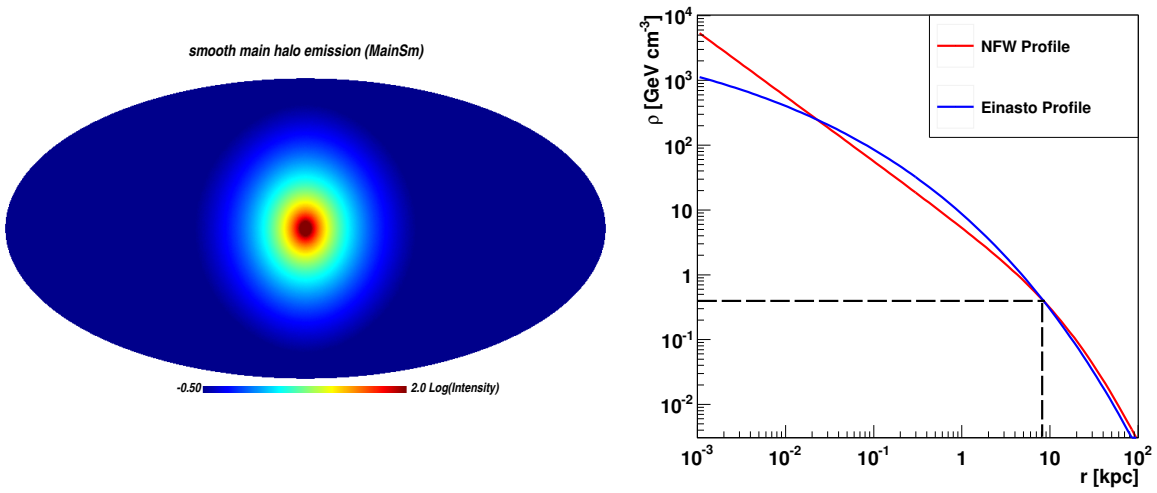

(a) (b)

Figure 1.10.: (a) The 2d main halo of a Milky Way like galaxy as it results from the Aquarius simulation. Image taken from arxiv version of Springel et al. (2008b). (b) Plot of the two different density profiles described in the text, which are assumed to describe the dark matter density in the Milky Way. The black dashed lines indicate the dark matter density at the position of the Sun.

iodide (DAMA/NaI, DAMA/LIBRA (DAMA, 2013)), and also liquid Xenon (XENON10, XENON100 (XENON, 2013)). In case of no signal upper limits on the nucleon-WIMP cross section between the dark matter particle and the nuclei of the target material are obtained. Results form the above mentioned experiments are shown in Fig. 1.11. Two of the experiments (DAMA and CoGeNT) have already claimed detections (e.g. in Bernabei et al. (2010) and Aalseth et al. (2011)). These experiments search for an annual modulation signal, which can be interpreted as dark matter. However so far their results have not been confirmed by other experiments.

Another direct way to search for dark matter is the creation of dark matter particles at a collider. With the start-up of the LHC, an interesting mass range addressed in many models has become accessible. The measurement idea is the following: Dark matter particles created in the collisions would escape the detector and the missing energy would be registered. So far only upper limits on the supersymmetric parameter space have been determined (for a summary the reader may consult Beringer et al. (2012c)). Nevertheless these limits already constrain the supersymmetric parameter space significantly and for the simplest models to fulfil all experimental constraints the masses of the dark matter particle have to be quite high (>500 GeV). Additionally a Higgs particle with a mass around 126 GeV (ATLAS Collaboration Aad et al., 2012) strongly restricts the supersymmetric parameter space, see e.g. Arbey et al. (2012).

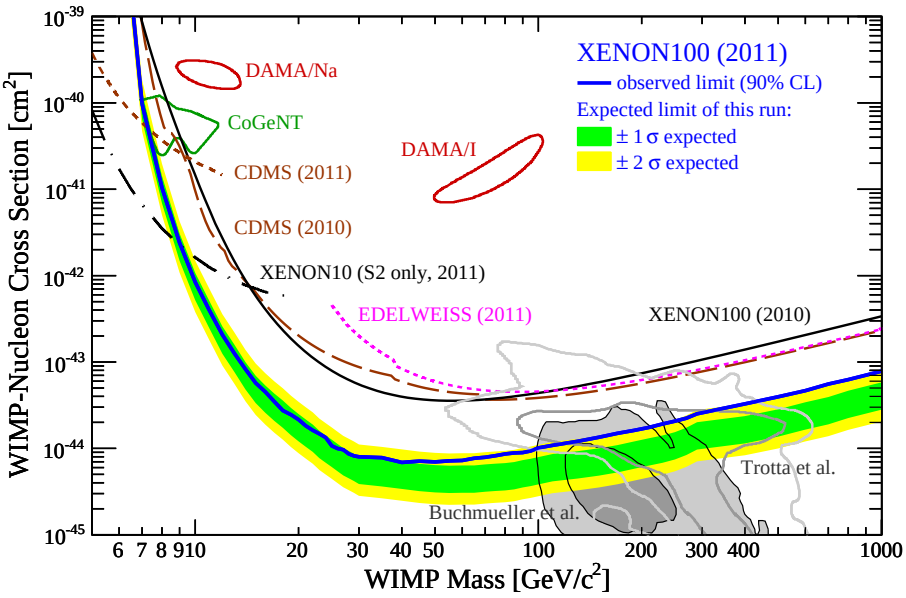

Figure 1.11.: Results (upper limits on or confidence regions for the nucleon-WIMP cross section depending on the hypothetical WIMP mass) from different experiments searching directly for dark matter. In the lower part also cross sections predicted by models are indicated (grey regions). Image from Aprile et al. (2011).

Indirect Detection

Beside the direct searches for dark matter also indirect searches exist. It was mentioned before that dark matter candidates, e.g. neutralinos, are annihilating and the products of this annihilation can be searched for. The main annihilation products used for indirect detection are gamma rays and neutrinos. Additionally also electrons, positrons and other standard model particles can be created in the annihilation process. An overview of the particles that can be created in such a neutralino annihilation, is shown in Fig. 1.12. Many different annihilation channels exists and the products of these channels further decay as indicated in Fig. 1.12. A peak was found in the cosmic ray electron spectrum which could be explained with dark matter (Chang et al., 2008). However, subsequent measurements with smaller experimental uncertainties failed to confirm the earlier findings ((Aharonian et al., 2009a), (Abdo et al., 2009)). Also an excess in cosmic-ray positrons (Adriani et al., 2009) recently confirmed by the Alpha Magnetic Spectrometer (AMS) on the International Space Station (Aguilar et al., 2013) can be interpreted in terms of dark matter e.g. Bergström et al. (2008). Additionally neutrino telescopes (IceCube (ICECUBE, 2013), ANTATRES (ANTARES, 2013)) search for dark matter. Finally also from gamma ray observations, by e.g Fermi or by imaging atmospheric Cherenkov telescopes (IACTs) like MAGIC, VERITAS and H.E.S.S., upper limits on the cross sections of WIMPs are derived (for a review see (Bringmann and Weniger, 2012)). More details on the upper limits derived from observations conducted by the H.E.S.S. experiment will follow in the next Section.

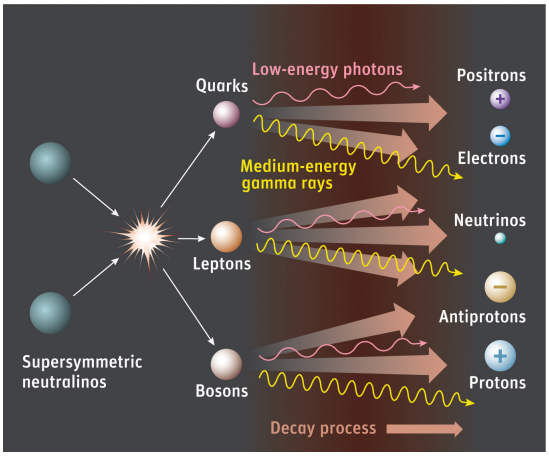

Figure 1.12.: Overview of the all the potential outcomes of a neutralino annihilation. Image credit: Sky & Telescope / Gregg Dinderman

1.1.6. Dark Matter Searches with H.E.S.S.

H.E.S.S. (see Section 3.2.) is an experiment which detects very high energy (VHE $> 100\,\mathrm{GeV}$) gamma rays. When dark matter annihilates also gamma rays are produced, see Fig. 1.12. For neutralinos $\tilde{\chi}$ there are in general three annihilation channels which lead to gamma rays:

- $\tilde{\chi}\tilde{\chi} \longrightarrow \gamma\gamma$,
- $\tilde{\chi}\tilde{\chi} \longrightarrow \gamma Z^0$,
- and the continuous gamma rays, which are secondary products from other annihilation products, mainly from neutral pions.

The first two processes can lead to a monochromatic line signal, peaked around the mass of the neutralino. However, the number of photons from these processes is rather small compared to the number of photons from the third process. In general the expected integrated continuous gamma ray flux due to dark matter annihilation in the galaxy at a detector on Earth is

$$\Phi_\gamma(\psi) = \underbrace{\int \frac{\mathrm{d}\Phi}{\mathrm{d}E}\mathrm{d}E}_{\text{particle physics}} \times \underbrace{J(\psi,\Delta\Omega)\Delta\Omega}_{\text{astrophysics}}. \tag{1.19}$$

The individual contributions to Eq. 1.19 will be introduced in the following:

- The first term is the integral over the energy of the differential flux due to the physics of the dark matter particle

$$\int_E \frac{\mathrm{d}\Phi}{\mathrm{d}E}\mathrm{d}E = \frac{1}{4\pi}\frac{\langle\sigma v\rangle}{M_\chi^2}\int_E \frac{\mathrm{d}N}{\mathrm{d}E}\mathrm{d}E, \tag{1.20}$$

with $\langle \sigma v \rangle$ being the velocity-averaged total cross section into gamma rays and M_χ being the mass of the dark matter particle. $\frac{dN}{dE}$ is the yield of the gamma rays or the spectrum of gamma rays per annihilation. For neutralino dark matter two parametrisations of the gamma ray yield are given here: The Bergstroem spectrum (Bergström et al., 1998) and the Tasitsiomi spectrum (Tasitsiomi and Olinto, 2002).

$$\left(\frac{\mathrm{d}N_\gamma}{\mathrm{d}E_\gamma}\right)_{\text{bergstr}} = \frac{0.73}{x^{\frac{3}{2}}} e^{-7.8x} \tag{1.21}$$

$$\left(\frac{\mathrm{d}N_\gamma}{\mathrm{d}E_\gamma}\right)_{\text{tasitsi}} = -\frac{5}{4}x^{\frac{1}{2}} + \frac{10}{3} - \frac{5}{2}x^{-\frac{1}{2}} + \frac{5}{12}x^{-\frac{3}{2}} \tag{1.22}$$

with $x = \frac{E_\gamma}{M_\chi}$. Both parametrisations represent featureless spectra, see Fig. 1.13(a). However, in Bringmann et al. (2008) additional contributions to the spectrum (and also to the monochromatic line) due to bremsstrahlung are discussed. These contributions could lead to a peak feature in the spectrum and yield even higher fluxes than the two parametrisations above. With the darkSUSY software spectra including the internal bremsstrahlung contributions for individual models can be calculated. The contributions from internal bremsstrahlung are strongly dependent on the choice of the supersymmetric model and vary from almost zero to quite significant values, see Fig. 1.13(b).

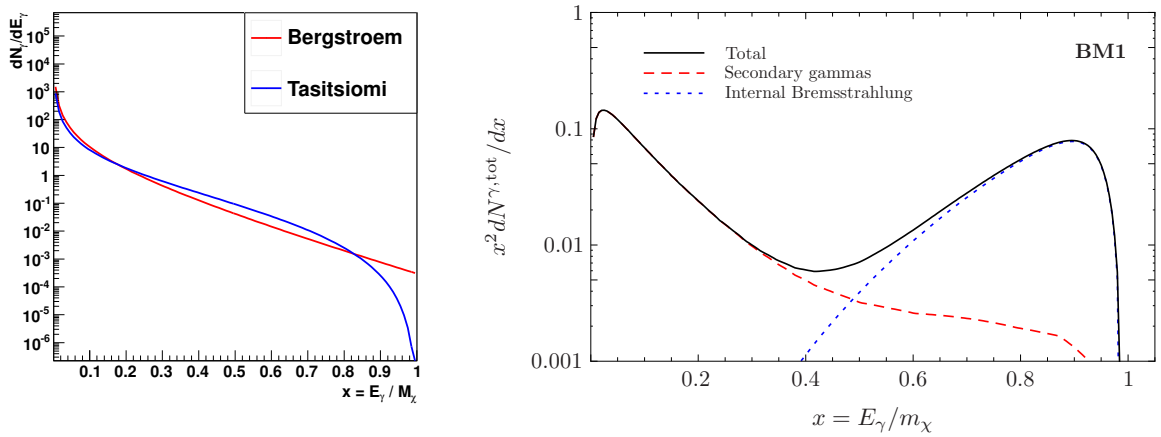

(a) (b)

Figure 1.13.: The different parametrisations for spectrum from dark matter annihilation (a). The spectrum with internal Bremsstrahlung contributions for a benchmark model (BM1) (b). Image (b) taken from Bringmann et al. (2008).

- The second term of Eq. 1.19 takes into account the dark matter density $\rho(r)$ along

the line of sight (l.o.s.) and the opening angle $\Delta\Omega$ of the detector:

$$J(\psi,\Delta\Omega) = \frac{1}{\Delta\Omega}\int_{\Delta\Omega} \mathrm{d}\Omega' \int_{\mathrm{l.o.s.}} \rho^2(\psi(l))\mathrm{d}l \tag{1.23}$$

Here ψ is the radial distance to the Galactic Centre in radian.

From Eq. 1.19 is follows immediately that the flux is highest for the regions where the dark matter density is highest. Therefore it is straightforward to search for a signal from dark matter annihilation in such regions. The Milky Way and especially its centre is clearly one of the favoured regions and it will be considered further in the next Section. Besides the Milky Way also local dwarf galaxies are supposed to have high dark matter densities with profiles similar to the one of the Milky Way. H.E.S.S. observed the Sgr Dwarf (Aharonian et al., 2008), (Aharonian et al., 2010), the Canis Major (Aharonian et al., 2009c) and the Carina and Sculptor galaxies (H.E.S.S. Collaboration et al., 2011). Furthermore galaxy clusters, which are also supposed to have high dark matter densities, were observed (Abramowski et al., 2011a), (Abramowski et al., 2012b). No dark matter signal was found and upper limits on the velocity-averaged cross section were obtained. In Fig. 1.15 recent upper limits are shown.
In case of the above mentioned dwarf galaxies and galaxy clusters no considerable astrophysical background (a gamma ray source) is in the field of view. This, however, is different for the Galactic Centre, as will be discussed in the next Section.

1.2. Dark Matter and the Galactic Centre

Considering the overall dark matter density throughout our Galaxy, the highest value is assumed to be reached at the Galactic Centre, see also Section 1.1.4. Therefore it naturally is a very interesting target for the search for dark matter. However, the Galactic Centre region also contains many individual astrophysical objects. In the following a short overview of the Galactic Centre region is given with a focus on the very-high-energy observations by H.E.S.S.

1.2.1. The Galactic Centre Region

In the following the term "Galactic Centre region" refers to the innermost region of the Galaxy up to about 600 pc in longitude and 200 pc in latitude. This falls within a single field of view of the H.E.S.S. I cameras. The main objects in the Galactic Centre region are

- Sgr A region
- Sgr A*
- Molecular clouds

The Sgr A region as well as Sgr A* were originally detected as a single radio source (Balick and Brown, 1974). But with improving resolution several other emission regions associated with different objects became distinguishable (for an overview see Goldwurm (2008)), among them an SNR shell and giant molecular clouds. Sgr A* is the counterpart of a supermassive black hole (SMBH) at the dynamical centre of our Galaxy. From the interplay of these objects high-energy gamma radiation is expected, but because of the density of the objects source identification is complicated. The molecular clouds offer an efficient target region for cosmic rays accelerated at the Galactic Centre.
In the VHE regime gamma ray emission from the Galactic Centre was observed by Whipple (Kosack et al., 2004) and CANGAROO (Tsuchiya et al., 2004) and in 2003 by 2 telescopes of H.E.S.S. (Aharonian et al., 2004a). The location of the source was found to be consistent with the position of the SMBH Sgr A* (Acero et al., 2010). The VHE source is called HESSJ1745-290 from now on. Deeper observations showed that besides HESSJ1745-290 there is another point source in the Galactic Centre region: The supernova remnant (SNR) G0.9+0.1 (Aharonian et al., 2005). Furthermore, also diffuse emission was detected (Aharonian et al., 2006c), see Fig. 1.14(b). The diffuse emission is elongated along the Galactic Plane around the Centre. The diffuse emission might be due to the molecular clouds and gamma rays propagating through the interstellar medium. However no conclusive understanding of the origin has been reached so far.

1.2.2. H.E.S.S. Dark Matter Searches at the Galactic Centre

When the source HESSJ1745-290 was discovered, it was tested, whether the source could be due to annihilating dark matter (Aharonian et al., 2006a). However, the spectrum extends to energies well above 5 TeV and a dark matter particle with such a high mass is not favourable. Hence the source is most probably originating from another emission process. Therefore the source HESSJ1745-290, the source G0.9+0.1 and the region with diffusive emission have to be excluded from an analysis which searches for a dark matter signal. In spite of these large excluded regions in the field of view (FoV) it is still possible to analyse the remaining region and this was done in H.E.S.S. Collaboration et al. (2013) and Abramowski et al. (2011b). In both publications searches for a signal from the dark matter halo are performed. In H.E.S.S. Collaboration et al. (2013) a spectrum from the Galactic Centre region, with the source at the centre and the Galactic Plane (up to a lattitude of $b = \pm 0.3$) excluded, is searched for peaks or line like signatures, which are predicted from dark matter annihilation (annihilation into two gammas or a gamma and a Z^0 boson with internal bremsstrahlung). With this upper limits are achieved, see Fig. 1.15(b).
Furthermore since the H.E.S.S. experiment has a large FoV of 5 ° the dark matter density changes significantly in a single FoV – from the highest density (100%) at the centre to lower values ($< 50\%$) 2.0° away from it. Therefore regions near the Galactic Centre (inside a 1° radius) are compared to regions away from it (in a ring between the radii 1.2° and 2.0°) but still in the same FoV - hence from the same observation. The region near the centre serves as target region and the region away from it is used for background estimation. The

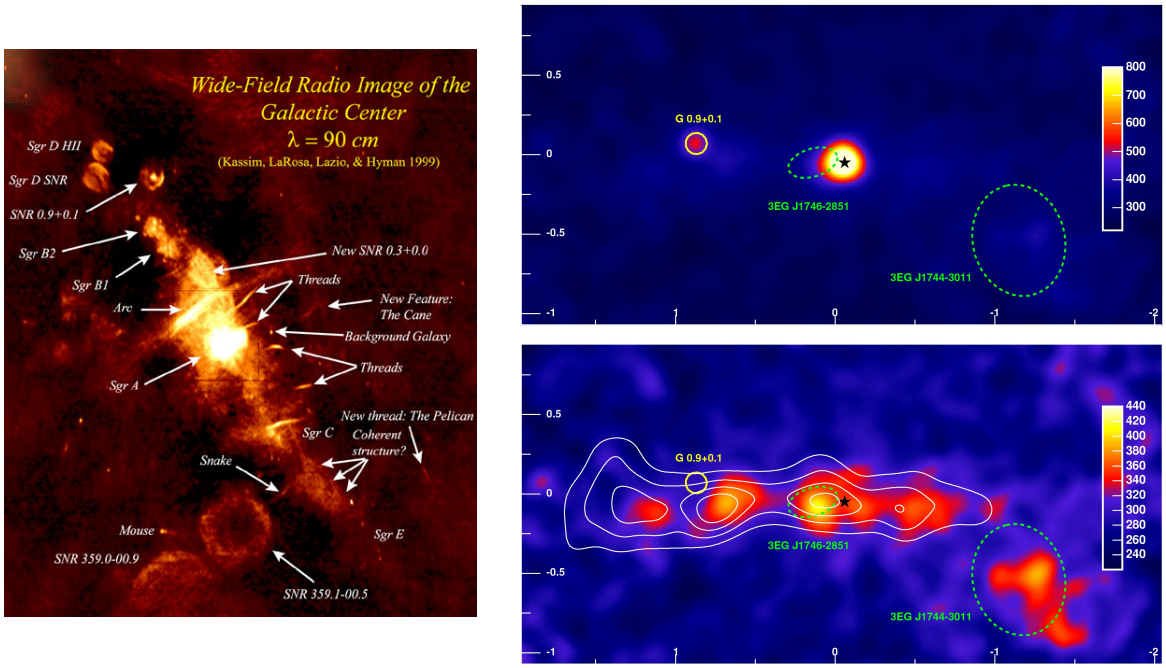

(a) (b)

Figure 1.14.: (a) The Galactic Centre region at radio wavelengths in RaDec coordinates. The Galactic Plane runs from the top left to the bottom right corner. Many of the individual objects in the crowded region are labelled. Image from Kassim et al. (1999). In (b) the same region in very high energy gamma rays in Galactic coordinates is shown. Here the Galactic Plane runs horizontally from left to right. In the lower image the two point sources visible above have been subtracted and the diffuse emission becomes visible. Image from Aharonian et al. (2006c).

selection of the regions is described in more detail in Abramowski et al. (2011b). From this analysis an upper limit can be derived, see Section 1.1.6. However, also in the region away from the Galactic Centre a signal due to dark matter annihilation is expected, because of the non-vanishing dark matter density, see the inlay in Fig. 1.16. This signal has to be taken into account when deriving the upper limit.
The results of both analyses are depicted in Fig. 1.15. The question now remains how to improve these upper limits. An idea is to compare the region at the Galactic Centre to regions far away from it (with radii $> 2.0°$) with almost vanishing dark matter density. This would reduce the expected signal in the background region and could lead to a lower upper limit. However, then no longer the same FoV - and therefore no longer the same observation - can be used to obtain the gamma rays in the target and the background region. This is illustrated in Fig. 1.16. There it is also indicated that the different regions might have been observed under different telescope positions (pointings). The efficiency of the detector and hence the number of expected gamma rays though, depend on the

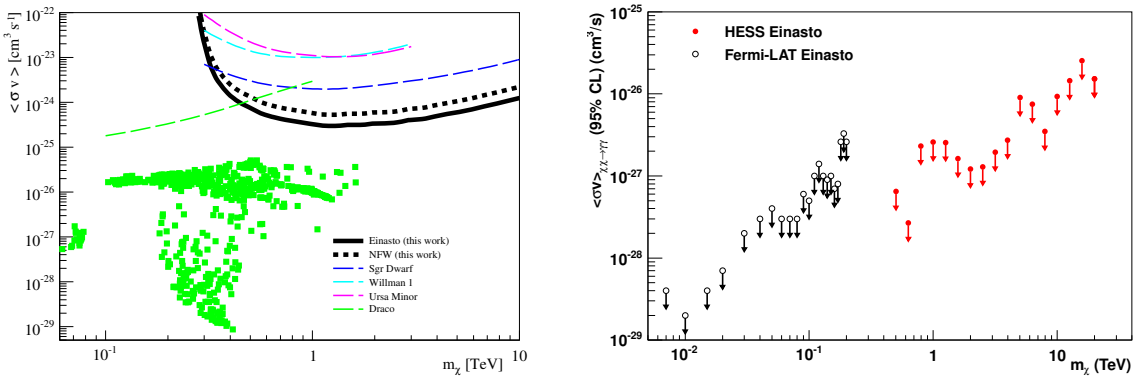

(a) (b)

Figure 1.15.: (a) Upper limits on the velocity-averaged cross section from neutralinos into continuous gamma rays obtained in searches for a γ-ray signal from the dark matter halo of the Milky Way and from other regions with high expected dark matter densities. The green squares are cross section values from supersymmetric models. In (b) upper limits on the velocity-averaged cross section from neutralinos into two gamma rays ($\tilde{\chi}\tilde{\chi} \longrightarrow \gamma\gamma$) from a search for peaks in the spectrum of the Galactic Centre region are shown. Images from Abramowski et al. (2011b) and H.E.S.S. Collaboration et al. (2013).

telescope position, therefore systematic effects enter the determination of the target and the background gamma ray counts. Furthermore also a change in other observation conditions, like e.g. the weather, implies systematic effects. All these effects need to be understood very well in order to produce a reliable upper limit. The understanding of these systematics was therefore one of the main aims of this work. Additionally the standard H.E.S.S. analysis so far only uses data from a single FoV to determine the target and the background gamma ray counts. A further aim was therefore the implementation of an analysis using regions from different FoVs for this determination.

In the next Chapter the basics for VHE gamma ray astrophysics are described and detailed information on the H.E.S.S. experiment is given and the calibration and analysis techniques used are introduced.

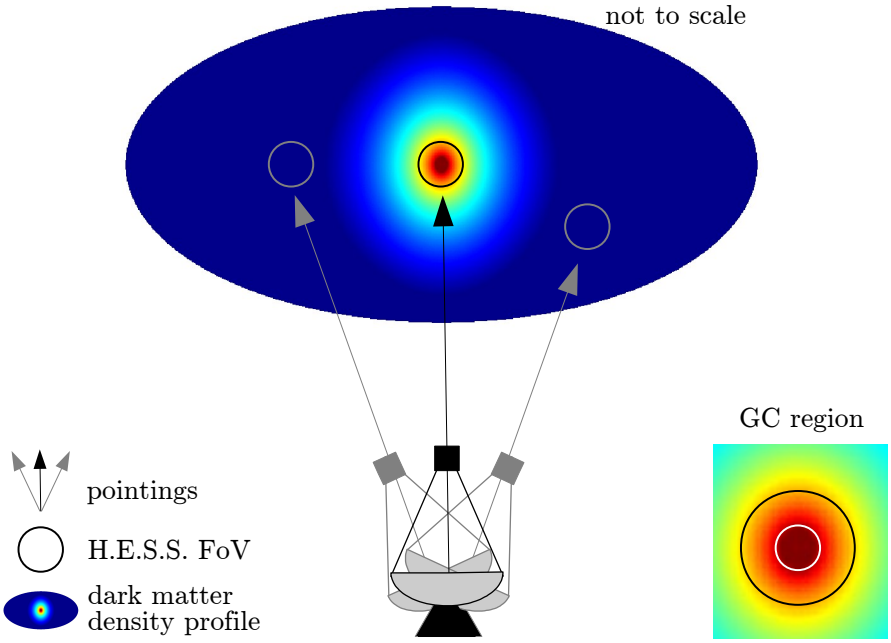

Figure 1.16.: Illustration of the observation principle aimed at searching for a signal from the dark matter halo in the Milky Way. On top of the dark matter density profile of the galaxy potential observation positions are drawn. It is indicated that for the different positions different telescope configurations (pointings) are used. The inlay on the right is a zoom inside the FoV centred on the Galactic Centre (GC) region. It is visible that the dark matter density is highest in the potential target region (white circle), but also in the background region up to the edge of the FoV (black circle), as used in Abramowski et al. (2011b), the density is not negligible. Hence particular off regions (grey circles) separate from the Galactic Centre have to be chosen in which the dark matter density is negligible.

2. Very High Energy Gamma Ray Astronomy with H.E.S.S.

In 1912 Victor Hess discovered the first hints for the existence of cosmic rays. He measured the ionisation of the atmosphere at high altitudes during seven balloon rides (Hess, 1912), see Fig. 2.1(a). His measurement, visible in Fig.2.1(b), showed an increase in the ionisation rate with increasing altitudes. Hess emphasised that this is best explained by a radiation coming from space to Earth and penetrating Earth's atmosphere.

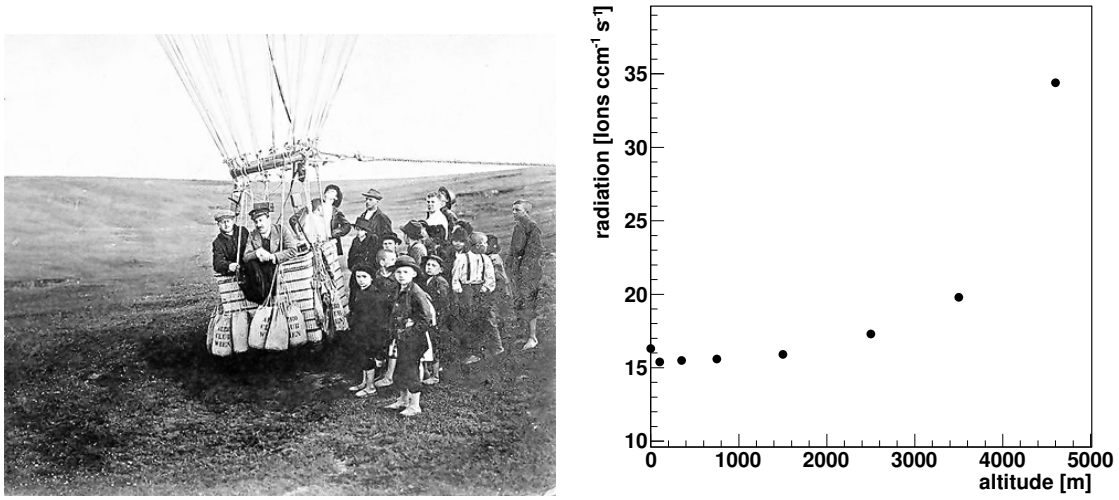

(a) (b)

Figure 2.1.: (a) Photograph of Victor Hess surrounded by onlookers before one of his balloon rides. Image credit: University of Innsbruck/Hess Society. In (b) the ionisation rate as measured with one of his three detectors and averaged over a total of seven balloon flights is plotted. The data are taken from Table. 3 in Hess (1912).

Today it is well established that radiation from the cosmos reaches Earth. This cosmic radiation consists of charged particles, such as electrons, protons and heavier hadrons, but also of photons and neutrinos. The latter two are neutral and therefore travel to Earth uninfluenced by interstellar magnetic fields. Hence they are searched for in order to locate

sources of cosmic radiation. In the following the search for cosmic ray photons is described a bit more.
Photons can be observed over a very large energy range from radio ($E \sim$ neV) over infrared ($E \sim$ meV) up to very high energy (VHE) gamma rays with $E > 100\,\mathrm{GeV}$. However not for all energies the direct detection on the ground is possible. This is illustrated in Fig. 2.2. There the opacity of the earth's atmosphere at different energies is shown. VHE gamma rays (as well as X-rays) do not reach the ground, because they are entirely absorbed in the atmosphere. A solution are space based observatories, which proved very successful as e.g. the Large Area Telescope (LAT) on board the Fermi satellite (Atwood et al., 2009). However, due to the limited payload on a satellite also the effective area of the detector is constrained, and as the gamma ray flux decreases with increasing energies, there is a natural upper limit to the energies, detectable with a satellite experiment for reasonable observation times. For Fermi, which covers the highest energy range among space-based observatories to date, this limit is in the range of about 100 GeV. To observe also VHE ($E > 100\,\mathrm{GeV}$) gamma rays a much larger effective detection area is needed, and this can only be achieved in ground-based experiments. Indeed the observation of VHE gamma rays on the ground is possible, because the interaction of the gamma rays in and with the atmosphere leads to air showers, which emit Cherenkov light. The Cherenkov light can then be measured and the properties of the particle that initiated the air shower can be reconstructed.

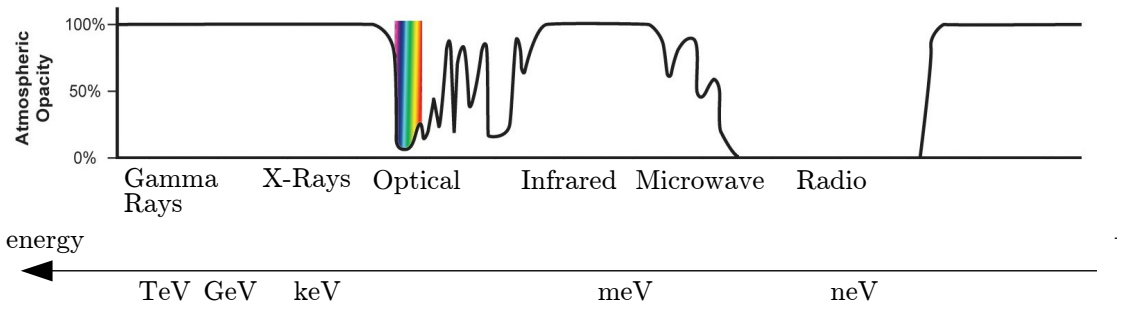

Figure 2.2.: Transparency of the Earth's atmosphere at different energy ranges.

The following Sections explain in more detail how the Cherenkov light is generated in the air shower and how the detection principle works. After that the H.E.S.S. experiment and its reconstruction and analysis techniques are described.

2.1. The Detection of Air Showers

2.1.1. Air Showers

Whenever a VHE particle enters the atmosphere it initiates a particle cascade, in which its energy is deposited. Usually such a cascade starts at a height of about 10 km to 20 km. In these particle cascades or air showers various mechanisms take place. If the primary particle is a VHE gamma ray the main processes above the critical energy are pair production and Bremsstrahlung. The critical energy E_{crit} is defined as the energy at which the losses for the charged particles (e+ and e-) due to Bremsstrahlung and to ionization become equal. Below the critical energy the shower dies out fast because of ionization and atomic excitation. A schematic development of an air shower above the critical energy with a gamma ray as primary particle is depicted in Fig. 2.3(a). There the development of the shower according to the simple model of Bethe and Heitler (Bethe and Heitler, 1934) is shown. In this model only Bremsstrahlung and pair production are considered. Furthermore the radiation length X_0 for both processes is assumed to be equal. The primary gamma converts after one radiation length into an electron-positron pair, each carries half the energy E_0 of the primary gamma. After another radiation length the electron and the positron each emit a photon due to Bremsstrahlung. The photon now carries half the energy of the electron (positron). The following properties of the shower can be obtained from this model:

- After n radiation lengths the shower contains $N(n) = 2^n$ particles, each with energy $E(n) = E_0 \cdot 2^{-n}$.
- The depth d_{max} of the maximum of the shower in units of radiation lengths can be determined from the condition, that the energy at d_{max} is equal to the critical energy. Then d_{max} is given by $d_{\mathrm{max}} = \frac{\ln(E_0/E_{\mathrm{crit}})}{\ln 2}$.
- The number of particles N_{max} in the shower at the maximum depth d_{max} is $N_{\mathrm{max}} = \frac{E_0}{E_{\mathrm{crit}}}$.

Now in Fig.2.3(b) a shower is sketched for the case where the primary particle is a hadron. There not only electromagnetic interactions take place but also other processes, like e.g. the generation of pions. The hadronic shower can be divided into different components, an electromagnetic component (containing e.g. photons from decaying neutral pions as well as muons from decaying charged pions), a strong mesonic component (containing mesons) and a strong nucleonic component (consisting of nucleons (N, P, n, p)).

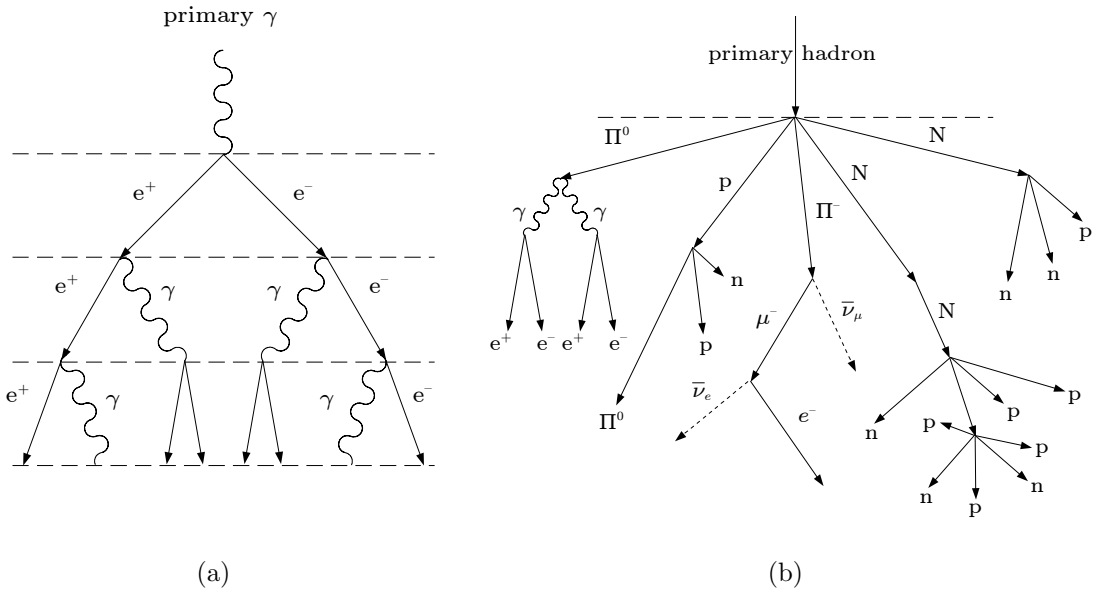

Figure 2.3.: The schematic development of particle showers in the atmosphere for two different primary particles. In (a) a sketch of a shower according to the Bethe Heitler model with a gamma as primary particle is shown. In (b) a shower with a hadron as primary particle is sketched.

2.1.2. Cherenkov Light

In the particle cascades of both air showers many charged particles are created, which have still very high energies. Therefore these particles move faster than light in the surrounding medium (air), which leads to the emission of Cherenkov light. The Cherenkov light is emitted under a fixed angle Θ_C, see Fig.2.4(a). Θ_C is determined by the refractive index of the medium (air) n_{air} and the speed of the particle v:

$$\cos\Theta_C = \frac{c}{n_{air} \cdot v} = \frac{1}{\beta \cdot n_{air}}. \tag{2.1}$$

The largest angle $\Theta_{C,max}$ is reached for an ultrarelativistic particle ($v \simeq c$) and is determined by the refractive index n_{air} of the surrounding medium only:

$$\cos\Theta_{C,max} = \frac{1}{n_{air}}. \tag{2.2}$$

Furthermore $\cos\Theta_C$ must not be larger than 1, therefore the minimum energy E_{min} of a charged particle, at which Cherenkov light can still be emitted, is

$$E_{min} = \gamma_{min} \cdot m_0 c^2 = \frac{m_0 c^2}{\sqrt{1 - n^{-2}}}, \tag{2.3}$$

where m_0 is the mass of the charged particle. Therefore light particles, like electrons, are responsible for most of the Cherenkov light.
The Cherenkov light from an air shower (from all the charged particles in the shower, that have energies above the minimum energy E_{min}) is emitted in a light cone, in which the light is distributed homogeneously around the shower axis (with a radius between 80 m to 100 m for a gamma-ray primary particle, see, e.g.,Funk (2005) Section 2.1.2). This light cone illuminates a certain area on the ground, as illustrated in Fig. 2.4(b). The Cherenkov light from the air shower can then be recorded with a telescope positioned inside this light pool. More on the detection of the Cherenkov light follows in the next Section.

2.1.3. Detection Principle

It was mentioned in the previous Section that a telescope can be used to measure Cherenkov light of air showers. The telescope essentially consists of a reflector, which focuses the Cherenkov light of the air shower onto the camera. This is sketched in Fig.2.5, where three light paths from different parts of the shower are drawn. Furthermore on the right the resulting image in the camera is indicated. There the image points corresponding to the three light paths are again highlighted. It is important that this imaging technique is angle preserving, and therefore the image is undistorted. However, the measurable Cherenkov light is merely a light pulse, only in the order of 10 to 100 ns. Therefore any camera measuring the Cherenkov light must be able to handle very short exposure times. Furthermore the

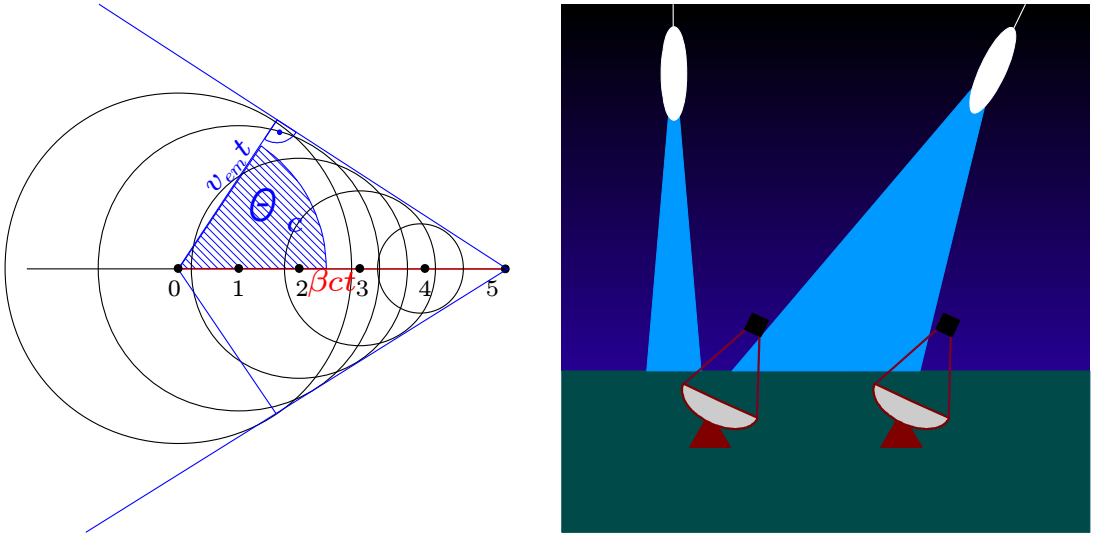

(a) (b)

Figure 2.4.: In (a) the development of Cherenkov light emitted from a single charged particle is shown. In red the path of the faster-than-light charged particle is shown. The circles indicate the waves of the Cherenkov light emitted at positions 1, 2, 3, 4 and 5. A wavefront is built under the Cherenkov angle. In (b) the light cone emitted from an air shower (many charged particles) and the area illuminated by it on the ground are indicated for two showers under different elevation angles.

light pulses have very low intensities and are only recordable if it is very dark. As mentioned before the Cherenkov light of the air shower is emitted in a cone around the direction of the primary particle, but the larger the lateral extent of the shower the wider is also the Cherenkov light cone. Therefore the light cone for a shower initiated by a hadron is wider than the cone for a shower initiated by a gamma ray. Furthermore the intensity of the light depends on the number of particles in the shower, which, in turn, depends on the energy E_0 of the primary particle (as visible already in the Bethe-Heitler model (Bethe and Heitler, 1934), see Section 2.1.1). These correlations are exploited in order to reconstruct the primary particle type and the particle properties. All this is taken into account and used by the H.E.S.S. experiment which is described in the following Sections.

2.2. H.E.S.S.

The high energy stereoscopic system (H.E.S.S.) in its first phase consists of four imaging atmospheric Cherenkov telescopes (IACTs) and is situated in Namibia in the Khomas highland at 1800 m above sea level (Aharonian et al., 2006b). Namibia was chosen as location for the experiment because of the good weather conditions with many clear nights

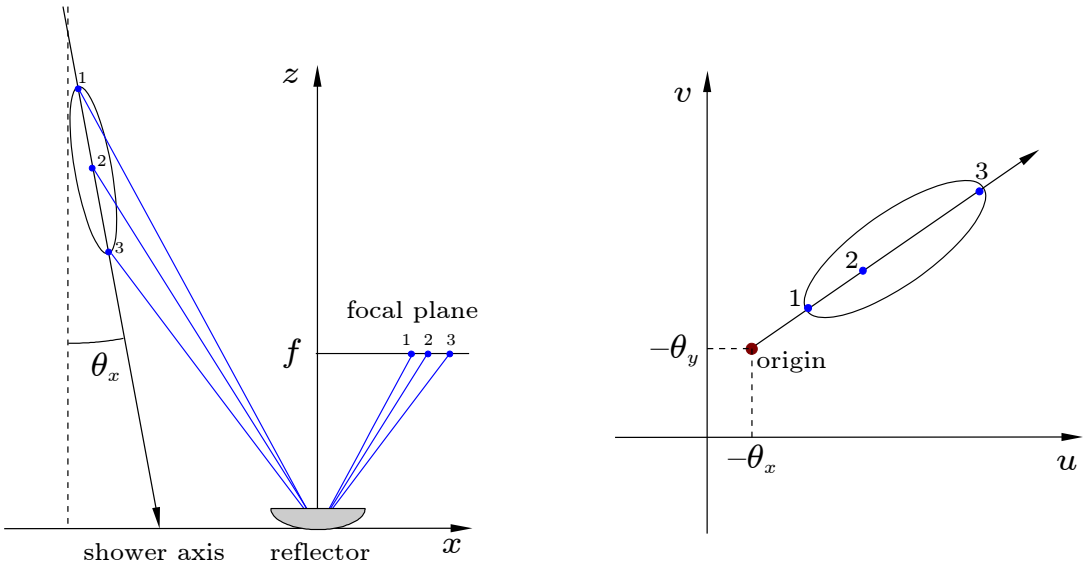

Figure 2.5.: The expected image of the shower in the camera can be constructed with geometric optics. Three light paths from the shower to the reflector and the camera are sketched in the ground system (x, z). The resulting image is shown in the camera system (u, v).

and little precipitation. Furthermore it lies in the southern hemisphere, which allows for observations of the Galactic Centre and most of the Galactic Plane. Additionally light pollution is negligible at the H.E.S.S. site since there are no big cities near by. The four telescopes are arranged in a square of 120 m side length. This configuration was chosen because it gives the best sensitivity, for a primary particle with an energy of 100 GeV. In mid 2012 a fifth telescope, which is bigger than the existing ones, has started operation. It was built in the central spot between of the first four telescopes and aims to reduce the energy threshold even below 100 GeV. It is not yet in routine operation, though. In this work only data from the four telescope system are used, therefore the fifth telescope is not described in the following. Nevertheless many aspects are similar for the large telescope, which together with the other four telescopes makes up H.E.S.S. phase 2. An image of the H.E.S.S. array is presented in Fig.2.6.
In the next Section the setup of the H.E.S.S. telescopes is described further.

2.3. Telescope Setup

Each of the four telescopes consists of a large reflector and a camera opposite of the mirror. They are carried by a steel construction (Bolz, 2004), which can be seen in Fig.2.7. The steel construction allows for tracking in altitude and azimuth. The dish of each telescope has a Davies Cotton (Davies and Cotton, 1957) design in order to have good imaging

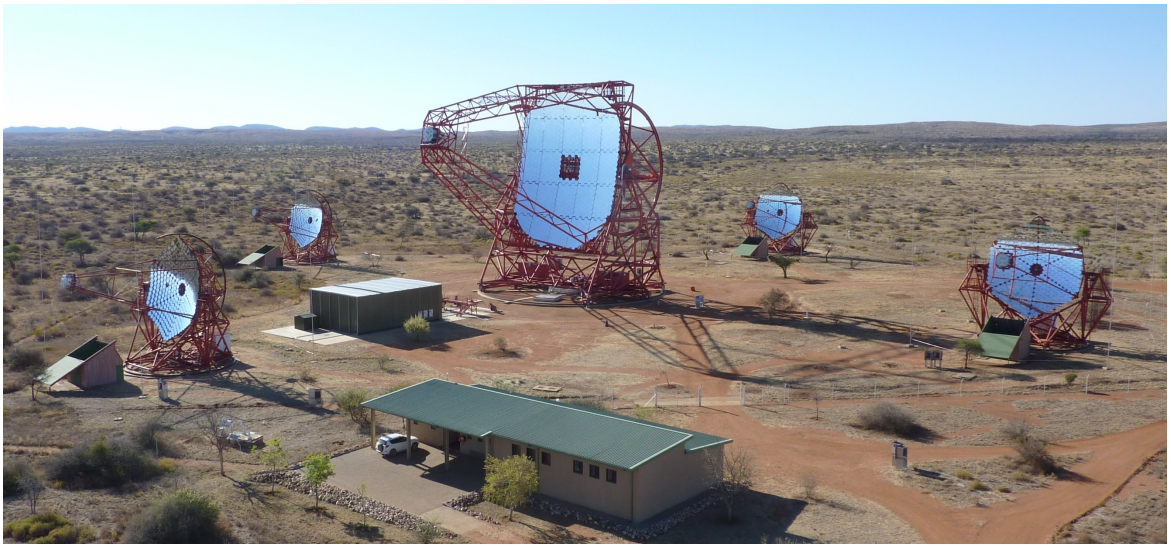

Figure 2.6.: The full H.E.S.S. array in September 2012. Image Credit: Kathrin Valerius

capabilities also off-axis. It has a diameter of 13 m (flat to flat). The total effective mirror surface area is 107 m^2 per telescope and is made of 382 single round mirrors each 60 cm in diameter (Bernlöhr et al., 2003). The centrepiece of the telescope is the camera. The camera consists of 960 photomultiplier tubes (PMTs), indicated as small hexagons in Fig.2.8(a), each covering an area on the sky of 0.16° in diameter. For a better light capture Winston cones are placed in front of every PMT. The Winston cones also limit the field of view of the PMTs and therefore reduce background light from the surroundings. The PMTs are divided into 60 drawers concerning the electronic structure. The drawers are indicated in red and lilac in Fig. 2.8(a). Each of these drawers takes care of 16 PMT (Vincent et al., 2003). Fig. 2.8(b) shows such a drawer and the underlying electronic structure. The overall field of view (FoV) of the system is 5° in diameter, which is large compared to other experiments. The whole four telescope system was finished and started operating in December 2003. In the following Sections the standard H.E.S.S. calibration, reconstruction and analysis techniques are described.

2.4. Coordinate Systems

In this Section four coordinate systems, which are frequently used in the following, are introduced.

- The *ground system* is a Cartesian coordinate system defined according to Fig. 2.9. In the ground system the zenith angle β_{zen} and the azimuth angle λ_{azi} are defined. They describe the telescopes pointing direction as well as the direction of air showers and can take values between 0° and 90° and 0° and 360°, respectively.

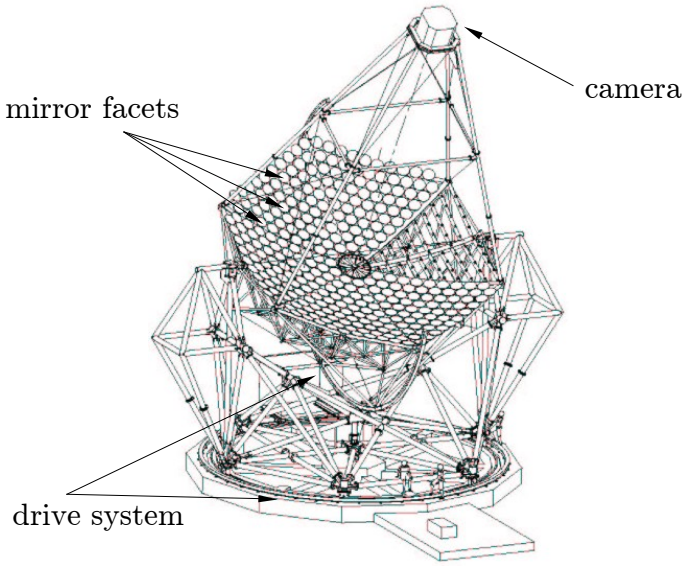

Figure 2.7.: The steel construction of a H.E.S.S. telescope.

- The *nominal* or *camera system* is defined inside the focal plane of a perfect camera. It is a two dimensional Cartesian system, which has its origin at the centre of the camera. Coordinates given in the nominal system can be transformed with the knowledge of the exact time (e.g. the modified Julian date (MJD)) in RaDec or Galactic Coordinates.
- The *RaDec coordinates* as well as the *Galactic coordinates* are used to describe positions in the sky. They are defined according to Fig. 2.10(a) and Fig. 2.10(b), respectively. These systems are both spherical systems. Though, only the angular parameters, right ascension (RA) and declination (dec) for the RaDec system and longitude (l) and latitude (b) for the Galactic system, are used. For astrophysical objects in general the distances are not exactly known, therefore under the assumption that the distances are large the angular parameters are the same from everywhere on Earth for a certain object. Furthermore both systems are rotating systems, the RaDec system rotates with the Earth and the Galactic System rotates with respect to the Galactic Centre.

2.5. Data Taking

In general for IACTs two observation strategies exist: Taking *wobble runs* or taking *on-off runs*. First of all the term *run* has to be explained. Data taking with the H.E.S.S. experiment is organised in observations with a length of about 28 minutes. Such an observation is called a run. During a run the H.E.S.S. telescopes point to a certain position in the sky. In order to track the position it is necessary to compensate the motion (rotation) of the Earth. This

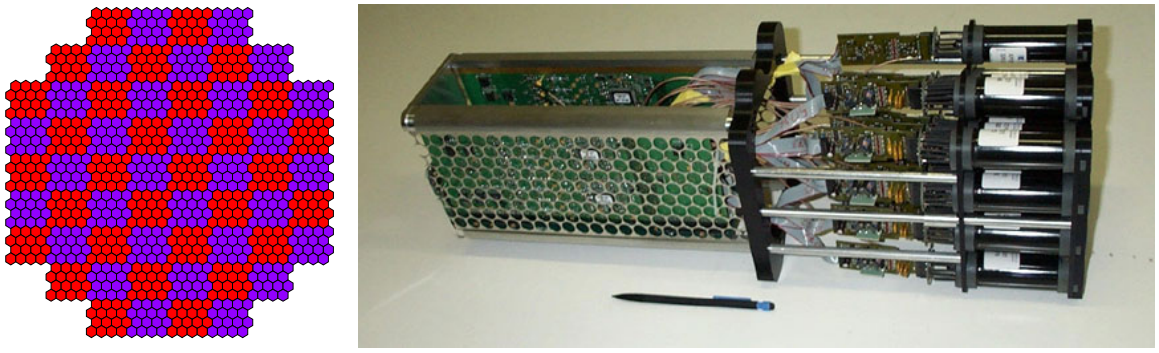

(a) (b)

Figure 2.8.: A schematic view of one of the H.E.S.S. cameras. The PMTs are indicated as small hexagons and the drawers are marked alternating in red and purple. In (b) a side-view photograph of a drawer with a pen to scale is shown.

is done by adapting the zenith and the azimuth angle of the telescopes continuously during a run.
A further important aspect considering the two observation strategies is the background estimation. When using the wobble technique the target (a potential gamma ray source) is not pointed at directly but with a small offset (in the order of 0.5° to 0.7°), i.e. the target is not in the centre of the FoV but slightly offset. For this kind of runs (wobble runs) the background can be estimated from within the same FoV, meaning the same run, see also Section 2.9.3. This ensures the same observation and hardware conditions for target and background data and therefore potential systematics are under control.
When using the on-off technique target (on) and background (off) data are taken from two different FoVs, meaning two different runs (an on- and an off-run). However to ensure also here similar or even identical observation and hardware conditions the two runs are taken consecutively. The runs are therefore also called "dedicated" on-off-runs. The on-run points directly at the target starting at a certain zenith and azimuth configuration ($\beta_{\text{zen},0}$, $\lambda_{\text{azi},0}$) and ending at some other configuration ($\beta_{\text{zen},1}$, $\lambda_{\text{azi},1}$), because of the tracking. The off-run (taken after the on-run here) covers the same range in zenith and azimuth, which results in pointing to a different position in the sky (about 7° away from the target). Of course therefore the off-run should not contain any potential gamma ray sources.
The major difference between the two observation strategies is that the observation time of a single potential gamma ray source is a factor of two larger for the on-off technique. Therefore the H.E.S.S. experiment uses almost entirely wobble observations and only very few dedicated on-off run-pairs exist.

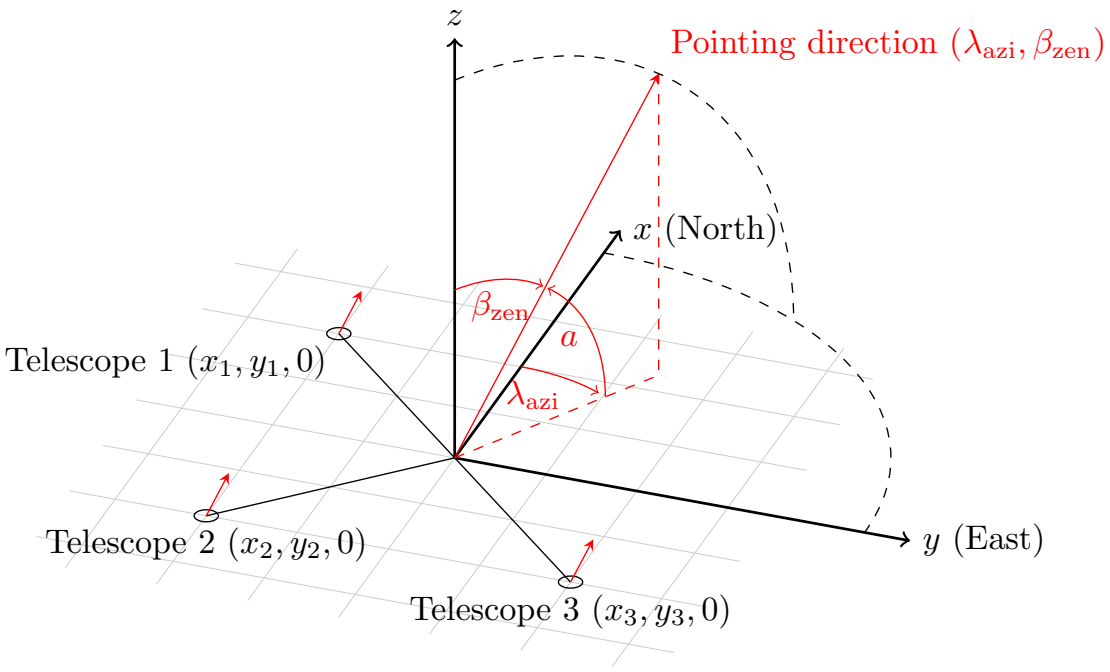

Figure 2.9.: Definition of the ground system in Cartesian coordinates (x, y and z) and of the zenith β_{zen} and the azimuth angle λ_{azi}. a is the altitude.

2.6. Calibration

The quality of the data taken with the H.E.S.S. experiment depends on ageing processes of the system (e.g. changes in the quantum efficiencies of the PMTs or in the reflectivity of the mirrors), and also on observation conditions (e.g. changes of the atmosphere (clouds) or the night sky background light). In order to take the ageing of the system into account it is regularly calibrated. Furthermore the observation conditions are well monitored. How the calibration works and what kind of monitoring devices are on site is described in the next Sections.

2.6.1. Calibration of the Camera

The main parameter, which is extracted from the camera, is the light intensity or amplitude of each pixel in photoelectrons (p.e.). Therefore every pixel is equipped with two amplification channels: A *high gain* (HG) and a *low gain* (LG) channel.
The amplitudes of each pixel obtained for the two channels have to be corrected for

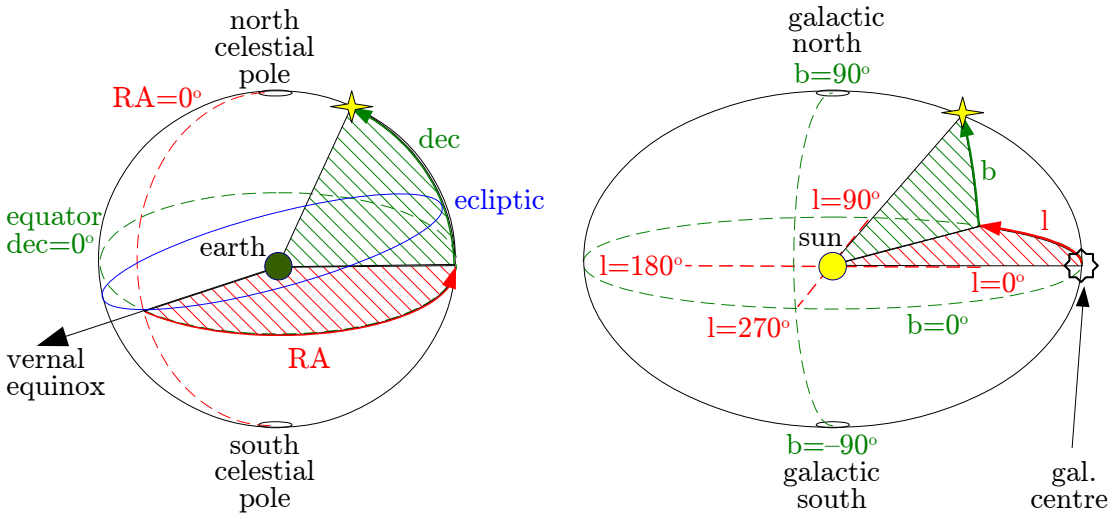

Figure 2.10.: (a) Definition of the RaDec System. The ecliptic is the apparent path of the Sun as seen from Earth's centre. The Earth's orbit lies in the plane given by the ecliptic. The vernal equinox is the point where the ecliptic and the equator intersect in spring (they also intersect in autumn). (b) Definition of the Galactic Coordinate system.

differences in the electronics, this is done according to the following formulae:

$$A^{\mathrm{HG}} = \frac{ADC^{\mathrm{HG}} - P^{\mathrm{HG}}}{\gamma_{\mathrm{e}}^{\mathrm{ADC}}} \cdot FF \tag{2.4}$$

$$A^{\mathrm{LG}} = \frac{ADC^{\mathrm{LG}} - P^{\mathrm{LG}}}{\gamma_{\mathrm{e}}^{\mathrm{ADC}}} \cdot \frac{HG}{LG} \cdot FF \tag{2.5}$$

- ADC^{HG} and ADC^{LG} are the measured charges in analogue to digital converter (ADC) counts in the HG and the LG.
- P^{HG} and P^{LG} are the pedestals (the electronic baselines) for the HG and the LG.
- $\gamma_{\mathrm{e}}^{\mathrm{ADC}}$ is the conversion factor (also called gain) between ADC counts and p.e.
- HG/LG is the amplification ratio between the two gains.
- FF is the flat-field coefficient, characterising the collecting efficiency of a single PMT relative to the average of the camera.

The determination of the gain, the pedestals and the flat-field coefficients is described further in the following Sections.

Flat-Field Coefficients

The flat-field coefficients are measured in special runs, which are taken roughly every two days. In these runs a LED flasher positioned in the mirror dish in about 15 m distance from the camera is used to illuminate the camera homogeneously. The inverse of the normalised measured pixel intensities (relative to the mean intensity over the whole camera) is then proportional to the flat-field coefficients.

Gain Determination

Like for the determination of the flat-field coefficients also for the determination of the gain special calibration runs are taken. There a flashing LED (with frequency of 70 Hz) placed in the camera shelter approximately 2 m away from the camera is used. The intensity of the LED is tunable in order to allow the measurement of the single photo-electron peak. However, because of the high resolution needed this calibration can only be applied to the HG. The recorded ADC counts are then filled into a histogram for each pixel and the following function is fitted to the distribution:

$$G(x) = N \cdot \left(\frac{e^{-\mu}}{\sqrt{2\pi}\sigma_{\mathrm{P}}} exp\left[-\frac{1}{2}\left(\frac{x-P}{\sigma_{\mathrm{p}}} \right) \right] + \right. \tag{2.6}$$

$$\left. + \kappa \sum_{\mathrm{n}=1}^{m \gg 1} \frac{e^{-\mu}}{\sqrt{2\pi}\sigma_{\mathrm{P}}} \frac{\mu^n}{n!} exp\left[-\frac{1}{2}\left(\frac{x-\left(P+n\gamma_{\mathrm{e}}^{\mathrm{ADC}}\right)}{\sqrt{n}\sigma_{\gamma_{\mathrm{e}}}} \right)^2 \right] \right) \tag{2.7}$$

The first term corresponds to the pedestal distribution and the second term to a signal from n photo-electrons (for details the reader may consult Section 6.2 of Aharonian et al. (2004b)). The Norm N is the only fixed parameter in the fit and its value is set according to the number of events in the run. κ describes how Poisson-like the distribution is, $\kappa = 1$ holds if the signal is a Poisson distribution. P is the pedestal position, σ_{p} the pedestal width and $\sigma_{\gamma_{\mathrm{e}}}$ the width of the single photo-electron peak. μ corresponds to the average luminosity. $\gamma_{\mathrm{e}}^{\mathrm{ADC}}$ finally is the value of the gain for the HG. An Example of a distribution of measured ADC counts and the result of a fit with Eq. 2.7 is shown in Fig.2.11. If for some reason the fit fails a default value of 80 ADC counts for the HG is assumed for the gain, which corresponds to the average value. The deviation from this value should then be corrected for by the flat-field coefficient.

Pedestal Determination and Night Sky Background

Different methods exist to determine the pedestal.
Again specific pedestal runs can be taken. There the camera lid is closed and only electronic noise is read out. With these runs the determination of the dependence of the pedestal on instrumental effects like, e.g., the camera temperature, are possible.

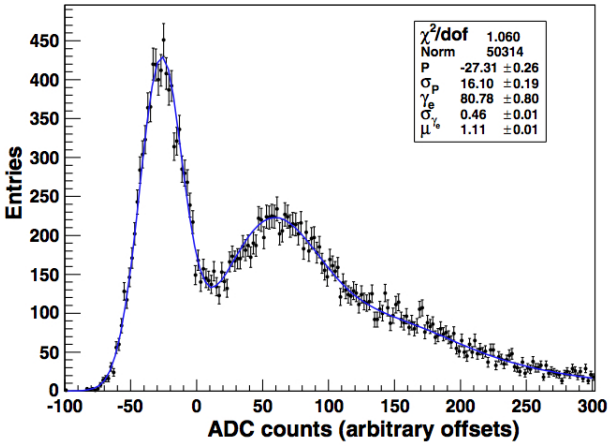

Figure 2.11.: Determination of the conversion factor from ADC counts to photo electrons. A function, see Eq.2.7, is fitted to the distribution of the ADC counts. The image is taken from Aharonian et al. (2004b).

However, different effects may influence the pedestal during observations, e.g. the NSB or the air temperature. Therefore, also during observations, pixels, which are not "contaminated" by Cherenkov light, are selected and their pedestal values are determined.
A further result from the pedestal determination during observations is the determination of the NSB, the NSB being responsible for a broadening of the pedestal. Additionally the level of NSB can also be estimated via the high voltage current of the PMT. Quite recently an other way to determine the NSB has been studied in Charbonnier (2011). A correlation, see Fig. 2.12, between the NSB estimated from the pedestals and the optical light coming from stars and so on in the range from $l = -40°$ to $l = +40°$ and for $-2° \leqslant b \leqslant +2°$ was identified. Taking an optical image and using this correlation the NSB over the whole sky can be estimated. However, this estimation does not take into account fluctuations due to hardware or observation conditions.

Non Functional Channels

Sometimes it happens that no calibration coefficients are determined for a certain pixel or channel (HG or LG). Most of the time this is due to hardware failures and the pixel is labelled broken. Also pixels are excluded from further analysis if they fire too often compared to their neighbours or significantly seldom.

2.6.2. Optical Response

Of course not only the electronic response of the camera but also of the whole optical system (dish-mirror-camera) needs to be characterised. In addition to the uncertainties in the

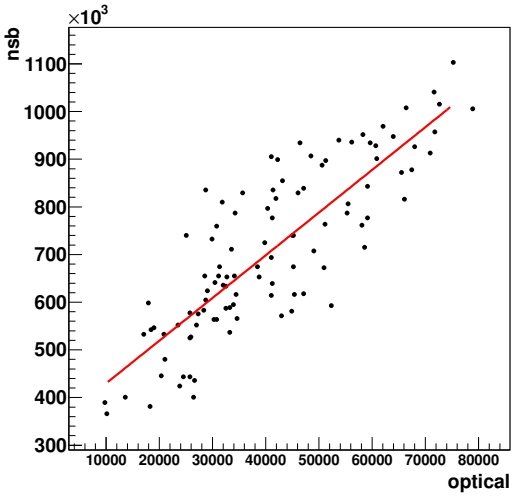

Figure 2.12.: The integrated NSB over the integrated optical intensity in the range from $l = -40°$ to $l = +40°$ and for $-2° \leqslant b \leqslant +2°$. The red line is a fit with a linear function. Adopted from Charbonnier (2011)

camera electronics there are uncertainties in the mirror reflectivity, the shadowing by the steel structure and atmospheric effects. These effects can be examined by studying muon rings in the camera (Bolz, 2004). Via the muon efficiencies also the ageing on timescales of years of the instrument is recordable. In the following it is shortly described how the calibration with muon events works. More details can be found in Bolz (2004).

Muon Efficiencies

Muons are produced in the atmosphere by the decay of charged pions or kaons in hadronic air showers.

$$\pi^{\pm} \longrightarrow \mu^{\pm} + \nu_{\mu}\,(\overline{\nu}_{\mu}) \tag{2.8}$$
$$K^{\pm} \longrightarrow \mu^{\pm} + \nu_{\mu}\,(\overline{\nu}_{\mu}) \tag{2.9}$$

The muons are more massive than electrons and lose their energy mainly via ionisation and not via bremsstrahlung or scattering. The muons have high energies and produce Cherenkov light. The Cherenkov light cone of a muon is narrower than that of an electron. Hence, when a local (created some hundred meters away from the telescope) muon hits the mirror the Cherenkov light cone is visible as a ring in the camera, see Fig. 2.13(b). With the knowledge of only a few geometric parameters of the muon (see Fig. 2.13(a)) it is possible to predict the amount of Cherenkov photons emitted by the muon. With this it is possible to model the intensity of the detected ring image. The muon efficiency is then defined as the

ratio between the predicted number of photons N_γ and the measured photo electrons $N_{\text{p.e.}}$:

$$\epsilon_\mu = \frac{N_{\text{p.e.}}}{N_\gamma} \tag{2.10}$$

Typical values for the muon efficiency ϵ_μ lie in the range between $[0.06 - 0.1]$. Detailed explanations on how the muon ring analysis works can be found in Bolz (2004) Section 3.

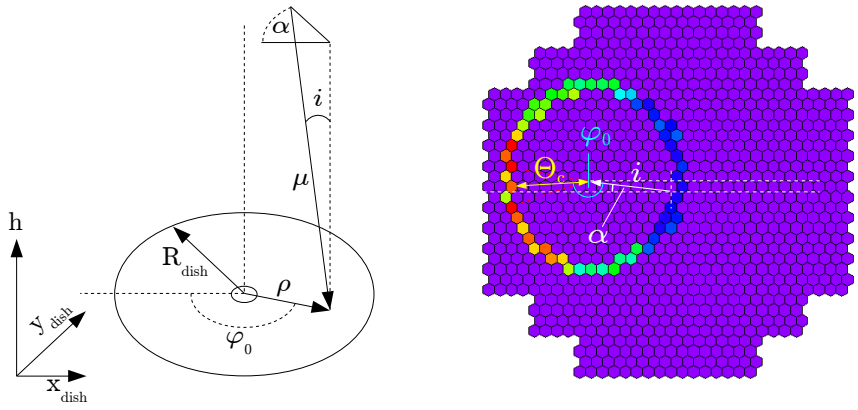

Figure 2.13.: Images illustrating the parameters necessary for the muon ring analysis in the different coordinate systems. In (a) the geometric situation is sketched. The plane of the dish is drawn and a muon μ passing through it. The important geometric parameter for the muon analysis are illustrated. In (b) a cleaned camera image with a muon ring is shown where the geometric parameters from above as well as the Cherenkov angle Θ_C are drawn. The colour scale indicates the intensity distribution along the ring.

2.6.3. Atmospheric Variations

It is evident that atmospheric conditions influence the data of an IACT (Bernlöhr, 2000), like the H.E.S.S. experiment. The main contributions come from Rayleigh scattering off atmospheric molecules and Mie scattering off aerosols. It is obvious that larger absorption in the atmosphere due to dust or smoke limits the detection efficiency, as do other weather-related effects like (partial) cloud cover[1].
In order to gain information about the status of the atmosphere during the observations, the H.E.S.S. experiment is equipped with several instruments (Aye et al., 2005). They are listed and shortly described in the following.

[1]Lightning or imminent rain will even cause operations to be stopped to protect the instrument from damage.

Weather Station

A fully automated weather station is positioned near the telescopes. The station measures air temperature, relative humidity, atmospheric pressure, wind speed, wind direction and rainfall continuously. The data taking is included in the DAQ framework and hence the parameters measured with the weather station can be attributed to the runs.

Radiometer

Beside the weather station four identical radiometers are attached par-axially to each telescope. These radiometers measure the radiation in the infrared between 8 and 14 μm. By comparing the measurement to a blackbody spectrum the radiometer calculates the radiative temperature of the sky. The resulting temperature is very sensitive to the presence of clouds and water vapour, which in turn influence the count rate of the detector, see Aye et al. (2005). Also at the moment studies are ongoing to identify a correlation between the radiometer and the system trigger rate of the H.E.S.S. telescopes (Daniels, 2012).

Ceilometer

At the start of operations of the array, H.E.S.S. was equipped with a commercial LIDAR[2] system. The LIDAR was expected to serve as a very good means to measure the aerosol layer and its structure. It detects the backscatter in a range of 905 nm up to a height of 7.5 km. In 2009 the feasibility of atmospheric corrections based on LIDAR measurements was successfully demonstrated with H.E.S.S. data (Nolan et al., 2010). Unfortunately the LIDAR stopped taking data in 2007. A new LIDAR has started data taking in 2010, but its data is not yet included in the standard data format. Therefore no correction due to the LIDAR measurement is included in the H.E.S.S. data analysis.

2.7. Data selection

In the previous Section it was pointed out that the camera is illuminated continuously with night sky background light (NSB). To prevent a large data load due to background events a trigger system is installed. It is used to increase the number of potential Cherenkov events against the background. Major backgrounds are the NSB, light from hadronic showers and single muons. Furthermore in order to reduce systematic uncertainties only data which fulfil certain quality conditions are used for the later analysis.
The next two Sections shortly explain the trigger system and point out the data quality cuts.

[2]LIDAR - Laser Imaging Detection and Ranging

2.7.1. Trigger system

The H.E.S.S. system trigger (Funk et al., 2004) consists of two levels. The first level is local at each telescope and has two requirements. The third trigger condition applies to the whole array and forms the second level trigger. It is coordinated by the central trigger system (CTS).
The first local trigger is a single pixel trigger. It requires a pixel to exceed a threshold of 4 p.e. The second local trigger is a coincidence trigger requiring at least 3 pixel threshold triggers in a sector in a time interval of about 1.5 ns. A sector is a square of 64 pixels defined in a way that leaves each camera with 38 overlapping sectors. The overlap ensures a homogeneous trigger efficiency over the whole field of view (FoV). The short time window of about 1.5 ns reduces the NSB events. The NSB events have larger timescales compared to the Cherekov light signal. The value of the pixel threshold (4 p.e.) as well as the value of the sector threshold (3) was chosen as a compromise between achieving a low energy threshold and discriminating enough background to have a stable and manageable trigger rate. If the local trigger level is reached the camera is triggered. The third and most important trigger for the H.E.S.S. array is requiring 2 telescopes to trigger (level two trigger) within a time window of 80 ns. This condition reduces the background, especially single muon events, very efficiently already at the hardware level. This hardware level reduction of the rate is necessary because of the read-out time, which could lead to large dead-time. The dead-time for IACTs varies between several 10 μs and several 10 ms depending on the DAQ. For H.E.S.S. the dead-time adds up to about 446 μs (Borgmeier et al., 2003). Important for the read-out is also that only the cameras which triggered are read out. A more detailed description also of technical aspects can be found in Funk et al. (2004).

2.7.2. Quality criteria

Systematic effects might be reduced by using only data taken under optimal or good observation conditions (Aharonian et al., 2006b). Conditions are not optimal when there are clouds or a lot of dust in the atmosphere. These can lead to absorption of the Cherenkov light. These absorptions are then visible as fluctuations in the system trigger rate (clouds) or as a significantly low trigger rate (dust). Hence it is possible to use the trigger rate to distinguish between good and not so good data. For the analysis only runs for which the mean trigger rate is not less than 70 % of the predicted rate (Funk et al., 2004) are used. Furthermore the rms variation of the trigger rate must not exhibit 10 %. Not only the quality of the trigger rate is checked, but also the accuracy of the tracking is controlled continuously in order to ensure an accurate reconstruction of the source position. Runs in which the DAQ reports distances larger than 10 arcseconds between the nominal and the actual pointing position are excluded from the analysis. Furthermore the pointing is checked by matching the known positions of stars. However, in general these position tests only lead to a marginally low loss of data. Another aspect of data quality is the amount of broken PMTs in an observation. If more than 10 % of the PMTs of a telescope are not

working at a time, the telescopes data is not used in the analysis. Reasons for missing PMTs are overcurrents due to stars, which lead to the PMTs being turned off (also in advance if a known stars passes through the FoV), or meteorites, lighting, air planes, satellites or other unexpected strong light sources as well as hardware failures in a single pixel .

2.8. Reconstruction

So far the hardware and the electronics as well as their calibration have been described. Additionally the conditions, under which data are taken, have been discussed. Now the recorded signals have to be interpreted in terms of cosmic rays. The next Sections illuminate how the properties of the primary particle of an air shower (event) are reconstructed from the electronic signals.

2.8.1. Image cleaning

In Fig.2.14(a) a raw camera image is shown. The colours correspond to different levels of intensity measured in the pixels. The task is now to distinguish the part of the image, which is due to an air shower from background fluctuations. The shower is expected to appear localised in the camera (see the imaging principle in Fig. 2.5).

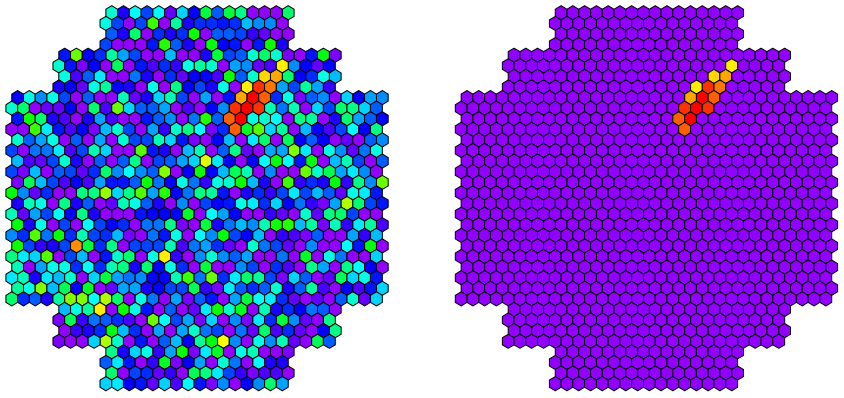

(a) (b)

Figure 2.14.: In (a) an example of an uncleaned camera image is shown. In (b) the image after applying the tail cuts is shown, only the shower is left.

Therefore an image cleaning can be applied: Certain conditions on the intensities of neighbouring pixels are implied. Two intensity thresholds are defined, a low threshold I_{low} and a high threshold I_{high}, both given in units of photoelectrons. Then only pixels which have an amplitude above I_{high} and a neighbour pixel above I_{low} or vice versa are kept in

the image. Typical values for I_{high} and I_{low} are 10 p.e. and 5 p.e. respectively. These image cleaning cuts are also called *tail cuts*. In Fig. 2.14(b) a cleaned camera image is shown. This image is used in the Hillas analysis to determine the Hillas parameters, which are explained in the next Section.

2.8.2. Hillas Parameters and Stereoscopy

The Hillas parameters (Hillas, 1985) can be derived from the moments of the cleaned camera image. They correspond to certain geometric parameters of the shower image in the camera. The shower image can be approximated by an ellipse, see Fig.2.15, and the Hillas parameters then correspond to

- the width of the ellipse w
- the length of the ellipse l
- the centre of gravity of the ellipse in camera coordinates (x, y)
- the amplitude or integrated intensity A_{I} over the pixels inside the ellipse (also called image size)
- and the orientation of the ellipse in the camera defined by the angle ϕ.

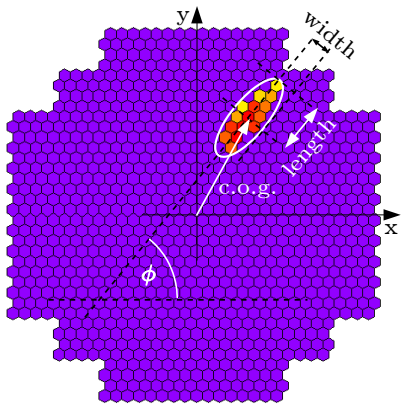

Figure 2.15.: A cleaned camera image overlaid with an ellipse. The geometric interpretation of the Hillas parameters is shown.

The Hillas parameters are extracted from each camera image for all of the triggered telescopes (two to four [3]) for each shower. With the Hillas parameters then the energy (see also next Section) and the direction of the primary particle as well as the shower impact point on the ground can be reconstructed. Moreover they can be used to distinguish between hadrons and gamma rays. More details on the discriminating power of the Hillas

[3]The data quality conditions always require at least two triggered telescopes.

parameters are given in Section 2.9.1.
For the reconstruction of the direction and the impact point a stereoscopic reconstruction is applied. The stereoscopic reconstruction technique was first used by the HEGRA collaboration (Daum et al., 1997). The major axis of the shower in the camera image defines a plane in the sky, compare also Fig.2.5. Now the camera images are overlaid in the nominal system and by intersecting the major axes from the images of the other telescopes the direction of the primary particle is reconstructed, see Fig.2.16(a) and 2.16(b). In a similar way also the impact point of the shower can be identified. For more details and also tests of different approaches to improve the reconstruction accuracy the reader may consult Hofmann et al. (1999). The angular resolution on the reconstructed direction lies in the range of 0.1° to 0.2°.

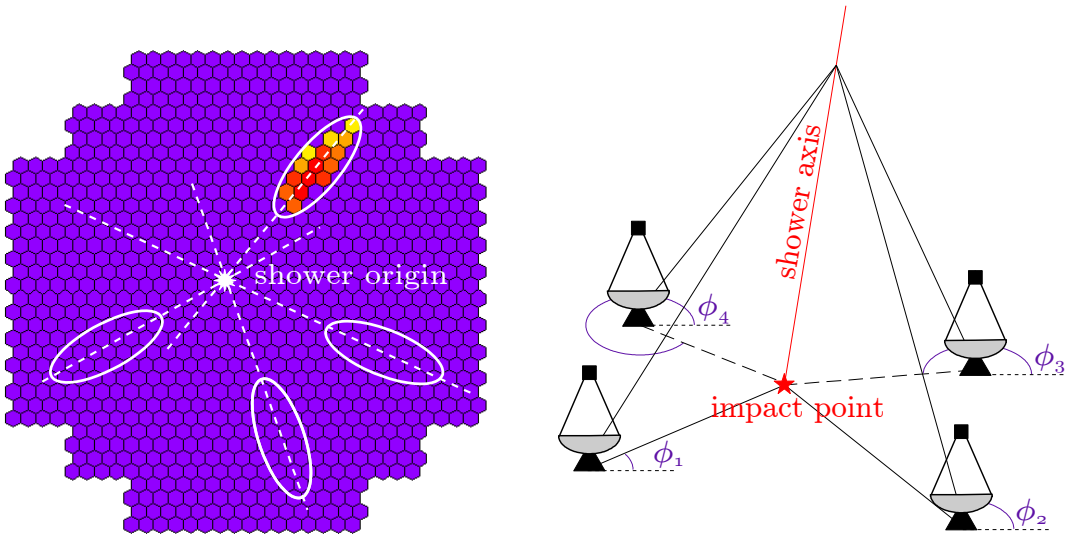

(a) (b)

Figure 2.16.: (a) Illustration of the stereoscopic reconstruction in the nominal system, where the ellipses from all four telescopes are overlaid. (b) Principle of the stereoscopic reconstruction of the impact point in the ground system.

Energy Resolution

After identifying the primary particle of shower as a gamma ray the energy of the gamma ray is reconstructed. In the Hillas analysis look-up values are used for this. The look up tables are functions of the image size and the impact distance (distance from the impact point of the shower to each telescope). The energy for an event is the mean of the energy derived for the single telescopes. This approach results in an error on the energy $\Delta E = (E_{\mathrm{reco}} - E_{\mathrm{true}})/E_{\mathrm{true}}$. The mean value of ΔE is also called energy bias and increases towards lower energies (the energy threshold). Usually only the energy range in which the bias is below 10% is used. The energy resolution is the width of the distribution of ΔE which may vary for different energy ranges. In general an energy resolution around 20% is assumed for the Hillas analysis.
The Hillas reconstruction proved to be a very stable method and the Hillas analysis uses essentially this method. However, recently a new method based on a log-likelihood comparison of the raw (uncleaned) camera images with a model prediction was implemented. This reconstruction technique is employed in this thesis and is described in the following.

2.8.3. Model++

The Model++ reconstruction (de Naurois and Rolland, 2009) is based on a log-likelihood comparison between a semi-analytical model prediction and the uncleaned camera image. The method was first introduced at the CAT experiment (Le Bohec et al., 1998). The following steps are necessary to develop and apply the Model++ reconstruction technique:

- Determination of a semi-analytical model predicting the lateral, longitudinal and angular distributions of charged particles in air showers induced by gamma rays from studies of Monte Carlo (MC) simulations of electromagnetic showers (KASCADE (Kertzman and Sembroski, 1994)).
- Include the detector response in the model to obtain expectation values for each pixel in each camera.
- Calculation of the model prediction for a sufficient amount of grid points of the parameter space.
- Introduction of the pixel-likelihood function and the goodness-of-fit variable, including influences from night sky background light (NSB).
- Application of the reconstruction (log-likelihood fitting procedure) to full detector MC simulations to characterise the performance of the Model++ reconstruction technique.

In the following the points above are described a bit more according to de Naurois and Rolland (2009).
First the distributions of the charged particles in an electromagnetic shower, which are used to gain the distributions of Cherenkov light, are modelled. Therefore electromagnetic showers are generated with the KASCADE shower simulation program (Kertzman and

Sembroski, 1994), which is comparable with other simulation programs, e.g. CORSIKA (Knapp and Heck, 1998). This method is numerically intensive, therefore the showers are not simulated continuously in energy but at fixed energies between 10 GeV and 20 TeV. The energies are chosen to cover the energy range of the H.E.S.S. experiment. Depending on the energy different numbers of showers are needed to generate a smooth model. The model here is an extension to the model proposed by Hillas in Hillas (1982). The *depth of the first interaction* is a new parameter and has a strong influence on the shower. Analytical descriptions are gained for the longitudinal distribution of particles of the shower (with a modified Greisen formula (Puppi et al., 1956)), the angular distribution of the particles in the shower (with the help of the Molière theory) and the lateral distribution of particles in the shower. The deviation of the analytical description from the simulated distributions lies in the order of 5% to 10% and is thus relatively small. With the knowledge of these distributions the Cherenkov light distribution of the shower can be predicted. The prediction contains the light distribution on the ground for a given primary particle depending on the particle *energy, direction, impact parameter* and *depth of first interaction*.

Now detector specific response parameters are included in the calculation of the light intensity $I_{(\mathrm{x,y})}$ in the camera image. This is done by an eight-fold integral

$$
\begin{aligned}
I_{(\mathrm{x,y})} = \int \mathrm{d}z \int \mathrm{d}E \quad & \times \quad \frac{\mathrm{d}N_\mathrm{e}}{\mathrm{d}E}(t,E) \times \frac{\mathrm{d}t}{\mathrm{d}z}(y) \quad \text{(longitudinal distribution)} \\
\int \mathrm{d}u \int \frac{\mathrm{d}\phi}{2\pi} \quad & \times \quad F_\mathrm{u}(u(E,s)) \quad \text{(angular distribution)} \\
\int \mathrm{d}X_\mathrm{r} \int \mathrm{d}Y_\mathrm{r} \quad & \times \quad F_\mathrm{XY}(X_\mathrm{r}, Y_\mathrm{r}, E, s, u) \quad \text{(lateral distribution)} \\
\int \mathrm{d}\phi_\mathrm{ph} \int \frac{\mathrm{d}\lambda}{\lambda^2} \quad & \quad \frac{\mathrm{d}^2 n_\gamma}{\cos\theta \mathrm{d}z \mathrm{d}\lambda} \quad \text{(Cherenkov photon production)} \\
& \times \quad \exp(-\tau(z,\lambda)) \quad \text{(atmospheric absorption)} \\
& \times \quad Q_\mathrm{eff}(\lambda) \quad \text{(detector quantum and mirror efficiency)} \\
& \times \quad Col(z, X_\mathrm{r}, Y_\mathrm{r}, u, \phi, \phi_\mathrm{ph}) \quad \text{(geometrical collection efficiency)}
\end{aligned}
$$

over

- altitude z or depth t (longitudinal development of the shower/distance to depth of first interaction),
- energy E of the electron/positron in the shower,
- electron direction with respect to the telescope (u and ϕ),
- electron position with respect to its direction (X_r and Y_r),
- Cherenkov photon wavelengths λ and

- Cherenkov photon azimuthal angle ϕ_{ph} around the electron (the angle between electron and the Cherenkov photon being fixed for a given electron energy).

Other influences from the detector like the point spread function (psf) and the electronic response, e.g. the trigger response, as well as the geometric light collection efficiency are also taken into account. The telescope response is simulated in detail and is parametrised in look-up tables, in which also the atmospheric absorption, the wavelength-dependent quantum efficiency and the reflectivity are listed. These parameters are then used in the calculation of the model prediction.
The model is generated for certain fixed values of the parameter space, namely for

- 40 different zenith angles β_{zen},
- 40 impact distances ranging from 0 to $400\,\mathrm{m}/\cos(\beta_{\mathrm{zen}})$ from the telescope,
- 65 different energies from $(50\,\mathrm{GeV})/\cos(\beta_{\mathrm{zen}})$ to $(20\,\mathrm{TeV})/\cos(\beta_{\mathrm{zen}})$ and
- 6 first interaction depths from $0\,X_0$ to $5\,X_0$.

Now the pixel likelihood $P(s|\mu,\sigma_{\mathrm{p}},\sigma_\gamma)$ for the observation of a signal of s photoelectrons for an expectation value of μ can be determined as

$$P(s|\mu,\sigma_{\mathrm{p}},\sigma_\gamma)=\sum_{\mathrm{n}}\frac{\mu^n e^{-\mu}}{n!\sqrt{2\pi(\sigma_{\mathrm{p}}^2+n\sigma_\gamma^2)}}\exp\left(-\frac{(s-n)^2}{2(\sigma_{\mathrm{p}}^2+n\sigma_\gamma^2)}\right). \tag{2.11}$$

There the detector electronics enter in form of the pedestal width σ_{p} (including also broadening due to NSB) and the width of the single photo electron peak σ_γ, both determined during calibration. The pixel log-likelihood used in the later minimisation (fit) procedure is defined as:

$$lnL=-2\times ln(P(s|\mu,\sigma_{\mathrm{p}},\sigma_\gamma)). \tag{2.12}$$

Additionally a telescope log-likelihood is defined as the sum over all the individual pixel log-likelihoods.
Next the log-likelihood fit is applied and the telescope likelihood is minimised using a Levenberg-Marquardt fit algorithm (Levenberg,K, 1944) and (Marquardt, 1963). The model prediction is therefore interpolated between the different parameters to yield the best fit result for the parameters of the primary gamma ray. Different starting points for the algorithm are derived by applying a standard Hillas analysis with different image cleaning cuts. The point yielding the best value of the log-likelihood is then chosen as start value. Finally the fit results in the 6 shower parameters (direction and impact point each with 2 parameters and depth of first interaction and energy), the correlation matrix of the best fit parameters and the final log-likelihood value.
A further parameter is now defined: *goodness-of-fit*. The *goodness-of-fit* is defined as a normalised sum over all pixels of the difference between the actual pixel log-likelihood and its expectation value. The *goodness-of-fit* defined in this way behaves asymptotically like a χ^2 distribution and therefore provides a good measure of the fit quality. Furthermore the *goodness-of-fit* can be calibrated to take influences from the NSB into account (resulting

from deviations of the gaussian shape assumed for the pedestal distribution).
In order to serve as discrimination variable between gamma ray induced showers and hadronic showers the *goodness-of-fit* is further divided according to two different pixel groups: Pixels belonging to the shower core construct a variable called *ShowerGoodness* (SG) and the remaining pixels, which are background pixels, construct the so called *BackgroundGoodness* (BG).
Eventually the reconstruction is applied to MC simulations to characterise the performance of the new technique. The results of these performace studies are shortly summarised in the next Section.

Energy and Angular Resolution

The energy of the particle, which is determined via the minimisation of the telescope log-likelihood function, has a better resolution as for the standard Hillas reconstruction. Typically values below 15% are reached (de Naurois and Rolland, 2009). Additionally also the energy bias for Model++ increases at energies lower than the energies for the Hillas analysis.
The angular resolution, defined as 68% containment radius, is also better than for the Hillas analysis. In the Model++ reconstruction the angular resolution is $\leq 0.1^\circ$ on average, see de Naurois and Rolland (2009).

2.9. Analysis

In this Chapter the focus lies on the analysis based on the Model++ reconstruction. For most subjects the standard Hillas analysis does not deviate much from the Model++ analysis. Nevertheless at some points, where the differences are important, both analysis are described.
After the reconstruction one still has to deal with the separation between the different particle types. Signals due to gamma rays interacting in the upper atmosphere have to be distinguished from hadronic interactions. How this is done is described in the following Section. After the separation of the particles one needs to search or test for the existence of a gamma ray source. This is described in Section 2.9.3. Finally this Chapter closes with further analyses that are possible to characterise a source such as determining its spectrum and its flux.

2.9.1. Gamma-Hadron Separation

Here the separation is described for both the standard Hillas analysis and the Model++ analysis. This is done because they use different parameters and have different separation powers.

Hillas Analysis

As mentioned before, the images of a gamma ray induced shower and a hadron induced shower might have different shapes, because of the width of the showers. These different shapes correspond to different ranges for the Hillas parameters. Also other differences between hadron and gamma ray induced showers are visible in the Hillas parameters. These correlations have been studied with Monte Carlo (MC) simulations and conditions for the discrimination of hadron induced showers have been derived. The conditions are based on the so called *Scaled Cuts*. The *Scaled Cuts* cut on the relations between the actual image width w and length l and their expectation values and variance, namely the *ScaledWidth* SW and *ScaledLength* SL:

$$SW = \frac{w - \langle w \rangle}{\sigma_{\mathrm{w}}}, \quad SL = \frac{l - \langle l \rangle}{\sigma_{\mathrm{l}}} \tag{2.13}$$

For the H.E.S.S. array with multiple telescopes these variables are extended to the so called mean reduced scaled width, $MRSW$, and mean reduced scaled length, $MRSL$, see Aharonian et al. (2006b):

$$MRSW = \frac{\sum_{\mathrm{tels}} SW}{ntels}, \quad MRSL = \frac{\sum_{\mathrm{tels}} SL}{ntels} \tag{2.14}$$

$ntel = 4$ for the H.E.S.S. array and the sum is over the four telescopes. Comparing the distribution for gamma-ray induced showers with hadron induced ones (both from from MC simulations) then yields the corresponding cut values for the parameters. In Fig. 2.17 the distributions from data and from MC simulations are compared.

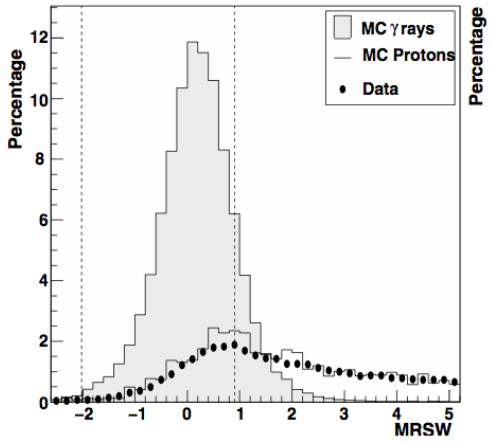

Figure 2.17.: A comparison of the distribution of the $MRSW$ for MC simulation and data. The data are background data and agree well with the simulations for protons. The vertical dashed lines indicate the cut values for the discrimination of showers due to hadrons. Figure taken from Aharonian et al. (2006b).

Model++ Analysis

For the Model++ analysis it is also necessary to find a way to distinguish between events due to gamma rays and events due to background. In the Model++ analysis this is done by applying cuts on the ShowerGoodness and the BackgroundGoodness or the MeanScaledShowerGoodness $MSSG$ and the MeanScaledBackgroundGoodness $MSBG$, respectively. The $MSSG$ and the $MSBG$ are derived in a similar way as the $MRSW$ and $MRSL$ in the Hillas framework. Additionally in the Model++ analysis also a NSB likelihood value is determined and cuts are applied there as well. The values for the cuts for different source types are listed in Table2.1. The *Standard Cuts* are most frequently used. The *Loose Cuts* are optimised for strong sources as they increase the gamma-ray efficiency but have a less powerful background suppression. Eventually the *Faint Cuts* are suited for sources with flux levels below a few percent of the Crab nebula. The cut on $\theta^2_{\max}$ is designed for point sources and is adapted to the source size when studying extended sources (this cut is also used in the Hillas analysis). The power of the separation of the Model++ analysis is stronger than for the Hillas analysis. However, the two analysis frameworks still use different information for the rejection of events. Therefore a combination of all the cut values might result in an even higher separation power.

Table 2.1.: Adopted from de Naurois and Rolland (2009): Cuts for minimal charge, maximum nominal distance, maximum ShowerGoodness, primary interaction depth range and maximum squared angular distance from the reconstructed shower position to the source. Two telescopes are required.

Name	Min. Charge (p.e.)	Max. Nom.Dist. (deg)	#Tels	$SG_{\max}$	t_0 (X_0)	$\theta^2_{\max}$ (deg^2)
Standard (Std)	60	2	2	0.6	[-1, 4]	0.01
Faint	120	2	2	0.4	[-1, 4]	0.005
Loose	60	2	2	0.9	N/A	0.0125

2.9.2. Acceptance

In order to further analyse the data it is necessary to determine the camera acceptance. The camera acceptance is expected to degrade towards the edges of the camera because the shower images are no longer fully contained inside the camera. The camera acceptance can be determined by studying events which are distributed homogeneously over the camera. There exist essentially two approaches to determine the camera acceptance. Both of these methods can be applied for gamma like events and for background events. The first approach relies on the assumption that the camera acceptance is radially symmetric around the

camera centre. This is mostly true for the inner parts, but at the edges of the camera this assumption does not hold. In order to calculate a radial acceptance the radial distribution of events is studied. However, regions need to be excluded from this study, if a gamma ray signal is expected there, because the events in this region are then no longer distributed homogeneously with respect to the rest of the camera. These regions are called *excluded regions* and are estimated with circular shapes in the H.E.S.S. analysis. For observations taken in wobble mode the target region, which is excluded from the acceptance calculation, is offset from the centre of the camera and the events in this region are weighted to account for the missing events. This is illustrated in Fig.2.18(a). The weight is simply defined as the fraction of the circle which does not intersect the excluded region:

$$w = \frac{\pi}{\pi - \theta}, \tag{2.15}$$

with

$$\cos\theta = \frac{r_0^2 + r^2 - d^2}{2 \cdot r_0 r} \tag{2.16}$$

In Fig.2.18(b) a radial profile of the acceptance over the squared offset ψ^2 for the a single run is shown.

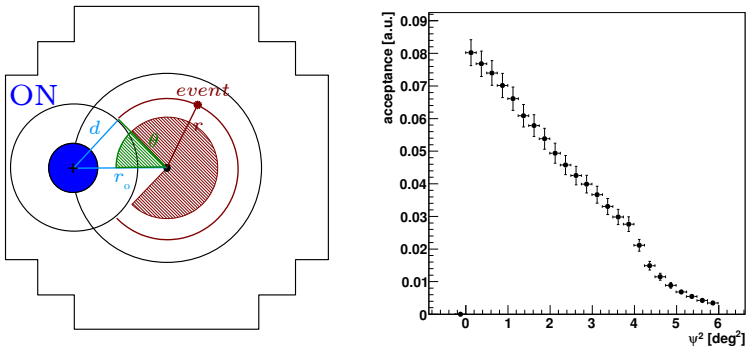

(a) (b)

Figure 2.18.: Determination of the event weight used for the calculation of the radial acceptance map (a) and the radial profile (b) of the acceptance for a single run.

However, the radial acceptance determination has some uncertainties. Especially at the edges of the FoV the uncircular shape of the camera might affect the camera acceptance. Additionally the assumption of radial symmetry might not always hold, since broken pixels or differences between the various drawers might appear. Furthermore the variation of the zenith angle across the FoV, especially for observations at larger zenith angles, effects the acceptance in a non radial way. Eventually if there are several sources in the FoV or a

large extended source the acceptance determination becomes tricky. Therefore a further approach to determine the acceptance is implemented in the Model++ analysis. This acceptance model is called bidimensional acceptance and it does not need any symmetry assumptions. There only the assumption that the events are homogeneously distributed is used. Furthermore the definition of the acceptance map is exploited. The acceptance map is defined as the ratio between the events map (a map filled with all events) and the exposure map (determination of this map see below) in the nominal system. This is illustrated in Fig. 2.19. There an events map and an exposure map for several runs with different excluded regions are indicated as well as the resulting acceptance map.

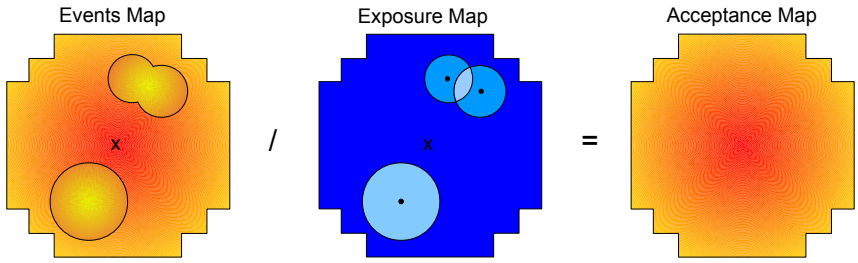

Figure 2.19.: Determination of the bidimensional acceptance map from events and exposure map.

It is important here that these maps result from the combination of several runs, where the positions of the excluded regions vary in the nominal system.
The exposure map is determined by filling two maps with background like events. In one map all events are filled ($map_{\text{allevents}}$), in the other map only the events not falling into excluded regions are filled (map_{excluded}). This is done for all runs of a data set and finally the bin-by-bin ratio $map_{\text{excluded}}/map_{\text{allevents}}$ is calculated, yielding the exposure map. From the acceptance map in the nominal system the acceptance on the sky can be derived. An example of the bidimensional acceptance for a single run is given in Fig. 2.20(a). There a hole due to an excluded region can be seen. In Fig. 2.20(b) the radial profile derived from the bidimensional acceptance map is shown. At this position the exposure is zero and the ratio $map_{\text{events}}/map_{\text{exposition}}$ can not be calculated. Therefore as mentioned above for the bidimensional acceptance determination more than one run is needed.
Concluding both methods to determine the acceptance yield comparable results and are used in the Model++ analysis.

2.9.3. Background Determination

Now eventually with the knowledge of the camera acceptance the detected events can be analysed further. However, in order to identify gamma ray sources the background has to be estimated. It was mentioned before already in the data taking Section, that in

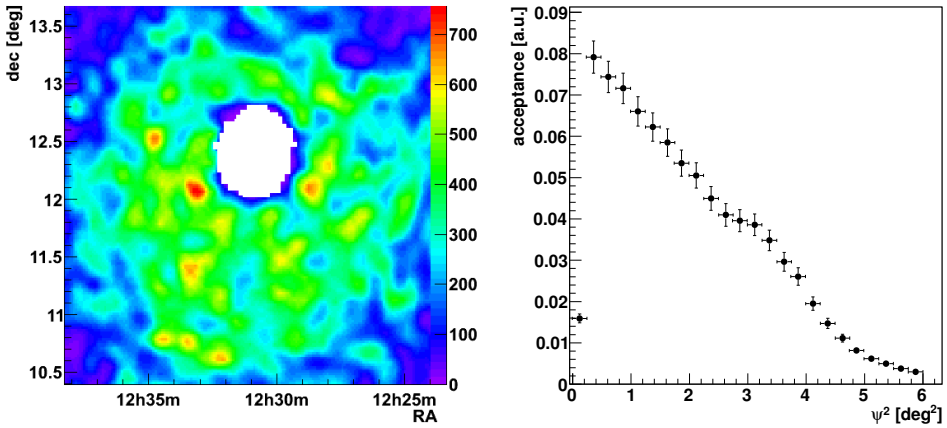

(a) (b)

Figure 2.20.: Example of a bidimensional acceptance map (a) and the radial profile of the map (b) for a single run.

principle dedicated on-off runs could be used but that this concept was soon replaced by the determination of the background in the same FoV, so with data from just one run. This is important as it guarantees identical observation conditions for the on and the off data. Several ways to find regions to determine the background are used in the H.E.S.S. analysis. Some of them are used merely for the significance calculation or the spectrum determination and some are used also to create sky maps. In the following some of these methods to estimate the background are described.

Multiple Off Background

The multiple off background estimation or reflected background (Berge et al., 2007) is used also in the Hillas analysis. It is used only for source detection and the determination of spectra but not for the generation of sky maps. The principle of the multiple off background is illustrated in Fig.2.21. The blue circle is the on or test region. It is positioned offset from the camera centre as is typical for wobble runs and also essential for the multiple off background method. The off regions, green in Fig.2.21, are chosen such that they have the same distance to the centre of the camera and a certain "safety" distance to the on region in order to avoid source events in the off regions. Of course in case of excluded regions in the FoV, see Fig.2.21(b), less off regions are used for background determination. Furthermore the off regions also have exactly the same size as the on region. Usually about seven off regions can be placed around an on region. The same distance to the camera centre and the same size implies a very similar or even equal acceptance in on and off regions, which limits the systematic uncertainties. The events falling into the on regions and the off regions

are called on and off events, N_{on} and N_{off}, respectively. How these numbers are treated to obtain the significance of the source is described later in Section 2.9.4. Now follows a further background estimation method.

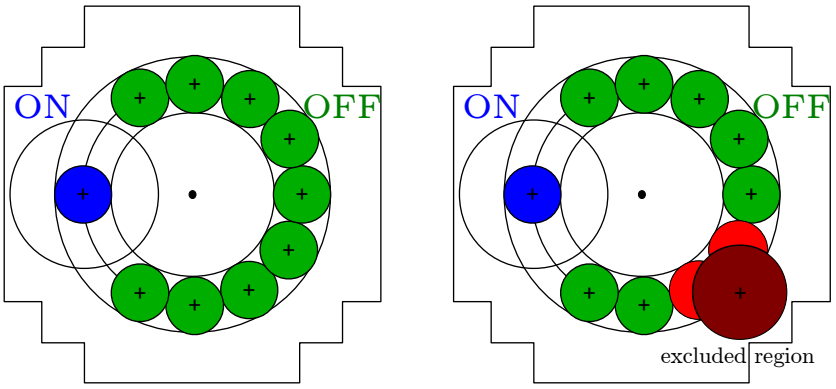

(a) (b)

Figure 2.21.: Illustration of the on and off regions in the multiple off background estimation method. In case without (a) and with (b) excluded regions.

Ring Background

The ring background estimation was introduced in Berge et al. (2007), but in the Model++ analysis two definitions are used. The ring background estimation method is used to determine the significance of a source, but also (as defined in Berge et al. (2007)) to create sky maps. Fig.2.22 shows the principles of both applications. In case of the significance determination the choice of the off region is very similar to the multiple off method, see Fig.2.22(a), at least for wobble observations. There the target is offset from the camera centre and a single off region in the shape of a ring is chosen, where the target region and other regions containing potential sources are excluded. The ring is constructed as indicated in Fig. 2.22(a) such that the width of the ring $d = r_{\text{outer}} - r_{\text{inner}}$ equals diameter of the on region. Additionally the points on the ring with radius $r_{\text{mid}} = 0.5 \cdot (r_{\text{outer}} + r_{\text{inner}})$ have the same distance to the centre of the camera as the centre of the target region. In case the target region is not (much) offset from the centre of the FoV the ring is chosen as described in Berge et al. (2007) and as indicated in Fig. 2.22(b). For the creation of a sky map the FoV is binned and every bin serves as test/target position. The background is then estimated as illustrated in Fig.2.22(b). A closed ring with the test position at its centre is chosen as off region and again N_{on} and N_{off} are determined for every bin. In the sky map often the excess or the significance is shown. More on excess and significance follows in the next Section.

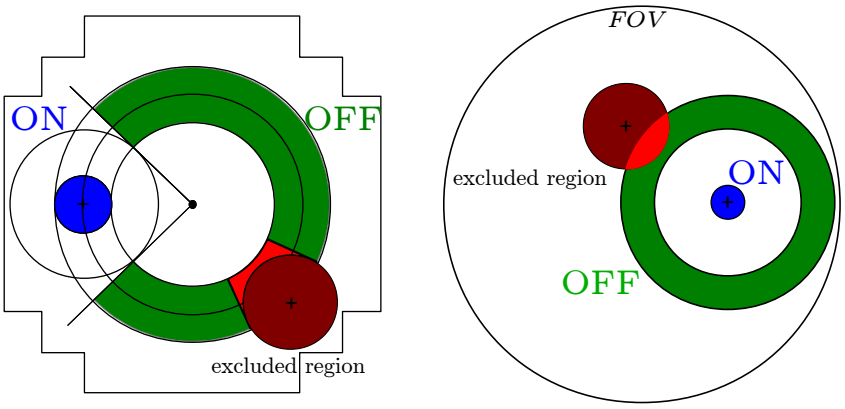

(a) (b)

Figure 2.22.: Illustration of the principle of the ring background estimation: (a) for significance determination and (b) for sky map creation.

2.9.4. Significance Determination

In the previous Section it is described how the numbers for on events N_{on} and off events N_{off} are obtained. Now it has to be decided whether a gamma ray source is detected in the on region. It has to be tested whether there are more on events N_{on} than off events N_{off} and if the more on events are due to a source or just a background fluctuation. A straight forward approach is therefore to subtract the numbers from each other to get the number of excess events $N_{\text{excess}} = N_{\text{on}} - N_{\text{off}}$. However, e.g. in case of the multiple off background we have much more off events due to the fact that the total off-region is a factor of $\alpha \approx 7$ larger than the on-region. This and also other effects which vary between the on and the off region, like e.g. the values of the acceptance, are all included in a normalisation β between the two event numbers.

$$\beta = \frac{t_{\text{on}}}{w(\tilde{A}, \tilde{A}_{\text{acc}}, \dots) \cdot t_{\text{off}}} \tag{2.17}$$

t_{on} and t_{off} are the observation times for the on- and the off-region. The weight $w(\tilde{A}, \tilde{A}_{\text{acc}})$ is made up from the ratios of parameters which are different for the on and the off region, e.g. in case of the multiple off background and a radial acceptance only the areas are different and $w = \tilde{A} = \frac{A_{\text{off}}}{A_{\text{on}}}$. Therefore in this case β is reduced to the factor between the geometrical sizes of the on and the off region, $\beta = \alpha$.
The correct excess is determined with

$$N_{\text{excess}} = N_{\text{on}} - \beta N_{\text{off}}. \tag{2.18}$$

In order to decide whether the excess is significant or just a background fluctuation it can simply be compared to its standard deviation (Eq. 8 from Li and Ma (1983))

$$\sigma\left(N_{\text{excess}}\right) = \sqrt{(N_{\text{on}} + \beta^2 N_{\text{off}})}. \tag{2.19}$$

The significance S is then defined as

$$S = \frac{N_{\text{excess}}}{\sigma\left(N_{\text{excess}}\right)} \tag{2.20}$$

However, it was shown by Li and Ma (Li and Ma, 1983) that this formula does not have the expected normal distribution for all values of $\beta \neq 1$. Hence, in Li and Ma (1983) they introduced a new method of estimating the significance S. They used the likelihood ratio method and came up with the following formula (Eq.17 from Li and Ma (1983)) for the significance:

$$S = \sqrt{2} \cdot \left\{ N_{\text{on}} \log\left[\frac{1+\beta}{\beta} \cdot \left(\frac{N_{\text{on}}}{N_{\text{on}} + N_{\text{off}}}\right)\right] + N_{\text{off}} \log\left[(1+\beta) \cdot \left(\frac{N_{\text{off}}}{N_{\text{on}} + N_{off}}\right)\right] \right\}^{\frac{1}{2}} \tag{2.21}$$

The significance S is a measure of the probability of the excess of being just a background fluctuation. The higher the significance the smaller the probability that the excess is due to a background fluctuation. The significance is given in units of the standard deviation σ of a normal distribution. In order to claim a gamma ray source discovery a significance well above $S = 5\sigma$ is requested by the H.E.S.S. Collaboration.

2.9.5. Accumulate Runs

The determination of the regions for the background estimation and the significance described above are valid for individual runs. A realistic measurement, however, uses multiple observation runs targeting a specific region of interest. The accumulating data are treated such that the significance determination with Eq. 2.21 stays valid. Therefore the total number of on and off events, $N_{\text{on,total}}$ and $N_{\text{off,total}}$, as well as the excess events, $N_{\text{excess,total}}$ are the sums of the corresponding numbers from each run i

$$N_{\text{on,total}} = \sum_{\text{i}} N_{\text{on,i}}, \quad N_{\text{off,total}} = \sum_{\text{i}} N_{\text{off,i}}, \quad N_{\text{excess,total}} = \sum_{\text{i}} N_{\text{excess,i}} \tag{2.22}$$

In order for these relations to hold the total normalisation factor β_{total} is defined in the following way:

$$\beta_{\text{total}} = \frac{\sum_{\text{i}} \beta_{\text{i}} N_{\text{off,i}}}{\sum_{\text{i}} N_{\text{off,i}}}. \tag{2.23}$$

The value of β_i for an individual run is the ratio of the on live time t_on and the weighted off live time t_off of the run (see Eq. 2.17):

$$\beta_\mathrm{i} = \beta = \frac{t_\mathrm{on}}{w(\tilde{A}, \tilde{A}_\mathrm{acc}, \dots) \cdot t_\mathrm{off}}. \tag{2.24}$$

2.9.6. Flux and Spectrum Determination

In this Section the determination of the spectral shape of the gamma-ray flux is described. A flux as well as a spectrum can only be given in case of a detection. If the source region has a significance below five sigma only an upper limit on the flux can be given, which is explained in the last paragraph of this Section.

Flux

A very important property of the source is its integrated flux, that is the number of particles N per area dA on the ground and per time dt, so $\Phi_\mathrm{flux} = \int_E \frac{\mathrm{d}\Phi_\mathrm{flux}}{\mathrm{d}E} = \int_E d^3N/(dEdAdt)$. The correlation between the number of excess events from a gamma ray source N_excess and the differential flux $\mathrm{d}\Phi_\mathrm{flux}/\mathrm{d}E$ is the following

$$N_\mathrm{excess} = \int_{\mathrm{t}_0}^{\mathrm{t}_1} \int_{E_\mathrm{thr}}^{\infty} A_\mathrm{eff}\left(E_\mathrm{true}|\beta_\mathrm{zen}, \theta, \epsilon_\mu\right) \cdot \frac{\mathrm{d}\Phi_\mathrm{flux}(E_\mathrm{true})}{\mathrm{d}E_\mathrm{true}}\, dE_\mathrm{true} dt \tag{2.25}$$

where A_eff is the effective area of the detector. To be able to use this correlation to determine the integral flux $\int_\mathrm{E} \Phi_\mathrm{flux}$ one needs to assume a shape for the spectrum $\mathrm{d}\Phi_\mathrm{flux}/\mathrm{d}E_\mathrm{true}$. In case of a simple power-law assumption $\Phi_\mathrm{flux} = \Phi_0 \left(\frac{E_\mathrm{true}}{E_0}\right)^2$, the flux normalisation Φ_0 at energy E_0 is determined via inverting Eq.2.25. In order to be able to do this and also for the spectrum determination it is important to know the threshold energy E_thr. How the energy threshold is defined for the H.E.S.S. experiment and how a spectrum is determined is described below.
An other method to determine the integrated flux without assuming any spectral shape is based on weighting every event with the corresponding effective area (de Naurois, 2012).

$$\Phi(E > E_\mathrm{thr}) = \sum \frac{\alpha_\mathrm{i}}{A_\mathrm{eff}(E_\mathrm{i}|\beta_\mathrm{zen}, \theta, \epsilon_\mu)} \tag{2.26}$$

There $\alpha_\mathrm{i} = 1$ for on events and $\alpha_\mathrm{i} = -\beta$ for off events, which yields

$$\Phi(E > E_\mathrm{thr}) = \sum_{\mathrm{N_{on}}} \frac{1}{A_\mathrm{eff}(E_\mathrm{i}|\beta_\mathrm{zen}, \theta, \epsilon_\mu)} - \beta \sum_{\mathrm{N_{off}}} \frac{1}{A_\mathrm{eff}(E_\mathrm{i}|\beta_\mathrm{zen}, \theta, \epsilon_\mu)}. \tag{2.27}$$

Effective Areas

The effective area A_{eff} corresponds to the area on the ground, in which gamma rays are seen by the detector. It is a measure for the sensitivity of the detector. The effective area A_{eff} depends on the true energy E_{true}, the zenith angle β_{zen}, the off-axis angle (offset) ψ and the optical efficiency ϵ_μ. It is determined from MC simulations. There the number of detected gamma events N_γ^{det} is compared to the number off all generated gamma events N_γ^{all} and multiplied with the simulated area A_{simu} in which the events appeared:

$$A_{\text{eff}} = \frac{N_\gamma^{\text{det}}}{N_\gamma^{\text{all}}} \cdot A_{\text{simu}} \tag{2.28}$$

An example of effective areas for different parameter configurations for the Model++ analysis is given in Fig.2.23.

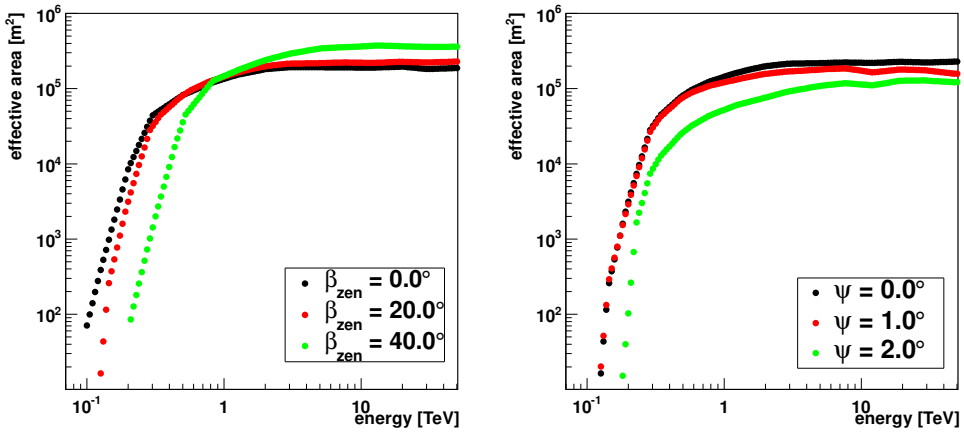

(a) (b)

Figure 2.23.: Effective areas over energy for the Model++ analysis for Std cuts (see Table 2.1) for different zenith angles (a) and offsets (b).

Energy Threshold

Different definitions of the energy threshold exist. In general the energy threshold is the minimum energy, at which the detector is still sensitive to gamma rays. However some uncertainties in the reconstruction exist around the minimal sensitivity of the detector therefore a higher, so-called "safe" energy threshold is defined.
One definition for a safe energy threshold is the lowest energy at which the bias (see Section 2.8.2) on the reconstructed energy is below 10%, plus an additional 10% (Aharonian et al.,

2006b). An other way to define the energy threshold is taking the peak of the differential rate over the energy (HEGRA Collaboration et al., 1999). In general this threshold is lower than the before defined safe threshold. For the Model++ analysis the safe energy threshold is lower than for the standard Hillas analysis, because of the smaller energy bias. A further, frequently used definition of the energy threshold relies on the effective area. The threshold is defined as the energy at which the effective area reaches a certain amount (typically around 50% for a safe threshold) of its maximum value.

Spectrum

The spectrum is important to determine the integrated flux but it also helps to understand the acceleration mechanisms of the source. In the Model++ analysis the spectrum is determined with a log-likelihood comparison. Therefore the expected number of excess (gamma) events $n_{\gamma,\mathrm{exp}}$ in a reconstructed energy bin $[E_1, E_2]$ is determined

$$n_{\gamma,\mathrm{exp}} = \int_{\mathrm{E_1}}^{\mathrm{E_2}} dE_{\mathrm{reco}} \int_0^{\infty} dE_{\mathrm{true}} \cdot A_{\mathrm{eff}}\left(E_{\mathrm{true}}|\beta_{\mathrm{zen}}, \theta, \epsilon_\mu\right) \cdot \Phi_{\mathrm{flux}}(E_{\mathrm{true}}, \vec{\alpha}) \cdot \wp(E_{\mathrm{true}}, E_{\mathrm{reco}}) \quad (2.29)$$

Here the spectral shape enters via the parameters $\vec{\alpha}$, e.g. the index in case of a power-law. $\wp(E_{\mathrm{true}}, E_{\mathrm{reco}})$ is the probability of measuring an event with reconstructed energy E_{reco} for a given true energy E_{true}. Similar to the effective area it depends on the true energy E_{true}, the zenith angle β_{zen} and the off-axis angle (offset) ψ. It is determined from MC simulations. For the calculation the measured events are divided into four-dim. bins of given zenith angle, offset angle, optical efficiency and reconstructed energy. If possible the energy bins are chosen in such a way that the significance in each bin is above three σ. Otherwise only an upper limit of the flux in the bin is given, see next Section. The expected number of gamma events $n_{\gamma,\mathrm{exp}}$ and the expected number of hadron (off) events $n_{\mathrm{h,exp}}$ in each bin are then used to calculate the bin-wise likelihood, which is the probability of observing N_{on} and N_{off} events when expecting $n_{\gamma,\mathrm{exp}}$ and $n_{\mathrm{h,exp}}$ events.

$$P(N_{\mathrm{on}}, N_{\mathrm{off}}|n_{\gamma,\mathrm{exp}}, n_{\mathrm{h,exp}}) = \frac{n_{\gamma,\mathrm{exp}} + \beta n_{\mathrm{h,exp}}^{\mathrm{N_{on}}}}{N_{\mathrm{on}}!} e^{-\left(\mathrm{n}_{\gamma,\mathrm{exp}} + \beta \mathrm{n}_{\mathrm{h,exp}}\right)} \cdot \frac{n_{\mathrm{h,exp}}^{\mathrm{N_{off}}}}{N_{\mathrm{off}}!} e^{-\mathrm{n}_{\mathrm{h,exp}}} \quad (2.30)$$

By maximising the logarithm of this likelihood the best estimation for $n_{\mathrm{h,exp}}$ is obtained. The final log-likelihood for the spectrum determination is then the sum of the log-likelihood over all bins. It is maximised to obtain the spectrum parameters $\vec{\alpha}$. The maximisation yields (de Naurois, 2012) the best fit parameters $\vec{\alpha}$ and their uncertainties as well as the covariance matrix between the parameters, the expected number of events in each bin and the maximum value of the log-likelihood. The uncertainty on the flux $\Phi_{\mathrm{flux}}(E)$ is determined with the inverse $W_{\mathrm{i,j}}$ of the covariance matrix and the partial derivatives of the flux at the spectral parameters $\vec{\alpha}$

$$d\Phi_{\mathrm{flux}}(E) = \sqrt{\sum_{\mathrm{i,j}} W_{\mathrm{i,j}} \frac{\Phi_{\mathrm{flux}}}{d\alpha_{\mathrm{i}}} \frac{\Phi_{\mathrm{flux}}}{d\alpha_{\mathrm{j}}}}. \quad (2.31)$$

Upper Limit

In case no significant signal from the source region is detected an upper limit on the flux can be derived. This is done with the profile likelihood method described in Rolke et al. (2005), which is a fully frequentist method. The advantage of this method is that it takes uncertainties in the background determination in account. An upper limit with a certain confidence level (typically 95% or 99%) can be determined. In order to determine the upper limit the spectrum is assumed to have a power-law shape with an index Γ. Upper limits can be calculated for the integrated as well as for the differential flux. Important for the upper limit calculations are the uncertainties of the measurement, which enter in the determination of the confidence level values.

3. Development of an On-Off Analysis based on Model++ Reconstruction

The development of the Model++ reconstruction and the resulting higher sensitivity of the Model++ analysis as described in the previous Chapter are a great success. Nevertheless, some challenges in the estimation of the background appear:

- The high sensitivity of the Model++ analysis leads to many source candidates in previously empty FoVs. These source candidates have to be excluded in the analysis and hence are no longer available as background (off-) regions. Using the same FoV for target (on-) region and off-region therefore becomes difficult in some cases.
  The Galactic Centre region is a good example. For the analysis with the less sensitive Hillas analysis framework used in Abramowski et al. (2011b) the excluded regions and the on-region were chosen as shown in Fig. 3.1 on the left. The on-region is a circle around the Galactic Centre with radius $r_{\mathrm{ON}} = 1^\circ$ (green in Fig. 3.1). The Galactic Plane is excluded up to a Galactic latitude of $b = \pm 0.3^\circ$ and the point source G0.9+0.1 is excluded as a circle with a radius of $r_{\mathrm{G09}} = 0.2^\circ$ (both red in Fig. 3.1). On the right in Fig. 3.1 the excluded regions (red) around the Galactic Centre in the Model++ analysis are shown. The excluded regions there are significantly larger due to the higher sensitivity of the analysis.

- Furthermore for large extended sources, e.g. Vela X (Abramowski et al., 2012a), finding off regions in the same FoV has always been challenging. The concept of dedicated on and off runs taken in the same night with the same detector configuration could serve as a potential solution for this problem, but with this kind of runs a lot of observation time is needed. Hence as already mentioned in Section 2.5 in the past this observation strategy has been used only in a few cases.

- The larger fifth telescope of the H.E.S.S. array has a smaller FoV ($\sim 3.5\,^\circ$) and offers therefore even less potential off-regions inside a single FoV.

These points show the need for an on-off-analysis. The basic principle of an on-off-analysis is, to take the on-region from one run (on-run) and the off-region from another run (off-run). This implies that the data in the on- and in the off-region were most probably taken under different observation conditions and detector configurations. These differences have an impact on the data and this impact needs to be taken into account when analysing the on-

and the off-data.
For the study of Vela X such an on-off-analysis has been developed in the Hillas analysis framework by Bernhard Glück (2011). However, the Model++ analysis takes into account the full camera information (raw data) and it will be shown, that the Model++ analysis depends more strongly on the observation conditions than the Hillas analysis.

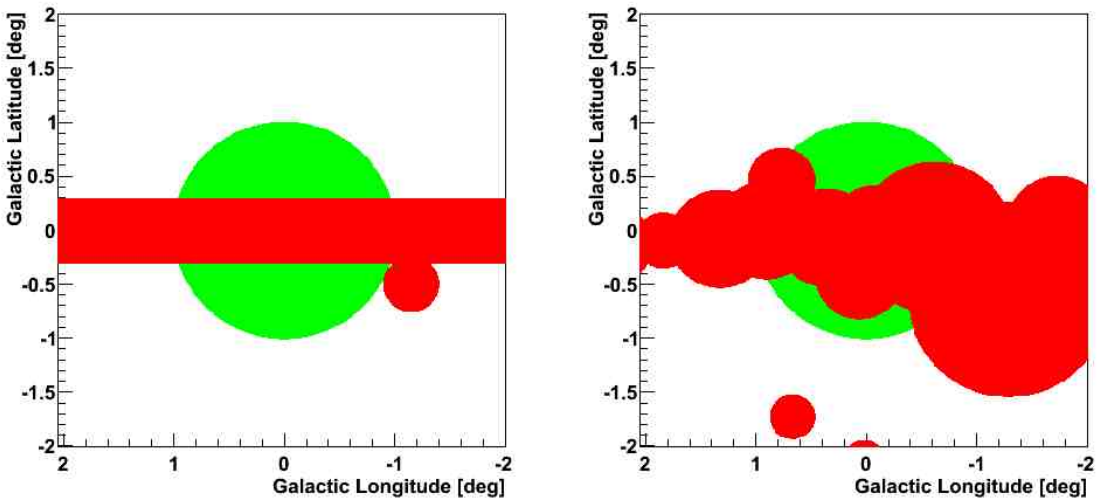

Figure 3.1.: Comparison of excluded regions around the Galactic Centre from different analysis. On the left the excluded regions and the on-region from Abramowski et al. (2011b) are shown. The excluded regions are red and the on-region is green. On the right the excluded regions as listed for the Model++ analysis are shown in red. In green the on-region from Abramowski et al. (2011b) is drawn for comparison.

In the following the systematic studies which were conducted in order to determine the influences of different parameters are described. First some prerequisites and definitions, like, e.g., the parameters which were included in the study, are introduced. Then the method used to determine the parameter dependencies is explained and the results for the different parameters are shown. Finally with the knowledge of the dependencies of the parameters two ways to implement an on-off-analysis are introduced and their performances are tested.

3.1. Prerequisites for Systematic Studies of Parameter Influences

This Section provides the basics needed to start the study of the parameter dependencies.

3.1.1. Parameters of Interest

First the parameters used in the systematic studies are introduced. The parameters are listed in Table 3.1 as well as their origin. Most of them are determined or monitored continuously during a run. However, for the later studies only the mean values of them over both – the run duration and the four telescopes – are used. This simple approach is sufficient for most of the parameters, as they do not change greatly during a run. However, this is not true for the zenith angle and the azimuth angle which constantly change because of the tracking of the target. Therefore for these two parameters also their value for each event (as obtained from the reconstruction) will be taken into account. Additionally, the ratio of actual and estimated trigger rate (see next Section) can be utilised as a means to evaluate atmospheric conditions (Glück, 2011). This parameter will be used in the following.

In order to study the parameters it is assumed that no strong correlation should exist

Table 3.1.: The mean parameters for each run. The mean corresponds here to both, the mean over the four telescopes as well as the mean over the whole run.

Parameter	Unit	max. Range	Determination
Zenith	Degree	0 – 90	from tracking
Azimuth	Degree	0 – 360	from tracking
Muon efficiency	-	0.0 – 0.1	from calibration
NSB	MHz	0 – 300	from calibration
Camera temperature	Degree Celsius	0 – 60	from cameras
Number of broken pixels	-	0 – 100	from calibration
Radiometer temperature	Degree Celsius	−80 – 0	from radiometers
Relative humidity	-	0 – 100	from weather station
Air temperature	Degree Celsius	−50 – 50	from weather station
Trigger rate	Hz	0 – 300	from daq

between them. To test this assumption the correlation coefficients ρ_{corr} as well as the corresponding plots have been determined for all parameters. The resulting coefficients are listed in Table 3.2. The corresponding plots can be found in Appendix A. Only two correlation coefficients show values above 0.5, which could indicate a linear correlation. A potential correlation is seen between the camera temperature and the air temperature. This correlation is easy to interpret since the camera temperature indeed cannot be lower than the air temperature, which implies a connection between the two variables. Nevertheless, the two parameters will be studied individually in the following. Additionally also between the NSB and the muon efficiency a correlation coefficient in the order of 0.5 was found. A potential correlation between these two parameters may be understood because a lower muon efficiency could lead also to a lower NSB. However, other effects should have a stronger influence on the NSB. Therefore also these parameters are studied individually.

In the following the selection of the H.E.S.S. data, which are used for the systematic studies, is described.

Table 3.2.: The correlation coefficients between the different parameters of interest.

	2	3	4	5	6	7	8	9	10
Zenith (1)	0.10	0.16	0.24	-0.14	0.03	0.13	0.07	0.05	0.06
Azimuth (2)	1.00	-0.02	0.08	-0.06	-0.07	-0.04	0.02	-0.07	0.01
Muon eff. (3)		1.00	0.51	-0.13	0.00	0.09	0.03	0.07	0.31
NSB (4)			1.00	0.16	0.02	0.03	0.04	-0.00	0.19
Broken pixels (5)				1.00	0.36	0.17	-0.05	0.33	0.06
Camera temp. (6)					1.00	0.27	-0.15	0.54	-0.10
Radiom. temp. (7)						1.00	0.10	0.38	-0.03
Relative hum. (8)							1.00	-0.15	0.21
Air temp. (9)								1.00	-0.03
Trigger ratio (10)									1.00

3.1.2. Data Selection

In order to understand the systematic influences on the background estimation, data from H.E.S.S. are studied. For the study only data passing similar quality criteria as described in the previous Chapter in Section 2.7.2 and as the ones chosen in Glück (2011) are used. Only good, high quality data, which is uncorrupted by bad observation or hardware conditions, is used. Eventually the following set of conditions, which have to be fulfilled by the data, are obtained:

- Duration of the run has to be between 1600 s and 1750 s (run not at the end of the night, no interruptions).
- All four telescopes have to be operational and at least two out of the four telescopes have to have been triggered (reducing background events, allowing for stereoscopy).
- The root mean square (rms) of the system trigger rate has to be smaller than 5 % (indication for no clouds).
- No less than 10 % of the PMTs are allowed to be broken (hardware problems).
- The observation position has to be at least 8° away from the Galactic Centre ($l = 0.0°$, $b = 0.0°$), because there only vanishing contributions due to the annihilation of dark matter in the halo are expected.
- Some runs are excluded due to a very hazy atmosphere during observation, see Glück (2011).

- Runs, which were taken after March 2010 (exceeding run number 55500) are excluded, because from then on the mirrors on individual telescopes were refurbished (exchanged) successively and therefore the mean muon efficiency is no longer a good measure for the overall muon efficiency.
- The system trigger rate R_{trig} has to be higher than 60 % of its estimate R_{trigest}.

An estimate R_{trigest} for the system trigger rate is obtained in a way similar to the one described in Glück (2011). The system trigger rate of the runs fulfilling all imposed requirements is plotted against the zenith angle and the muon efficiency in Fig. 3.2. These two parameters have major influence on the trigger rate. In Fig. 3.2(a) the dependence of

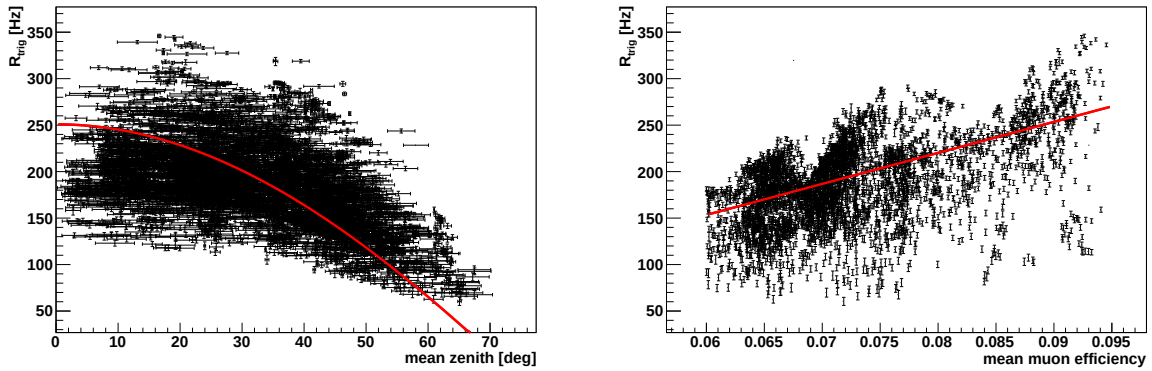

(a) (b)

Figure 3.2.: Two different dependencies of the system trigger rate. In (a) the system trigger rate over the mean zenith angle is drawn. The red line is a fit with a cosine. In (b) the system trigger rate over the mean muon efficiency is shown with the red line being a linear fit.

the trigger rate on the mean zenith is indicated with a cosine function (red). This behaviour is expected from Monte Carlo simulations (Bernlöhr, 2000) and was also seen in Glück (2011). In Fig. 3.2(b) a linear rise (red) of the trigger rate with the muon efficiency can be assumed. If these two plots are combined to a two dimensional plot, shown in Fig. 3.3, a clear correlation is visible. The trigger rate estimate is given by the two dimensional fit of Fig. 3.3 with the formula:

$$R_{\text{trigest}}\left(\alpha_{\text{zen}}, \epsilon_\mu\right) = R_{\text{norm}} \cdot \epsilon_\mu \cdot \cos\left(\alpha_{\text{zen}}\right), \tag{3.1}$$

where α_{zen} is the mean zenith angle and ϵ_μ is the mean muon efficiency of the run. The fit results in $R_{\text{norm}} = 3.15785 \cdot 10^3 \text{Hz}$. Now with this estimate for the trigger rate the quality cuts are applied.
In the next Section the background rate is introduced.

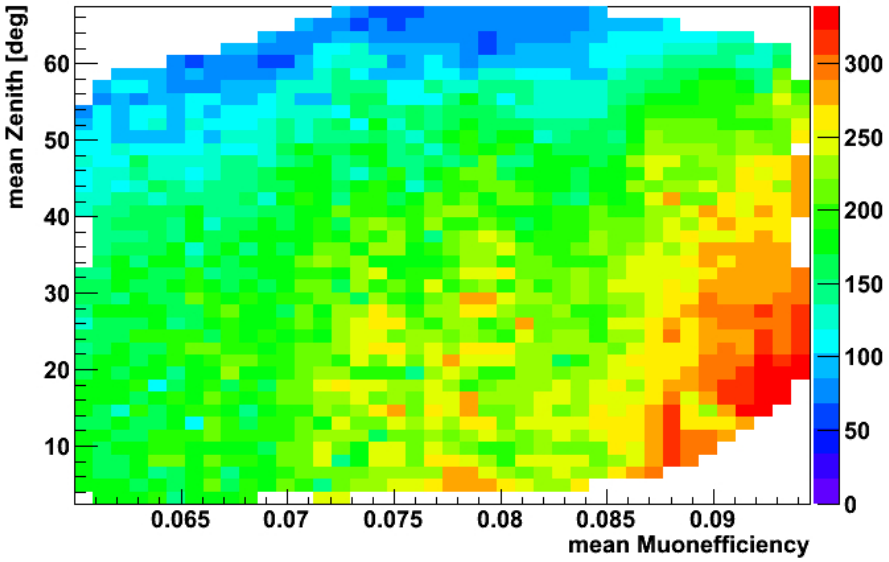

Figure 3.3.: The system trigger rate over the mean zenith angle and the mean muon efficiency.

3.1.3. Introduction of the Background Rate

In order to study the systematic effects of various detector and observation parameters on the background, a quantitative parameter has to be defined. A natural parameter to use is the background rate, with the assumption that the background rate is homogeneous over the whole sky (beside Poisson fluctuations). This assumption is justified since the background for H.E.S.S. are mostly hadronic cosmic rays, which appear gamma-like in the detector. The background rate R depends on all the parameters listed in Table 3.1, which vary because of different observation conditions and detector effects. In the following Section the rate is defined and its uncertainties are discussed.

Definition of the Background Rate

The background rate is defined as the number of gamma-like events N in a source-free area A on the sky in a certain time t.

$$R_{\mathrm{bg}} = \frac{N}{A \cdot t}. \tag{3.2}$$

The unit of R_{bg} is therefore $\mathrm{s}^{-1}\,\mathrm{deg}^{-2}$.
The background rate for a single run consists of all the events passing gamma selection cuts (the results shown in the following are for Std cuts, see Table 2.1), that do not fall into excluded regions and lie within a certain radius r from the observation position. The corresponding area is then the area of the circle on the sky with radius r without the areas

that are excluded. The corresponding time is the live time of the run. Calculating the background rate in this way takes into account that both the different excluded regions and observation times may vary from run to run.
In order to obtain better statistics the background rate is accumulated over several runs. The summation can be done in several ways, on the one hand by simply calculating the mean R_{mean} of the background rate over several runs n, and on the other hand by determining an accumulated rate R_{acc}, which differs slightly from R_{mean}. The mean and the accumulated rates are acceptable measures for the distribution, as the distribution of the individual/ runwise rates is sufficiently symmetric. For the mean rate R_{mean} the following holds:

$$R_{\mathrm{mean}} = \frac{1}{n} \cdot \sum_{\mathrm{i}} R_{\mathrm{i}}. \tag{3.3}$$

Here the summation index i denotes the number of runs, therefore R_{i} is the rate of an individual run. The error of R_{mean} is calculated taken the uncertainties on the area ΔA, the event count ΔN and the live time Δt into account as follows:

$$\Delta R = \frac{1}{n} \cdot \sqrt{\left(\sum \Delta R_{\mathrm{i}}^2\right)}, \tag{3.4}$$

$$\Delta R_{\mathrm{i}} = \sqrt{\frac{N_{\mathrm{i}}}{(A_{\mathrm{i}} \cdot t_{\mathrm{i}})^2} + \left[\frac{N_{\mathrm{i}}}{A_{\mathrm{i}}^2 \cdot t_{\mathrm{i}}} \cdot \Delta A_{\mathrm{i}}\right]^2 + \left[\frac{N_{\mathrm{i}}}{A_{\mathrm{i}} \cdot t_{\mathrm{i}}^2} \cdot \Delta t_{\mathrm{i}}\right]^2}. \tag{3.5}$$

While for the uncertainty on the event count ΔN a Poissonian error is assumed, $\Delta N = \sqrt{N}$, the error estimate on the time Δt and on the area ΔA are given in the next Section.
For the accumulated rate R_{acc} the summation is a bit different. The result is quite similar to the mean rate, but the calculation of this overall rate is more intuitive when summing over several runs with different areas and times (see example for two runs in Appendix A.2). Hence the accumulated rate R_{acc} is used in the parameter studies:

$$R_{\mathrm{acc}} = \frac{N}{V}, \;\; N = \sum N_{\mathrm{i}}, \;\; V = A \cdot t = \sum V_{\mathrm{i}}. \tag{3.6}$$

The number of events N and the parameter V are simply summed up over all runs i. V_{i} corresponds to the exposure of the observation of each run that is equal to the product of the area and the time: $V_{\mathrm{i}} = A_{\mathrm{i}} \cdot t_{\mathrm{i}}$. The propagated error for the accumulated rate is

$$\Delta R_{\mathrm{acc}} = \sqrt{\frac{1}{V^2} \cdot \sum \Delta N_{\mathrm{i}}^2 + \frac{\sum N_{\mathrm{i}}^2}{V^4} \cdot \sum (t_{\mathrm{i}}^2 \cdot \Delta A_{\mathrm{i}}^2 + A_{\mathrm{i}}^2 \cdot \Delta t_{\mathrm{i}}^2)}. \tag{3.7}$$

Here the same uncertainties as above for ΔN, ΔA and Δt are used (see next Section).
In addition to the uncertainties discussed above also a statistical uncertainty will be given in the following. This statistical uncertainty is determined as the error ΔR_{stat} on the

determination of the mean or accumulated rate. ΔR_{stat} is estimated in the following way:

$$\Delta R_{\text{stat}} = \frac{S}{\sqrt{m}} = \frac{1}{\sqrt{m}} \cdot \sqrt{\frac{\sum_i \left(R_{\text{acc}} - R_{\text{i}}\right)^2}{m-1}}. \tag{3.8}$$

Here m is the number of all runs i used for the calculation of R_{acc}. S is the standard deviation.
Eventually R_{acc} is determined to $R_{\text{acc}} \pm \Delta R_{\text{acc}} \pm \Delta R_{\text{stat}}$.

Estimating Uncertainties on the Background Rate

The uncertainties for ΔN, ΔA and Δt are discussed now. As already mentioned ΔN is assumed to be the Poisson error $\Delta N = \sqrt{N}$. Another potential source of uncertainty lies in the reconstruction of the position of the event, which is only exact up to 0.1 ° (de Naurois and Rolland, 2009). This might lead to more or less events in the fixed regions on the sky. However this effect is not taken into account here, because the reconstruction error is assumed to appear uniformly over the whole FoV. Therefore the mean expected event count in a fixed region is assumed to be not affected by the reconstruction error.

The area was calculated numerically with a binwise integration in order to be able to

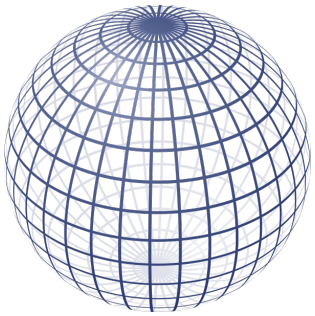

Figure 3.4.: A grid on a shpere is shown. It nicely illustrates the different binsizes and areas on the sphere which have to be taken into account when numerically calculating areas on it.

handle arbitrary shaped excluded regions in a simple manner. A lower limit of the error on the area calculation was estimated by comparing the result of the numerical calculation to the analytical result for ring regions (which can be derived from the analytical expression for a circle [1]). Due to the fact that the areas on the sky are areas on a sphere different bin sizes or bin areas have to be taken into account when integrating. In Fig. 3.4 a sphere with a grid is shown to illustrate this binning effect. The comparison between the analytical and the numerical calculation revealed only very small deviations (below 1%). Nevertheless, a conservative error estimate (also with regard to the neglect of the direction error) on the

[1] $A_{\text{circle}}(\theta) = 2\pi \cdot (1 - \cos\ \theta)$.

area of $\Delta A = 5\% A = 0.05A$ was chosen.
Now the uncertainty in the determination of the live time Δt has to be estimated. For this variable two cases are considered.

- A fixed live time.
- A variable live time chosen according to some constraints.

The first case is straight forward. There the live time is simply fixed to 1560 s, choosing only events that have arrived after the first minute (> 60 s) and before the last minute (< 1620 s). With this fixed choice the error Δt vanishes and $\Delta t = 0$ holds.
In the second case a time window is chosen with respect to the dependence of other parameters on the time. These other parameters are the zenith and the azimuth angle. Both angles change during an observation in order to track a target on the sky and therefore compensate the Earth's rotation. To be able to determine the accumulated rate dependence on a certain parameter it is necessary to restrict the other parameter ranges. In case of the zenith and azimuth angle this is done with a cut on the time. Therefore the behaviour of the zenith and the azimuth angle with time must be known for each run. The change in azimuth over time can be described by a parabola whereas in case of the zenith a linear fit is sufficient:

$$\lambda_{\text{azi}}(t) = a_\lambda \cdot t^2 + b_\lambda \cdot t + c_\lambda, \tag{3.9}$$
$$\beta_{\text{zen}}(t) = a_\beta \cdot t + b_\beta. \tag{3.10}$$

In Fig. 3.5 the nominal position of the zenith and the azimuth angle is fitted with the corresponding functions (red) and the zenith and azimuth values of the measured events scatter around these nominal values inside the FoV. Now in order to get a cut condition on the time Eqns. 3.9 and 3.10 have to be inverted:

$$t = \frac{-b_\lambda \pm \sqrt{b_\lambda^2 - 4a_\lambda (c_\lambda - \lambda_{\text{azi}})}}{2a_\lambda}, \tag{3.11}$$
$$t = \frac{\beta_{\text{zen}} - b_\beta}{a_\beta}. \tag{3.12}$$

If, e.g., the zenith angle range has to be restricted between $\beta_{\text{zen,low}}$ and $\beta_{\text{zen,up}}$ a corresponding time interval between t_{low} and t_{up} is chosen. This choice then contains the uncertainty of the time Δt. In case of the zenith angle the restriction yields an estimate of Δt of

$$\Delta t \approx \frac{2}{a_\beta} \cdot \Delta\beta_{\text{zen}}, \tag{3.13}$$

where for $\Delta\beta_{\text{zen}}$ the deviation between the fit and the actual nominal position is used (uncertainties on the fit parameters a_β and b_β have been neglected here). This deviation

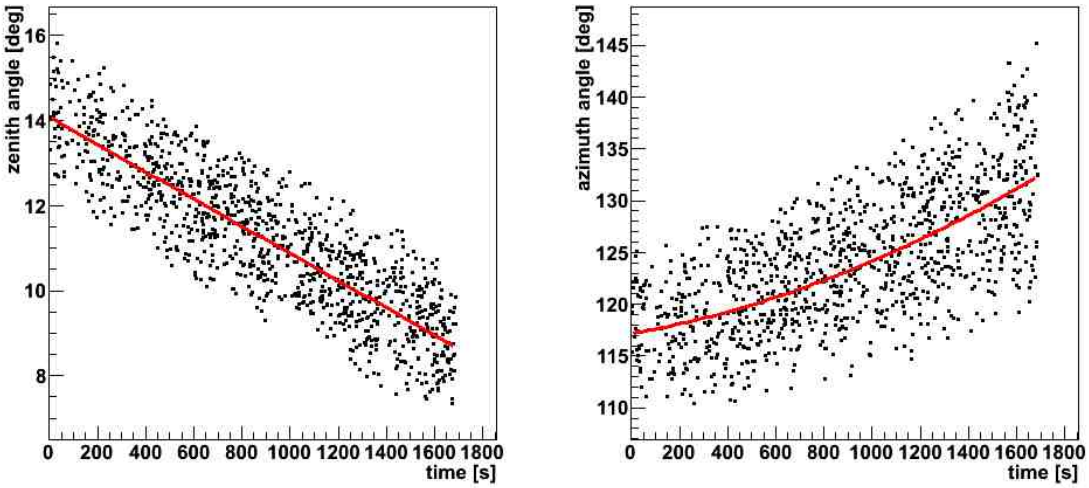

Figure 3.5.: On the left: Zenith angle over time for a run. The red line corresponds to a linear fit to the nominal position of the zenith. On the right: Azimuth angle over time for a run. The red line corresponds to a parabola fit to the nominal position of the azimuth angle.

lies in the order of one percent. Hence

$$\Delta t \approx \frac{2}{a_\beta} \cdot 0.01 \cdot \overline{\beta_{\text{zen}}}, \tag{3.14}$$

with $\overline{\beta_{\text{zen}}}$ being the mean value of the zenith angle between $\beta_{\text{zen,low}}$ and $\beta_{\text{zen,up}}$, is used. Similarly the resulting uncertainty of the live time for a mean azimuth angle $\overline{\lambda_{\text{azi}}}$ is determined to

$$\Delta t \approx \frac{2}{b_\lambda^2 - 4a_\lambda \left(c_\lambda - \overline{\lambda_{\text{azi}}}\right)} \cdot 0.01 \cdot \overline{\lambda_{\text{azi}}}. \tag{3.15}$$

In the following two Sections the energy threshold and the acceptance used in the systematic studies are introduced.

3.1.4. Energy Threshold

In this Section the energy threshold for the on-off analysis and the systematic studies is determined. The energy threshold depends on the zenith angle and potentially the muon efficiency and the offset. Therefore the dependence of the background rate on these parameters could be shadowed by the energy threshold of the detector. In order to use a safe energy threshold a slightly different definition than the one described in Section 2.9.6 is introduced in the following.

At first the background rate is plotted over the energy. The zenith angle, the offset and the muon efficiency are restricted to fixed values here, in order to test their influences. The zenith angle is fixed in a range $\beta_{\text{zen}} \pm 1.5°$ via the time condition described in Section 3.1.3. Furthermore the runs have been split into intervals according to their muon efficiencies. Every interval contains approximately the same amount of runs, therefore the intervals – or bin sizes – are not equidistant. The intervals and the number of runs inside each interval as well as the mean muon efficiency and the first and last run in the interval are listed in Table 3.3. Muon efficiencies below 0.06 are very rare and indicate bad observation or hardware conditions. Therefore runs with such low muon efficiencies are not included in the analysis. The offset is restricted to ranges between $[0.0°, 0.25°]$, $[0.25°, 0.75°]$,$[0.75°, 1.25°]$,

Table 3.3.: The runs are split up into intervals of similar size according to their muon efficiencies.

Limits	# Runs	mean ϵ_μ	first run	last run
$[0.000, 0.060]$	104	0.0490	20936	55315
$[0.060, 0.0642]$	600	0.0627	40946	60266
$[0.0642, 0.0659]$	600	0.0651	40217	60265
$[0.0659, 0.0679]$	600	0.0669	19270	65430
$[0.0679, 0.0697]$	600	0.0690	29384	65431
$[0.0697, 0.0711]$	600	0.0704	28828	65434
$[0.0711, 0.0729]$	600	0.0719	27608	65376
$[0.0729, 0.0769]$	600	0.0749	24472	64961
$[0.0769, 0.0862]$	600	0.0809	21010	30892
$[0.0862, 0.1000]$	423	0.0894	18491	21550

$[1.25°, 1.75°]$ and $[1.75°, 2.25°]$. For the offset and the muon efficiency the step size is given by the intervals whereas for the zenith angle a step size of 2° is chosen. For all the different configurations of zenith angle, offset, and muon efficiency the background rate divided by the bin width in energy is plotted over the energy. Figure 3.6 is an example of such a plot for the configuration with zenith angle $\beta_{\text{zen}} = 10° \pm 1.5°$, muon efficiency between $\epsilon_\mu \in [0.06, 0.0642]$ and offset $\theta \in [0.25°, 0.75°]$. There the background rate drops towards lower energies. This is attributed to the efficiency of the detector. Only above a certain energy threshold the effective areas become large enough to enable the reconstruction of all events, see Section 2.9.6. For this thesis the energy threshold is therefore defined as the position of the peak of the differential background rate over the energy (the background rate in a certain energy bin divided by the bin width). This choice was suggested by the HEGRA Collaboration et al. (1999) and is also discussed in Glück (2011). The energy threshold has been determined for different zenith angles, muon efficiencies and offset angles. While the energy threshold rises with increasing zenith angle and slightly drops with increasing muon efficiency, it appears to be independent of the offset. In Fig. 3.7(a) the resulting energy threshold is plotted as a function of zenith angle for the lowest muon efficiency interval, $[0.06, 0.0642]$, and an offset between $[0.25°, 0.75°]$. In Fig. 3.7(b) the peak positions are drawn over the different muon efficiency intervals for a fixed zenith angle of 10° and the

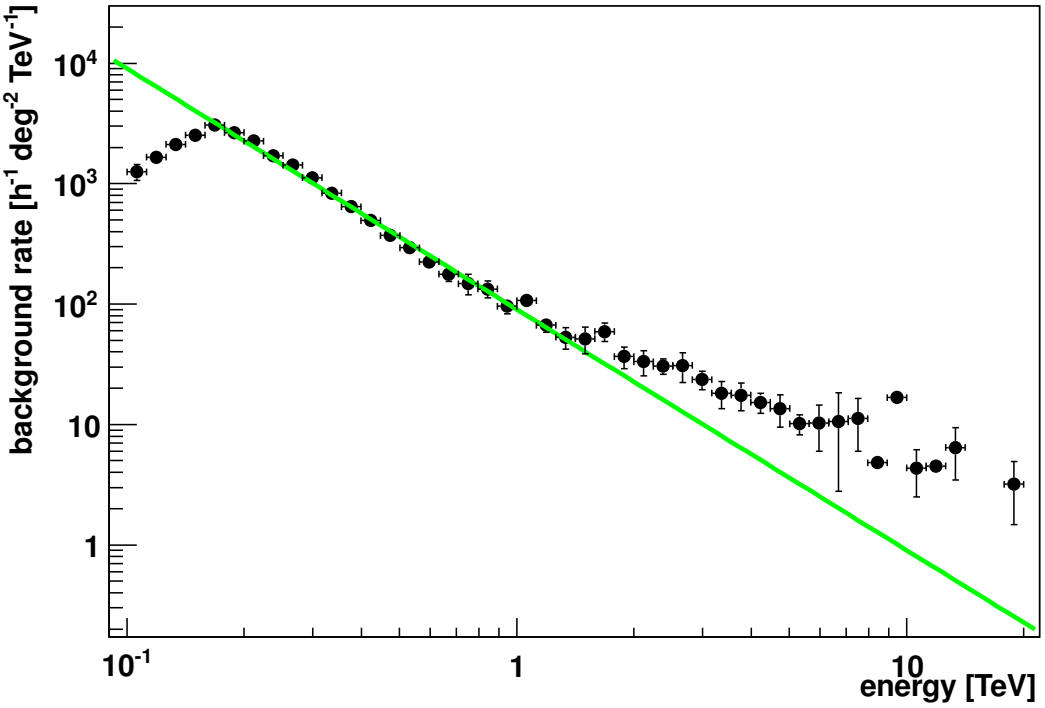

Figure 3.6.: The background rate is plotted over the energy in TeV for a zenith angle of $10° \pm 1.5°$, a muon efficiency $\epsilon_\mu \in [0.06, 0.0642]$ and an offset $\theta \in [0.25°, 0.75°]$. As the background rate per energy over energy follows a power-law, like $a \cdot E^{-\Gamma}$, or the sum of two power-laws, $a \cdot E^{-\Gamma_1} + b \cdot E^{-\Gamma_2}$ the axes are logarithmic. As an example a power-law (green line) with index $\Gamma = 2.0$ and $a = 90.5\,\mathrm{s}^{-1}\mathrm{deg}^{-2}\mathrm{TeV}^{-1}$ is shown. The errors in this plot are the propagated errors.

same offset range as before. It becomes clear that the dependence on the zenith angle is very strong, whereas considering the muon efficiency the energy threshold can conservatively be set to a constant which agrees with the value found for the lowest muon efficiency. The overall energy threshold is parametrised as

$$E_{\mathrm{thr}}\left(\beta_{\mathrm{zen}}\right) = a \cdot \beta_{\mathrm{zen}}^4 + b \cdot \beta_{\mathrm{zen}}^2 + c \tag{3.16}$$

with $a = 7.263 \cdot 10^{-8}\,\mathrm{TeV\,deg}^{-4}$, $b = 4.785 \cdot 10^{-5}\,\mathrm{TeV\,deg}^{-2}$ and $c = 0.2\,\mathrm{TeV}$. This corresponds to the red line in Fig. 3.7(a) and is a conservative estimate of the energy threshold for the on-off-analysis with Model++ std cuts. This estimate is independent of the offset and the muon efficiency.
From now on a cut on the event energy requiring an energy above E_{thr} is applied on the data. Furthermore, for energies above 10 TeV not much data is left, as is visible also in Fig. 3.6, that is why in the following the events are restricted to energies $\leq 10\,\mathrm{TeV}$. The

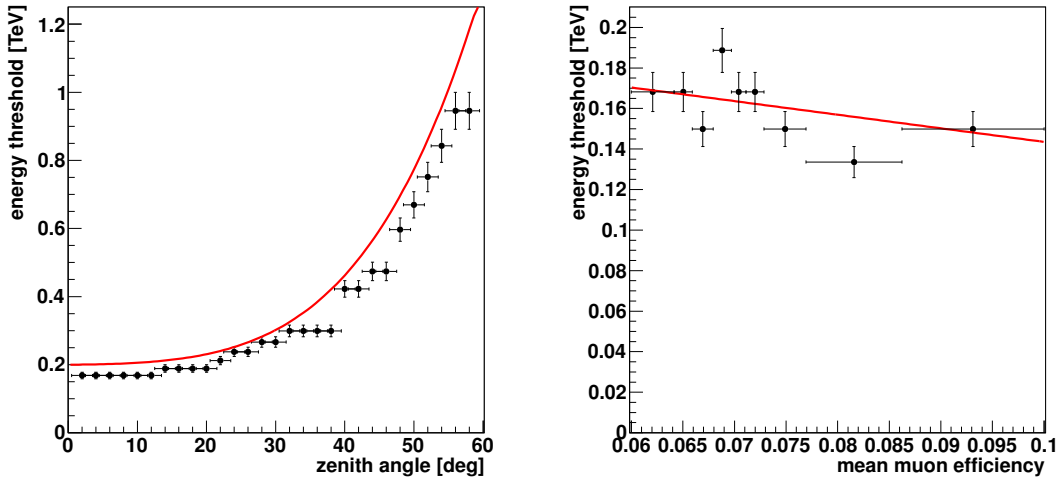

(a) (b)

Figure 3.7.: In (a) the energy threshold over the zenith angle for the lowest muon efficiency interval $[0.06, 0.0642]$ and an offset around 0.5° is shown. The errors on the energy threshold are the binwidths of the bins corresponding to the peak position. The error on the zenith angle is set to ±1.5° The red line shows a conservative choice of the energy threshold following a 4th order polynomial $E_{\mathrm{thr}} = a \cdot \beta_{\mathrm{zen}}^4 + b \cdot \beta_{\mathrm{zen}}^2 + c$. In (b) the energy threshold over the muon efficiency for a fixed zenith angle at $10° \pm 1.5°$ and offset around 0.5° is drawn. The errors are the width of the energy bin and the width of the muon interval, respectively. The red line corresponds to a fit with a linear function.

influence of the energy threshold on the background rate makes it worthwhile to study not only the full energy range from 0.1 to 10 TeV, but also an energy range well above the threshold from 1.5 to 10 TeV.
In the next Section follows the determination of the acceptance used for the on-off-analysis and the systematic studies.

3.1.5. Acceptance

In the previous Section it was mentioned that the energy threshold is independent of the offset. Nevertheless the dependence of the background rate on the offset might depend on the energy. The offset ψ dependence is the same as the H.E.S.S. camera acceptance, which needs to be determined for the analysis. The acceptance for the on-off-analysis is determined in a way similar to the radial acceptance, see Chapter 2 Section 2.9.2. The background rate is drawn over the offset squared ψ^2, because equidistant bins on the ψ^2 axis correspond to rings with similar areas on the sky. The potential influence of the zenith

angle on the rate is taken into account by setting the zenith angle to fixed values like for the determination of the energy threshold ($\pm 1.5°$). The muon efficiency is not fixed here, since each offset bin contains the same runs and therefore the same distribution of muon efficiencies. Furthermore the influence of the muon efficiency is assumed to be independent of the influence of the offset and not restricting the muon efficiency yields more data in the bins. In Fig. 3.8 the background rate is plotted over the offset squared ψ^2 for five different zenith angles from 10° to 50° and muon efficiencies between 0.06 and 0.1. In Fig. 3.8(a) the energy range is set to $0.1\,\text{TeV} \leq E \leq 10.0\,\text{TeV}$ and in Fig. 3.8(c) to $1.5\,\text{TeV} \leq E \leq 10.0\,\text{TeV}$. It can be seen that the background rate behaves similarly for the different zenith angles. Though in Fig. 3.8(a) additionally an effect of the energy threshold (or zenith angle) is visible. For lower zenith angles up to about 30° the energy threshold is lower than for the higher zenith angles. Therefore events at low energies are missing for high zenith angles and the rates at high zenith angles are lower. For energies well above the energy threshold in Fig. 3.8(c) this is not the case. There the rates are highest for highest zenith angles. In order to obtain the acceptance for the analysis for a certain energy range a two dimensional map of the background rate over the zenith and the squared offset ψ^2 is used. The two maps used for the full energy range and the high energies are shown in Fig. 3.8(b) and Fig. 3.8(d). The values have been determined in steps of 5.0° for the zenith and $0.4\,\text{deg}^2$ for ψ^2. In between bilinear interpolation (Wikipedia, 2013) is used. When applying an acceptance correction an event with squared offset ψ^2_{event} and zenith angle $\beta_{\text{zen,event}}$ is weighted relative to the value of the background rate at $\psi^2 = 0$ and $\beta_{\text{zen}} = \beta_{\text{zen,event}}$. With this varying shapes of the acceptance due to the zenith angle are taken into account, but the overall normalisation, which contains the main zenith dependence, stays unchanged. The zenith dependence, which is also influenced by the energy threshold, is studied in detail in the next Section. In the following the acceptance correction described above will be applied.

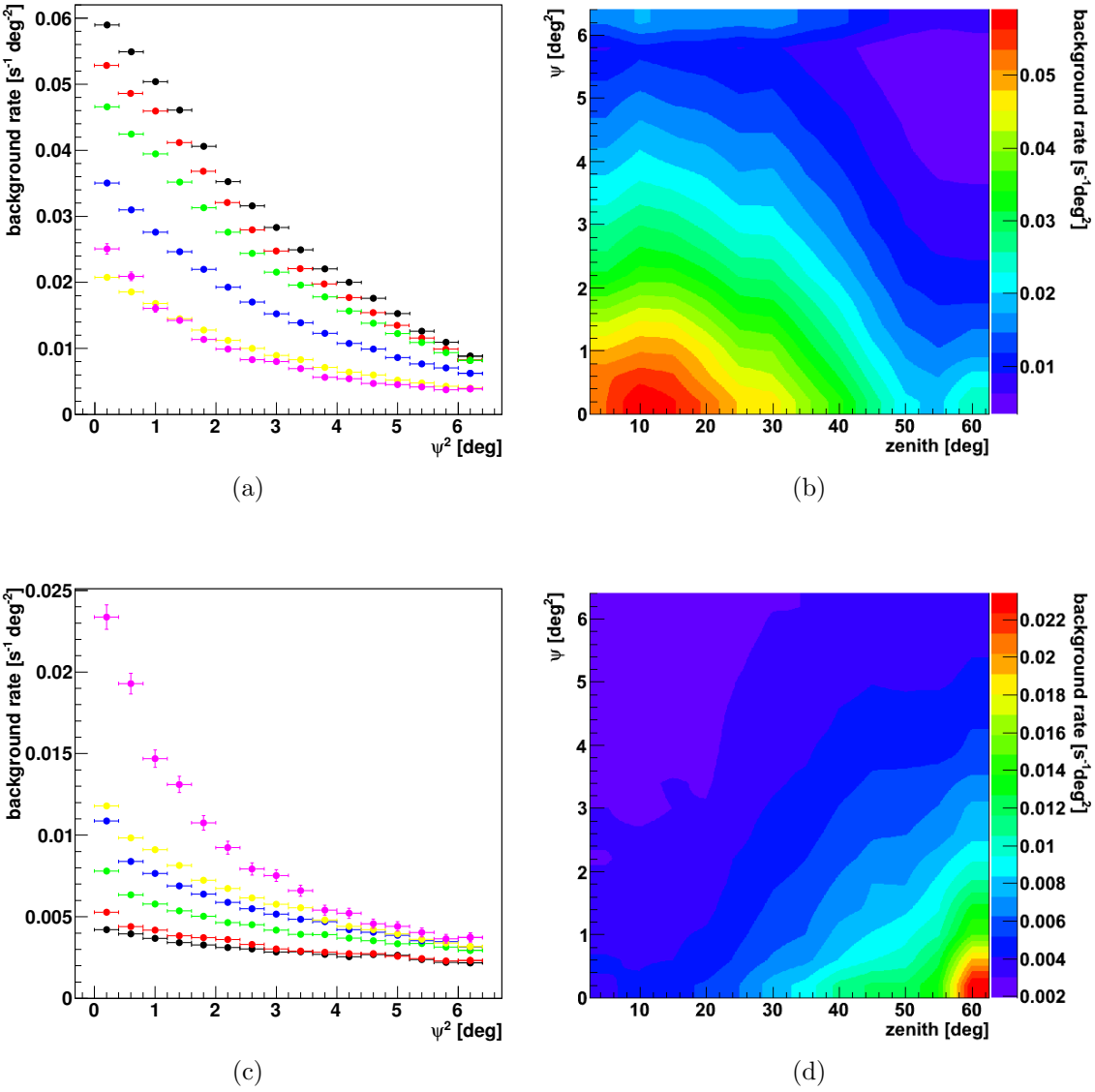

Figure 3.8.: (a) and(c): The background rate over the square of the offset for five different zenith angles and two energy ranges is shown. The colors correspond to the zenith angles (10° = black, 20° = red, 30° = green, 40° = blue, 50° = yellow, 60° = pink). The errors on the x-axis are the bin widths. In (a) the energy range from $0.2\,\text{TeV} \leq E \leq 10.0\,\text{TeV}$ is shown and in (c) from $1.5\,\text{TeV} \leq E \leq 10.0\,\text{TeV}$. In (b) and (d) the corresponding two dimensional plots over offset and zenith angle are shown. The offset squared is binned like in (a) and(c), whereas the zenith is binned in steps of 5° here. Between the points bilinear interpolation has been used. From these two dimensional images the acceptance correction is determined for the two energy ranges ($0.2\,\text{TeV} \leq E \leq 10.0\,\text{TeV}$ (b) and $1.5\,\text{TeV} \leq E \leq 10.0\,\text{TeV}$ (d)).

3.2. Systematic Studies to determine Parameter Influences

The necessary basics for the study of the parameter influences have been described in the previous Sections. In the following first the methods used to determine the dependence of the background rate on the various parameters are described. Afterwards the results are presented.

3.2.1. Two Ways to determine Parameter Influences

The aim of this Section is to familiarise the reader with the used methods of determining the parameter dependencies. The subsequent Sections about the individual parameters will focus on the results.

Method A

In order to determine the influences of the various parameters on the background rate a straight forward approach would be to just study the background rate over the parameter of interest, sort the runs according to the parameter of interest and draw the accumulated background rate for the runs in a certain bin of the parameter of interest. This simple approach, though, contains many potential sources of errors, because dependencies on other parameters might shadow the influence of the parameter of interest. To use this method it is necessary to take some precautions. It is again easy to anticipate that all other parameters apart from the parameter of interest have to be set to fixed values or at least fixed ranges to reduce their influence on the background rate or better to keep their influence constant. Considering the data given here (see distributions of the runs over the different parameters in Appendix A.3), this is not possible for all parameters, because not enough data is left if split up according to all parameters. Nevertheless, the method could still be used to unveil (the strongest) dependencies. If the influences of the various parameters are independent of each other and the remaining parameters are distributed homogeneously over the bins of the parameter of interest, all data can be used. Another important aspect is the trade-off between the amount of data needed for good statistics and the restriction of the parameter space. This method of plotting the background rate over the parameter of interest with certain other parameters fixed is called “method A” in the following and has already been used for the determination of the energy threshold and the acceptance. However, results obtained with method A are only shown for the zenith angle in the following, because of the before mentioned difficulties with the selection and the statistics of the data. Nevertheless, more results obtained with method A are given in Appendix A.4.

Method B

Another way to determine the dependence of the background rate on the parameters, which is called "method B" from now on, is to sort the runs again in bins according to the parameter of interest. Then the bin containing the largest number of runs is chosen as reference bin. Afterwards a kind of on-off-analysis is done for each bin. For each bin the runs are paired with runs from the reference bin. The pairing is done by selecting runs that agree very well in all parameters beside the parameter of interest. This is done similar to the procedure utilised in Glück (2011). A weight W is determined for every run pair (ref, bin). The weight W is defined as follows:

$$W\left(\mathrm{ref}, \mathrm{bin}\right) = \sum_{\mathrm{par}} \left(w_{\mathrm{par}} \cdot X_{\mathrm{par}}\right)^2 . \tag{3.17}$$

There $X_{\mathrm{par}} = par_{\mathrm{ref}} - par_{\mathrm{bin}}$ is the difference between the value of the parameter *par* in the reference run (ref) and the run from the bin (bin). w_{par} is a weighting coefficient, which accounts for the different sizes of $X_{\mathrm{par}} = par_{\mathrm{ref}} - par_{\mathrm{bin}}$ for the various parameters (e.g. $X_{\mathrm{muon}} = \epsilon_{\mu,\mathrm{ref}} - \epsilon_{\mu,\mathrm{bin}} \leq 0.04$ while $X_{\mathrm{zenith}} = \beta_{\mathrm{zen,ref}} - \beta_{\mathrm{zen,bin}} \leq 60°$) and also for their respective impact on the background rate. For the study of the parameter dependencies the weighting coefficients have been set to the a priori values listed in Table 3.4 normalised to the impact of the zenith angle. Furthermore the difference in the mean zenith angle is restricted to 3°, because of the presumably strong zenith dependence. In order to find the runs with the best matching parameters $W\left(\mathrm{ref}, \mathrm{bin}\right)$ is minimised. The reference run, which yields the lowest $W\left(\mathrm{ref}, \mathrm{bin}\right)$, is then paired with the run from the bin. This chosen reference run (ref) is no longer available for other pairs from this bin, in order to avoid a bias due to using a potentially corrupted/special run more than once. Then a matching reference run for the next run from the bin is searched for. In case no satisfactory match for the run from the bin is found in the reference interval a high value for $W\left(\mathrm{ref}, \mathrm{bin}\right)$ is obtained. Therefore, in order to only use sufficiently well matching run pairs, $W\left(\mathrm{ref}, \mathrm{bin}\right)$ is required to be below a certain limit ($W\left(\mathrm{ref}, \mathrm{bin}\right) < 10$). The runs for which no such weight is found are not used in the following analysis. The a priori weight coefficients were chosen in a way such that enough pairs are found and the allowed maximum deviation of a parameter ($\Delta par = \sqrt{W\left(\mathrm{ref}, \mathrm{bin}\right)/w_{\mathrm{par}}^2}$) does not lead to large deviations in the background rate. The expected deviations on the background rate Δ_{Rate} due to the studies performed in Glück (2011) are given in Table 3.4 as well as the deviations corresponding to the results found for the Model++ analysis. For the resulting pairs the background rates are accumulated for all runs in the reference bin and for all runs in the other bin. The obtained accumulated rate from the bin is then divided by the accumulated rate from the reference. The ratio of the two is drawn over the value of the bin. The exact agreement in all other parameters should now reduce effects due to these other parameters and only the effect of the parameter of interest should be visible in the resulting plot. Here also problems can occur if only very few run pairs are found, because then statistical fluctuations might dominate.

The results in the following are obtained with method B. However, in case of enough data the two methods are of course expected to yield comparable (within statistical errors the same) results.

Table 3.4.: The a priori weighting coefficients chosen for the studies of the parameter influences and the allowed maximal deviations of the rates resulting from applying a limit of $W(\text{on}, \text{off})_{\text{max}} = 10.0$ (derived from Glück (2011) for the Hillas analysis and from the later results for the Model++ analysis).

Parameter	Weight w_{par}	Δ_{Rate} Hillas	Δ_{Rate} Model++
Zenith	1.0	15%	10%
Azimuth	0.1	5%	10%
Muon efficiency	1000.0	$< 5\%$	15%
NSB	0.1	$< 10\%$	10%
Camera temperature	0.1	12%	30%
Number of broken pixel	0.01	10%	15%
Radiometer temperature	0.1	-	10%
Relative humidity	0.1	-	15%
Air temperature	0.1	-	20%
Rrigger rate ratio	10.0	30%	30%

3.2.2. Zenith Angle

In Section 3.1.4 it was pointed out that the dependence of the energy threshold on the zenith angle has to be taken into account when studying the dependence of the background rate on this parameter. Lower zenith angles have lower energy thresholds and therefore higher event counts and rates. In the following it is studied whether the dependence of the background rate on the zenith angle at low energies is merely a product of the dependence at high energies and the energy threshold or whether the dependence is energy dependent. In order to get a better understanding of the influence of the energy threshold a simulation was done, where zenith angle and energy were assigned to events according to certain expected distributions. For simplicity the energy dependence is modelled by a power-law with $R(E) = R_{\text{norm}} \cdot E^{-\Gamma}$ and $\Gamma = 2.0$. As a first test the effect of applying a cut on the energy of the events is studied for a uniform input distribution of zenith angles and an energy threshold depending linearly on the zenith angle.

$$E_{\text{thr}}(\beta_{\text{zen}}) = 0.1\,\text{TeV} + b \cdot \beta_{\text{zen}} \tag{3.18}$$

With $b = 0.015\,\text{TeV}\,\text{deg}^{-1}$ a strong influence is attributed to the zenith angle. In Fig. 3.9 the results of a simultation with 100,000 events are shown. The input distributions are shown in the top panel. In the lower panel the same distributions are plotted but this time after applying an energy cut: The event energy has to be higher than the energy threshold

defined in Eq. 3.18. The green lines in Fig. 3.9 are fits to the input distributions, the red lines are fits to the distributions after applying the energy cut. It is clearly visible that the loss of events due to this cut has a significant effect on the distribution for the zenith angle when plotted over the full energy range, from 0.1 TeV to 10 TeV. However, if the energy range is restricted to energies above the highest threshold, which is 1 TeV here, the resulting distributions will have the same shape as the input distributions. Assuming that the dependence of the background rate on the zenith angle stays the same for all energy ranges, this dependence can be derived by looking at the background rate over the zenith angle for energies higher than the energy threshold. The energy threshold E_{thr} from Eq. 3.16 is used in the simulation. In this case it only depends on the zenith angle. The dependence of the background rate on the zenith angle for energies well above the energy threshold of $E_{\text{thr}}\,(\beta_{\text{zen}} = 60°) = 1.24\,\text{TeV}$ is derived. In Fig. 3.11 the background rate is plotted over the zenith angle Fig. 3.11 for energies between 1.5 and 10.0 TeV for method A (Fig. 3.11(a)) and method B (Fig. 3.11(b)). For method A the muon efficiencies have again been restricted and the distribution for muon efficiencies between [0.06,0.065] is shown.
The dependence of the background rate on the zenith angle for high energies ($\geq 1.5\,\text{TeV}$), see Fig. 3.11, is well described for both methods (A and B) by the following function:

$$R_{\text{acc}}\,(\beta_{\text{zen}},\, E \geq 1.5\,\text{TeV}) = a \cdot \beta_{\text{zen}}^4 + b \cdot \beta_{\text{zen}}^2 + c, \tag{3.19}$$

where $a = -2.95 \cdot 10^{-11}$, $b = 4.06 \cdot 10^{-6}$ and $c = 4.95 \cdot 10^{-3}$. A potential explanation for this kind of dependence could be that for larger zenith angles the volume of the atmosphere seen by the detector is larger. Therefore more events are detected. That this is not the case for particles with lower energies is due to absorption in the atmosphere and the energy threshold of the detector.
Looking again at the simulation, the input distribution of events over the zenith angle is now set to Eq. 3.19 and the energy threshold as defined in Eq. 3.16 is used. The distribution of the simulated events over the zenith angle after applying the energy cut is compared to the distribution of the actual data (obtained with method A) in Fig. 3.10(a). There the distribution of the simulated events over the zenith angle for energies between 0.1 TeV and 10 TeV is plotted as a black line. The index in the energy dependence has been set to $\Gamma = 2.0$. The distribution is scaled to be in the same range as the actual data which are the red points. A gaussian (dashed line) nicely fits the simulated distribution. The data and the simulated curve show a similar behaviour. However, the result of the simulation varies strongly for different spectral indices. The correct index is not known. Therefore three different indices have been tested in the simulation: 2.0, 2.7 and 3.2 (with an index of 2.7 expected for cosmic ray hadrons). In Fig. 3.10(b) fits with gaussians of the results of repeated simulations for three indices are shown in shades of green. It can be seen, that the simulation and the data agree quite well for the higher indices. This leads to the conclusion that the zenith angle dependence of the background rate seen at low energies is an effect of the energy threshold only and that the dependence seen at high energies can be assumed to be valid over the full energy range. The distribution of the background rate over the zenith angle for the full energy range is again shown in Fig. 3.12 for both methods. A fit with a

gaussian

$$R_{\mathrm{acc}}\left(\beta_{\mathrm{zen}},\, E \geq 0.1\,\mathrm{TeV}\right) = a \cdot \exp\left[-0.5 \cdot \left(\frac{\beta_{\mathrm{zen}} - b}{c}\right)^2\right] \tag{3.20}$$

results in $a = 0.0582$, $b = 10.60°$ and $c = 27.79°$. Considering again the full (Fig. 3.12) and the high energy case (Fig. 3.11) the largest deviations from the fit are seen in both cases for zenith angles above 50°, therefore in the following only data with zenith angles $\beta_{\mathrm{zen}} \leq 54°$ are used. For the observations of the Galactic Centre also only very few runs exceed this limit.
Note: If the dependence of the background rate on the zenith angle is corrected for the full energy range, the number of events is corrected, but this most probably distorts the spectrum. Therefore this correction can only be applied when determining the significance of a source but must not be applied when determining the spectrum.

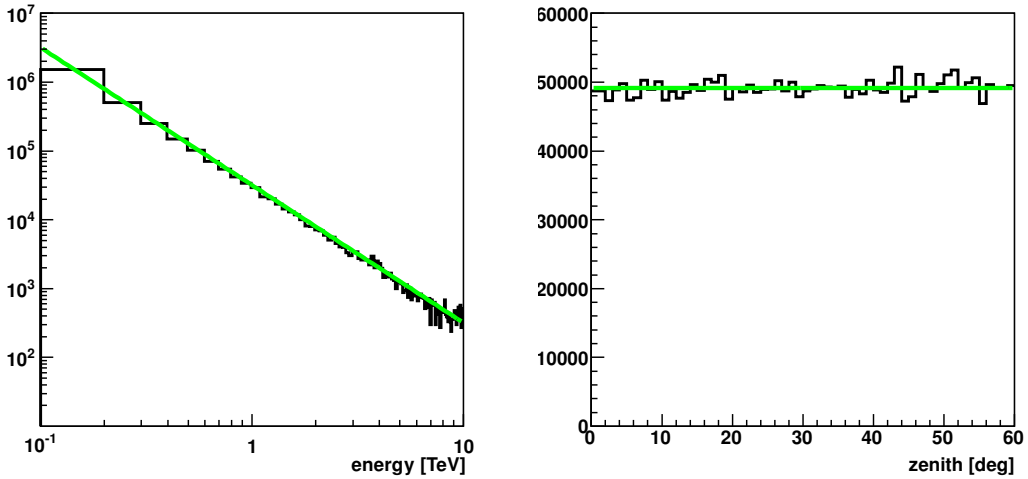

(a)

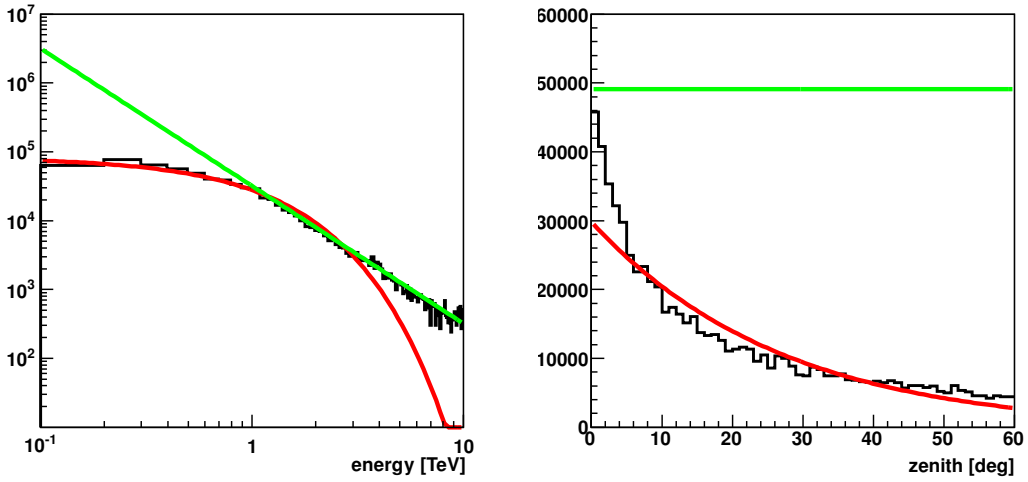

(b)

Figure 3.9.: Results of a simulation to understand the influence of the energy threshold on the zenith angle. (a) The simulated input distributions for the energy ($\sim E^{-2}$) and the zenith angle (a constant) for a total of 100,000 events. In (a) the corresponding distributions after applying an energy cut as described in Eq. 3.18. The green lines are fits to the input distributions and the red lines are fits with an exponential function and a gaussian to the distributions with the energy cut for energy and zenith, respectively.

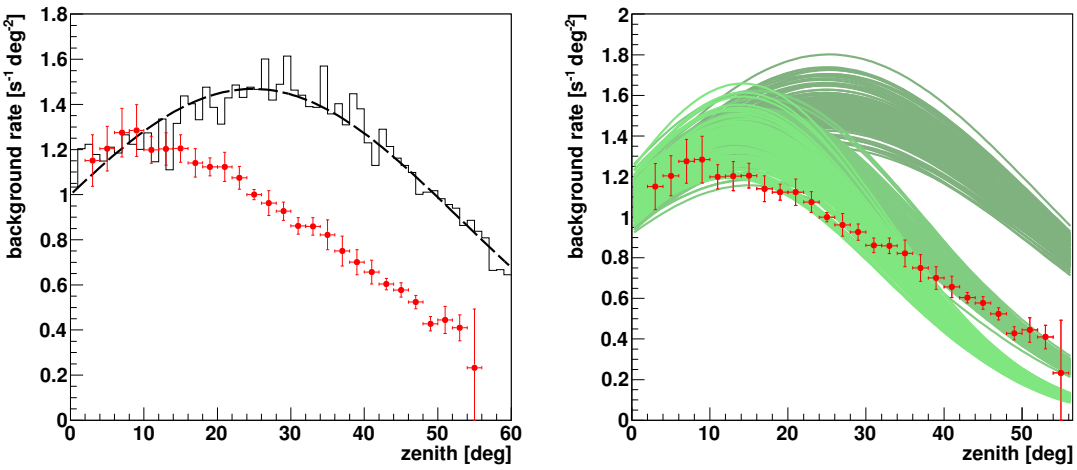

(a) (b)

Figure 3.10.: The scaled distribution of the simulated events over the zenith angle is shown as a black line. 100,000 events have been distributed in zenith angle according to Eq. 3.19 and in energy following a power-law with $E^{-\Gamma}$. The full energy range from 0.1 to 10 TeV has been used and an energy threshold cut following Eq.3.16 has been applied. The resulting distribution has then been scaled to the third of the red points from the left. The red points are the actual distribution of the backrgound rate over the zenith angle for the same energy range. In (a) the simulated distribution (black line), for which a spectral index of $\Gamma = 2.0$ was chosen, is fitted well by a gaussian (black dashed line). In (b) three different indices were chosen for the simulation, namely $\Gamma = 2.0$, $\Gamma = 2.7$ and $\Gamma = 3.2$ from dark to lighter green. Then the simulation was repeated 100 times for each index and the resulting gaussian fits are overlaid in different shades of green. Again the results are scaled (according to the value of the third bin) to be comparable to the data (red points).

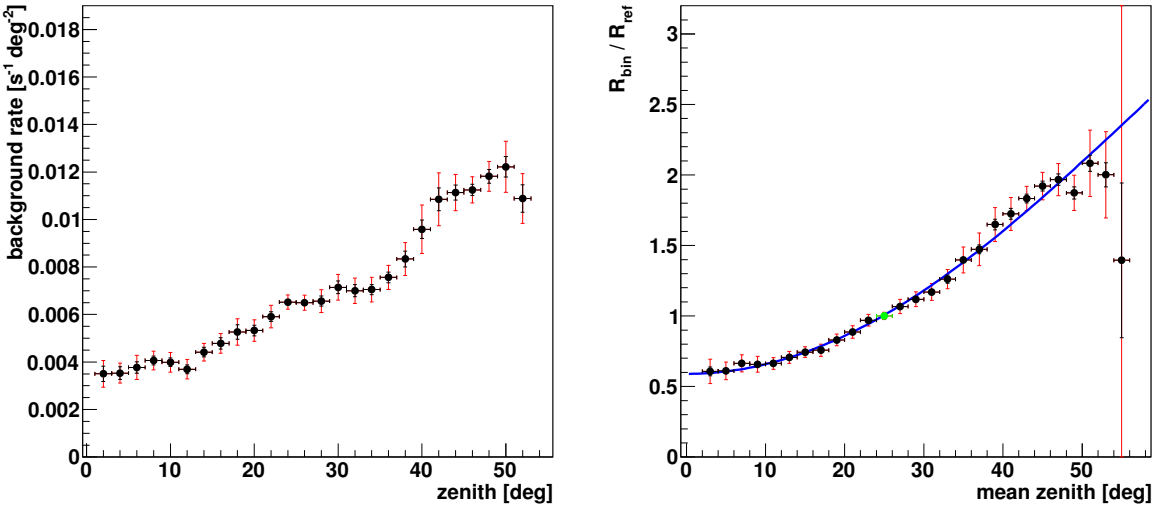

(a) (b)

Figure 3.11.: The background rate over the zenith angle for energies between 1.5 TeV and 10.0 TeV obtained eventwise with method A (a) and runwise with method B (b). The blue line shows a fit with a symmetric polynomial of fourth order.

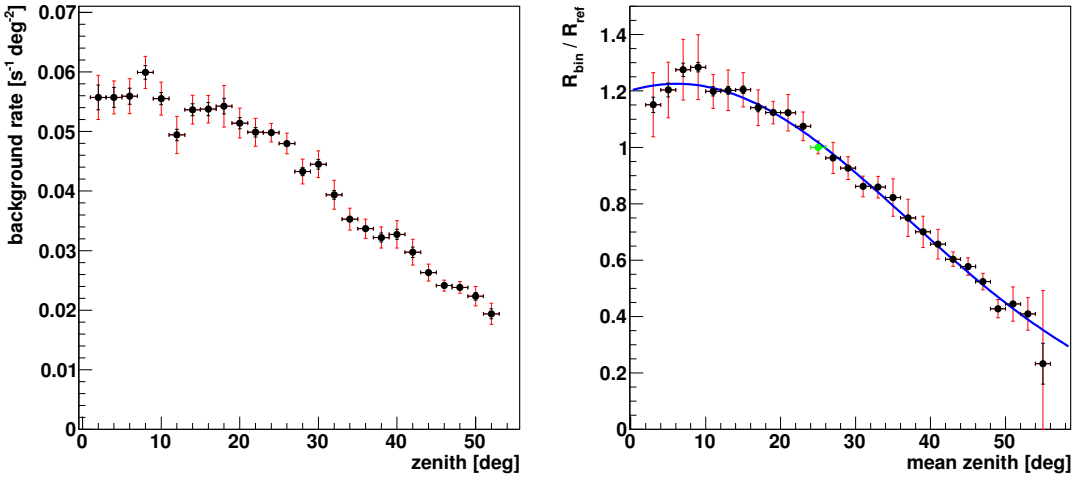

(a) (b)

Figure 3.12.: The background rate over the zenith angle for energies between 0.1 TeV and 10.0 TeV for method A (a) and method B (b). The blue line is a fit with a gaussian.

3.2.3. Muon Efficiency

After the study of the zenith angle now a closer look at the dependence on the muon efficiency is taken. Naturally the H.E.S.S. array (mainly the mirrors but also the electronics) degrades with time, which translates into a decrease in the muon efficiencies and potentially also in the background rate. In order to study the dependence of the background rate on the muon efficiency the mean muon efficiency over all telescopes is used. Again the two energy ranges, 0.1 TeV to 10 TeV and 1.5 TeV to 10 TeV, are studied. The resulting plots obtained with method B are shown in Fig. 3.13(a) and Fig. 3.13(b), respectively. The acceptance correction derived above was applied. Furthermore also a correction due to the zenith angle dependence is used. The rates are scaled to the value at a zenith angle of 10° (more on the corrections in Section 3.3.2). For the full energy range (Fig. 3.13(a)) as well as for the high energies (Fig. 3.13(b)) a strong influence is seen. A fit with a piecewise defined linear function (blue curve)

$$\frac{R_{\mathrm{bin}}}{R_{\mathrm{ref}}}\left(\epsilon_\mu\right) = f\left(\epsilon_\mu\right) = \begin{cases} a + b \cdot \epsilon_\mu, & \epsilon_\mu \leq x_{\mathrm{break1}} \\ f(x_{\mathrm{break1}}) + c \cdot \epsilon_\mu, & x_{\mathrm{break1}} < \epsilon_\mu \leq x_{\mathrm{break2}} \\ f(x_{\mathrm{break2}}) + d \cdot \epsilon_\mu, & \epsilon_\mu > x_{\mathrm{break2}} \end{cases} \tag{3.21}$$

in the range from 0.06 to 0.1 results in $a = 0.769$, $b = 3.312$, $c = 24.896$ and $d = -2.019$ for fixed values of $x_{\mathrm{break1}} = 0.0725$ and $x_{\mathrm{break2}} = 0.0825$ for the full energy range and $a = 1.054$, $b = -0.861$, $c = 17.001$ and $d = -10.637$ for the high energy range. For both energy ranges an influence of the muon efficiency on the background rate is clearly visible. The influence follows the expected trend that the background rate rises with increasing muon efficiencies. However, this strong dependence on the muon efficiency is in contrast to the results found for the Hillas analysis in Glück (2011). There only an influence in the order of $5\% - 10\%$ has been found. A potential explanation is that the muon efficiencies in the Model++ analysis enter directly into the fitting procedure. Therefore the analysis might be more sensitive to uncertainties in this parameter.

3.2.4. Atmospheric Variations

A further potentially strong influence of the background rate are atmospheric variations. It was pointed out before in Section 2.6.3 that corrections on the trigger rate derived with LIDAR measurements are feasible (Nolan et al., 2010). However, not for all measurements LIDAR data are available. Therefore in Glück (2011) another parameter to quantify atmospheric changes was introduced, namely the ratio between the actual trigger rate R_{trig} of the run and the estimated trigger rate R_{trigest} (see Eq. 3.1). In case this ratio is above 1 the atmospheric conditions have been good, smaller values indicate less optimal conditions. Again the background rate might follow this behaviour and be higher for higher ratios. In Fig. 3.14 the corresponding plots for method B are shown. The two energy ranges show a similar behaviour. The dependence on the trigger rate is fitted by a piecewise linear

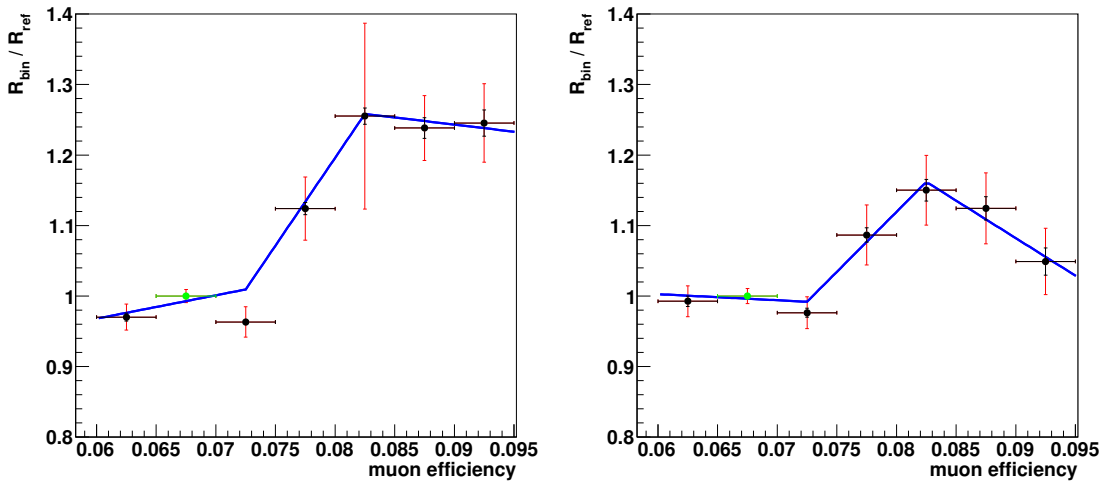

(a) (b)

Figure 3.13.: The accumulated background rate R_{bin} of the bin divided by the accumulated background rate R_{ref} from the reference bin (green) over the muon efficiency for energies between 0.1 TeV and 10.0 TeV (a) and between 1.5 TeV and 10.0 TeV (b). The black error bars correspond to the uncertainties ΔR_{acc} and the red error bars include the statistical errors ($\Delta R_{\text{acc}} + \Delta R_{\text{stat}}$). The blue line is a fit with a piecewise defined linear function with fixed breaks at 0.0725 and 0.0825. (Obtained with Method B)

function (blue curve) with one fixed break at 1.1, where the dependence seems to change.

$$\frac{R_{\text{bin}}}{R_{\text{ref}}}\left(\frac{R_{\text{trig}}}{R_{\text{trigest}}}\right) = f\left(\frac{R_{\text{trig}}}{R_{\text{trigest}}}\right) = \begin{cases} a + b \cdot \epsilon_\mu, & \frac{R_{\text{trig}}}{R_{\text{trigest}}} \leq x_{\text{break1}} \\ f(x_{\text{break1}}) + c \cdot \epsilon_\mu, & \frac{R_{\text{trig}}}{R_{\text{trigest}}} > x_{\text{break1}} \end{cases} \tag{3.22}$$

The following values are obtained: For the full energy range $a = 0.133$, $b = 0.846$ and $c = -1.356$ and for the high energy range $a = 0.320$, $b = 0.662$ and $c = -0.867$. The dependence is also very prominent and shows the expected trend. Similar results have been found for the Hillas analysis in Glück (2011).

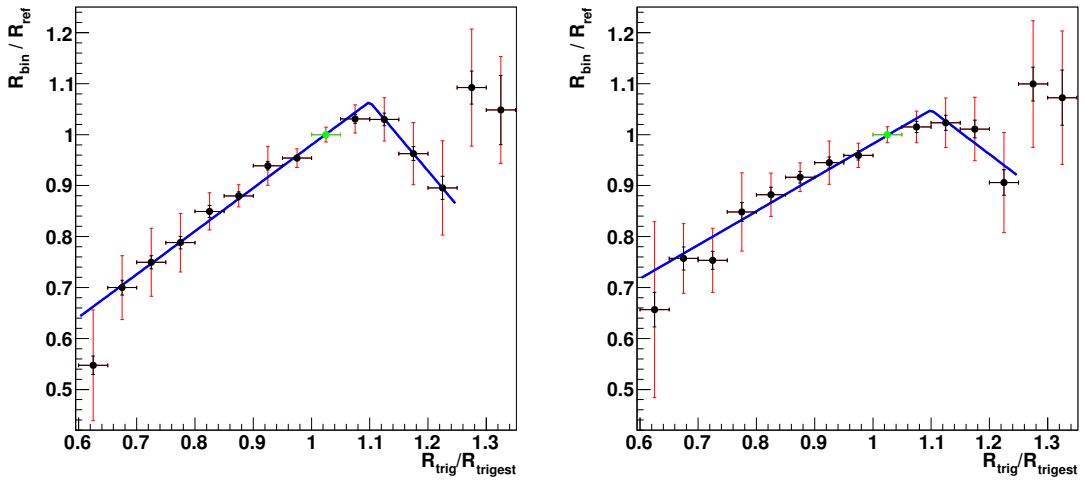

(a) (b)

Figure 3.14.: The background rate ratio over the trigger rate ratio for energies between 0.1 TeV and 10 TeV (b) and for energies between 1.5 TeV and 10 TeV (b). The blue curve is a fit with a piecewise linear function with one break at 1.1. (Obtained with Method B)

3.2.5. Azimuth angle

Together with the zenith angle β_{zen} the azimuth angle λ_{azi} defines the pointing direction of the telescope. Monte Carlo studies (Bernlöhr, 2005) indicate that the trigger rate might show a sinusoidal dependence on the azimuth due to the Earth's magnetic field. This dependence might survive the gamma cuts and might be transferred also to the background rate. The distributions of the background rate ratios over the azimuth angle for the two energy ranges are shown in Fig. 3.15. The behaviour in the two energy ranges is again similar. However, the expected sinusoidal shape is not clearly recognizable. Nevertheless, a sinusoidal fit (blue) is included in the plots.

$$\frac{R_{\text{bin}}}{R_{\text{ref}}}\left(\lambda_{\text{azi}}\right) = a \cdot \sin(\lambda_{\text{azi}} + b) + c, \tag{3.23}$$

with $a = -0.097$, $b = -0.952$, and $c = 1.061$ for the full energy range and $a = -0.088$, $b = -1.006$, and $c = 1.058$ for the high energy range. The overall influence ($\sim 15\%$) is in the same range as for the Hillas analysis, see Glück (2011).

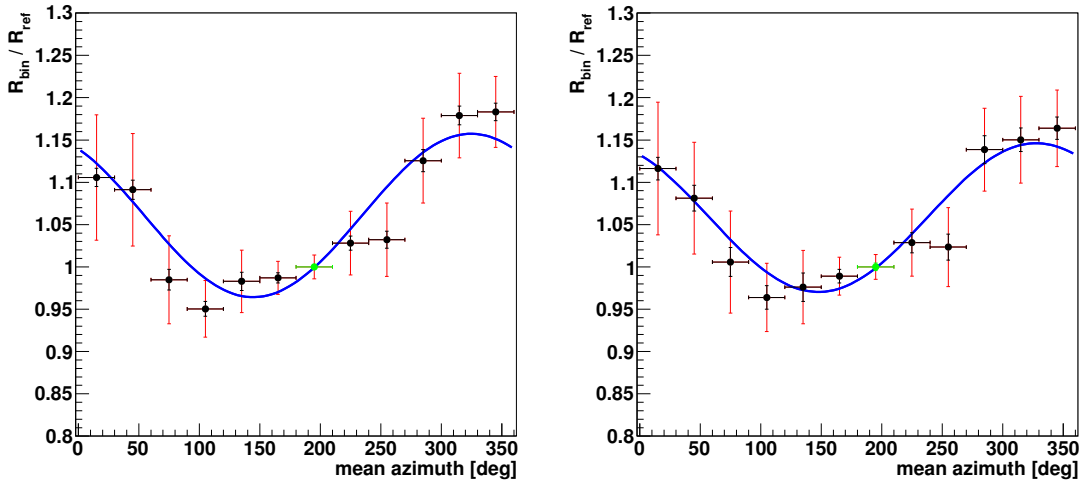

(a) (b)

Figure 3.15.: The background rate ratios over the mean azimuth angle for energies between 0.1 TeV and 10 TeV (a) and for energies between 1.5 TeV and 10 TeV (b). The blue curves correspond to a sinusoidal fit. (Obtained with Method B)

3.2.6. Night Sky Background

The NSB can be estimated in three different ways as described in Section 2.6.1. For the following analysis the value gained from the pedestal width will be used, because this method is stable and does not require an exact calibration of the high voltage, see Section 7.4.1 in de Naurois (2012). The estimation due to the optical correlation is also stable, but does not include local effects, like, e.g., broken pixels or random light sources. The NSB gained from the pedestal width is averaged over the whole FoV and over all four telescopes. This averaged value is then used for the study. This is in contrast to de Naurois (2012), where a map of the NSB at each pixel position (accumulated over several runs) is used for testing the correlation with the gamma like event rate. However, the reconstructed direction of an event in the sky never falls within the shower image in the camera, therefore no correlation between the event rate at the exact position of the high NSB values is expected and no dependence on the NSB was found in de Naurois (2012). The effect of pixels with high NSB is expected to affect events reconstructed at positions on a circle around the pixels, see Fig. 3.16 for an illustration. In Fig. 3.17 the background rate ratio

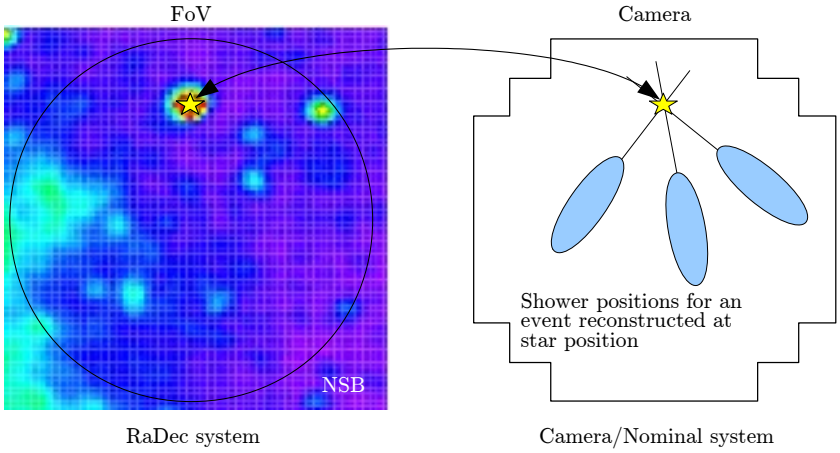

Figure 3.16.: Illustration of the influence of high NSB values in a pixel/ at a certain sky position.

over the NSB is plotted for the two energy ranges with method B. An influence in the order of ±10% is seen. This is larger than the influence determined for the Hillas analysis in Glück (2011). A potential explanation is the inclusion of the NSB (via the pedestal width and the goodness-of-fit calibration) into the fitting procedure. The blue curve in Fig. 3.17 corresponds to a fit with the following function

$$\frac{R_{\mathrm{bin}}}{R_{\mathrm{ref}}}(NSB) = f(NSB) = \begin{cases} a + b \cdot NSB, & NSB \leq x_{\mathrm{break1}} \\ f(x_{\mathrm{break1}}) + c \cdot NSB, & NSB > x_{\mathrm{break1}} \end{cases} \tag{3.24}$$

with $x_{\text{break1}} = 90\,\text{MHz}$ and $a = 0.768$, $b = 0.004$ and $c = 0.000$ for the full energy range and $a = 0.660$, $b = 0.005$ and $c = -0.001$
Additionally in Fig. 3.17 one point at $NSB \sim 115\,\text{MHz}$ is far offset from the other points. Remarkably also the error (red) including the statistical uncertainty is quite large. It will become clear later that the large offset of this point is due to the uncertainties left over in the selection of the runs.

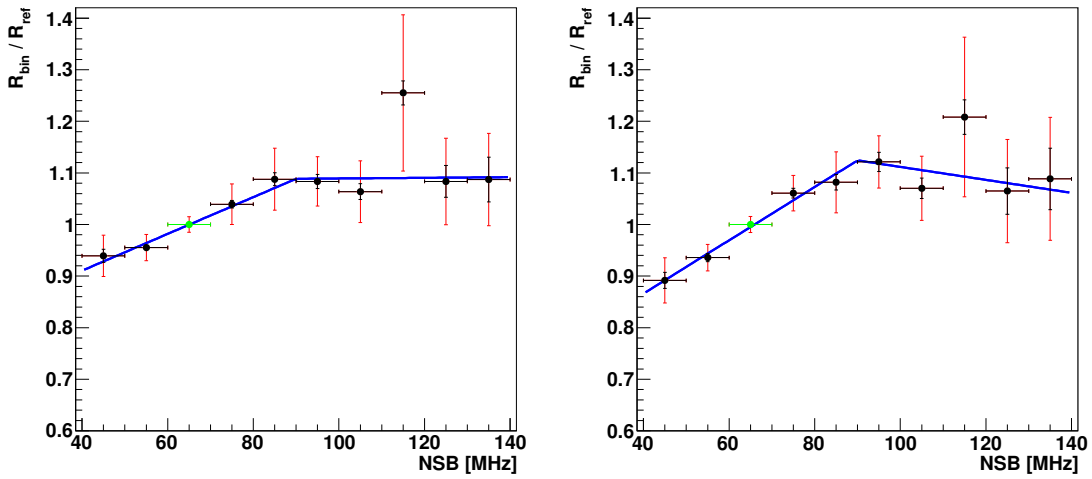

(a) (b)

Figure 3.17.: The background rate ratio over the NSB. For the full energy range (0.1 TeV - 10 TeV) (a) and the high energy range (1.5 TeV - 10 TeV) (b). The blue curve is a fit with a piecewise defined linear function with a break at 90 MHz. (Obtained with Method B)

3.2.7. Camera Temperature

Now a potential dependence of the background rate on the camera temperature is investigated. The camera temperature is mostly connected to changes in the noise level of the electronics. In Fig. 3.18 the results obtained with method B for the two energy ranges are shown. A fit with a piecewise defined linear function with two breaks

$$\frac{R_{\mathrm{bin}}}{R_{\mathrm{ref}}}\left(T_{\mathrm{camera}}\right) = f(T_{\mathrm{camera}}) = \begin{cases} a + b \cdot T_{\mathrm{camera}}, & T_{\mathrm{camera}} \leq x_{\mathrm{break1}} \\ f(x_{\mathrm{break1}}) + c \cdot T_{\mathrm{camera}}, & x_{\mathrm{break1}} < T_{\mathrm{camera}} \leq x_{\mathrm{break2}} \\ f(x_{\mathrm{break2}}) + d \cdot T_{\mathrm{camera}}, & T_{\mathrm{camera}} < x_{\mathrm{break2}} \end{cases} \tag{3.25}$$

results for breaks at $x_{\mathrm{break1}} = 20.0°\mathrm{C}$ and $x_{\mathrm{break2}} = 27.5°\mathrm{C}$ in $a = 1.501$, $b = -0.023$, $c = -0.003$ and $d = -0.017$ for the full energy range and $a = 1.268$, $b = -0.013$, $c = 0.001$ and $d = -0.013$ for the high energy range. The general trend of the influence, yielding lower background rates for higher camera temperatures, has also been observed for the Hillas analysis (Glück, 2011). However, for the Model++ analysis again the influence seems to be stronger (in the order of ±20% in contrast to ±10% for the Hillas analysis). This might again be due to the calibration of the electronics, which enters directly in the fitting procedure for the Model++ analysis.

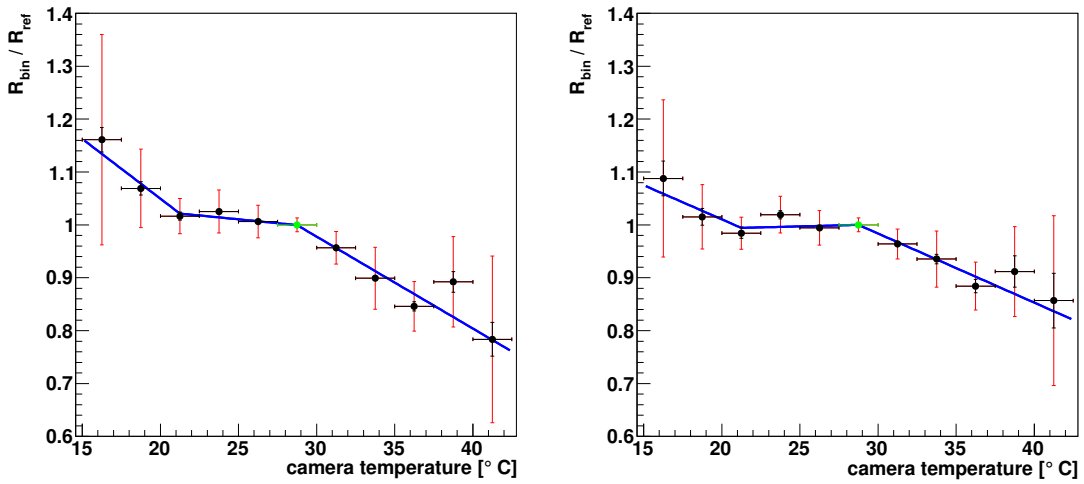

(a) (b)

Figure 3.18.: The Camera dependence of the background rate ratio for the full (0.1 TeV - 10 TeV) (a) and the high (1.5 TeV - 10 TeV) (b) energy range. The blue curve corresponds to a fit with a piecewise defined linear function with two breaks: one break at 20.0°C and the other at 27.5°C. (Obtained with Method B)

3.2.8. Broken Pixels

The dependence on the amount of broken pixels (PMTs not working) is difficult to estimate. This dependence might strongly depend on the distribution of the broken pixels in the cameras. If many neighbouring pixels are effected a stronger influence than in the case of many single pixels is expected. The amount of broken pixels in a telescope is restricted to be less than 10% by the quality cuts. Therefore only up to about 100 broken pixels are considered. In Fig. 3.19 the background rate ratios over the mean number of broken pixels of the full array are shown. A tendency to lower rates for a higher number of broken pixels is seen and is indicated by a fit with a linear function (blue)

$$\frac{R_{\mathrm{bin}}}{R_{\mathrm{ref}}}\left(N_{\mathrm{bp}}\right) = a + b \cdot N_{\mathrm{bp}}, \tag{3.26}$$

with $a = 1.069$ and $b = -0.001$ for the full energy range and $a = 1.085$ and $b = -0.002$ for high energies. This was also seen for the Hillas analysis (Glück, 2011). An explanation for this kind of dependence is that for higher numbers of broken pixels the images of some events in the camera have holes, which might prevent the fit from converging.
The parameters described in the following Sections have not been studied in Glück (2011). Nevertheless, they indicate further changes of the observation conditions and are therefore also important to study.

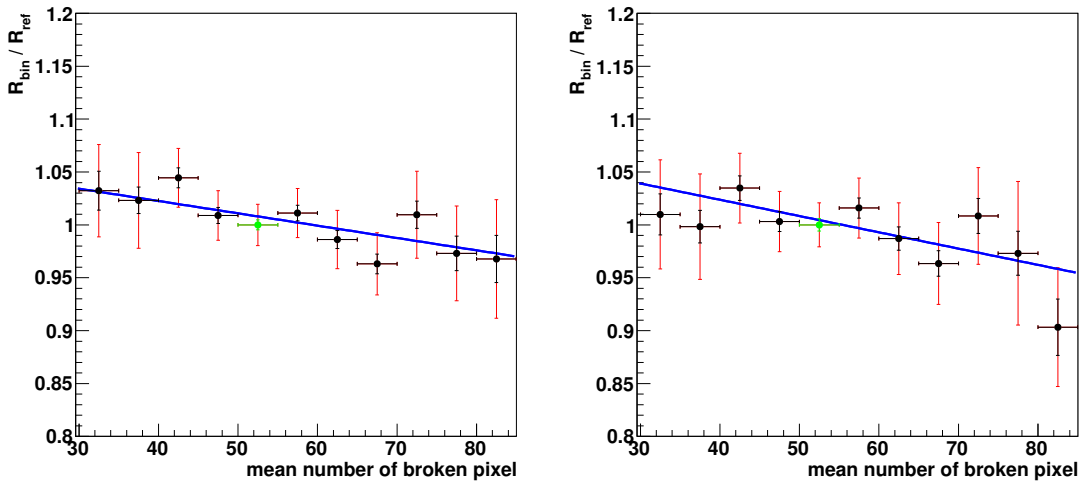

(a) (b)

Figure 3.19.: Background rate ratios over the amount of broken pixels in all four telescopes. In (a) the full energy range (0.1 TeV - 10 TeV) and in (b) the high energy range (1.5 TeV - 10 TeV) is drawn. The blue line corresponds to a fit with a linear function. (Obtained with Method B)

3.2.9. Radiometer temperature

The temperature measured by the radiometer might be a further indication for atmospheric variations. Therefore also the dependence on the radiometer temperature is studied. It was pointed out before, that work is ongoing to determine the influence of the radiometer temperature on the trigger rate (Daniels, 2012). For lower radiometer temperatures the atmosphere is expected to be in general cleaner and therefore a higher background rate is expected as well. This trend is also seen in Fig. 3.20. However, for the lowest and especially for the highest radiometer temperature deviations from this trend are observed. Similar to the NSB, these deviations can be explained by influences from other parameters included in the selection uncertainties. There the results obtained with method B for the two energy ranges are shown. The blue curve corresponds to a fit with

$$\frac{R_{\mathrm{bin}}}{R_{\mathrm{ref}}}\left(T_{\mathrm{radio}}\right) = f(T_{\mathrm{radio}}) = \begin{cases} a + b \cdot T_{\mathrm{radio}}, & T_{\mathrm{radio}} \leq x_{\mathrm{break1}} \\ f(x_{\mathrm{break1}}) + c \cdot T_{\mathrm{radio}}, & x_{\mathrm{break1}} < T_{\mathrm{radio}} \leq x_{\mathrm{break2}} \\ f(x_{\mathrm{break2}}) + d \cdot T_{\mathrm{radio}}, & T_{\mathrm{radio}} < x_{\mathrm{break2}} \end{cases} \tag{3.27}$$

The result of the fit for the energy range between 0.1 TeV and 10 TeV is $a = 1.660$, $b = 0.013$, $c = -0.008$ and $d = 0.026$ and for the energy range between 1.5 TeV and 10 TeV $a = 1.251$, $b = 0.005$, $c = -0.005$ and $d = 0.018$.

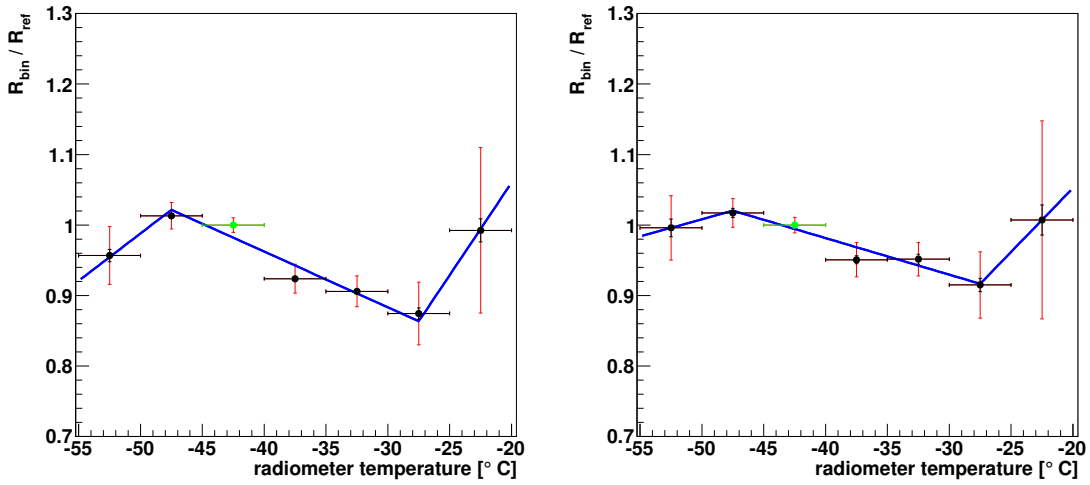

(a) (b)

Figure 3.20.: The background rate ratio over the radiometer temperature for both energy ranges (0.1 TeV - 10 TeV) ((a) and (1.5 TeV - 10 TeV)(b)). The blue curve corresponds to a fit with a piecewise defined linear function. (Obtained with Method B)

3.2.10. Air temperature

The weather station at the H.E.S.S. measures the air temperature regularly. A potential dependence of the background rate on the mean air temperature of each run is therefore investigated. It was pointed out already that the air temperature and the camera temperature are related. Therefore a similar dependence as for the camera is expected. Nevertheless, the air temperature also indicates changes in the weather, which might influence the detector performance. The results of method B are shown in Fig. 3.21. Indeed for higher temperature lower rate ratios are found. For low temperatures, however, deviations from the expected trend are observed. Whether they are due to the uncertainties in the selection or whether the detector response really changes for lower air temperatures has to be further investigated (see Section 3.3.2). For now in Fig. 3.21 a piecewise defined linear function

$$\frac{R_{\mathrm{bin}}}{R_{\mathrm{ref}}}\left(T_{\mathrm{air}}\right) = f(T_{\mathrm{air}}) = \begin{cases} a + b \cdot T_{\mathrm{air}}, & T_{\mathrm{air}} \leq x_{\mathrm{break1}} \\ f(x_{\mathrm{break1}}) + c \cdot T_{\mathrm{air}}, & T_{\mathrm{air}} > x_{\mathrm{break1}} \end{cases} \tag{3.28}$$

with a break at $x_{\mathrm{break1}} = 7.5°\mathrm{C}$ is used to describe the behaviour and results in $a = 0.945$, $b = 0.007$ and $c = -0.013$ for energies $\in [0.1, 10.0]\,\mathrm{TeV}$ and $a = 0.945$, $b = 0.007$ and $c = -0.008$ for energies $\in [1.5, 10.0]\,\mathrm{TeV}$.

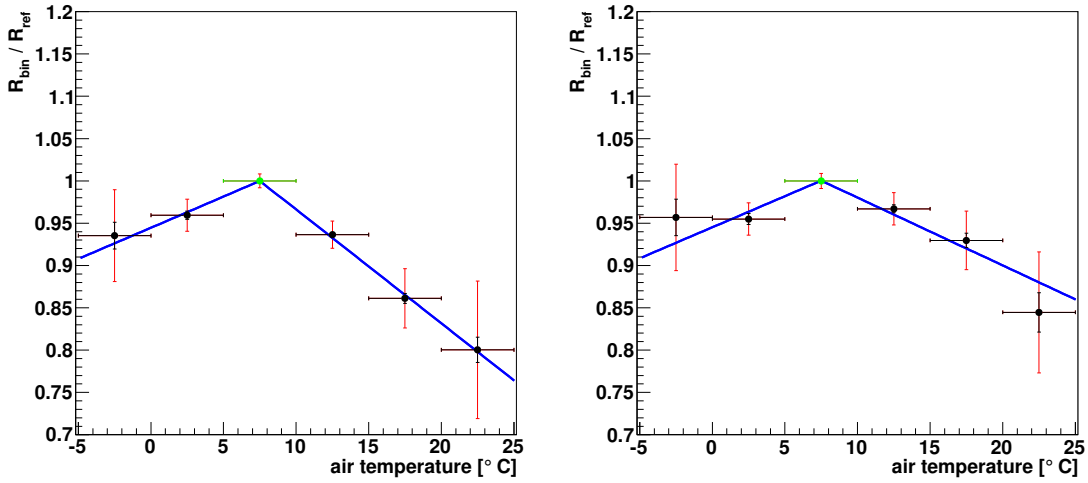

(a) (b)

Figure 3.21.: The background rate ratios over the air temperature for both energy ranges (0.1 TeV - 10 TeV) and (1.5 TeV - 10 TeV). (Obtained with Method B)

3.2.11. Relative Humidity

The relative humidity might be a hint of atmospheric variations, which might in turn influence the electronics. The change in the background rate ratios with respect to the relative humidity is studied in Fig. 3.22 for the two energy ranges. There a rather unexpected influence is seen. The background rate seems to increase toward higher humidities. However, the overall change is no larger than 15%. A fit with the following function is included in Fig. 3.22:

$$\frac{R_{\mathrm{bin}}}{R_{\mathrm{ref}}}\,(hum) = f(hum) = \begin{cases} a + b \cdot hum, & hum \leq x_{\mathrm{break1}} \\ f(x_{\mathrm{break1}}) + c \cdot hum, & hum > x_{\mathrm{break1}} \end{cases} \tag{3.29}$$

with $x_{\mathrm{break1}} = 40\%$ and $a = 0.825$, $b = 0.006$ and $c = -0.005$ for energies $\in [0.1, 10.0]$ TeV and $a = 0.875$, $b = 0.004$ and $c = -0.004$ for energies $\in [1.5, 10.0]$ TeV

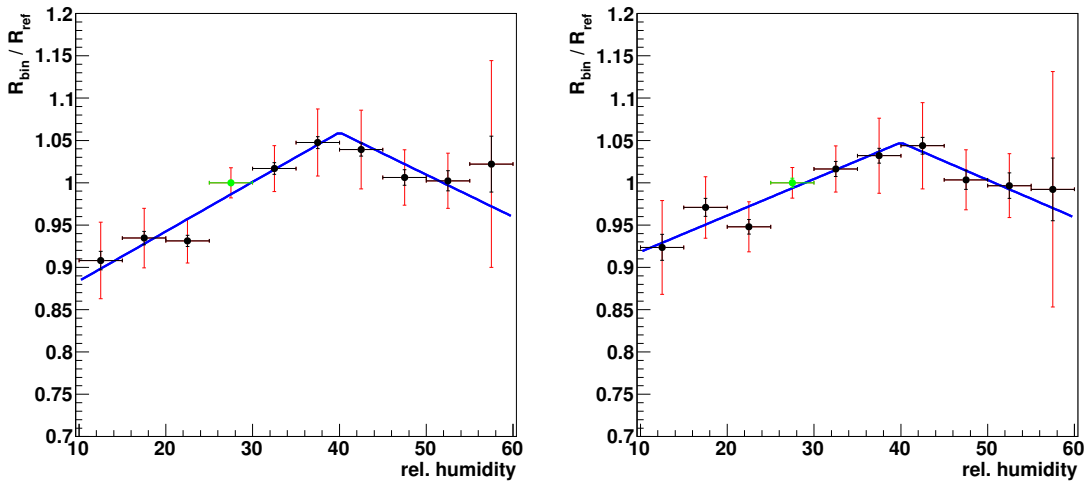

(a) (b)

Figure 3.22.: The background rate ratio over the mean relative humidity for both energy ranges (0.1 TeV - 10 TeV) and (1.5 TeV - 10 TeV). The blue curve corresponds to a fit with a piecewise defined linear function. (Obtained with Method B)

3.2.12. Other parameters

The above studied parameters certainly contain many aspects of the detector and the observation conditions which are influencing the background rate. Nevertheless one might also think of further parameters. Another parameter which might also help to indicate weather (especially season) dependent changes of the observation conditions, is the date (e.g. the month), at which a run was taken. In the plots shown above this parameter has not been taken into account for the selection and it is assumed that a good agreement in the other parameters (especially air temperature and humidity) already lead to a certain matching of the seasons, in which the runs were taken. Nevertheless, in Fig. 3.23 the results of applying method B to the parameter month of data taking are shown. It is clearly visible that the first few months of the year correspond to the rainy season. Because of the smaller number of available runs in the rainy season there the statistics are not so good and large error bars (red) appear. Also over the following months a change in the background rate ratio is observed. This influence might already be taken care of by the other parameters. Nevertheless, adding the parameter month to the list of selection parameters for the pairing of on- and off-runs is recommended. In the following therefore run pairs are only used if they were taken in the same (± 1) month (not the same year though).

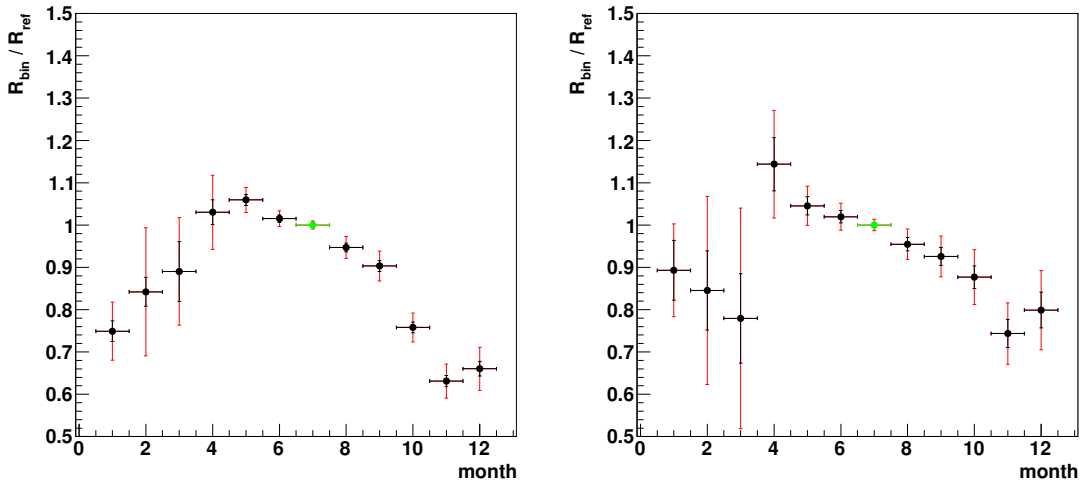

(a) (b)

Figure 3.23.: The background rate ratio over the month, in which the runs were taken, for both energy ranges (0.1 TeV - 10 TeV) and (1.5 TeV - 10 TeV). (Obtained with Method B)

3.2.13. Summary

It was shown that in general the Model++ analysis is more sensitive to the studied parameters than the Hillas analysis. This can be understood because of the large influence of the calibration in the Model++ event reconstruction. Besides the fact that the background rate ratios show different dependencies on the parameters, this also stresses again how important a stable and reliable calibration is for the Model++ reconstruction. Certainly future studies will need to determine the exact influence of miscalibrations on the Model++ reconstruction.
In the next Section the observed parameter dependencies are used in two different ways to implement an on-off-analysis in order to determine the significance of a source.

3.3. On-Off-Analysis

In previous Section certain parameter dependencies have been observed. In this Section it is described, how these observations can be used in an on-off-analysis. The later analysis will focus on the determination of the significance, therefore in the following always the energy range from 0.1 TeV to 10 TeV is studied. No spectrum will be determined here.
Like for the determination of the parameter dependencies also for the on-off-analysis several approaches exist.

- The first method relies on the possibility to correct for the various parameter influences. How such corrections can be included in an analysis and how they are determined will be explained in Section 3.3.2. The advantage of this method is that almost all of the existing data can serve as off-data (at least all data falling into parameter ranges which are well understood).
- The second method does not require any corrections. There the on-runs are simply paired with off-runs according to their parameters, similar to method B from Section 3.2. Now, though, the size of the influence of the different parameters is estimated with the help of the studies described in the previous Chapter and the weights w_{par} in Eq. 3.17 are set accordingly. This is described further in Section 3.3.1. With this selection the uncertainty of the analysis is reduced. On the downside, however, since for the Model++ analysis strict selections are necessary, not for every on-run a matching off-run can be found and the amount of usable data might shrink significantly.
- A third method, which can be applied for sources smaller than the extent of the FoV, does not need to know anything about the systematics affecting the background rate, but simply scales the background rate of the off-run according to the squared offset distribution of the events in the on-run. For both runs histograms are filled with the gamma-like events over the squared offset to the target. Then the histogram for the off run at large offsets is scaled to the histogram of the on-run at large offsets. However, since for the dark matter halo in the Galactic Centre region the extent of

the signal region is expected to be comparable to the whole FoV, this approach can not be used here and is therefore not discussed further in the following.

Additionally, of course, the first two described approaches can be combined and certain parameters can be corrected, while other parameters must match between on- and off-run. In the following it will be shown that such a combined approach is needed for the Model++ analysis. This combined approach will be called *On-Off-Selection method* and is described in more detail in the next Section. Then afterwards the first method (*Correction method*) and especially the determination and inclusion of the corrections is described further.

3.3.1. On-Off-Selection Method

For the On-Off-Selection method new weights w_{par} are determined according to the parameter influences derived in Section 3.2. Therefore for each parameter the gradient for the background rate ratio is determined from the fitted functions (blue curves in Figures 3.12 – 3.22). These gradients can then be used as new weighting coefficients. However, to be comparable to the a priori coefficients chosen before in Section 3.2.1 they are scaled to the weighting coefficient of the zenith. Both, the gradients and the scaled weighting coefficients, are given in Table 3.5. Now again a limit on the weight $W(\mathrm{on}, \mathrm{off})$ (see Eq. 3.17, where now on corresponds to an on-run and off corresponds to a potential off-run) to reduce the allowed deviations has to be chosen. A value of $W(\mathrm{on}, \mathrm{off})_{\mathrm{max}} = 10.0$ now corresponds to allowed deviations in the range of 10% for all parameters. Additionally the runs have to be taken in the same time of the year ($month \pm 1$). However these criteria are so restrictive, that no off-runs are found for the Galactic Centre region.
A potential solution is to dismiss the limit on the weight $W(\mathrm{on}, \mathrm{off})$ and instead minimise the sum of individual weights $\sum_{\mathrm{onruns}} W(\mathrm{on}, \mathrm{off})$ to get a homogeneous sample. However, then, also larger deviations for individual pairs might be included and only if the statistics are large enough and deviations in both directions (more off-events and less off-events) exist in the sample a null result (statistically the same amount of on- and off-events) is obtained. This method then of course has a larger uncertainty, which has to be taken into account when studying the results. It is therefore not further discussed in this thesis.
A different approach is to correct dependencies of single parameters and therefore set their weighting coefficients to zero. These parameters are then not used in the selection of pairs of runs. This approach was used in Glück (2011), there the trigger rate ratio was corrected and not included in the run selection. The parameters for which corrections are applied should then be well understood. In the following for the On-Off-Selection method the weighting coefficients for the muon efficiency, the radiometer and the camera temperature as well as for the NSB will be set to zero and the dependencies on these parameters are corrected instead. The correction of so many parameters is necessary for Model++, because otherwise not enough off-runs are found. How the corrections are determined and how they are included in the analysis is presented in the next Section together with the Correction method.

Table 3.5.: The new weighting coefficients chosen form the studies of the parameter influences and the allowed deviations of the rates resulting from applying a limit of $W(\text{on}, \text{off})_{\text{max}} = 10.0$. Additionally in the last column the reference points for the different parameters are listed.

Parameter	Gradient $[[par]^{-1}]$	scaled w_{par}	reference value
Zenith	-0.0240	1.0	24
Azimuth	0.00169	0.0704	190
Muon efficiency	24.9	1037.5	0.0675
NSB	0.00356	0.148	65
Camera temperature	-0.0226	0.942	28.75
Number of broken pixel	-0.00117	0.0488	52.5
Radiometer temperature	-0.00791	0.330	-42.5
Relative humidity	0.00586	0.244	27.5
Air temperature	-0.0135	0.563	7.5
Trigger rate ratio	0.846	35.25	1.025

3.3.2. Correction Method

The correction method uses the dependencies of the background rate on the parameters derived in Section 3.2 and corrects them. This is done by scaling the rates from the on and the off run to a certain reference configuration (given by the reference points listed in the third column of Table 3.5). Therefore it is assumed that the corrections for the different parameters can be treated multiplicatively, i.e. the parameters are independent of each other. In order to scale the rates to a reference value the events are weighted with a correction factor c_{i}. This correction factor can be determined eventwise (if the parameter whose influence is corrected is determined for every event, so for the zenith, the azimuth and the offset) or runwise (for parameters that are fixed for each run, like, e.g., for the muon efficiency). Applying such a correction on the accumulated rate Eq. 3.6 changes to

$$R_{\text{acc}} = \frac{1}{V} \cdot \sum_{\text{runs}} \sum_{\text{events}} c_{\text{i}} \left(\beta_{\text{zen}}, \mu, \psi, \cdots\right) \tag{3.30}$$

with the correction factor for each event i being

$$c_{\text{i}} \left(\beta_{\text{zen}}, \mu, \psi, \dots\right) = c_{\text{zen}} \cdot c_{\mu} \cdot c_{\psi} \cdot \dots \tag{3.31}$$

In order to take the uncertainty resulting from the correction into account and also to include the corrections later in the analysis a global correction factor C_{corr} is defined

$$C_{\text{corr}} = \frac{\sum_{\text{runs}} \sum_{\text{events}} c_{\text{i}}}{\sum_{\text{runs}} \sum_{\text{events}} 1} \tag{3.32}$$

and the corrected/scaled rate can be written as

$$R_{\mathrm{acc}} = \frac{C_{\mathrm{corr}} \cdot N}{V} = \frac{N}{\frac{V}{C_{\mathrm{corr}}}}, \tag{3.33}$$

where N is the number of total events. With this the uncertainty on the event count $\Delta N = \sqrt{N}$ changes to $\Delta N = C_{\mathrm{corr}} \cdot \sqrt{N}$. In the analysis the corrections enter in form of the global correction factor C_{corr} and are simply included into the exposure for the on- and the off-runs and the events are summed up just like in the standard analysis. With this the factor β_{corr} from before (see Section 2.9.4) can be used for the determination of the significance and also the formula from Eq. 2.21 still holds. Though β_{corr} now is

$$\beta_{\mathrm{corr}} = \frac{A_{\mathrm{on}} T_{\mathrm{on}} C_{\mathrm{off}}}{A_{\mathrm{off}} T_{\mathrm{off}} C_{\mathrm{on}}} \tag{3.34}$$

with A being the area on the sky, T the live time and C the correction factor for the on- as well as the off-runs.
How the correction factors c_{i} are determined and how good the corrections work is discussed in the following.

Determination of Correction Factors

In a first attempt the corrections are simply chosen according to the fits $f(par)$ (blue curves in Figures 3.12 – 3.22) from the previous Sections. Furthermore the parameter ranges are reduced to those visible in the plots shown in these Figures 3.12 – 3.22, because only for those regions enough run pairs were found to predict the dependence. In Appendix A.3 the limits of the parameter ranges are indicated in the run distribution plots for each parameter. These limits reduce the set of potential off runs to about 3000. The correction factors for each event are given by the inverse value of the fitted function $1/f(par)$. These corrections are now applied and the background rate ratios for the different parameters are determined again. The a priori weighting coefficients from Table 3.4 are still used. This time, though, no limit on the weight $W(\mathrm{ref}, \mathrm{bin})$ is requested. Therefore now all runs in a bin can be paired with a reference run and larger statistics are gained. The corrections should scale the background rates relative to the background rate in the reference bin. Therefore, in case the corrections work perfect, all background rate ratios are expected to be equal to one. In the following the results for the radiometer temperature are shown and discussed as an example. The plots for all other parameters can be found in the Appendix A.5.
In Fig. 3.24(a) again the plot from which the function $f(T_{\mathrm{radio}})$ (see Eq. 3.27) for the correction of the radiometer temperature dependence was derived is shown. In Fig. 3.24(b) the corrections for all parameters have been applied. There a blue line at a background rate ratio of 1 is drawn in order to see how well the corrections work. However, in case of the radiometer temperature the deviations from a background rate ratio of one are still as large as before. Only for points close to the reference bin (green point) the deviations are small.

In general for some parameters the deviations from the blue line at one are very small and the corrections seem to work very well already (e.g. Fig. A.4(b)), but for others large deviations ($\sim 20\%$) from a background rate ratio of 1.0 are still found (e.g. Fig. A.5(b)). Therefore, in order to further improve the corrections, the background rate ratios are plotted over each parameter of interest with all corrections applied except the correction of the parameter under study. The aim is here to reduce the uncertainties in the selection, see Table 3.4. The uncertainties of the corrections have on average been smaller than the uncertainties in the selection, which can be seen in the plots in Appendix A.5 labelled *b*). The application of the derived corrections also leads to larger statistics because like before the weight W is not required to be below a certain value. The resulting plot for the radiometer temperature is shown in Fig. 3.24(c). There the background rate ratio shows a linear dependence with the radiometer temperature. The first and the last point, which are offset from this linear dependence in Fig. 3.24(a), lie now nicely on the blue curve, a linear fit with

$$\frac{R_{\text{bin}}}{R_{\text{ref}}}\left(T_{\text{radio}}\right) = f(T_{\text{radio}}) = a + b \cdot T_{\text{radio}}, \tag{3.35}$$

where $a = 1.073$ and $b = -0.010$. For the radiometer temperature this linear behaviour was expected (Daniels, 2012). Therefore the usage of the corrections helped to unveil the actual dependence, which was distorted by uncertainties in the selection before. Also for the other parameters new functions are fitted, which are given in Appendix A.5. These functions are implemented as new corrections (iterated corrections) and the new corrections are again tested like before. The resulting plot for the radiometer temperature is shown in Fig. 3.24(d). There again a blue line at a background rate ratio of one is drawn. For the radiometer temperature the background rate ratios are now much closer to the blue line and even the last point deviates only by about 3%. However this is not the case for all parameters. In order to determine whether the iterated corrections are really better than the first attempt the quadratic deviation from the background rate ratio of one is calculated

$$\chi^2 = \sum_{\text{p.o.i.}} \sum_{\text{i}} \frac{\left(y_{\text{i,p.o.i.}} - 1.0\right)^2}{\sigma^2_{\text{i,p.o.i.}}}. \tag{3.36}$$

Here $y_{\text{i,p.o.i.}}$ is the value of the background rate ratio in bin i for a certain parameter of interest (p.o.i.) and σ_{i} is the corresponding error (red in the following plots). The summation runs over all the bins and over all the parameters of interest. For the first set of corrections a value of $\chi^2 = 277.5$ and for the new corrections a value of $\chi^2 = 146.1$ is found. The lower value for the new corrections indicates that the overall deviation is smaller and therefore the new corrections are used in the following. A further iteration was tested, but did not yield a lower χ^2 value.
In general the corrections seem to work very well for most parameters, however for some parameters the corrected rate is always too low (e.g. for the muon efficiency) and for others always to high (e.g. for the NSB). Nevertheless, in the overall sample these effects (partially) annihilate each other. Therefore always the complete set of corrections (or at least corrections counteracting on each others biases) should be used. Now with the new

corrections the largest remaining deviation from the blue line at $R_{\mathrm{ref}}/R_{\mathrm{bin}} = 1.0$ is found for the NSB and lies in the range of 0.2, which corresponds to a deviation of 20%. For the other parameters the deviation is $\leq 10\%$.
Apart from the selection of the on- and off-runs the analysis is very similar for both methods. The only difference is the determination of the normalisation β for the Correction method, which was described at the beginning of this Section. In the following Sections now other aspects of the analysis, which are identical for both methods, are discussed.

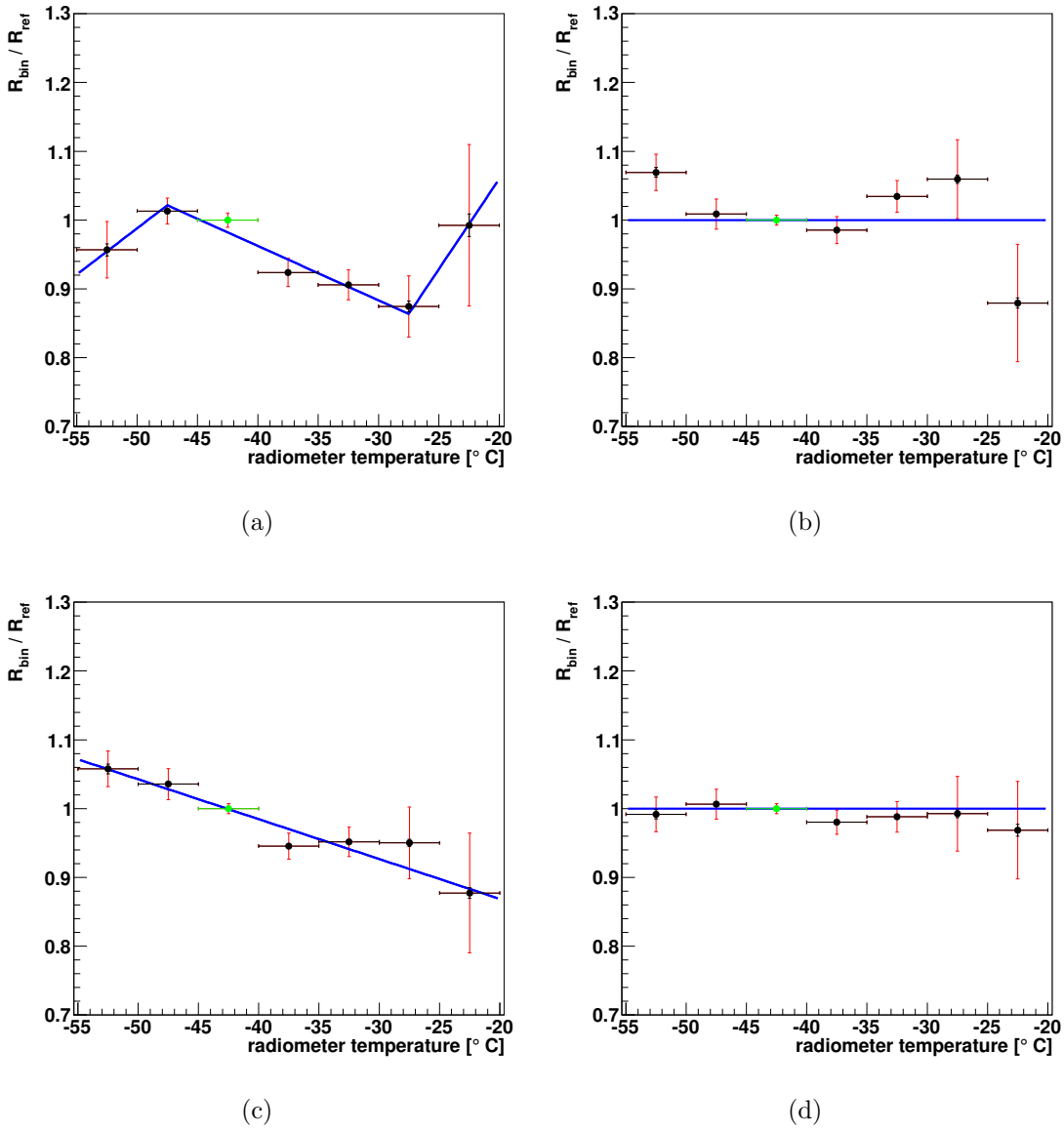

Figure 3.24.: In (a) the background rate ratio over the radiometer temperature for energies between 0.1 TeV and 10 TeV is plotted. The blue line is a fit with the function given in Eq. 3.27. In (b) the corrections for all parameters have been applied and the corrected background rate ratio over the radiometer temperature is plotted. The blue line is drawn at a background rate ratio of 1.0. The deviations of the points from this line indicate how well the corrections worked. In (c) all corrections have been applied except the correction for the radiometer temperature. The background rate ratio over the radiometer temperature shows a linear dependence here. The blue line is a fit with a linear function. In (d) the new corrections have been applied on the background rates and the deviations from the blue line at 1.0 are smaller than in (b). (All plots are obtained with Method B)

3.3.3. Selection of Regions

The on-off-analysis, despite the afore mentioned selections and corrections, in general follows the standard analysis procedure described in Chapter 2. However, a further difference has to be mentioned, which is the selection of the off region suitable to the on region. This is described shortly in the following.
In order to reduce the influence of the acceptance, if possible the same regions in the FoV are chosen in on- and off-run. In Fig. 3.25 the matching of the on and off position for a run pair is illustrated. The FoV of the on-run overlaps with the target region. The resulting on region (green) is matched by the red region in the corresponding off-run. This is achieved by determining the transformation (rotation) between the observation position of the on-run and the observation position of the off-run and applying it also to the target position. The distance of the off region from the centre of the FoV of the off-run is then the same as for the on region in the on-run. Additionally, the regions which are excluded in the on-run are also excluded in the off-run, as are the excluded regions of the off-run. With the assumption of a radially symmetric acceptance the two regions therefore have a very similar acceptance distribution. The two regions only differ slightly in the size of the area, because of the different positions on the sky and potentially more excluded regions in the off-run.

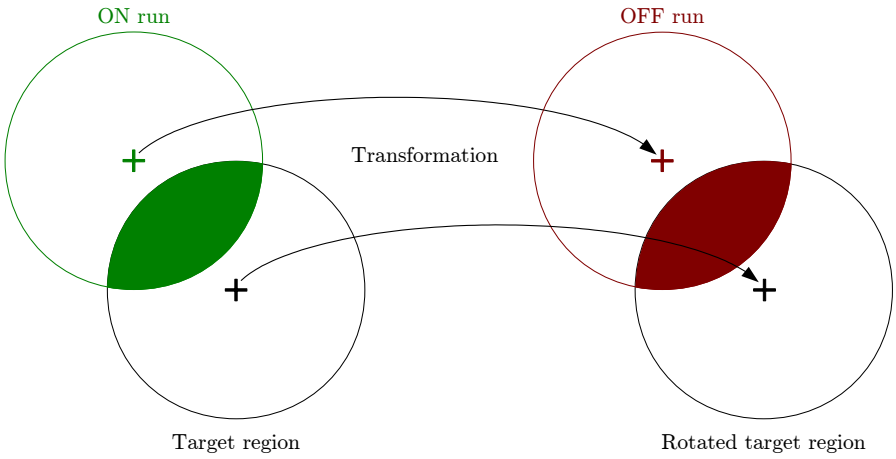

Figure 3.25.: Illustration of the matching of an on region in the on run with an off region in an off run.

3.3.4. Summary

Two methods of dealing with the on-off-analysis have been described, the Correction method and the On-Off-Selection method. While for the Correction method for all runs that lie inside the parameter ranges, in which corrections are determined, off runs are found, for the On-Off-Selection method only for a subset of runs off runs can be determined. Nevertheless, both methods are studied in the following in order to determine the uncertainties of the analysis, especially in the determination of the source significance.

3.4. Performance of the On-Off-Analysis

The methods described in the previous Section are now tested for their accuracy.

3.4.1. Determination of the Uncertainty of the Significance Determination

In order to study the uncertainty in the significance determination with the two different analysis methods and the potential background runs selected here (about 3000), different studies are performed.
First in order to study the systematic uncertainties, studies with a zero significance expectation value are carried out. Afterwards in order to show that also sources are detectable with the on-off-analysis a known gamma-ray source is analysed.

Expecting $\sigma = 0$

For the Correction method random samples (pairs of on- and off-runs) are chosen from the selected runs (> 3000). Additionally different sample sizes/number of run pairs (10 run pairs, 50 run pairs, 100 run pairs and 150 run pairs) are chosen. For each sample size then 1000 random pairs are selected and an on-off-analysis including the corrections is performed. No particular on region is chosen, but instead for each run simply the complete FoV up to 2° and the corresponding excluded regions are used. The analysis is done as described before and the accumulated significances for each sample are filled into a histogram. A normal distribution around zero is expected. The width of the distribution indicates systematic uncertainties in the sample. In Fig. 3.26(a) an example for the distribution of significances for a sample size of 150 run pairs is shown. The distribution is symmetric around zero and the fit with a gaussian (red curve) results in a mean value of -0.075 and a width of $\sigma = 4.06$. In Fig. 3.26(b) the width of the gaussian fitted to the corresponding distributions is plotted over the various sample sizes. The width of the gaussian seems to shrink slightly for larger sample sizes. However, it does not decrease below a value of 4.0, thus indicating

that the sample still contains systematics, which are not accounted for by the corrections. Otherwise the width is expected to be in the order of $1\,\sigma$. Nevertheless, the distribution is symmetric around zero, therefore the systematics do not bias the analysis.

For the Selection method a similar approach is used, though here of course the weighting

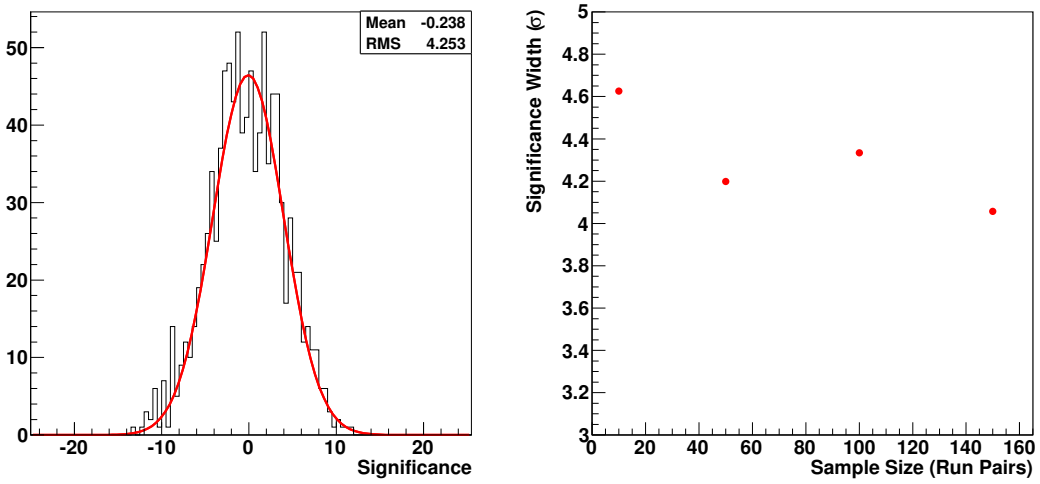

(a) (b)

Figure 3.26.: (a) The distribution of accumulated significances for 1000 test samples with a sample size of 150 run pairs. (b) The width of the gaussian fit to the significance distribution over the corresponding sample size.

is applied and therefore not for every random on-run a matching off-run is found. Therefore only a sample size around 100 (± 20 depending on how many pairs are found) is studied. The value of 100 is chosen because for the Galactic Centre region in particular 108 run pairs are found. Again 1000 different samples are used. The distribution of accumulated significances is shown in Fig. 3.27. Like before a normal distribution is obtained and the fit with a gaussian results in a mean of 0.61 and a width of $\sigma = 2.93$. The mean is slightly shifted to positive values, which might indicate a selection bias. However, this bias is small compared to the width of the distribution and will be neglected in the following. The width of the distribution is smaller than for the Correction method. This shows that the exact weighting reduces the systematic effects, as expected.

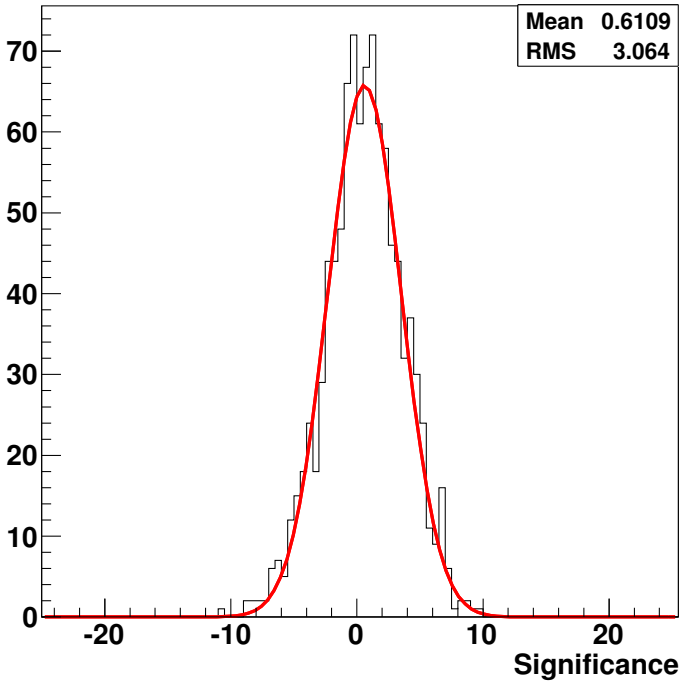

Figure 3.27.: The distribution of accumulated significances for 1000 test samples with a sample size of about 100 run pairs for the On-Off-Selection method. The red curve corresponds to a gaussian fit.

Expecting $\sigma \gg 5$

For the studies with a non-zero significance expectation value the Crab Nebula is chosen. However due to the high zenith angle under which the Crab Nebula is observed and due to the other parameter ranges only a short runlist with 11 runs is used. For those runs the zenith angles are below 50° and also the other parameters lie in the required ranges (see Appendix A.3). For the On-Off-Selection method no suitable off-runs are found for the 11 on-runs, which again shows that the method is not very promising considering the Model++ analysis. Now for the Correction method the on-region is chosen as a circle with a radius of 0.1°, which is very small compared to the whole FoV. As off-regions the full FoV up to a radius of 2.0° of the off-runs minus their corresponding excluded regions is used. 1000 random samples of off-runs are chosen and the distribution of the accumulated significances is studied, Fig. 3.28. The distribution is again fitted with a gaussian. The mean value of the gaussian is found to be 79.2 with a width of 0.9. The small width can be understood considering the relative fluctuations of the events with respect to the size of the regions. The obtained value for the significance is compatible with values obtained with other background estimation methods and the Model++ analysis.

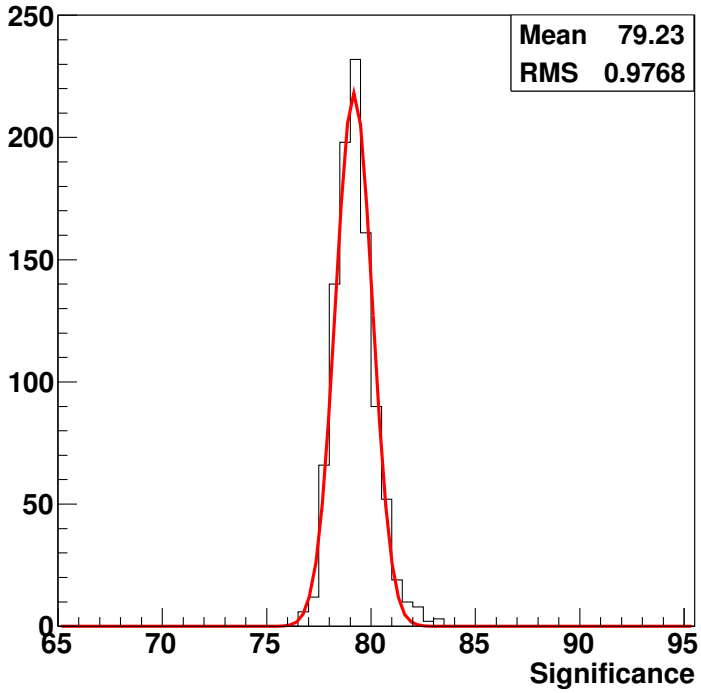

Figure 3.28.: The significance distribution of 1000 analyses of the Crab region with the Correction method and 11 on-runs and 11 random off-runs. The red line is a fit with a gaussian.

Up to now the systematic uncertainties of the analyses have been studied and the detection of a source has been tested. In the next Chapter the results for the Galactic Centre region are discussed.

4. Analysis of the Galactic Centre Region and Search for a Dark Matter Signal

The Galactic Centre region has already been described in Section 1.2.1. The focus of this Chapter therefore lies on the application of the on-off-analysis and the discussion of the results as well as a short introduction on how the upper limit on the velocity-weighted cross section is determined.

4.1. Upper Limit Calculation

In this Section the formulas needed to determine the upper limit on the velocity-averaged cross section of dark matter are given and the expected improvement of the upper limit resulting from the choice of the regions used in this thesis is determined.
The expected gamma-ray flux of continuous gamma-rays due to dark matter annihilation is given by Eq. 1.19, which states

$$\Phi_\gamma(\psi) = \underbrace{\int \frac{\mathrm{d}\Phi}{\mathrm{d}E}\mathrm{d}E}_{\text{particle physics}} \times \underbrace{J(\psi,\Delta\Omega)\Delta\Omega}_{\text{astrophysics}}. \tag{4.1}$$

Taking into account the effective area A_{eff} of the detector and the observation time T_{obs}, the number of expected gamma rays N_γ (the excess due to dark matter annihilation) can be determined:

$$\begin{aligned} N_\gamma &= T_{\text{obs}} \cdot \int_{\mathrm{E}\leq\mathrm{M}_\chi} A_{\text{eff}}(E_\gamma)\frac{\mathrm{d}\Phi_\gamma}{\mathrm{d}E_\gamma}\mathrm{d}E_\gamma & (4.2)\\ &= T_{\text{obs}} \cdot \int_{\mathrm{E}\leq\mathrm{M}_\chi} A_{\text{eff}}(E_\gamma)\frac{1}{4\pi}\frac{\langle\sigma v\rangle}{M_\chi^2}\frac{\mathrm{d}N}{\mathrm{d}E_\gamma} \cdot J(\psi,\Delta\Omega)\Delta\Omega\mathrm{d}E_\gamma & (4.3)\\ &= \frac{T_{\text{obs}}}{4\pi} \cdot \frac{\langle\sigma v\rangle}{M_\chi^2} \cdot J(\psi,\Delta\Omega)\Delta\Omega \int_{\mathrm{E}\leq\mathrm{M}_\chi} A_{\text{eff}}(E_\gamma)\frac{\mathrm{d}N}{\mathrm{d}E_\gamma}\mathrm{d}E_\gamma. & (4.4) \end{aligned}$$

Now from the measurement an upper limit on the excess of gamma rays $N_\gamma^{95\%\text{C.L.}}$ is determined (Rolke et al., 2005) and inverting Eq. 4.4 gives the upper limit on $\langle\sigma v\rangle^{95\%\text{C.L.}}$

depending on the mass of the dark matter particle M_χ:

$$\langle\sigma v\rangle^{95\%\text{C.L.}} = \frac{4\pi}{T_{\text{obs}}} \cdot \frac{M_\chi^2}{J(\psi,\Delta\Omega)\Delta\Omega} \cdot \frac{N_\gamma^{95\%\text{C.L.}}}{\int_{\text{E}\leq\text{M}_\chi} A_{\text{eff}}(E_\gamma)\frac{\text{d}N}{\text{d}E_\gamma}\text{d}E_\gamma}. \tag{4.5}$$

However, Eq. 4.4 is only valid if no gamma rays from dark matter annihilation are expected in the off region. In case of the observation of the extended dark matter halo of the Milky Way the off regions are chosen to be well separated from the Galactic Centre. However, the dark matter density there is still not negligible and gamma rays from dark matter annihilation are expected. This has to be taken into account when calculating the expected number of gamma rays N_γ due to dark matter:

$$\begin{aligned} N_\gamma &= N_\gamma^{\text{On}} - \beta N_\gamma^{\text{Off}} && (4.6)\\ &= \alpha \cdot [J(\psi_{\text{On}},\Delta\Omega_{\text{On}})\Delta\Omega_{\text{On}} - \beta J(\psi_{\text{Off}},\Delta\Omega_{\text{Off}})\Delta\Omega_{\text{Off}}] && (4.7)\\ \text{with } \alpha &= \frac{T_{\text{obs}}}{4\pi} \cdot \frac{\langle\sigma v\rangle}{M_\chi^2} \cdot \int_{\text{E}\leq\text{M}_\chi} A_{\text{eff}}(E_\gamma)\frac{\text{d}N}{\text{d}E\gamma}\text{d}E_\gamma. && (4.8) \end{aligned}$$

Here N_γ^{On} corresponds to the expected number of gamma-rays in the on region (the Galactic Centre region) and N_γ^{Off} corresponds to the expected number of gamma-rays away from the Galactic Centre due to dark matter annihilation. The different astrophysical factors $J(\psi_{\text{On}},\Delta\Omega_{\text{On}})\Delta\Omega_{\text{On}}$ and $J(\psi_{\text{Off}},\Delta\Omega_{\text{Off}})\Delta\Omega_{\text{Off}}$ correspond to the different dark matter densities in the regions, while β is the normalisation according to the different area sizes:

$$\beta = \frac{A_{\text{Off}}}{A_{\text{On}}}. \tag{4.9}$$

Accordingly also the formula for the upper limit changes to

$$\begin{aligned} \langle\sigma v\rangle^{95\%\text{C.L.}} = \frac{4\pi}{T_{\text{obs}}} \cdot \frac{M_\chi^2}{[J(\psi_{\text{On}},\Delta\Omega_{\text{On}})\Delta\Omega_{\text{On}} - \beta J(\psi_{\text{Off}},\Delta\Omega_{\text{Off}})\Delta\Omega_{\text{Off}}]} \cdot \\ \cdot \frac{N_\gamma^{95\%\text{C.L.}}}{\int_{\text{E}\leq\text{M}_\chi} A_{\text{eff}}(E_\gamma)\frac{\text{d}N}{\text{d}E_\gamma}\text{d}E_\gamma}. \end{aligned} \tag{4.10}$$

This theoretical view raises the question how much the upper limit obtained from the Galactic Centre region in Abramowski et al. (2011b) can be improved (lowered) by reducing N_γ^{Off}. Therefore the values of the astrophysical factor $J = J(\psi,\Delta\Omega)\Delta\Omega$ have been calculated (as described in Section 1.1.6) for different on and off regions (for the ones chosen in Abramowski et al. (2011b) and for regions similar to the ones chosen in this thesis). A sketch of the different regions is shown in Fig. 4.1. For consistency in the determination method the values of J_{On} and J_{Off} from Abramowski et al. (2011b) are recalculated. The results for all regions from Fig. 4.1 are given in Table 4.1. The improvement of the upper limit can be up to a factor of ~ 3.2 for the NFW profile and up to ~ 3.9 for the Einasto profile in case of no signal in the background region, $N_{\text{off}} = 0$. For a distance of the off

region from the Galactic Centre of about 8° still an improvement of a factor of ~ 2.9 for the NFW and ~ 3.6 for the Einasto profile can be achieved.
In the following now the results of the on-off-analysis are presented.

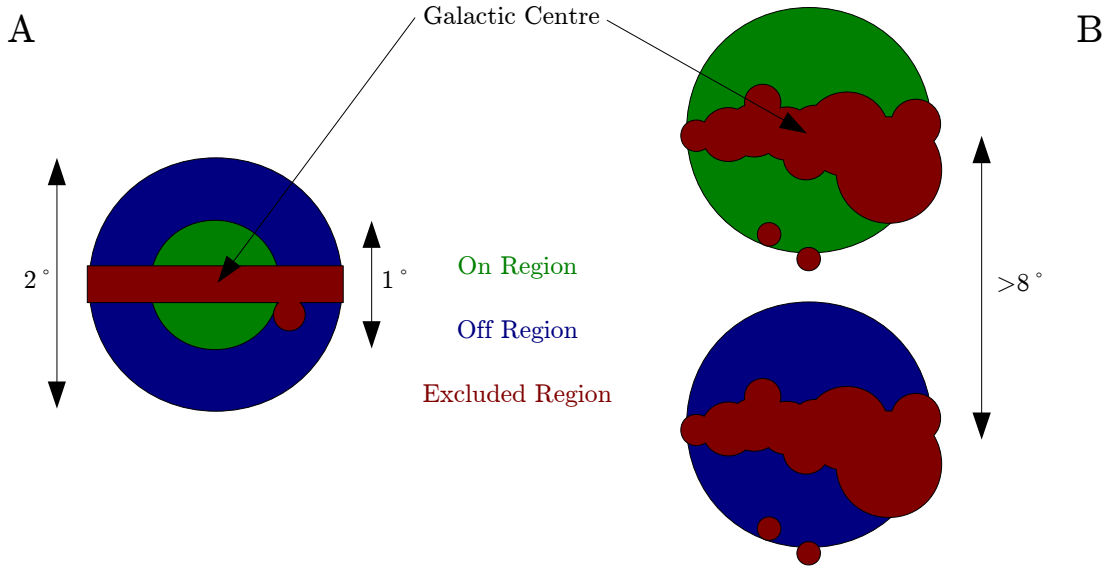

Figure 4.1.: Sketch illustrating the different on and off regions. Case A corresponds to the regions chosen in Abramowski et al. (2011b) and case B to the regions chosen in this thesis.

Table 4.1.: The astrophysical factor J in units of $10^{21}\,\mathrm{GeV^2cm^{-5}}$ for different on and off regions.

	$J_{\mathrm{on}}^{\mathrm{NFW}}$	$\beta J_{\mathrm{off}}^{\mathrm{NFW}}$	$J_{\mathrm{on}}^{\mathrm{Einasto}}$	$\beta J_{\mathrm{off}}^{\mathrm{Einasto}}$
A in Fig. 4.1	1.7	0.7	4.4	2.1
B in Fig. 4.1	3.2	0.3	8.9	0.7

4.2. On-Off Analysis and results

4.2.1. Run Selection

The analysis starts with the run selection. Therefore again the quality criteria introduced in Section 3.1.2 are applied and runs are selected as target (on-) runs, if their observation position lies within a 2° radius around the Galactic Centre ($l = 0.0°$, $b = 0.0°$). 222 runs are selected. However, corrections only exist for certain parameter ranges, in which enough statistics were collected. Therefore the runs are further restricted according to their parameters. The distributions of the runs over the different parameters of interest and the corresponding parameter ranges are shown in Fig. 4.2. The blue shaded regions are the parameter ranges, in which corrections are determined. Unfortunately not all of the on-runs are covered by these regions (especially for the NSB and the humidity) and therefore only 166 runs remain usable for the analysis. Also for the On-Off-Selection analysis some parameter ranges are restricted (muon efficiency, NSB, camera temperature and radiometer temperature), leaving 178 on-runs for the On-Off-Selection method. However, after the matching of the runs with the limit on $W = 10$ only for 108 of them suitable off-runs are found.

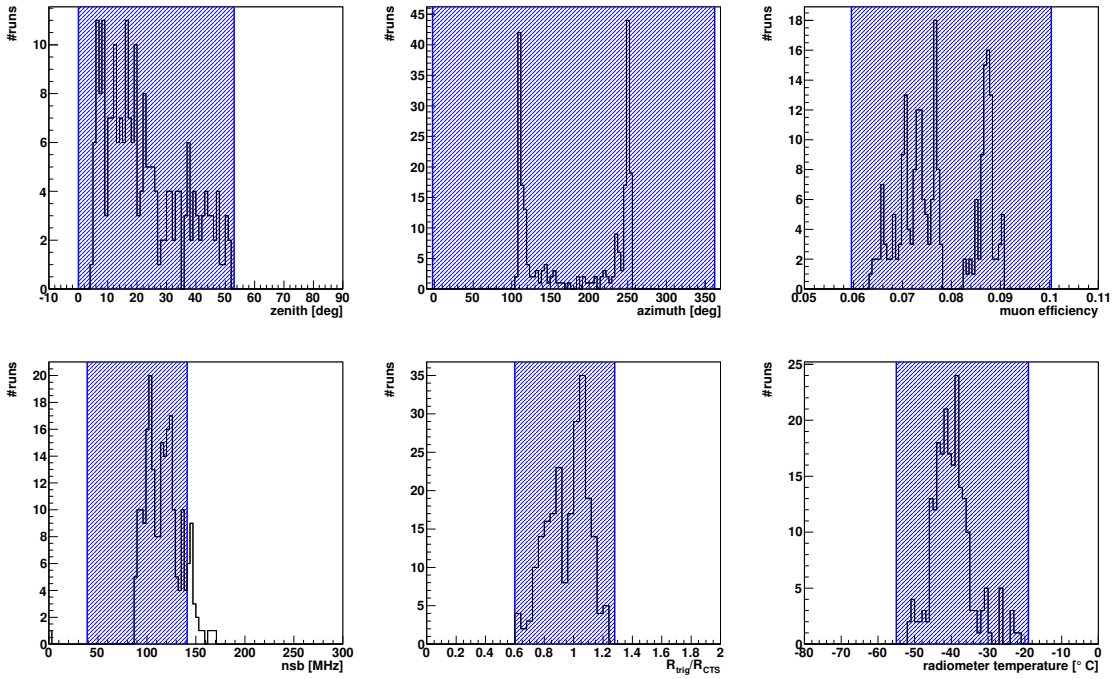

Figure 4.2.: See next page. Figure continues there.

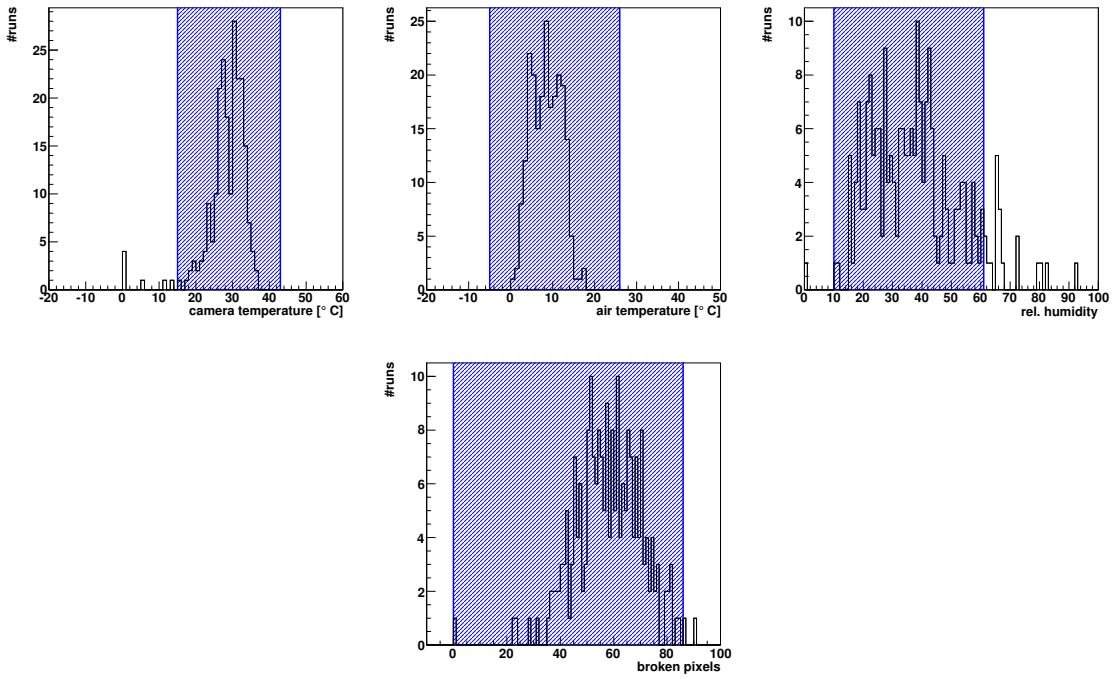

Figure 4.2.: The distribution of the Galactic Centre region runs with regard to the parameters of interest. For the blue shaded regions corrections were derived.

4.2.2. Significance Determination

After the run selection the significance is determined with both methods. First the approach and the results for the On-Off-Selection method then for the Correction method are described.

On-Off-Selection Method

For the On-Off-Selection method a single sample of off-runs with the matching weight is chosen. The uncertainty on the result is assumed as $\pm 3\sigma$ from the systematic studies shown in the previous Chapter. The accumulated values of the analysis for the 108 run pairs are $N_{\text{on}} = 32631$, $N_{\text{off}} = 27381$, with $\beta = 1.18$. This results in a significance of 1.2σ with an uncertainty of $\pm 3\sigma$.

Correction Method

For the Correction method, similar to the previous studies of the analyses (see Section 3.4.1), all potential off-runs are used. In order to include the systematics of the potential off-runs, again 1000 random (no weight applied) samples of off-runs are chosen. Each

sample contains 166 runs and for each sample an on-off-analysis is performed. In Fig. 4.3 the resulting distribution of the accumulated significances is shown. A large shift of the mean value to 7.6σ is found and the width of the distribution is relatively small (2.2σ). The shift indicates that there are more gamma rays in the Galactic Centre region than in the chosen off-runs. However, this is not necessarily due to dark matter annihilation, as will be shown in the following. The assumption is that the shift in the significance is due to higher

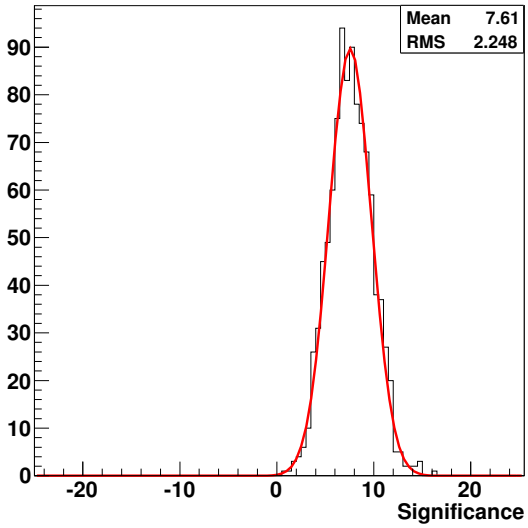

Figure 4.3.: The distribution of the accumulated significances for 1000 analysis of the Galactic Centre region with random samples of off-runs. The red line is a fit with a gaussian.

gamma-ray rates inside the Galactic Plane than outside. In the analysis the on-runs are positioned inside the Galactic Plane ($b \leq 2°$), the off-runs, however, are positioned inside as well as outside the Galactic Plane. In order to test the assumption two further checks are performed. For the first test all off-runs are required to lie inside ($b \leq 2°$) the Galactic Plane. This reduces the amount of available off-runs to about 1000. From those 1000 runs then 100 different samples are chosen and the accumulated significances are shown in Fig. 4.4(a). For the second test the off-runs are required to lie outside the galactic plane ($b \geq 4°$), which allows for about 2000 runs. Here again 100 samples are chosen and the significance distribution is shown in Fig. 4.4(b). The result is quite convincing, for the first test the mean of the distribution is at 1.4σ, whereas for the second test an even larger shift to 11.2σ is found. This strongly points to higher gamma-ray emission from the Galactic Plane. In order to further confirm this effect also the background runs (8° away from the Galactic Centre region) have been tested for this behaviour. Runs inside the Galactic plane ($b \leq 2°$) are chosen as on-runs and outside the plane ($b \geq 4°$) as off-runs. A sample size of 150 run pairs is used and 100 random samples are generated. There also a shift in the mean significance to $\sim 11.2\sigma$ is seen. For completeness the two other cases (on-runs and

off-runs inside the plane and on-runs and off-runs outside the plane) have also been tested. The resulting distributions for the tests with the background runs are given in Appendix A.6. The larger amount of emission inside the Galactic Plane may have various reasons.

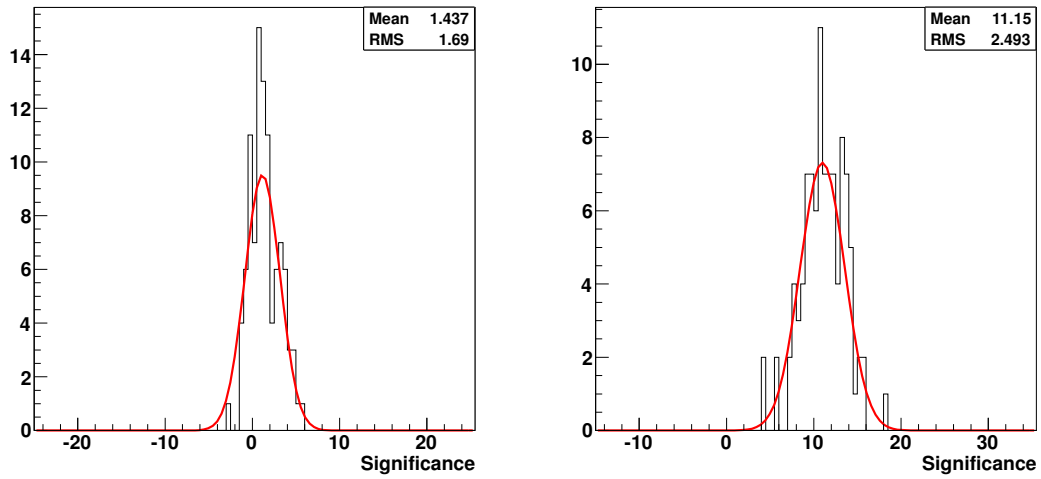

(a) (b)

Figure 4.4.: (a) The distribution of accumulated significances for the Galactic Centre region with 100 off-run samples from all off-runs inside the Galactic plane ($b \leq 2°$). (b) The distribution of accumulated significances for the Galactic Centre region with 100 off-run samples from all off-runs outside the Galactic plane ($b \geq 4°$). The red curves correspond to fits with a gaussian.

Potential explanations are uncertainties in the excluded regions, an effect of the corrections or physical reasons, like, e.g., diffuse emission inside the plane. This is certainly a very interesting question and was also discussed in de Naurois (2012), however it will not be studied further in this thesis.
For the analysis of the Galactic Centre region now the result obtained with off-runs inside the Galactic plane is used. The distributions of the events (N_{on} and $\beta \cdot N_{\text{off}}$) and again the accumulated significance are shown in Fig. 4.5. The distribution of on-events is of course a simple peak at the number of on-events, since always the same on-runs are used. For $\beta \cdot N_{\text{off}}$ a broader distribution is found. The final results and the uncertainties are then extracted from those distributions yielding $N_{\text{on}} = 50138$, $\beta \cdot N_{\text{off}} = 49684$ and a mean significance of $1.4\sigma \pm 2.0\sigma$.

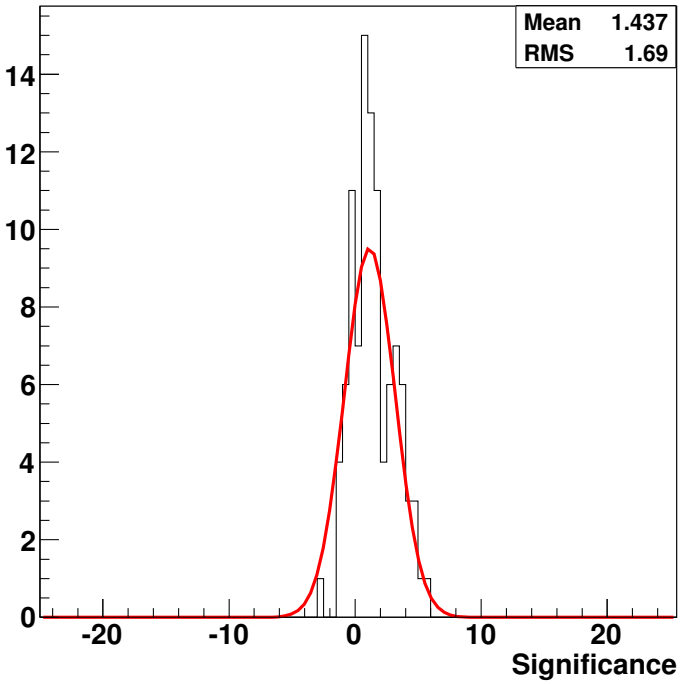

(a)

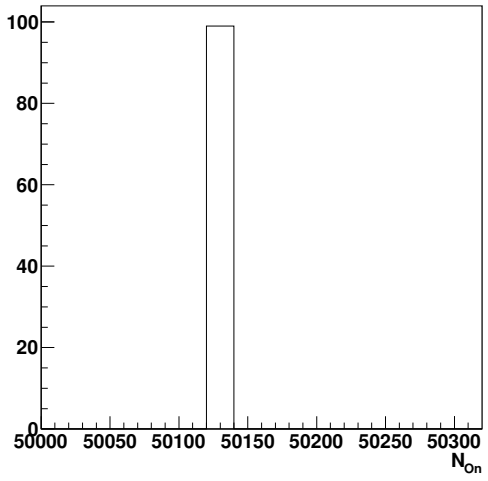

(b)

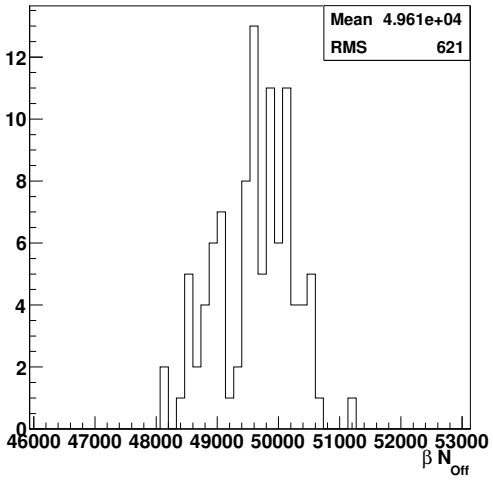

(c)

Figure 4.5.: (a) The distribution of accumulated significances for the Galactic Centre region with 100 off-run samples with all off-runs inside the Galactic plane ($b \leq 2°$). The red curve correspond to a fit with a gaussian. (b) The distribution of accumulated on events N_{On} for the Galactic Centre region. (c) The distribution of accumulated off events times the normalisation factor $\beta \cdot N_{\mathrm{Off}}$ for the 100 off-run samples with all off-runs inside the Galactic plane ($b \leq 2°$).

4.2.3. Upper Limit

Now the upper limit on the velocity-averaged cross section is determined, since with both methods no signal has been found. As shown in the first Section of this Chapter, the values which enter are

- the total live time T_{obs},
- the dark matter properties ($\mathrm{d}N/\mathrm{d}E$ and J)
- the detector effective area A_{eff} and
- the upper limit (95% confidence level) on the number of excess gamma rays.

For the total live time simply the total observation time of all used runs is taken. Hence for the Correction method $T_{\mathrm{obs}} \approx 72\,\mathrm{h}$ and for the On-Off-Selection method $T_{\mathrm{obs}} \approx 47\,\mathrm{h}$.
For the dark matter spectrum the parametrisations of Bergstroem and Tasitsiomi as given in Eq. 1.21 and Eq. 1.22 are used. The astrophysical factor in units of $10^{21}\,\mathrm{GeV^2cm^{-5}}$ is $J_{\mathrm{Einasto}} = J_{\mathrm{on}} - J_{\mathrm{off}} = 8.2$ for the Einasto profile and $J_{\mathrm{NFW}} = 2.9$ for the NFW profile, see Table 4.1.
The effective area is determined from look-ups in the following way: A skymap of the target region with a small binning (0.02°) is chosen. For each run the effective area in each bin depending on the mean zenith of the run and the offset of the bin (position from the observation position of the run) is summed up and normalised to the number of bins

$$A_{\mathrm{eff}}(E) = \sum_{\mathrm{runs}} \sum_{\mathrm{bins}} A_{\mathrm{eff}}(E, \psi_{\mathrm{bin}}, \beta_{\mathrm{zen,run}}) \tag{4.11}$$

Additionally in the summation the effective area is set to zero if the energy is below the energy threshold $E_{\mathrm{thr}}(\beta_{\mathrm{zen,run}})$ for the mean zenith of the run. In Fig. 4.6 the effective area obtained for the Galactic Centre analysis is shown. The differences in the effective areas for the two analysis methods (Correction/On-Off-Selection) are negligible. The energy threshold (or starting point of the effective area) of the analysis is determined to be $E_{\mathrm{thr}} = 201\,\mathrm{GeV}$. The limit on the number of excess gamma rays was determined according to Rolke et al. (2005) with the assumption of Poissonian background. The 95% confidence level is $N_\gamma^{95\,CL} = 1073$ for the Correction method and $N_\gamma^{95\,CL} = 843$ for the On-Off-Selection method. The lowest limits are obtained with the Correction method. These resulting upper limits are shown in Fig. 4.7 together with the limits obtained in Abramowski et al. (2011b). The shaded bands around the limits correspond to the uncertainty resulting from the uncertainty on the number of off-events, $\Delta N_{\mathrm{off}} = \pm 600$. The upper limits are compatible with the previously published ones and lie in the expected range. The observation times and the effective areas are smaller than the ones used in Abramowski et al. (2011b) (obtained in Nekrassov (2010)), however, due to the higher sensitivity of the Model++ analysis, the slightly lower energy threshold of 201 GeV (compared to 230 GeV) and the larger astrophysical factor J overall an improvement of a factor of about 3 is gained. Therefore at the moment these are the most sensitive limits on the velocity-averaged cross-section for dark matter annihilation into continuous gamma rays.

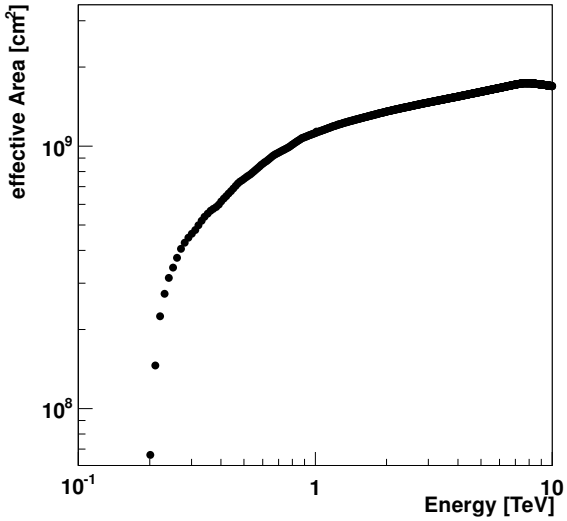

Figure 4.6.: The effective areas determined from look-ups for the Galactic Centre analysis.

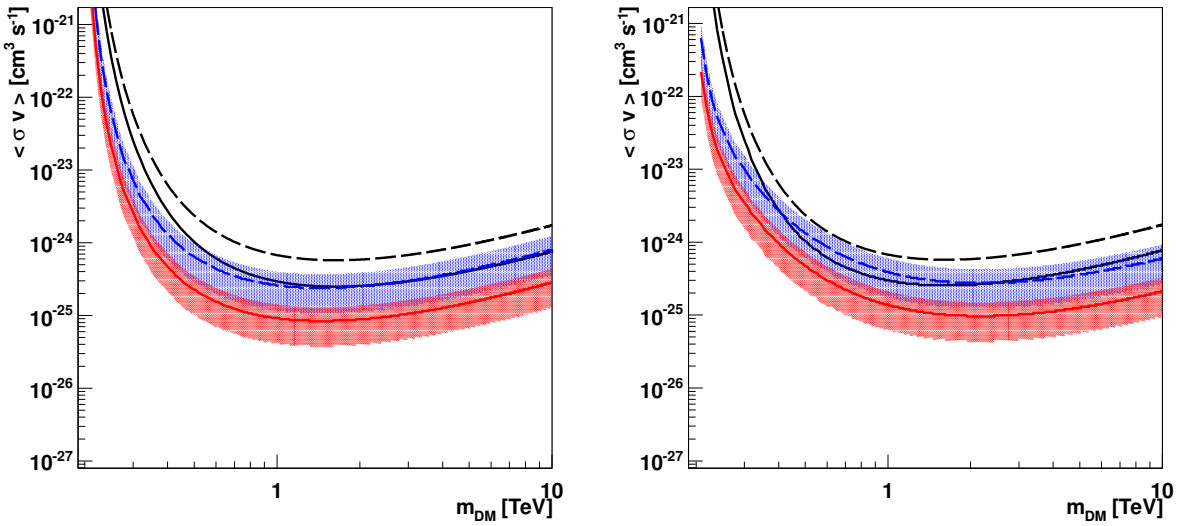

(a) (b)

Figure 4.7.: (a) The upper limits obtained with the Correction method are shown for the Einasto (red line) and the NFW profile (dashed blue line), respectively. The black lines are the corresponding limits derived from Abramowski et al. (2011b). For all limits the Tasitsiomi parametrisation was used. In (b) the black lines are the same, but for the other lines the Bergstroem parametrisation was used.

5. Conclusion and Outlook

The aim of this thesis was the development and quantification of an on-off-analysis for the H.E.S.S. experiment in order to search for a gamma-ray signal from the annihilation of dark matter in the halo of the Milky Way.
The H.E.S.S. experiment (High Energy Stereoscopic System) is an array of four Imaging Atmospheric Cherenkov Telecopes (IACTs) situated in the Khomas Highland in Namibia. They are able to detect gamma rays with energies between about 0.1 and 50 TeV.
Simulations of structure formation (e.g. Springel et al. (2005) or Springel et al. (2008a)) suggest that the dark matter distribution in the Milky Way exhibits radial symmetry with respect to the Galactic Centre and that the highest dark matter density is reached there. Accordingly, the largest gamma-ray signal due to dark matter annihilation is expected at the Galactic Centre region[1], making it an interesting target for the search for dark matter. H.E.S.S. has observed the Galactic Centre region for over 100 hours and an upper limit on the velocity-averaged dark matter annihilation cross-section into continuous gamma rays has been derived (Abramowski et al., 2011b). However, so far the estimation of the excess gamma rays due to dark matter annihilation was based on the comparison of the gamma-rays from different regions (on- and off region) within a single field of view (FoV) of the H.E.S.S. experiment, which is 5° in diameter. The comparison is necessary in order to estimate the gamma-ray- and residual cosmic-ray background (from the off region). The dark matter density, however, may decrease by only about 50% in a single FoV, and therefore also in the off region gamma rays due to dark matter annihilation are expected. This significantly reduces the overall expected signal when choosing the target (on-) and the off region from within a single FoV.
Therefore an on-off-analysis was proposed using H.E.S.S. observations taken further away from the Galactic Centre region as off regions, which should contain much less gamma rays from dark matter annihilation. However, such an on-off-analysis encounters many systematic effects because the observations are made under different conditions, which might affect the data differently. These dependencies on the detector configuration and on the observation conditions have to be taken into account when comparing gamma rays from on and off regions from different observations.
Recently systematic studies quantifying these influences based on the very robust Hillas reconstruction have been conducted (Glück, 2011). However, a more sensitive reconstruction technique, the so-called Model++ reconstruction (de Naurois and Rolland, 2009), has been developed in the mean time. The Model++ reconstruction takes into account the full camera information and performs a likelihood-fit in order to determine the parameters of

[1]The region contained within a radius of $r \sim 2.5°$ around the dynamical centre of the Galaxy at $b = l = 0°$.

the primary gamma ray.
In the thesis presented here the dependencies on various parameters for the Model++ analysis have been studied and quantified for the first time. Summarising, the effects were found to be relatively large compared to ones found for the Hillas analysis (Glück, 2011). This is attributed to the usage of the full camera data in the Model++ reconstruction and especially the inclusion of calibration parameters in the fitting procedure. It has to be pointed out that the exact influence of potential miscalibrations on the Model++ reconstruction has to be the subject of future studies.
Once identified and quantified, the systematic effects can be dealt with in an on-off-analysis in different ways. Two possibilities were described and tested here.

- The first way is called *On-Off-Selection method*. Each on-run (observation made at the Galactic Centre) is paired with a suitable off-run (observation made far from the Galactic Centre). The conditions (determined via various parameters) under which the off-run was taken have to match those of the on-run within fixed limits. The allowed mismatch is determined for each parameter according to the derived dependencies and the required accuracy of the analysis.

- The second way is called *Correction method*. For each parameter a correction is included in the analysis according to the derived dependency. The corrections, however, still contain systematic uncertainties. Therefore not only one sample of off-runs is analysed but a lot of random samples of off-runs chosen from the list of all available off-runs are used. The result (the mean) and the uncertainty (the width) of the analysis are then extracted from the distribution of results of the analyses for all samples.

When testing the two methods the *On-Off-Selection method* was found to have disadvantages, because of the strict selection criteria necessary for the Model++ analysis. The dependencies are so strong that for remaining uncertainties to be in the range of 10% several parameters have to match very well in the on- and the off-run. Then, however, only a few off-runs fulfil these matching criteria and not for all on-runs corresponding off-runs can be found. This then leads to the dismissal of many on-runs and therefore also reduces the usable observation time.
The *Correction method* worked quite well concerning the uncertainties of the corrections. The uncertainty of the final analysis was not much larger compared to the *On-Off-Selection method*. Nevertheless, also there on-runs had to be dismissed due to the restriction of the parameter ranges. Not for all ranges of the parameter space enough statistics existed to be able to determine the influences.
Concluding, both implementations work and yield satisfying results. The main result of the analyses was the determination of the source significance S in terms of Li and Ma (1983). The significance S is used to decide whether a real source was found (typically, $S > 5\sigma$) or just a fluctuation of the background ($S < 5\sigma$). In case of the search for a signal due to dark matter annihilation from the Galactic Centre, if present at all, the significance is expected to be very small ($S < 3\sigma$). The uncertainties on the determination of the significance of

the two methods lie in the range of $3-5\,\sigma$. Therefore the analyses are better suited for regions containing a strong gamma-ray source with a high significance ($S \gg 5\sigma$).
For the Galactic Centre region both analyses resulted in significances around 1σ, which are compatible with no gamma-ray excess. However, for the *Correction method* first a shift to larger significances around 7σ was observed. This shift could be explained by larger gamma-ray emission from the Galactic Plane, which was proven by further checks comparing observations inside the Plane with observations outside the Plane. There the shift was even more prominent with $S \sim 11\sigma$. This certainly will need to be studied further in order to determine the origin of these shifts to higher significances and whether it has anything to do with diffuse emission inside the Galactic Plane, which was also mentioned by de Naurois (2012). For the analysis of the Galactic Centre region off-runs from inside the Plane were chosen assuming a similar size of the emission along the Plane and the previously mentioned 1σ result was found.
For both methods then upper limits on the velocity-averaged cross-section were determined. The uncertainty on the upper limits is larger than for other analyses. Nevertheless, the upper limits show a slight improvement compared to the previous upper limits (Abramowski et al., 2011b) determined from regions within a single FoV.
The Galactic Centre remains a very interesting region, not only for dark matter searches. Future experiments like the Cherenkov Telescope Array (CTA) are also going to put new limits on the dark matter cross section as they will also extend the energy range towards lower energies. The prospects for dark matter searches, also at the Galactic Centre, with CTA are discussed in Doro et al. (2013), a study which also comprises results obtained in the course of this thesis. Furthermore, already in the near future further improvements on the upper limit can be expected from H.E.S.S. II, which will be able to detect gamma rays at energies down to 50 GeV.
The on-off-analyses presented here can still be improved. First of all since, the start of this thesis project additional observational data have been collected. These data should help to determine the influences also in parameter ranges where so far not enough statistics existed. This might include looking at parameters of single telescopes, since some parameters might change drastically from one telescope to the other. An example are the mirror reflectivities, for some periods the mirrors on some, but not all telescopes had been exchanged. Furthermore, the calibration, the Model++ reconstruction and analysis are improved continuously and the existing data are reprocessed and reanalysed with the improved methods. Additionally, the determination of spectra can be added to the developed on-off-analysis.
The results presented here show that the on-off-analysis of H.E.S.S. data with Model++ is possible. The systematics entering the analysis have been studied in detail and the resulting uncertainties have been quantified.
Also in the future the on-off-analysis will certainly be needed. It serves as one of the few methods to study very extended sources and provides background estimations to FoVs with many excluded regions (source candidates). Additionally, it will be important for H.E.S.S. II observations since the FoV of H.E.S.S. II is only about 3.2° in diameter and therefore smaller than the FoV of H.E.S.S. I (5°).

A. Auxiliary Information

A.1. Correlations between the Parameters of Interest

The parameters of interest are introduced in Section 3.1.1 and listed in Table 3.1. Their correlations with each other are studied and in Table 3.2 the correlation coefficients are given. Here the corresponding correlation plots for all parameters of interest with each other are shown. The correlation coefficient is also given.

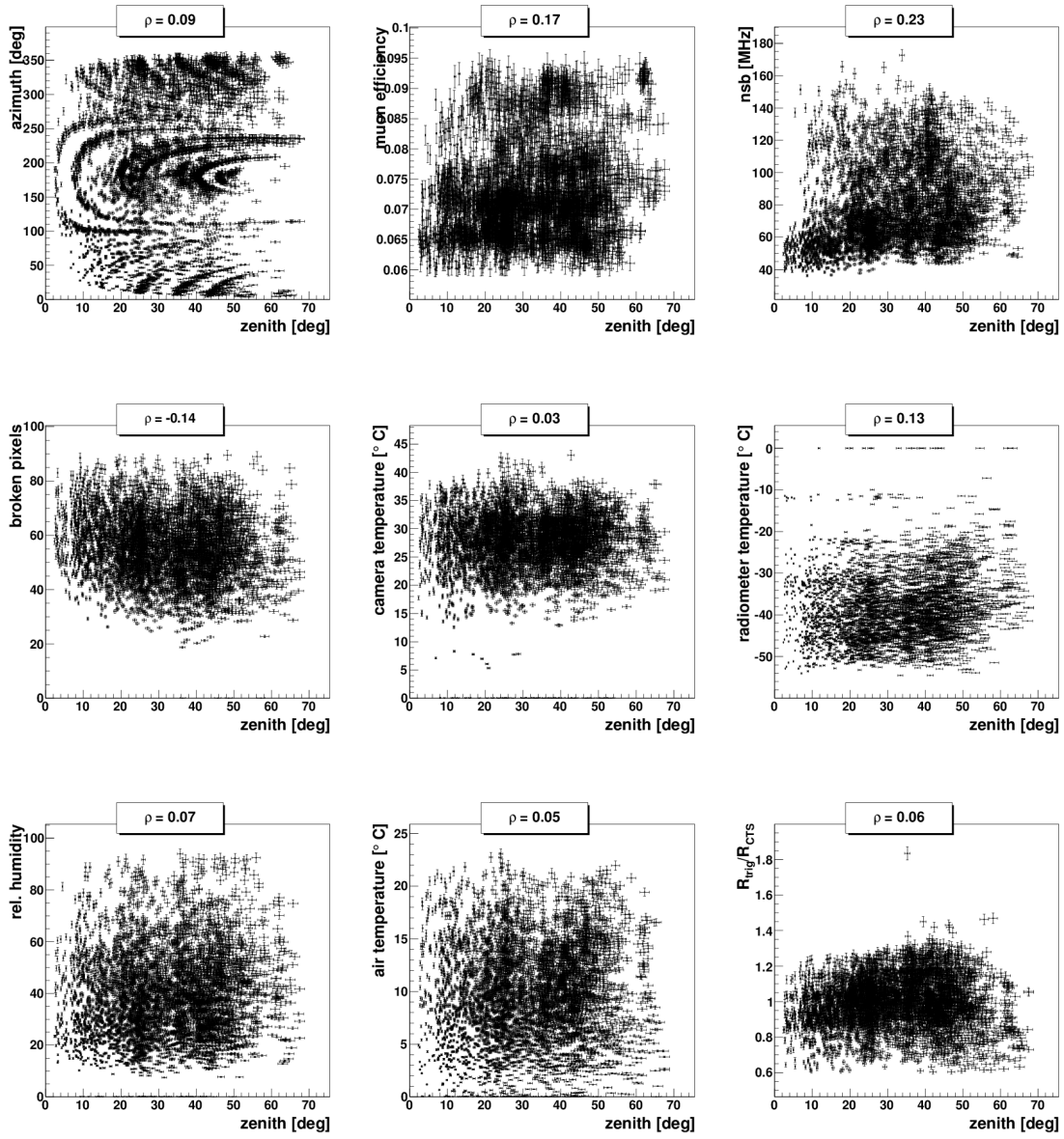
ρ = 0.09
azimuth [deg]
zenith [deg]
ρ = 0.17
muon efficiency
zenith [deg]
ρ = 0.23
nsb [MHz]
zenith [deg]
ρ = -0.14
broken pixels
zenith [deg]
ρ = 0.03
camera temperature [° C]
zenith [deg]
ρ = 0.13
radiometer temperature [° C]
zenith [deg]
ρ = 0.07
rel. humidity
zenith [deg]
ρ = 0.05
air temperature [° C]
zenith [deg]
ρ = 0.06
R_{trig}/R_{CTS}
zenith [deg]

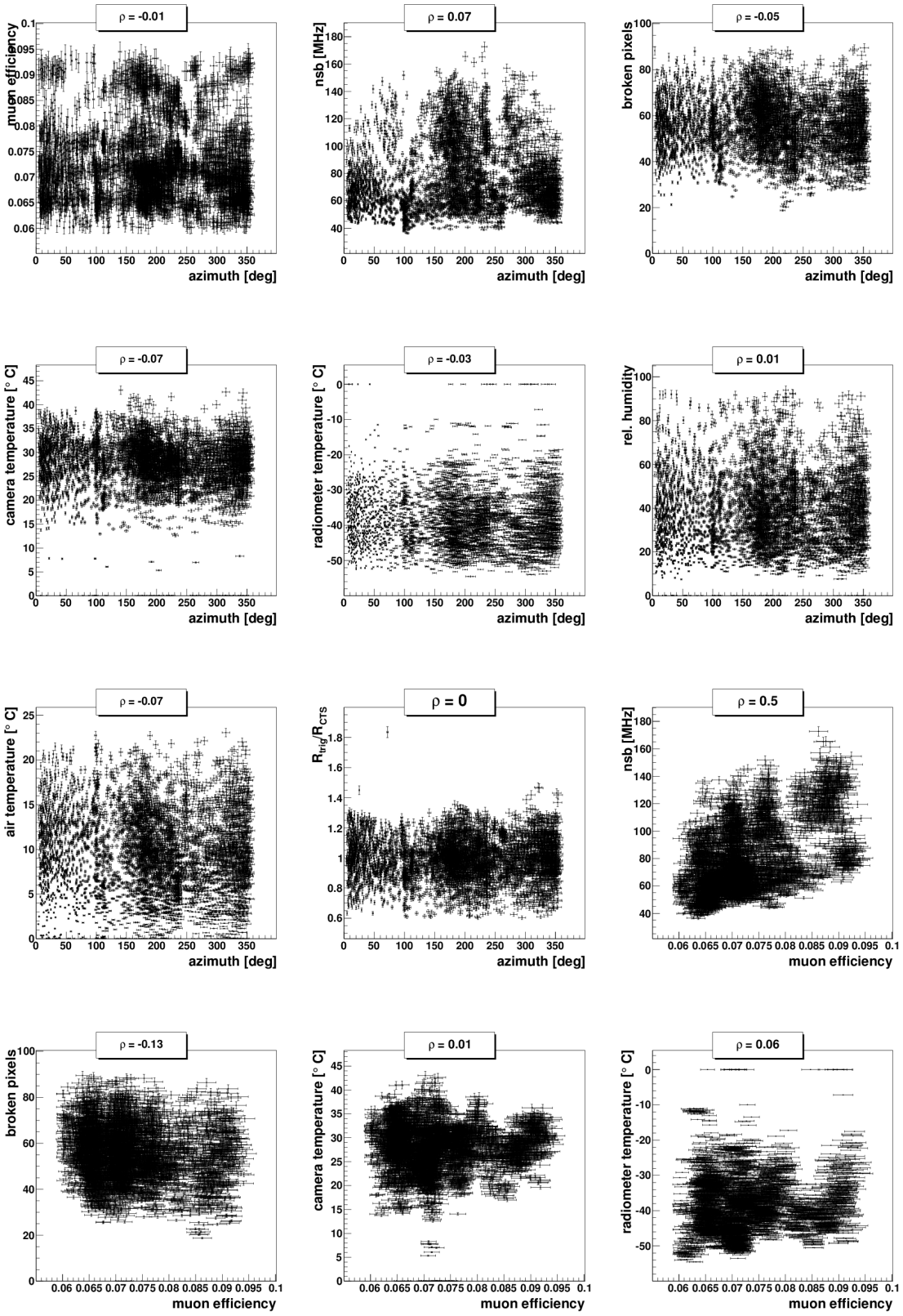
ρ = -0.01
muon efficiency
azimuth [deg]
ρ = 0.07
nsb [MHz]
azimuth [deg]
ρ = -0.05
broken pixels
azimuth [deg]
ρ = -0.07
camera temperature [° C]
azimuth [deg]
ρ = -0.03
radiometer temperature [° C]
azimuth [deg]
ρ = 0.01
rel. humidity
azimuth [deg]
ρ = -0.07
air temperature [° C]
azimuth [deg]
ρ = 0
R_trig/R_CTS
azimuth [deg]
ρ = 0.5
nsb [MHz]
muon efficiency
ρ = -0.13
broken pixels
muon efficiency
ρ = 0.01
camera temperature [° C]
muon efficiency
ρ = 0.06
radiometer temperature [° C]
muon efficiency

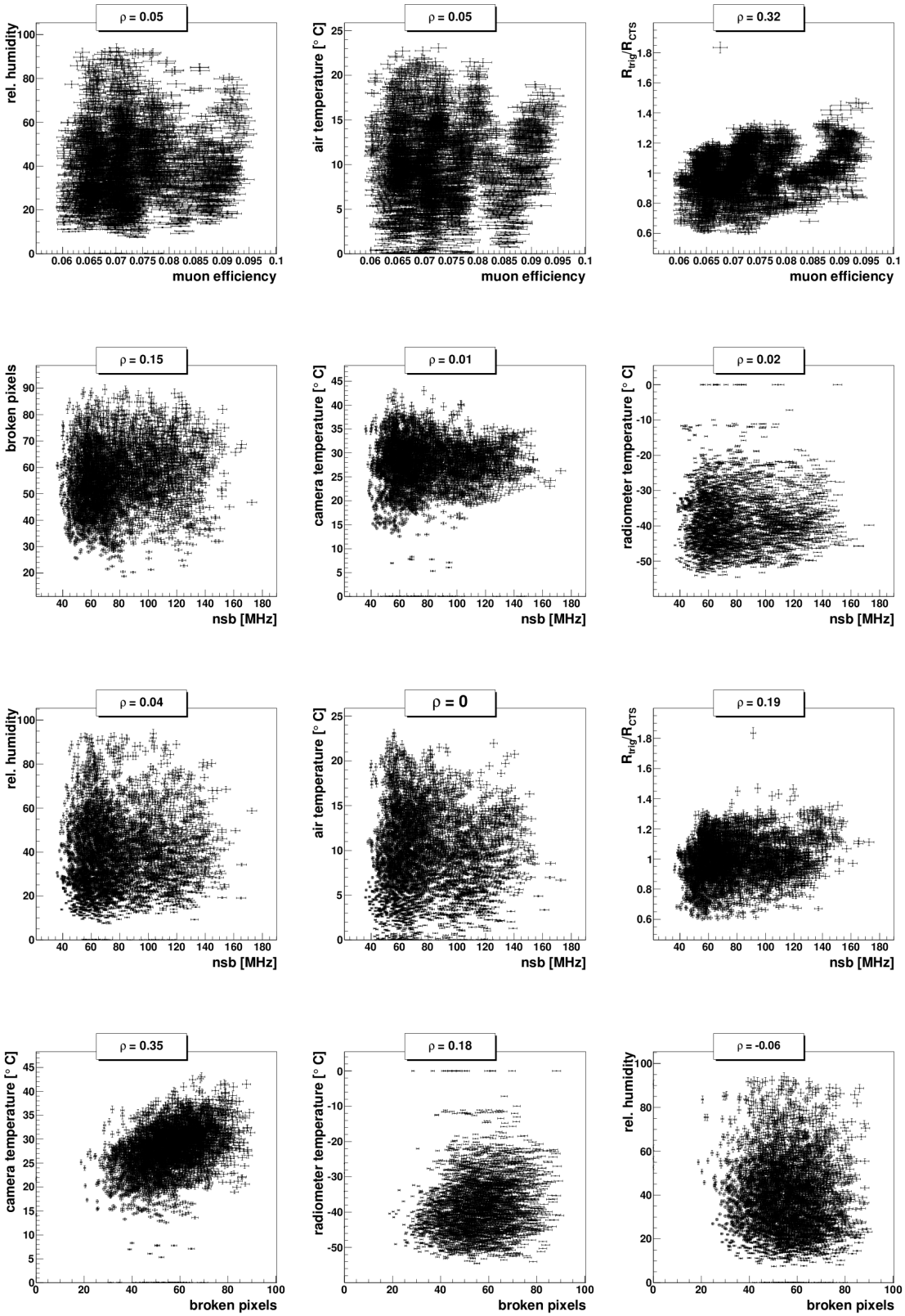
ρ = 0.05
rel. humidity
muon efficiency
ρ = 0.05
air temperature [° C]
muon efficiency
ρ = 0.32
R_trig/R_CTS
muon efficiency
ρ = 0.15
broken pixels
nsb [MHz]
ρ = 0.01
camera temperature [° C]
nsb [MHz]
ρ = 0.02
radiometer temperature [° C]
nsb [MHz]
ρ = 0.04
rel. humidity
nsb [MHz]
ρ = 0
air temperature [° C]
nsb [MHz]
ρ = 0.19
R_trig/R_CTS
nsb [MHz]
ρ = 0.35
camera temperature [° C]
broken pixels
ρ = 0.18
radiometer temperature [° C]
broken pixels
ρ = -0.06
rel. humidity
broken pixels

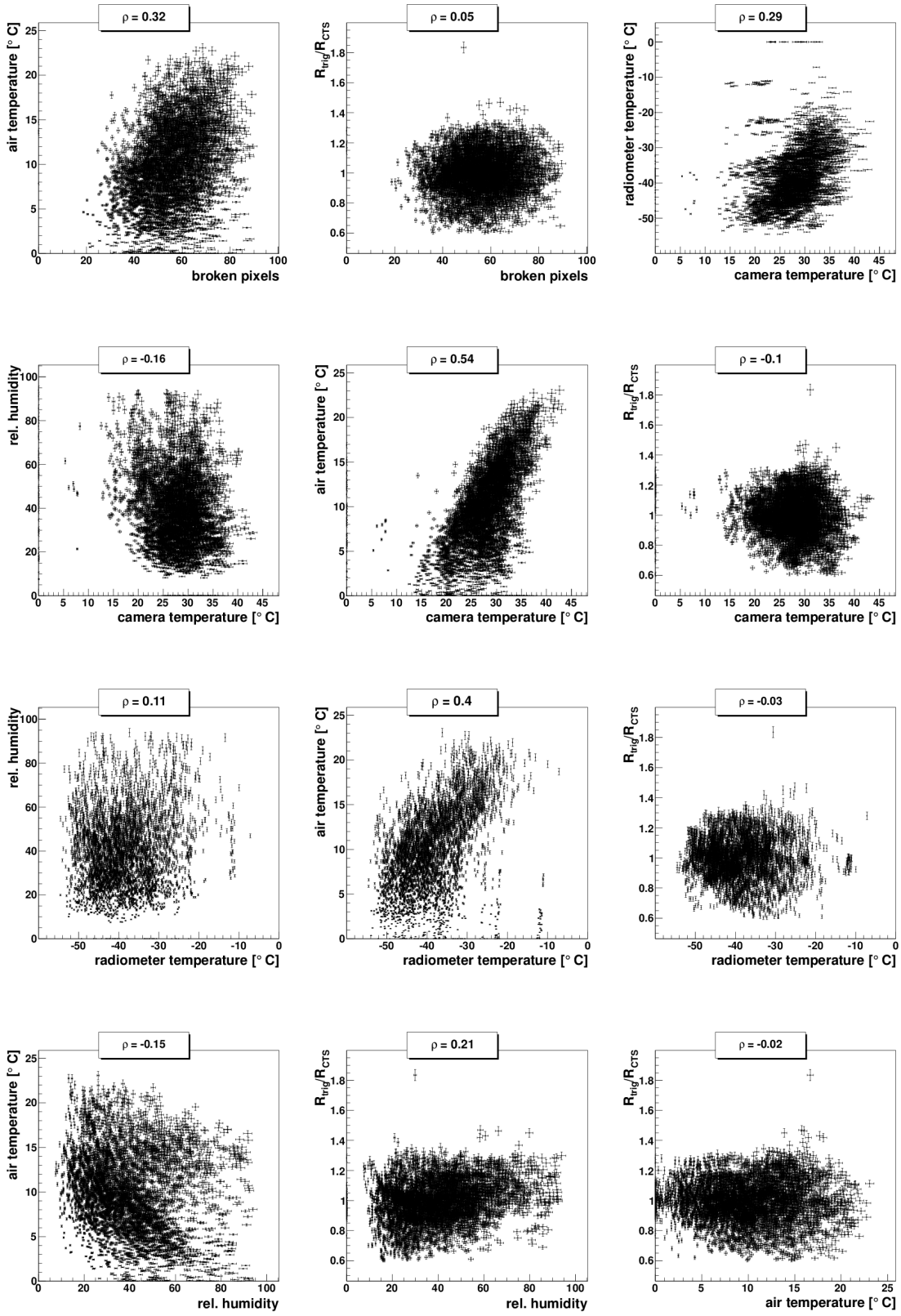
ρ = 0.32
air temperature [° C]
broken pixels
ρ = 0.05
R_trig/R_CTS
broken pixels
ρ = 0.29
radiometer temperature [° C]
camera temperature [° C]
ρ = -0.16
rel. humidity
camera temperature [° C]
ρ = 0.54
air temperature [° C]
camera temperature [° C]
ρ = -0.1
R_trig/R_CTS
camera temperature [° C]
ρ = 0.11
rel. humidity
radiometer temperature [° C]
ρ = 0.4
air temperature [° C]
radiometer temperature [° C]
ρ = -0.03
R_trig/R_CTS
radiometer temperature [° C]
ρ = -0.15
air temperature [° C]
rel. humidity
ρ = 0.21
R_trig/R_CTS
rel. humidity
ρ = -0.02
R_trig/R_CTS
air temperature [° C]

A.2. Example motivating the use of the Accumulated Rate

The difference between the mean rate R_{mean} and the accumulated rate R_{acc} is nicely illustrated when studying the case for just two runs. In Fig. A.1 on the left the definition of the rate is illustrated symbolising the exposure as a 3 dimensional box. The rate is defined as $R = \frac{N}{A \cdot t}$. Now we assume that the rate is split up into two runs, which have the same observation time t, but the observed areas on the sky are different, A_1 and A_2 respectively. Now we calculate both the mean rate and the accumulated rate for those two runs, with N_1 and N_2 being the events in each run and $N = N_1 + N_2$ and $A = A_1 + A_2$

$$R_{\text{mean}} = \frac{1}{2}(R_1 + R_2) = \frac{1}{2}\left(\frac{N_1}{A_1 t} + \frac{N_2}{A_2 t}\right) = \frac{N_1 A_2 + N_2 A_1}{2 \cdot (A_1 A_2) t} \tag{A.1}$$

$$R_{\text{acc}} = \frac{N_1 + N_2}{(A_1 t) + (A_2 t)} = \frac{N}{(A_1 + A_2) t} = \frac{N}{A \cdot t}. \tag{A.2}$$

We see that only for the accumulated rate the desired definition of the rate is obtained, whereas for the mean rate the result is different.

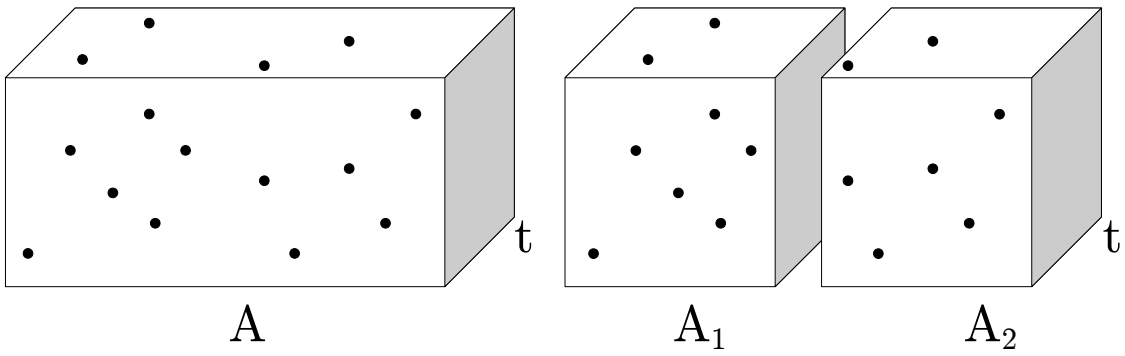

Figure A.1.: Illustration of the definition of the rate and the splitting of the rate into two runs. The black points are events.

A.3. Distribution of the Runs over the Parameters of Interest

In Section 3.1.2 runs are selected according to certain quality criteria. The distribution of these runs over the different parameters of interest (listed in Table 3.1) is shown here.

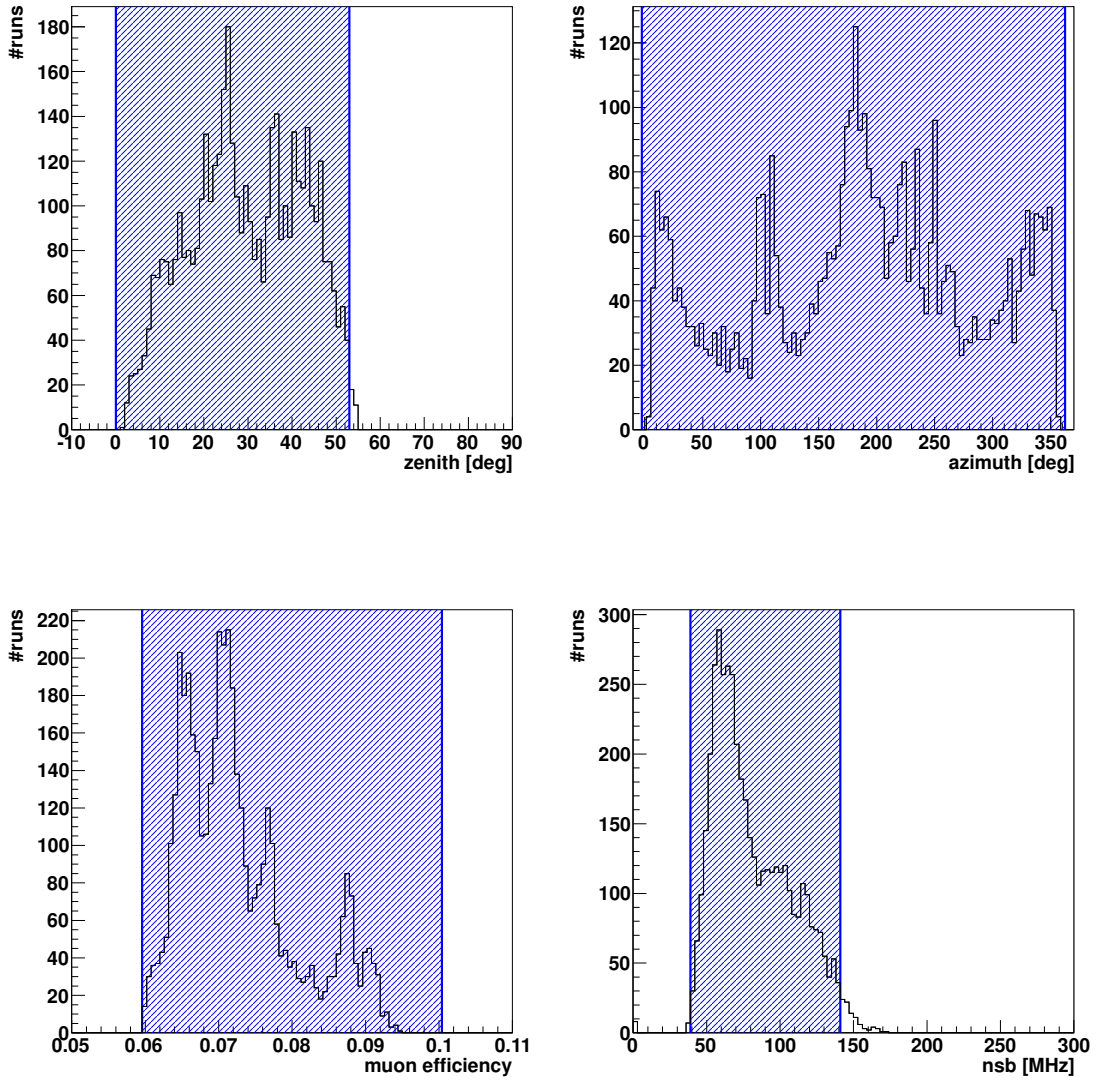

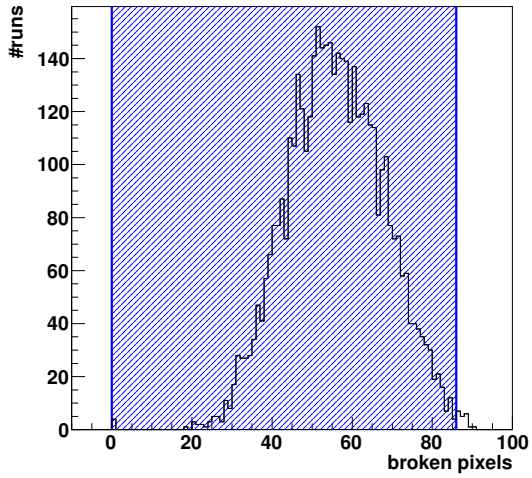
#runs
broken pixels

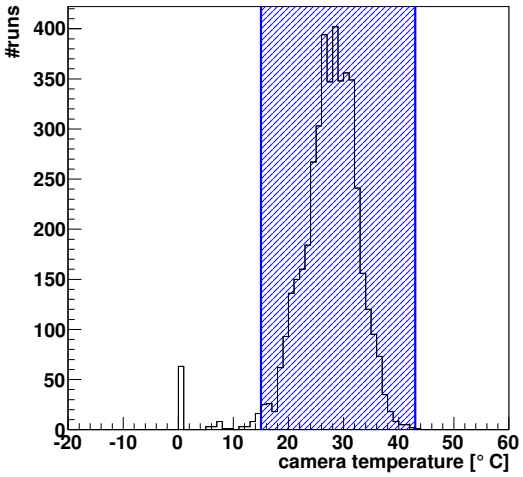
#runs
camera temperature [° C]

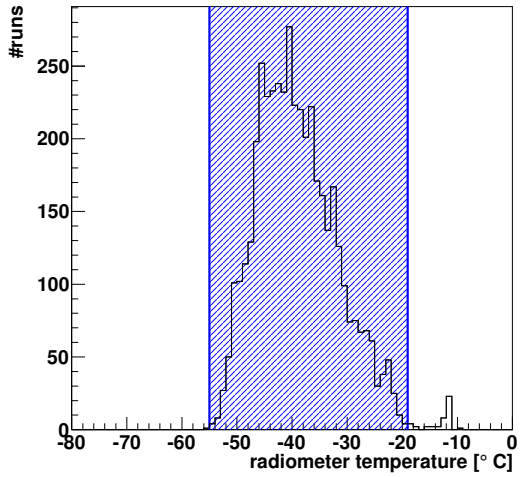
#runs
radiometer temperature [° C]

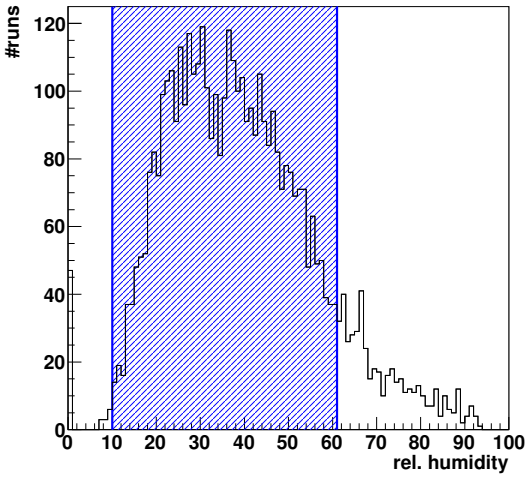
#runs
rel. humidity

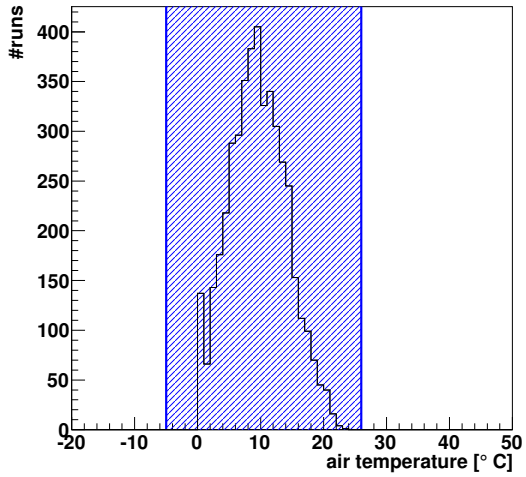
#runs
air temperature [° C]

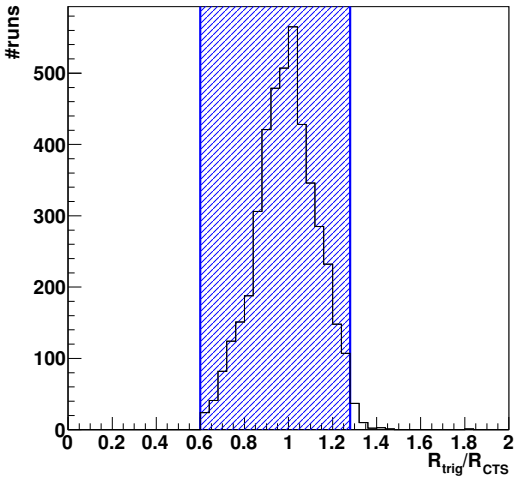
#runs
R_trig/R_CTS

A.4. Plots obtained with Method A

In Section 3.2 the dependence of the background rate on different parameters is studied. Therefore two methods are introduced in Section 3.2.1, method A and B. The results for method B are shown in the main text (Sections 3.2.2-3.2.12) Here plots obtained with method A in the energy range between 0.1 TeV and 10 TeV are shown. In order to use most of the data the corrections derived with method B were applied. However, the correction for the parameter of interest was not included. The behaviour seen here is similar to the one observed with the corrections and method B.

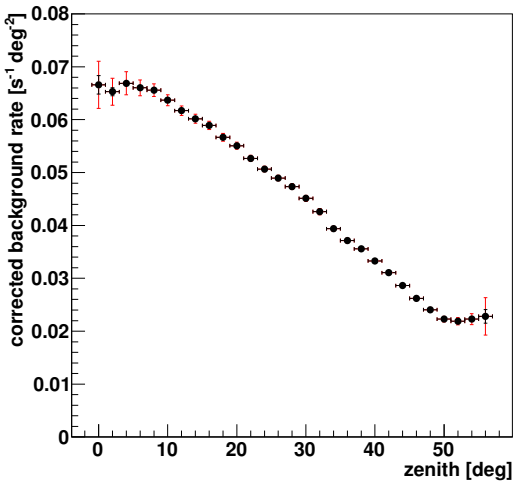

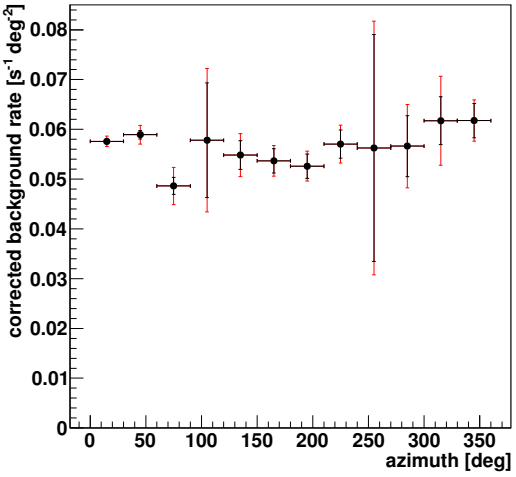

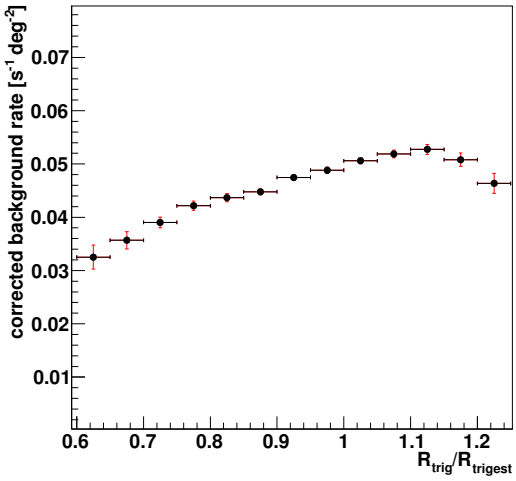

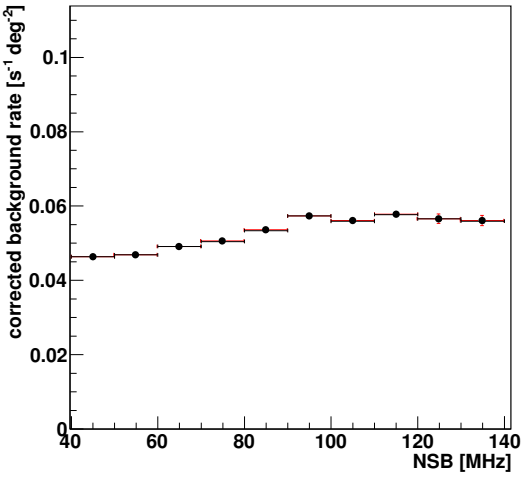

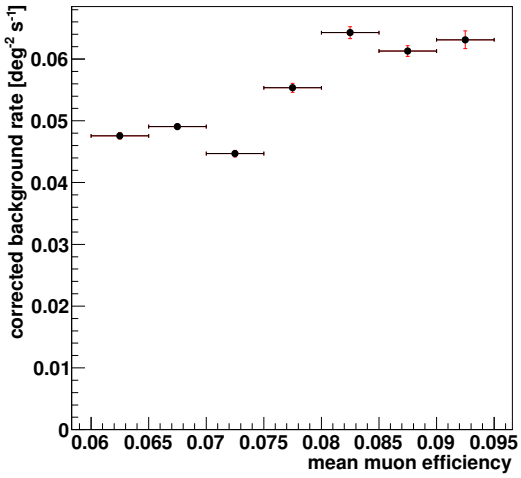
corrected background rate [deg^{-2} s^{-1}]
0.06 0.065 0.07 0.075 0.08 0.085 0.09 0.095
mean muon efficiency

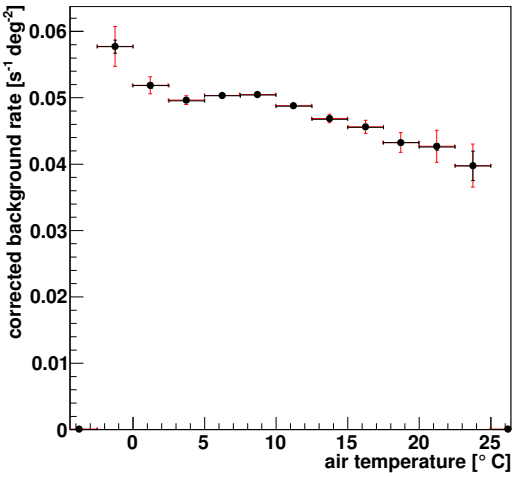
corrected background rate [s^{-1} deg^{-2}]
0 5 10 15 20 25
air temperature [° C]

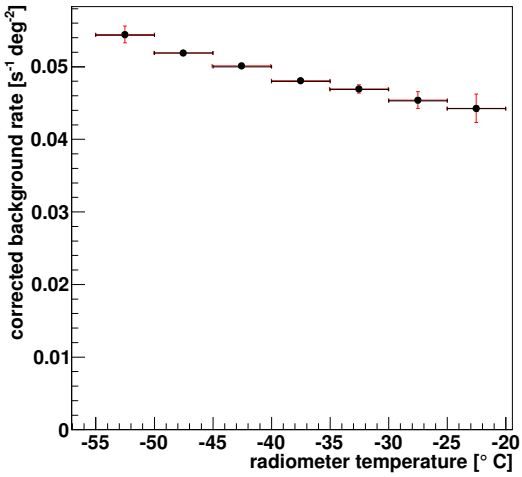
corrected background rate [s^{-1} deg^{-2}]
-55 -50 -45 -40 -35 -30 -25 -20
radiometer temperature [° C]

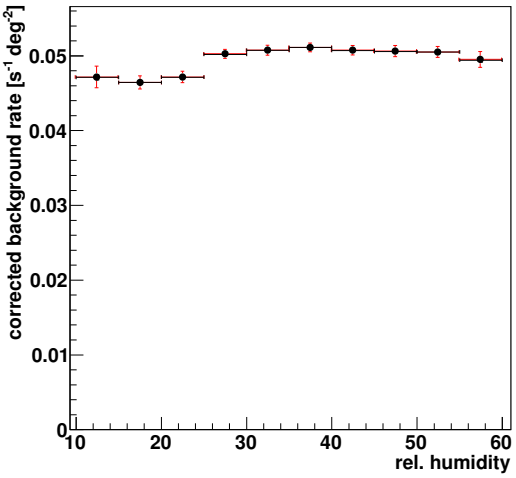
corrected background rate [s^{-1} deg^{-2}]
10 20 30 40 50 60
rel. humidity

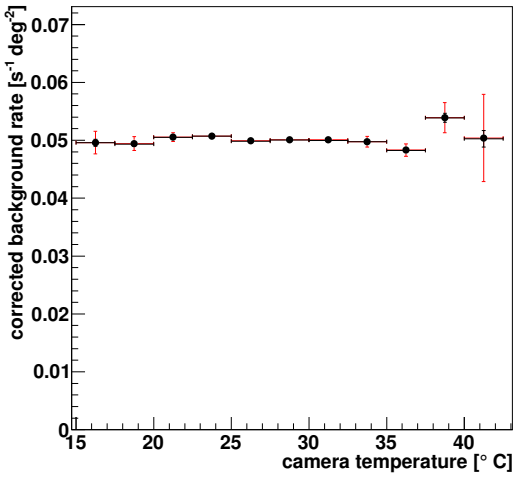
corrected background rate [s^{-1} deg^{-2}]
15 20 25 30 35 40
camera temperature [° C]

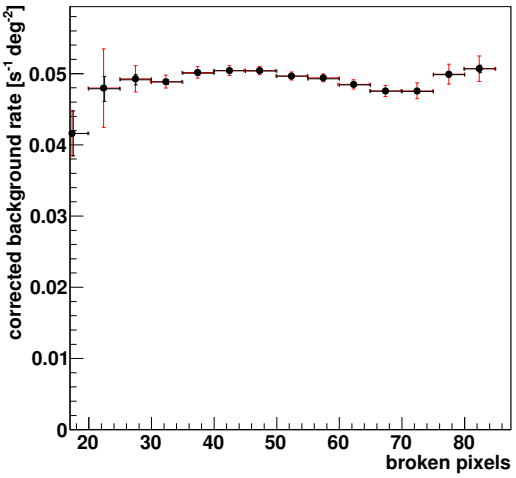
corrected background rate [s^{-1} deg^{-2}]
20 30 40 50 60 70 80
broken pixels

A.5. Determination of the correction factors

In the following the plots, which were used to determine the corrections, for all the parameters are shown (except for the plot of the radiometer temperature, which is shown in the main text already in Section 3.3.2). In Section 3.3.2 is also described how these plots were obtained. Additionally, here the functions, which were fitted to the various plots are given as well as the fit results. For the zenith angle the function

$$f\left(\beta_{\text{zen}}\right) = a \cdot \exp\left[-0.5 \cdot \left(\frac{\beta_{\text{zen}} - b}{c}\right)^2\right] \tag{A.3}$$

was used and the fit (Fig. A.2(c)) results in $a = 1.234$, $b = 4.645$ and $c = 31.892$.
For the azimuth angle the function given in Eq.3.23 was used and the fit (Fig. A.3(c)) results in $a = -0.114$, $b = -1.333$ and $c = 1.107$.
The NSB plot (Fig. A.4(c)) was fitted with the following function:

$$f(NSB) = \begin{cases} a + b \cdot NSB, & NSB \leq x_{\text{break1}} \\ f(x_{\text{break1}}) + c \cdot NSB, & NSB > x_{\text{break1}} \end{cases} . \tag{A.4}$$

The result of the fit for a fixed break at $x_{\text{break1}} = 95\,\text{MHz}$ is $a = 0.733$, $b = 0.004$ and $c = -0.002$.
For the air temperature in Fig. A.5(c) simply a linear function

$$f(T_{\text{air}}) = a + b \cdot T_{\text{air}} \tag{A.5}$$

was used. The result is $a = 1.073$ and $b = -0.010$.
The camera temperature (Fig. A.6(c)) was fitted with

$$f(T_{\text{camera}}) = \begin{cases} a + b \cdot T_{\text{camera}}, & T_{\text{camera}} \leq x_{\text{break1}} \\ f(x_{\text{break1}}) + c \cdot T_{\text{camera}}, & x_{\text{break1}} < T_{\text{camera}} \end{cases} . \tag{A.6}$$

The fit for the fixed break at $x_{\text{break1}} = 32.5°\text{C}$ results in $a = 0.985$, $b = 0.000$ and $c = -0.020$.
For the trigger rate ratio (Fig. A.7(c)) the following function was used:

$$\frac{R_{\text{bin}}}{R_{\text{ref}}}\left(\frac{R_{\text{trig}}}{R_{\text{trigest}}}\right) = f(\frac{R_{\text{trig}}}{R_{\text{trigest}}}) = \begin{cases} a + b \cdot \epsilon_\mu, & \frac{R_{\text{trig}}}{R_{\text{trigest}}} \leq x_{\text{break1}} \\ f(x_{\text{break1}}) + c \cdot \epsilon_\mu, & \frac{R_{\text{trig}}}{R_{\text{trigest}}} > x_{\text{break1}} \end{cases} . \tag{A.7}$$

The fit results for a fixed break at $x_{\text{break1}} = 1.1$ in $a = 0.228$, $b = 0.765$ and $c = -0.739$.
For the muon efficiency in Fig. A.8(c) no fit was used, but instead linear interpolation between the points.
The relative humidity in Fig. A.9(c) is described with

$$f(hum) = \begin{cases} a + b \cdot hum + c \cdot hum^2, & hum \leq x_{\text{break1}} \\ f(x_{\text{break1}}) + d \cdot hum, & hum > x_{\text{break1}} \end{cases} \tag{A.8}$$

and the fit for $x_{\text{break1}} = 25.0$ results in $a = 1.338$, $b = -0.048$, $c = 0.001$ and $d = 0.001$. The number of broken pixels in Fig. A.10(c) is fitted with

$$f\left(N_{\text{bp}}\right) = \begin{cases} a + b \cdot N_{\text{bp}}, & N_{\text{bp}} \leq x_{\text{break1}} \\ f(x_{\text{break1}}) + c \cdot N_{\text{bp}}, & N_{\text{bp}} > x_{\text{break1}} \end{cases}, \tag{A.9}$$

where $x_{\text{break1}} = 42.5$ and $a = 0.591$, $b = 0.010$ and $c = -0.003$.

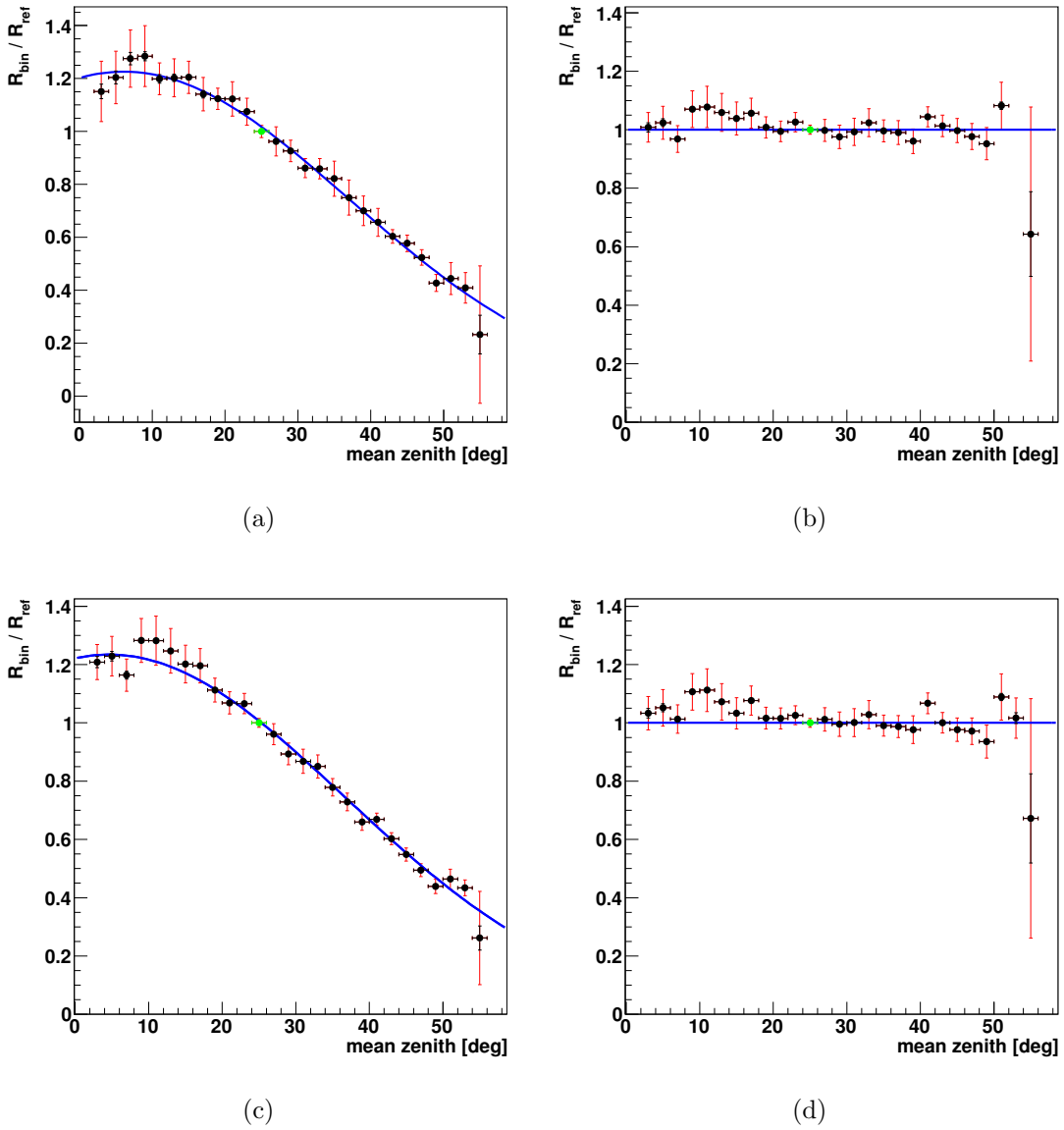

Figure A.2.: In (a) the background rate ratio over the zenith angle for energies between 0.1 TeV and 10 TeV is plotted. The blue line is a fit with the function given in Eq. A.3. In (b) the corrections for all parameters have been applied and the corrected background rate ratio over the zenith angle is plotted. The blue line is drawn at a background rate ratio of 1.0. The deviations of the points from this line indicate how well the corrections worked. In (c) all corrections have been applied except the correction for the zenith angle. The background rate ratio over the zenith angle is very similar to (a). The blue line is a fit with the function given in Eq. A.3. In (d) the new corrections have been applied on the background rates and the deviations from the blue line at 1.0 are also very similr to those in (b). (All plots are obtained with Method B)

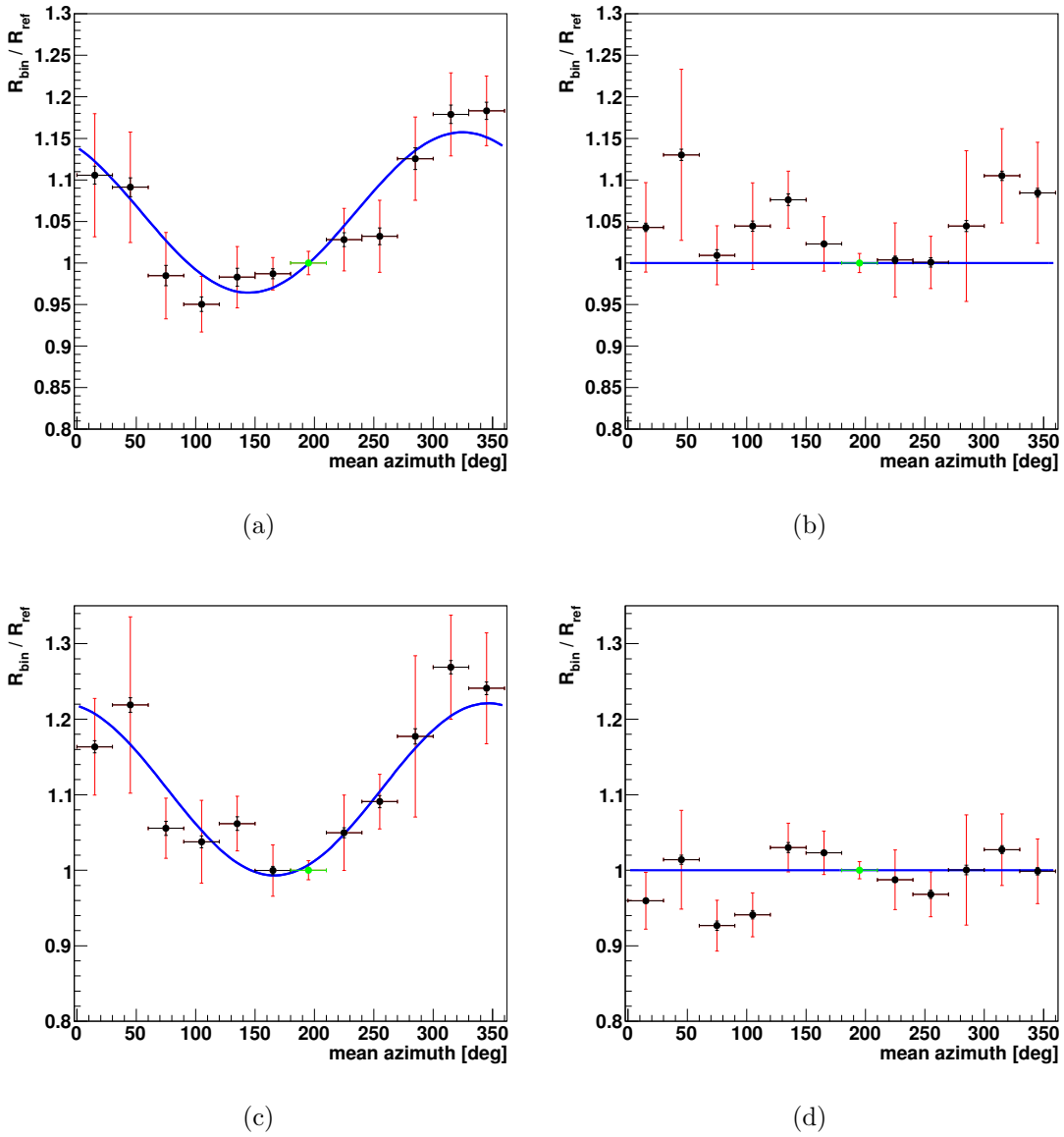

Figure A.3.: In (a) the background rate ratio over the azimuth angle for energies between 0.1 TeV and 10 TeV is shown. The blue line is a fit with the function given in Eq. 3.23. In (b) the corrections for all parameters have been applied and the corrected background rate ratio over the azimuth angle is plotted. The blue line is drawn at a background rate ratio of 1.0. The deviations of the points from this line indicate how well the corrections worked. In (c) all corrections have been applied except the correction for the azimuth angle. The background rate ratio over the azimuth angle shows a similar dependence as in (a). The blue line is a fit with the function given in Eq. 3.23. In (d) the new corrections have been applied on the background rates and the deviations from the blue line at 1.0 are on average smaller than in (b). (All plots are obtained with Method B)

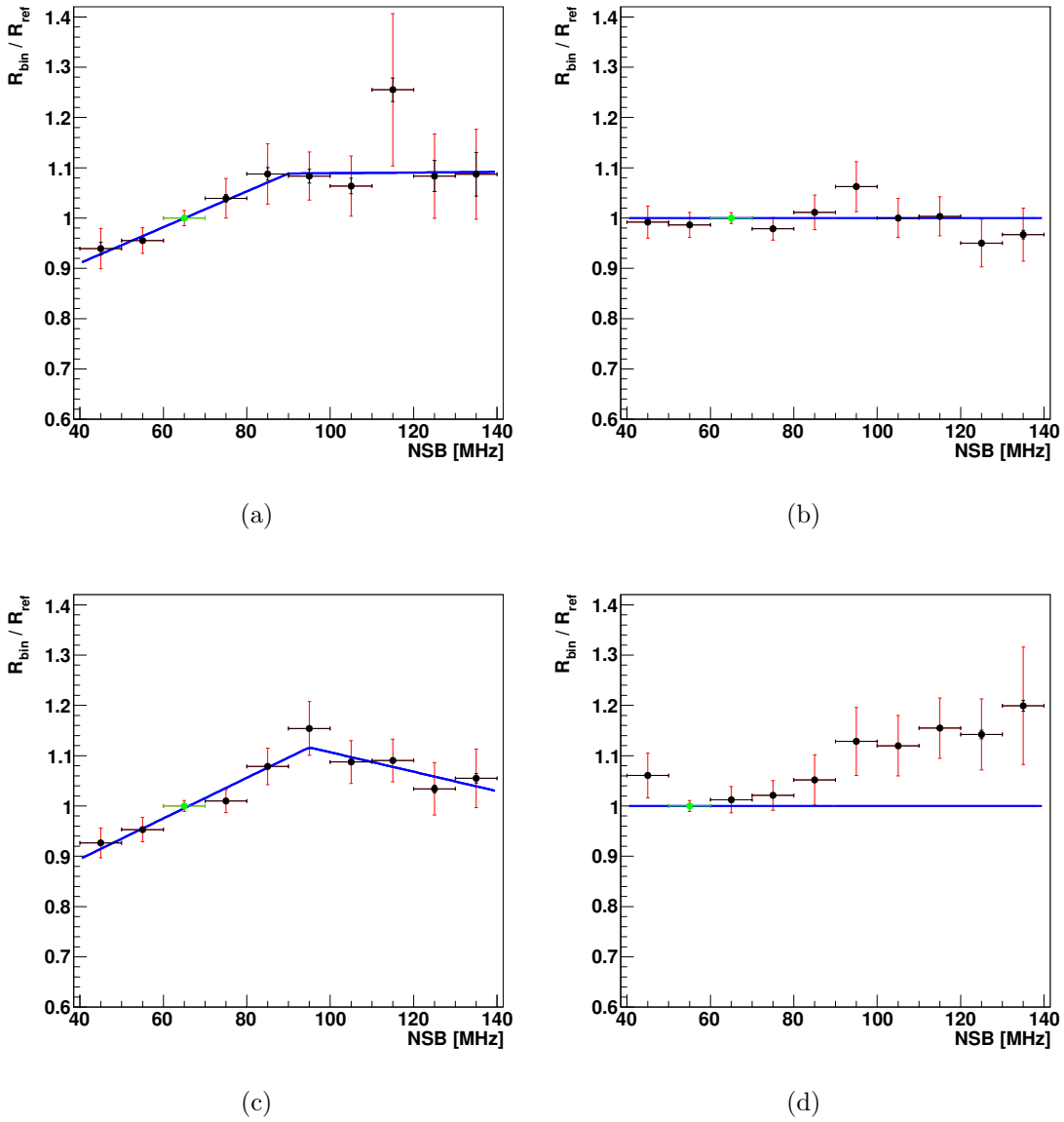

Figure A.4.: In (a) the background rate ratio over the NSB for energies between 0.1 TeV and 10 TeV is shown. The blue line is a fit with the function given in Eq. 3.24. In (b) the corrections for all parameters have been applied and the corrected background rate ratio over the NSB is plotted. The blue line is drawn at a background rate ratio of 1.0. The deviations of the points from this line indicate how well the corrections worked. In (c) all corrections have been applied except the correction for the NSB. The background rate ratio over the NSB shows a similar behaviour as in (a). However, the third point from the right is now not as far away from the other points as before. This can be attributed to the missing uncertainties of the selections. Now only the uncertainties of the corrections enter the plot. The blue line is a fit with the function given in Eq. A.4. In (d) new corrections have been applied on the background rates. However, the deviations from the blue line at 1.0 are larger than in (b). (All plots are obtained with Method B)

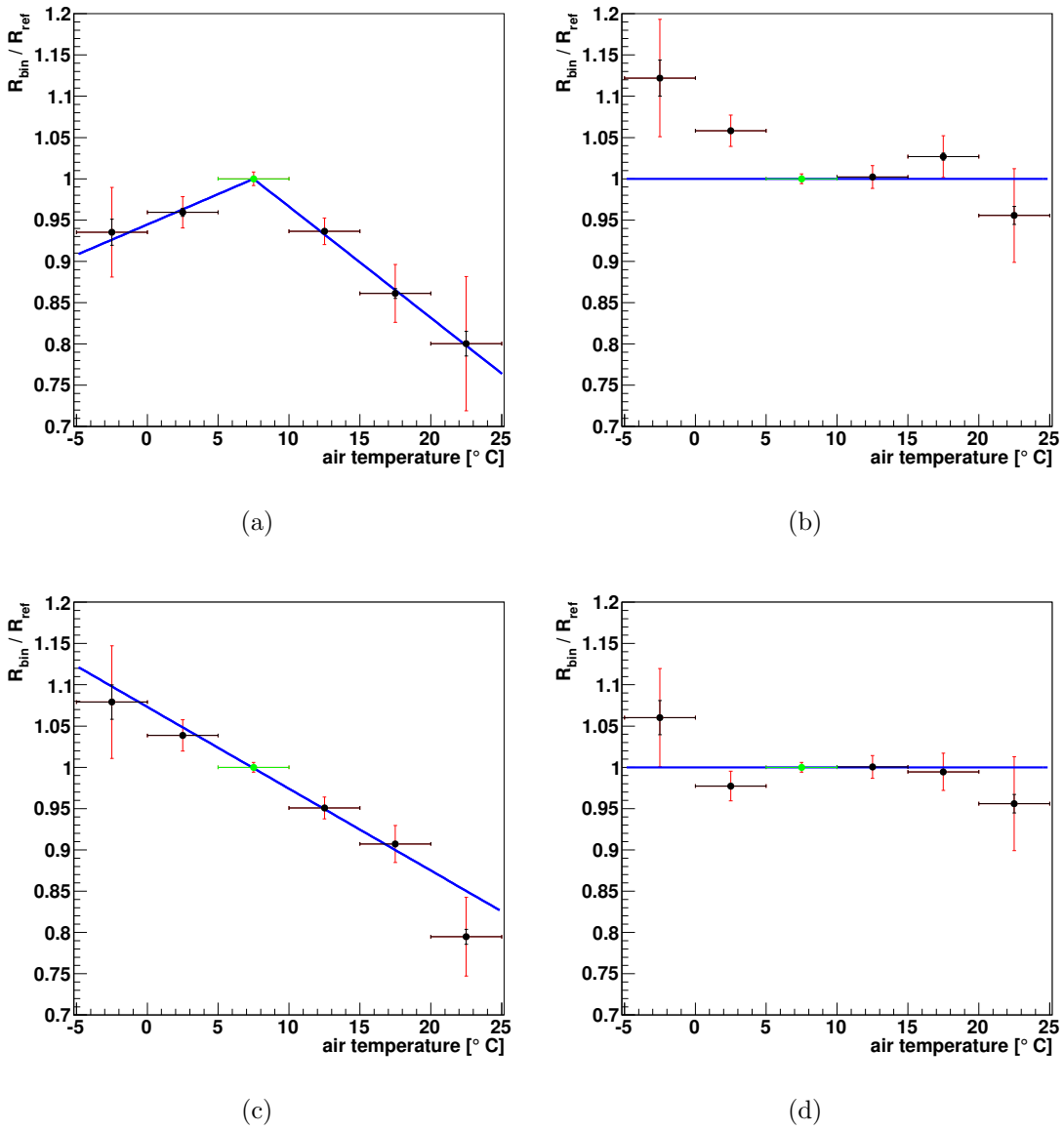

Figure A.5.: In (a) the background rate ratio over the air temperature for energies between 0.1 TeV and 10 TeV. The blue line is a fit with the function given in Eq. 3.28. In (b) the corrections for all parameters have been applied and the corrected background rate ratio over the air temperature is plotted. The blue line is drawn at a background rate ratio of 1.0. The deviations of the points from this line indicate how well the corrections worked. In (c) all corrections have been applied except the correction for the air temperature. The background rate ratio over the air temperature shows a linear dependence here. The blue line is a fit with a linear function. In (d) the new corrections have been applied on the background rates and the deviations from the blue line at 1.0 are smaller than in (b). (All plots are obtained with Method B)

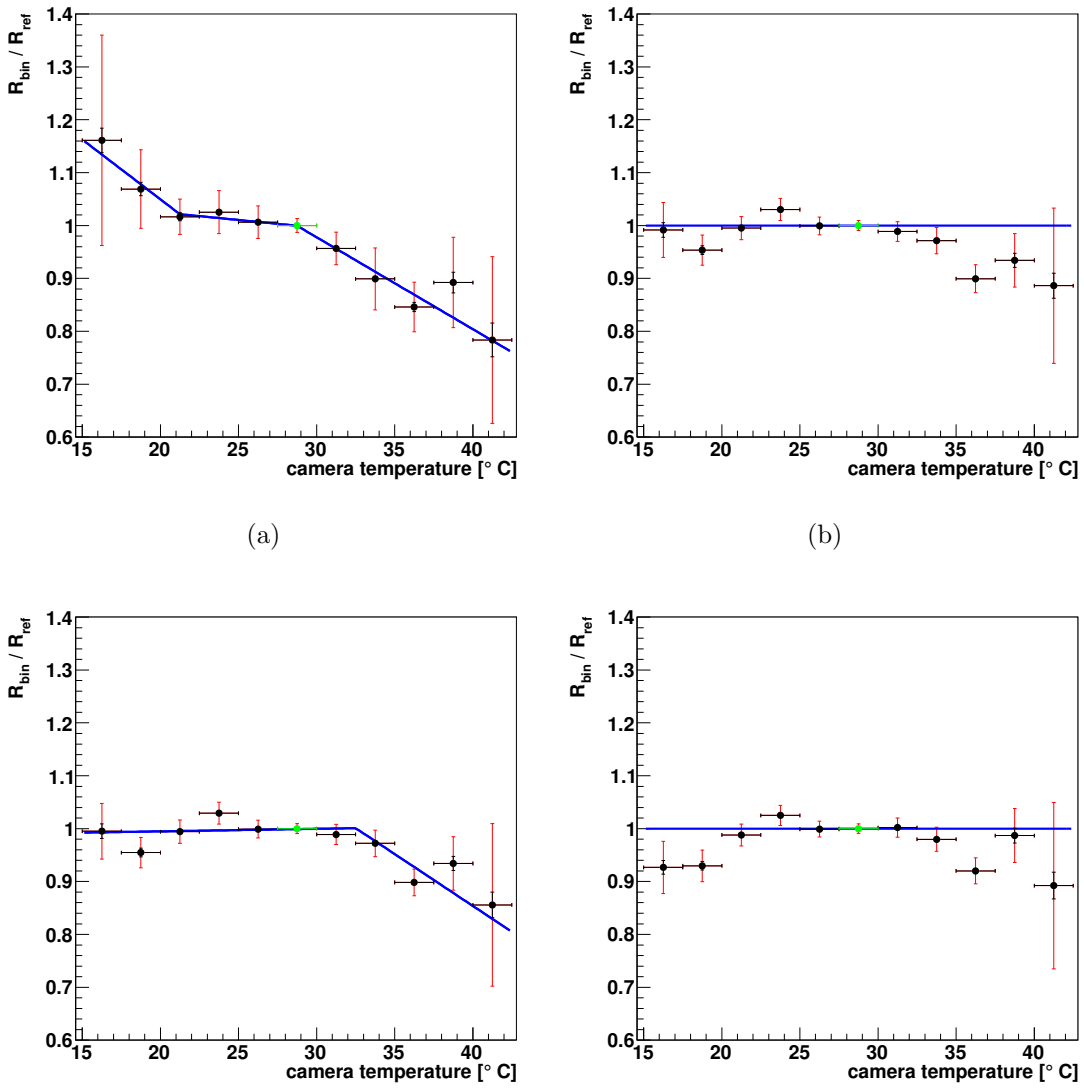

Figure A.6.: In (a) the background rate ratio over the camera temperature for energies between 0.1 TeV and 10 TeV. The blue line is a fit with the function given in Eq. 3.25. In (b) the corrections for all parameters have been applied and the corrected background rate ratio over the camera temperature is plotted. The blue line is drawn at a background rate ratio of 1.0. The deviations of the points from this line indicate how well the corrections worked. In (c) all corrections have been applied except the correction for the camera temperature. The background rate ratio over the camera temperature shows a less strong dependence here. The blue line is a fit with the function given in Eq. A.6. In (d) the new corrections have been applied on the background rates. The deviations from the blue line at 1.0 are about the same as in (b). (All plots are obtained with Method B)

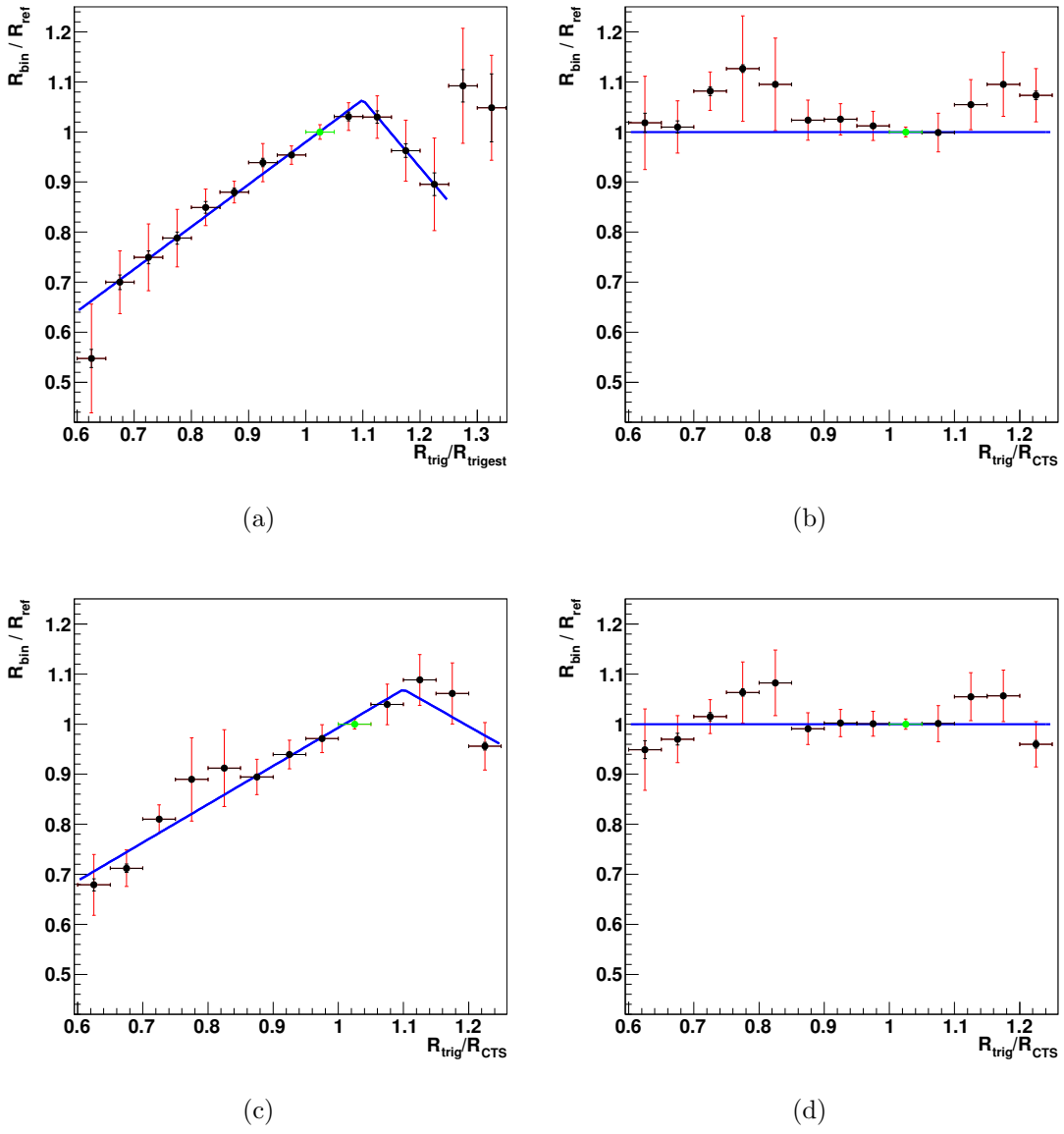

Figure A.7.: In (a) the background rate ratio over the trigger rate ratio for energies between 0.1 TeV and 10 TeV is plotted. The blue line is a fit with the function given in Eq. 3.22. In (b) the corrections for all parameters have been applied and the corrected background rate ratio over the trigger rate ratio is plotted. The blue line is drawn at a background rate ratio of 1.0. The deviations of the points from this line indicate how well the corrections worked. In (c) all corrections have been applied except the correction for the trigger rate ratio. The background rate ratio over the trigger rate ratio shown only minor changes compared to (a). The blue line is a fit with the function given in Eq. A.7. In (d) the new corrections have been applied on the background rates and the deviations from the blue line at 1.0 are on average smaller than in (b). (All plots are obtained with Method B)

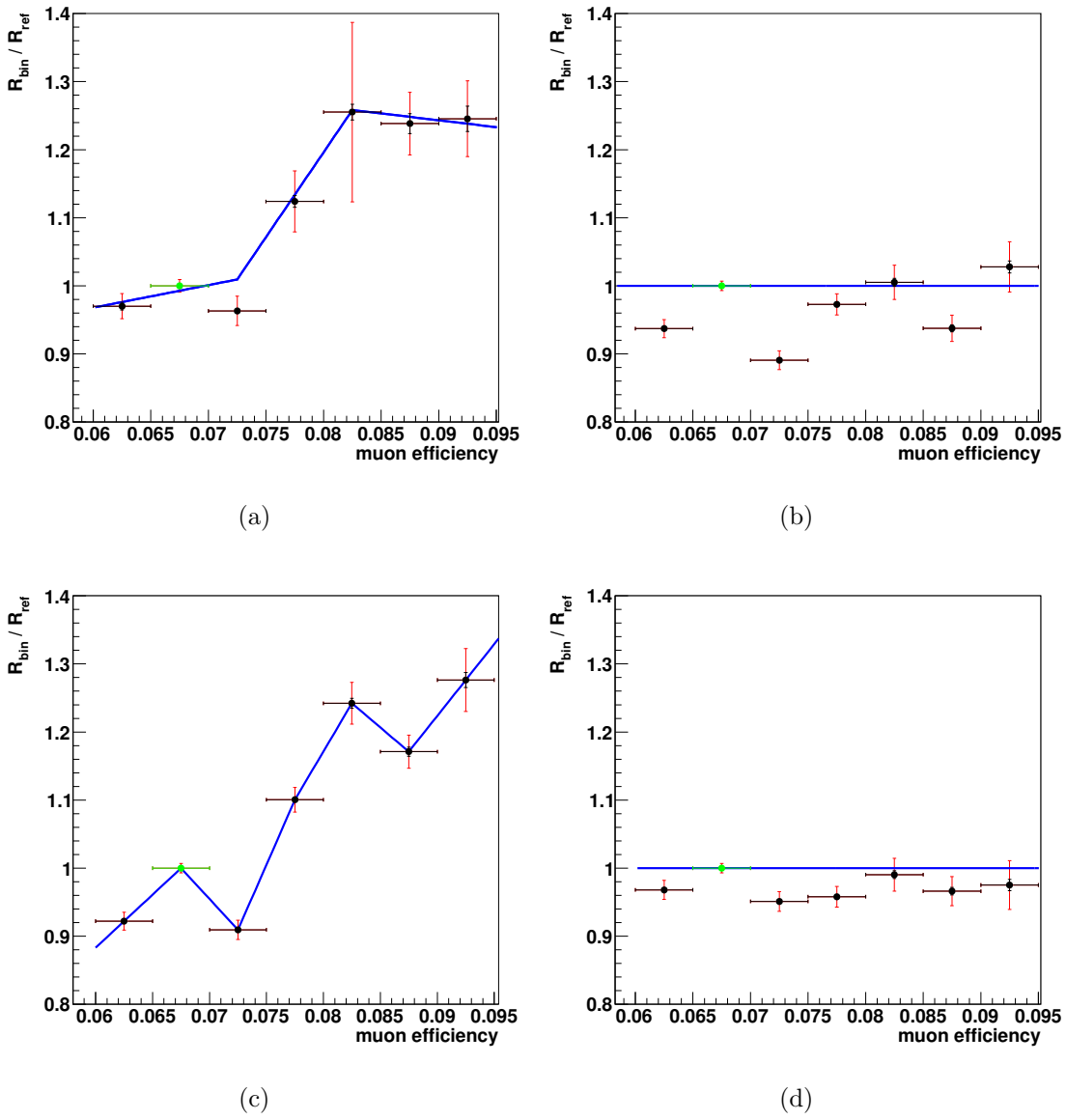

(a) (b)

(c) (d)

Figure A.8.: In (a) the background rate ratio over the muon efficiency for energies between 0.1 TeV and 10 TeV is shown. The blue line is a fit with the function given in Eq. 3.21. In (b) the corrections for all parameters have been applied and the corrected background rate ratio over the muon efficiency is plotted. The blue line is drawn at a background rate ratio of 1.0. The deviations of the points from this line indicate how well the corrections worked. In (c) all corrections have been applied except the correction for the muon efficiency. The background rate ratio over the muon efficiency shows no clear behaviour. Therefore the blue line is simply a linear interpolation between the points. In (d) the new corrections have been applied on the background rates and the deviations from the blue line at 1.0 are smaller than in (b). (All plots are obtained with Method B)

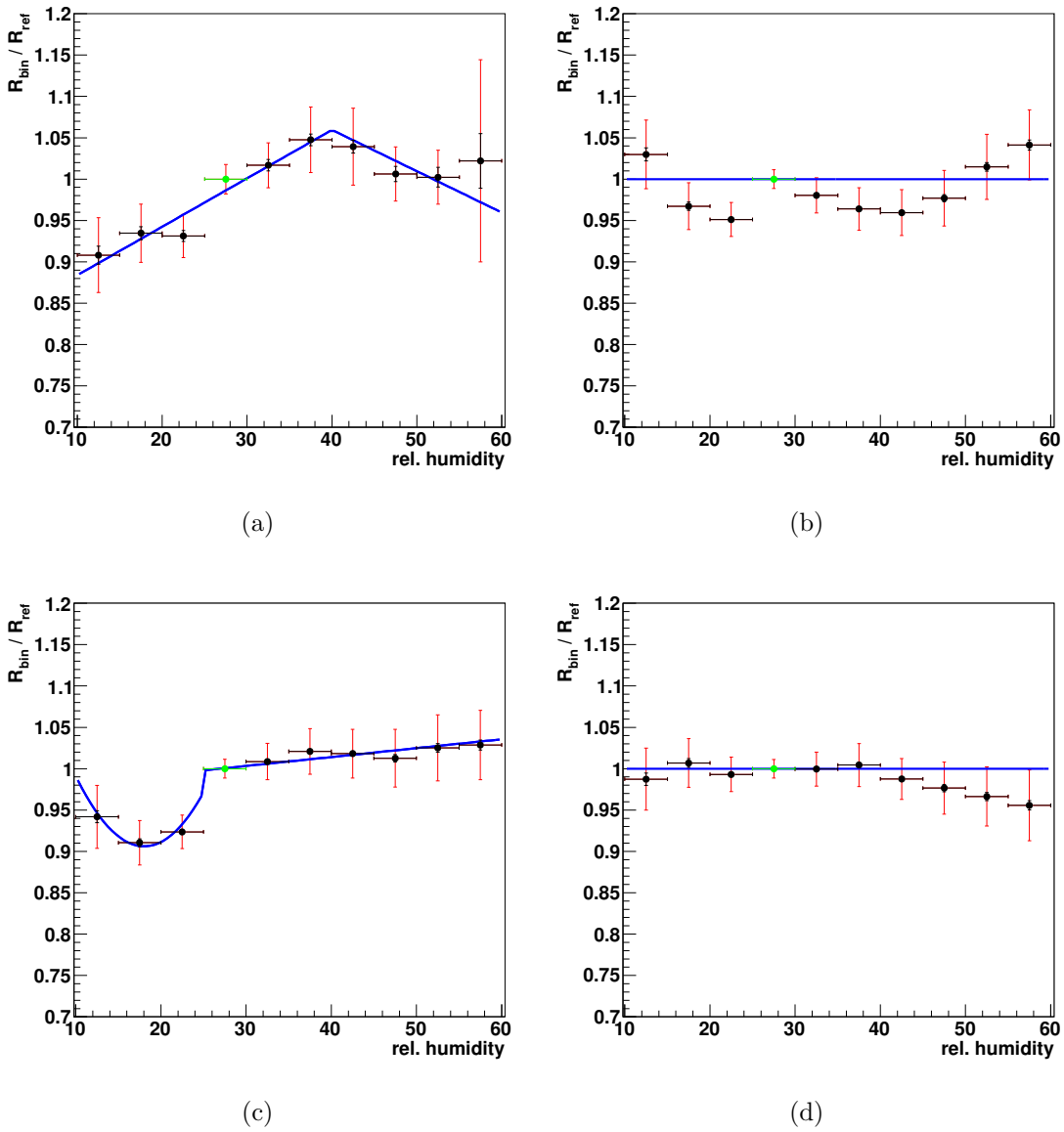

Figure A.9.: In (a) the background rate ratio over the relative humidity for energies between 0.1 TeV and 10 TeV is plotted. The blue line is a fit with the function given in Eq. 3.29. In (b) the corrections for all parameters have been applied and the corrected background rate ratio over the relative humidity is plotted. The blue line is drawn at a background rate ratio of 1.0. The deviations of the points from this line indicate how well the corrections worked. In (c) all corrections have been applied except the correction for the relative humidity. The dependence of the background rate ratio over the relative humidity has changed compared to (a). The blue line is a fit with the function given in Eq. A.8. In (d) the new corrections have been applied on the background rates and the deviations from the blue line at 1.0 are smaller than in (b). (All plots are obtained with Method B)

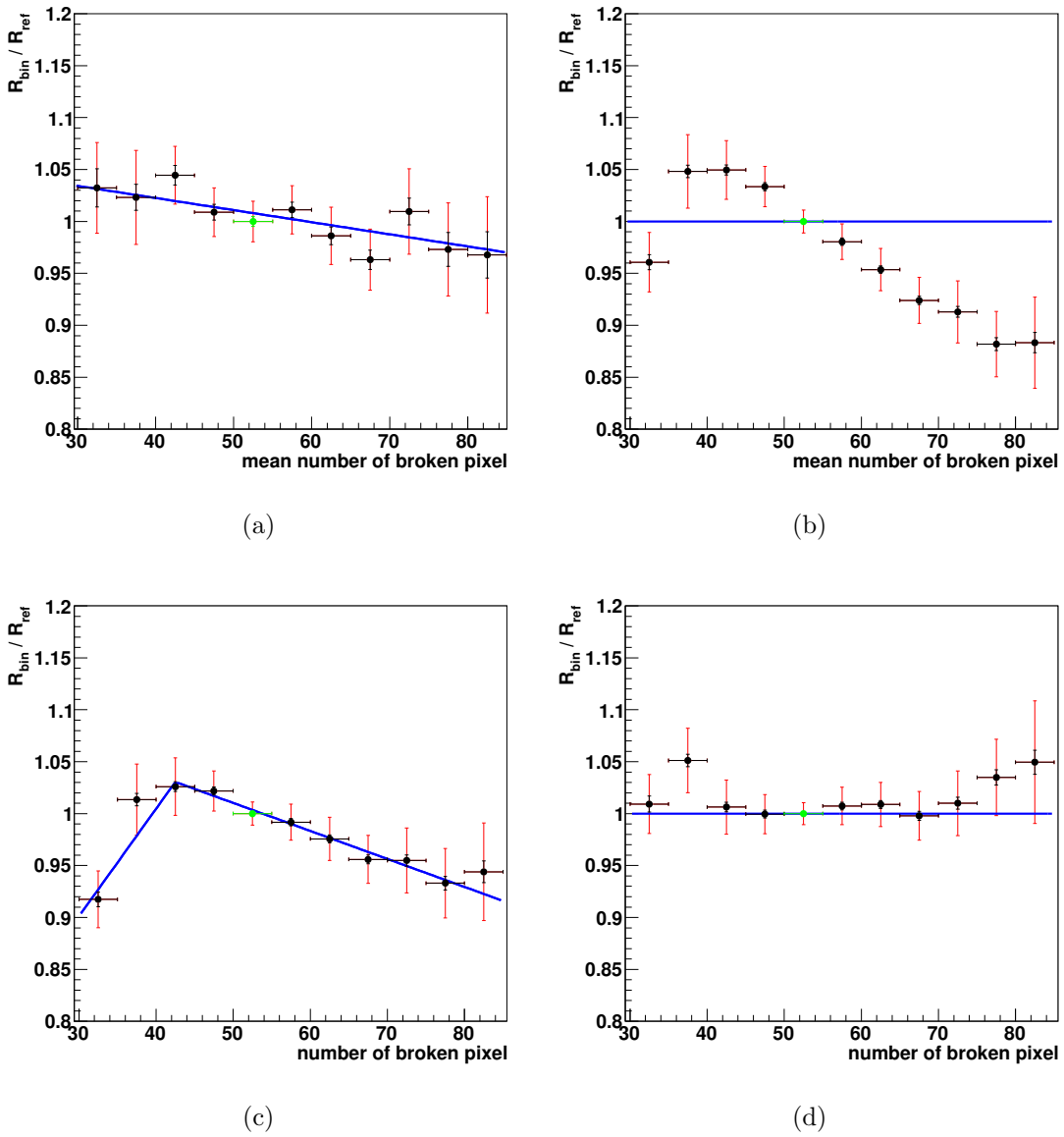

Figure A.10.: In (a) the background rate ratio over the number of broken pixels for energies between 0.1 TeV and 10 TeV is plotted. The blue line is a fit with the function given in Eq. 3.26. In (b) the corrections for all parameters have been applied and the corrected background rate ratio over the number of broken pixels is plotted. The blue line is drawn at a background rate ratio of 1.0. The deviations of the points from this line indicate how well the corrections worked. In (c) all corrections have been applied except the correction for the number of broken pixels. The background rate ratio over the number of broken pixels shows a mostly linear dependence here. The blue line is a fit with the function given in Eq. A.9. In (d) the new corrections have been applied on the background rates and the deviations from the blue line at 1.0 are smaller than in (b). (All plots are obtained with Method B)

A.6. On-Off-Analysis of Background Data Inside and Outside the Galactic Plane

This Section contains a further check of the assumption made in Section 4.2.2 that more emission is found inside the Galactic Plane. The plots in Fig. A.11 show the on-off-analysis with the Correction method for on- and off-runs from inside ($b \leq 2°$) the Galactic Plane, outside ($b \geq 2°$) the Galactic Plane and on-runs inside and off-runs outside the Plane. For the first two cases the mean is not far away from zero, considering the root mean square of the distributions. For the third case, however, a shift to a mean value of about 11σ is found. This strongly indicates a higher emission from inside the Galactic Plane.

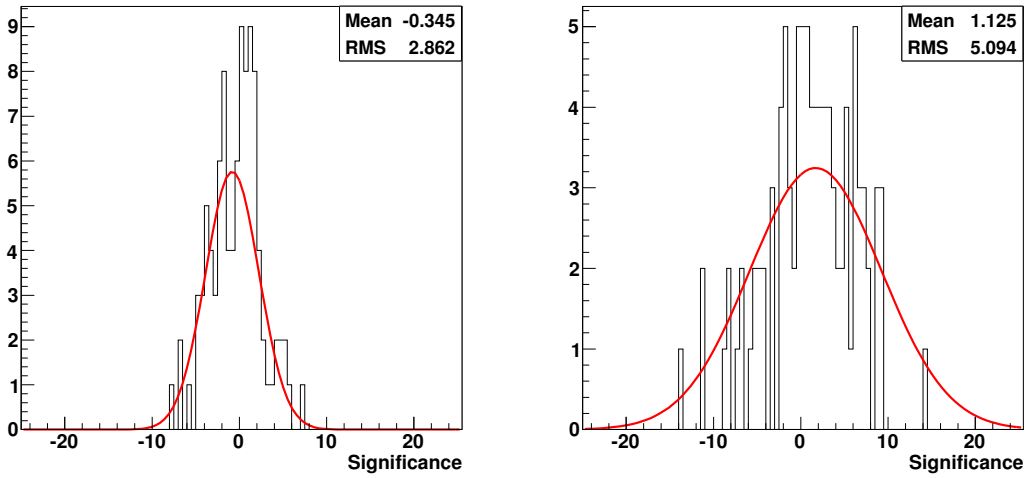

(a) (b)

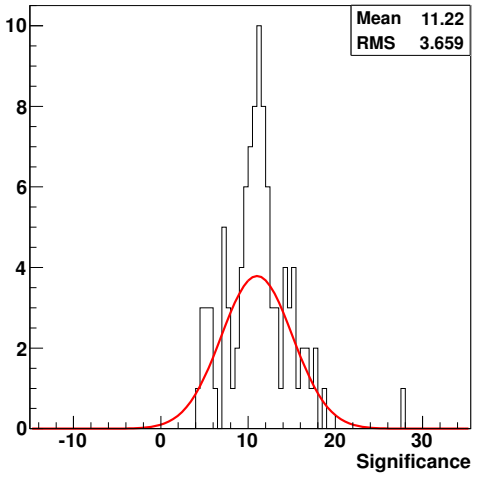

(c)

Figure A.11.: On-Off Analyses of background runs (runs more than 8° away from the Galactic Centre). (a) Distribution of the significances of 100 analyses where the on-regions and the off-regions are both inside ($b \leq 2°$) the Galactic Plane. (b) Distribution of the significances of 100 analyses where the on-regions and the off-regions are both outside ($b \geq 4°$) the Galactic Plane. (c) Distribution of the significances of 100 analyses where the on-regions are inside ($b \leq 2°$) and the off-regions are outside ($b \geq 4°$) the Galactic Plane.

Bibliography

Aalseth, C. E., Barbeau, P. S., Bowden, N. S., et al. (2011). Results from a Search for Light-Mass Dark Matter with a p-Type Point Contact Germanium Detector. *Physical Review Letters*, 106(13):131301.

Aalseth, C. E., Barbeau, P. S., Colaresi, J., et al. (2012). CoGeNT: A Search for Low-Mass Dark Matter using p-type Point Contact Germanium Detectors. *ArXiv e-prints*. arXiv:astro-ph/1208.5737.

Abdo, A. A., Ackermann, M., Ajello, M., et al. (2009). Measurement of the Cosmic Ray e^++e^- Spectrum from 20GeV to 1TeV with the Fermi Large Area Telescope. *Physical Review Letters*, 102(18):181101.

Abramowski, A., Acero, F., Aharonian, F., et al. (2012a). Probing the extent of the non-thermal emission from the Vela X region at TeV energies with H.E.S.S. *Astronomy and Astrophysics*, 548:A38.

Abramowski, A., Acero, F., Aharonian, F., et al. (2011a). H.E.S.S. Observations of the Globular Clusters NGC 6388 and M15 and Search for a Dark Matter Signal. *Astrophysical Journal*, 735:12.

Abramowski, A., Acero, F., Aharonian, F., et al. (2012b). Search for Dark Matter Annihilation Signals from the Fornax Galaxy Cluster with H.E.S.S. *Astrophysical Journal*, 750:123.

Abramowski, A., Acero, F., Aharonian, F., et al. (2011b). Search for a Dark Matter Annihilation Signal from the Galactic Center Halo with H.E.S.S. *Physical Review Letters*, 106(16):161301.

Acero, F., Aharonian, F., Akhperjanian, A. G., et al. (2010). Localizing the VHE γ-ray source at the Galactic Centre. *Monthly Notices of the RAS*, 402:1877–1882.

Adriani, O., Barbarino, G. C., Bazilevskaya, G. A., et al. (2009). An anomalous positron abundance in cosmic rays with energies 1.5-100GeV. *Nature*, 458:607–609.

Aguilar, M., Alberti, G., Alpat, B., et al. (2013). First result from the alpha magnetic spectrometer on the international space station: Precision measurement of the positron fraction in primary cosmic rays of 0.5˘350 gev. *Phys. Rev. Lett.*, 110:141102.

Aharonian, F., Akhperjanian, A. G., Anton, G., et al. (2009a). Probing the ATIC peak in the cosmic-ray electron spectrum with H.E.S.S. *Astronomy and Astrophysics*, 508:561–564.

Aharonian, F., Akhperjanian, A. G., Anton, G., et al. (2009b). Spectrum and variability of the Galactic center VHE γ-ray source HESS J1745-290. *Astronomy and Astrophysics*, 503:817–825.

Aharonian, F., Akhperjanian, A. G., Aye, K.-M., et al. (2005). Very high energy gamma rays from the composite SNR G 0.9+0.1. *Astronomy and Astrophysics*, 432:L25–L29.

Aharonian, F., Akhperjanian, A. G., Aye, K.-M., et al. (2004a). Very high energy gamma rays from the direction of Sagittarius A*. *Astronomy and Astrophysics*, 425:L13–L17.

Aharonian, F., Akhperjanian, A. G., Aye, K.-M., et al. (2004b). Calibration of cameras of the H.E.S.S. detector. *Astroparticle Physics*, 22:109–125.

Aharonian, F., Akhperjanian, A. G., Bazer-Bachi, A. R., et al. (2006a). HESS Observations of the Galactic Center Region and Their Possible Dark Matter Interpretation. *Physical Review Letters*, 97(22):221102.

Aharonian, F., Akhperjanian, A. G., Bazer-Bachi, A. R., et al. (2006b). Observations of the Crab nebula with HESS. *Astronomy and Astrophysics*, 457:899–915.

Aharonian, F., Akhperjanian, A. G., Bazer-Bachi, A. R., et al. (2006c). Discovery of very-high-energy γ-rays from the Galactic Centre ridge. *Nature*, 439:695–698.

Aharonian, F., Akhperjanian, A. G., Bazer-Bachi, A. R., et al. (2008). Observations of the Sagittarius dwarf galaxy by the HESS experiment and search for a dark matter signal. *Astroparticle Physics*, 29:55–62.

Aharonian, F., Akhperjanian, A. G., Bazer-Bachi, A. R., et al. (2010). Erratum to "Observations of the Sagittarius dwarf galaxy by the HESS experiment and search for a dark matter signal" [Astropart. Phys. 29(1) (2008) 55-62]. *Astroparticle Physics*, 33:274–275.

Aharonian, F., Akhperjanian, A. G., de Almeida, U. B., et al. (2009c). A Search for a Dark Matter Annihilation Signal Toward the Canis Major Overdensity with H.E.S.S. *Astrophysical Journal*, 691:175–181.

Akerlof, C. W., Cawley, M. F., Chantell, M., et al. (1991). Locating very high energy gamma-ray sources with arcminute accuracy. *Astrophysical Journal, Letters*, 377:L97–L100.

Alcock, C., Allsman, R. A., Alves, D. R., et al. (2000). The MACHO Project: Microlensing Results from 5.7 Years of Large Magellanic Cloud Observations. *Astrophysical Journal*, 542:281–307.

Alpher, R. A. (1948). A Neutron-Capture Theory of the Formation and Relative Abundance of the Elements. *Physical Review*, 74:1577–1589.

Alpher, R. A., Bethe, H., and Gamow, G. (1948). The Origin of Chemical Elements. *Physical Review*, 73:803–804.

Alpher, R. A. and Herman, R. C. (1949). Remarks on the Evolution of the Expanding Universe. *Physical Review*, 75:1089–1095.

ANTARES (2013). `http://antares.in2p3.fr/`. visited in January 2013.

Aprile, E., Arisaka, K., Arneodo, F., et al. (2011). Dark Matter Results from 100 Live Days of XENON100 Data. *Physical Review Letters*, 107(13):131302.

Arbey, A., Battaglia, M., Djouadi, A., Mahmoudi, F., and Quevillon, J. (2012). Implications of a 125 GeV Higgs for supersymmetric models. *Physics Letters B*, 708:162–169.

ATLAS Collaboration Aad, G., Abajyan, T., Abbott, B., et al. (2012). Observation of a new particle in the search for the Standard Model Higgs boson with the ATLAS detector at the LHC. *Physics Letters B*, 716:1–29.

Atwood, W. B., Abdo, A. A., Ackermann, M., et al. (2009). The Large Area Telescope on the Fermi Gamma-Ray Space Telescope Mission. *Astrophysical Journal*, 697:1071–1102.

Aye, K.-M., Brown, A. M., Chadwick, P. M., et al. (2005). Atmospheric sensing for the H.E.S.S. array. In Aharonian, F. A., Völk, H. J., and Horns, D., editors, *High Energy Gamma-Ray Astronomy*, volume 745 of *American Institute of Physics Conference Series*, pages 724–729.

Balick, B. and Brown, R. L. (1974). Intense sub-arcsecond structure in the galactic center. *Astrophysical Journal*, 194:265–270.

Bennett, C. L., Larson, D., Weiland, J. L., et al. (2012). Nine-Year Wilkinson Microwave Anisotropy Probe (WMAP) Observations: Final Maps and Results. *ArXiv e-prints*. arXiv:astro-ph/1212.5225.

Berge, D., Funk, S., and Hinton, J. (2007). Background modelling in very-high-energy γ-ray astronomy. *Astronomy and Astrophysics*, 466:1219–1229.

Bergström, L., Bringmann, T., and Edsjö, J. (2008). New positron spectral features from supersymmetric dark matter: A way to explain the PAMELA data? *Physical Review D*, 78(10):103520.

Bergström, L., Ullio, P., and Buckley, J. H. (1998). Observability of gamma rays from dark matter neutralino annihilations in the Milky Way halo. *Astroparticle Physics*, 9:137–162.

Beringer, J., Arguin, J.-F., Barnett, R. M., et al. (2012a). Review of Particle Physics. *Physical Review D*, 86(1):275–279.

Beringer, J., Arguin, J.-F., Barnett, R. M., et al. (2012b). Review of Particle Physics. *Physical Review D*, 86(1):177–198.

Beringer, J., Arguin, J.-F., Barnett, R. M., et al. (2012c). Review of Particle Physics. *Physical Review D*, 86(1):1437–1447.

Bernabei, R., Belli, P., Cappella, F., et al. (2010). New results from DAMA/LIBRA. *European Physical Journal C*, 67:39–49.

Bernlöhr, K. (2000). Impact of atmospheric parameters on the atmospheric Cherenkov technique. *Astroparticle Physics*, 12:255–268.

Bernlöhr, K. (2005). Geomagnetic effects on showers relevant for the H.E.S.S. experiment - a study with simulated showers. Internal Note.

Bernlöhr, K., Carrol, O., Cornils, R., et al. (2003). The optical system of the H.E.S.S. imaging atmospheric Cherenkov telescopes. Part I: layout and components of the system. *Astroparticle Physics*, 20:111–128.

Bethe, H. and Heitler, W. (1934). On the Stopping of Fast Particles and on the Creation of Positive Electrons. *Royal Society of London Proceedings Series A*, 146:83–112.

Bolz, O. (2004). *Absolute Energiekalibration der abbildenden Cherenkov-Teleskope des H.E.S.S. Experiments und Ergebnisse erster Beobachtungen des Supernova-Überrests RX J1713.7-3946*. PhD thesis, Ruprecht-Karls Universität Heidelberg.

Borgmeier, C., Komin, N., de Naurois, M., et al. (2003). The Central Data Acquisition System of the H.E.S.S. Telescope System. In *International Cosmic Ray Conference*, volume 5 of *International Cosmic Ray Conference*, page 2891.

Bringmann, T., Bergström, L., and Edsjö, J. (2008). New gamma-ray contributions to supersymmetric dark matter annihilation. *Journal of High Energy Physics*, 1:49.

Bringmann, T. and Weniger, C. (2012). Gamma ray signals from dark matter: Concepts, status and prospects. *Physics of the Dark Universe*, 1:194–217.

Catena, R. and Ullio, P. (2010). A novel determination of the local dark matter density. *Journal of Cosmology and Astroparticle Physics*, 8:4.

CDMS (2013). `http://cdms.berkeley.edu/`. visited in January 2013.

Chang, J., Adams, J. H., Ahn, H. S., et al. (2008). An excess of cosmic ray electrons at energies of 300-800GeV. *Nature*, 456:362–365.

Charbonnier, A. (2009). private communication.

Charbonnier, A. (2011). *De la recherche de matière noire à l'émission diffuse de rayons gamma dans l'expérience H.E.S.S.* Phd thesis, Laboratoire e Physique Nucléaire et de Hautes Energies.

Clowe, D., Bradač, M., Gonzalez, A. H., et al. (2006). A Direct Empirical Proof of the Existence of Dark Matter. *Astrophysical Journal, Letters*, 648:L109–L113.

COGENT (2013). `http://cogent.pnnl.gov/`. visited in January 2013.

Colless, M., Dalton, G., Maddox, S., et al. (2001). The 2dF Galaxy Redshift Survey: spectra and redshifts. *Monthly Notices of the RAS*, 328:1039–1063.

Cornils, R., Gillessen, S., Jung, I., et al. (2003). The optical system of the H.E.S.S. imaging atmospheric Cherenkov telescopes. Part II: mirror alignment and point spread function. *Astroparticle Physics*, 20:129–143.

DAMA (2013). `http://people.roma2.infn.it/~dama/web/home.html`. visited in January 2013.

Daniels, M. (2012). private communication.

Daum, A., Hermann, G., Hess, M., et al. (1997). First results on the performance of the HEGRA IACT array. *Astroparticle Physics*, 8:1–11.

Davies, J. M. and Cotton, E. S. (1957). Design of the quartermaster solar furnace. *J. Solar. Energy Sci. Eng.*, 1:16–21.

de Naurois, M. (2012). *L'astronomie γ de très haute energie. Ouverture d'une nouvelle fe$\widehat{e}$ntre astronomique sur l'Univers non thermique.* Habilitation, ILaboratoire Leprince-Ringuet, Ecole polytechnique.

de Naurois, M. and Rolland, L. (2009). A high performance likelihood reconstruction of γ-rays for imaging atmospheric Cherenkov telescopes. *Astroparticle Physics*, 32:231–252.

Diemand, J., Kuhlen, M., Madau, P., et al. (2008). Clumps and streams in the local dark matter distribution. *Nature*, 454:735–738.

Doro, M., Conrad, J., Emmanoulopoulos, D., et al. (2013). Dark matter and fundamental physics with the Cherenkov Telescope Array. *Astroparticle Physics*, 43:189–214.

Dyson, F. W., Eddington, A. S., and Davidson, C. (1920). A Determination of the Deflection of Light by the Sun's Gravitational Field, from Observations Made at the Total Eclipse of May 29, 1919. *Royal Society of London Philosophical Transactions Series A*, 220:291–333.

EDELWEISS (2013). `http://edelweiss.in2p3.fr/`. visited in January 2013.

Einasto, J. (1965). On the Construction of a Composite Model for the Galaxy and on the Determination of the System of Galactic Parameters. *Trudy Astrofizicheskogo Instituta Alma-Ata*, 5:87–100.

Einstein, A. (1916). Die Grundlage der allgemeinen Relativitätstheorie. *Annalen der Physik*, 354:769–822.

Eisenstein, D. J., Zehavi, I., Hogg, D. W., et al. (2005). Detection of the Baryon Acoustic Peak in the Large-Scale Correlation Function of SDSS Luminous Red Galaxies. *Astrophysical Journal*, 633:560–574.

Feldman, G. J. and Cousins, R. D. (1998). Unified approach to the classical statistical analysis of small signals. *Physical Review D*, 57:3873–3889.

Friedman, A. (1922). Über die Krümmung des Raumes. *Zeitschrift fur Physik*, 10:377–386.

Friedmann, A. (1924). Über die Möglichkeit einer Welt mit konstanter negativer Krümmung des Raumes. *Zeitschrift fur Physik*, 21:326–332.

Funk, S. (2005). *A new population of very high-energy γ-ray sources detected with H.E.S.S. in the inner part of the Milky Way.* Phd thesis, Ruberto-Carola University of Heidelberg.

Funk, S., Hermann, G., Hinton, J., et al. (2004). The trigger system of the H.E.S.S. telescope array. *Astroparticle Physics*, 22:285–296.

Gamow, G. (1946). Expanding Universe and the Origin of Elements. *Physical Review*, 70:572–573.

Glück, B. (2011). *A Detailed Study of the Pulsar Wind Nebula HESS J0835-455 (Vela X) in TeV Gamma-Rays.* PhD thesis, Friedrich-Alexander Universität Erlangen Nürnberg.

Goldwurm, A. (2008). A Multiwavelength View of High-Energy Processes in the Galactic Center Region. In Aharonian, F. A., Hofmann, W., and Rieger, F., editors, *American Institute of Physics Conference Series*, volume 1085 of *American Institute of Physics Conference Series*, pages 135–145.

Gondolo, P., Edsjö, J., Ullio, P., et al. (2004). DarkSUSY: computing supersymmetric dark matter properties numerically. *Journal of Cosmology and Astroparticle Physics*, 7:8.

HEGRA Collaboration, Konopelko, A., Hemberger, M., et al. (1999). Performance of the stereoscopic system of the HEGRA imaging air Čerenkov telescopes: Monte Carlo simulations and observations. *Astroparticle Physics*, 10:275–289.

Hess, V. (1912). Über Beobachtungen der durchdringenden Strahlung bei sieben Freiballonfahrten. *Physikalischen Zeitschrift*, 13:1084.

H.E.S.S. Collaboration, Abramowski, A., Acero, F., et al. (2013). Search for photon line-like signatures from Dark Matter annihilations with H.E.S.S. *ArXiv e-prints*. arXiv:astro-ph/1301.1173.

H.E.S.S. Collaboration, Abramowski, A., Acero, F., et al. (2011). H.E.S.S. constraints on dark matter annihilations towards the sculptor and carina dwarf galaxies. *Astroparticle Physics*, 34:608–616.

Hillas, A. M. (1982). Angular and energy distributions of charged particles in electron-photon cascades in air. *Journal of Physics G Nuclear Physics*, 8:1461–1473.

Hillas, A. M. (1985). Cerenkov light images of EAS produced by primary gamma. In Jones, F. C., editor, *International Cosmic Ray Conference*, volume 3 of *International Cosmic Ray Conference*, pages 445–448.

Hinshaw, G., Larson, D., Komatsu, E., et al. (2012). Nine-Year Wilkinson Microwave Anisotropy Probe (WMAP) Observations: Cosmological Parameter Results. *ArXiv e-prints*. arXiv:astro-ph/1212.5226.

Hinton, J. A. (2004). The status of the HESS project. *New Astronomy Review*, 48:331–337.

Hofmann, W., Jung, I., Konopelko, A., et al. (1999). Comparison of techniques to reconstruct VHE gamma-ray showers from multiple stereoscopic Cherenkov images. *Astroparticle Physics*, 12:135–143.

Hubble, E. (1929). A Relation between Distance and Radial Velocity among Extra-Galactic Nebulae. *Proceedings of the National Academy of Science*, 15:168–173.

ICECUBE (2013). `http://icecube.wisc.edu/`. visited in January 2013.

Kaluza, T. (1921). Zum Unitätsproblem der Physik. *Sitzungsberichte der Königlich Preußischen Akademie der Wissenschaften (Berlin), Seite p. 966-972*, pages 966–972.

Kassim, N. E., Larosa, T. N., Lazio, T. J. W., and Hyman, S. D. (1999). Wide Field Radio Imaging of the Galactic Center. In Falcke, H., Cotera, A., Duschl, W. J., Melia, F., and Rieke, M. J., editors, *The Central Parsecs of the Galaxy*, volume 186 of *Astronomical Society of the Pacific Conference Series*, page 403.

Kertzman, M. P. and Sembroski, G. H. (1994). Computer simulation methods for investigating the detection characteristics of TeV air Cherenkov telescopes. *Nuclear Instruments and Methods in Physics Research A*, 343:629–643.

Klein, O. (1926). Quantentheorie und fünfdimensionale Relativitätstheorie. *Zeitschrift fur Physik*, 37:895–906.

Knapp, J. and Heck, D. (1998). Extensive air shower simulations with the CORSIKA code. *Nachr. Forschungszent. Karlsr., Vol. 30, No. 1, p. 27 - 37*, 30:27–37.

Kosack, K., Badran, H. M., Bond, I. H., et al. (2004). TeV Gamma-Ray Observations of the Galactic Center. *Astrophysical Journal, Letters*, 608:L97–L100.

Kowalski, M., Rubin, D., Aldering, G., et al. (2008). Improved Cosmological Constraints from New, Old, and Combined Supernova Data Sets. *Astrophysical Journal*, 686:749–778.

Langacker, P. (2003). Structure of the Standard Model. *ArXiv High Energy Physics - Phenomenology e-prints*. arXiv:hep-ph/0304186.

Le Bohec, S., Degrange, B., Punch, M., et al. (1998). A new analysis method for very high definition imaging atmospheric Cherenkov telescopes as applied to the CAT telescope. *Nuclear Instruments and Methods in Physics Research A*, 416:425–437.

Lemaître, G. (1931). Expansion of the universe, A homogeneous universe of constant mass and increasing radius accounting for the radial velocity of extra-galactic nebulae. *Monthly Notices of the RAS*, 91:483–490.

Levenberg,K (1944). *The Quarterly of Applied Mathematics* **2**, pages 164–168.

Li, T.-P. and Ma, Y.-Q. (1983). Analysis methods for results in gamma-ray astronomy. *Astrophysical Journal*, 272:317–324.

Linde, A. (2008). Inflationary Cosmology. In Lemoine, M., Martin, J., and Peter, P., editors, *Inflationary Cosmology*, volume 738 of *Lecture Notes in Physics, Berlin Springer Verlag*, page 1.

Markevitch, M. (2006). Chandra Observation of the Most Interesting Cluster in the Universe. In Wilson, A., editor, *The X-ray Universe 2005*, volume 604 of *ESA Special Publication*, page 723.

Marquardt, D. (1963). *SIAM Journal on Applied Mathematics* **11**, pages 431–441.

Martin, S. P. (1998). A Supersymmetry Primer. In Kane, G. L., editor, *Perspectives on Supersymmetry*, page 1. arXiv:hep-ph/9709356.

Milgrom, M. (1983). A modification of the Newtonian dynamics as a possible alternative to the hidden mass hypothesis. *Astrophysical Journal*, 270:365–370.

Moore, B., Governato, F., Quinn, T., Stadel, J., and Lake, G. (1998). Resolving the Structure of Cold Dark Matter Halos. *Astrophysical Journal, Letters*, 499:L5.

Narayan, R. and Bartelmann, M. (1996). Lectures on Gravitational Lensing. *ArXiv Astrophysics e-prints*. arXiv:astro-ph/9606001.

Navarro, J. F., Frenk, C. S., and White, S. D. M. (1996). The Structure of Cold Dark Matter Halos. *Astrophysical Journal*, 462:563.

Nekrassov, D. (2010). *A Detailed Study of the H.E.S.S. data from the Galactic Center region*. PhD thesis, Ruberto-Carola University of Heidelberg.

Newton, Isaac, S. (1687). Philosophiae naturalis principia mathematica.

Nishino, H., Clark, S., Abe, K., et al. (2009). Search for Proton Decay via $p \rightarrow e^+\pi^0$ and $p \rightarrow \mu^+\pi^0$ in a Large Water Cherenkov Detector. *Physical Review Letters*, 102(14):141801.

Nolan, S. J., Pühlhofer, G., and Rulten, C. B. (2010). Detailed studies of atmospheric calibration in imaging Cherenkov astronomy. *Astroparticle Physics*, 34:304–313.

Oort, J. H. (1932). The force exerted by the stellar system in the direction perpendicular to the galactic plane and some related problems. *Bulletin Astronomical Institute of the Netherlands*, 6:249.

Peccei, R. D. and Quinn, H. R. (1977). CP conservation in the presence of pseudoparticles. *Physical Review Letters*, 38:1440–1443.

Penzias, A. A. and Wilson, R. W. (1965). A Measurement of Excess Antenna Temperature at 4080 Mc/s. *Astrophysical Journal*, 142:419–421.

Percival, W. J., Reid, B. A., Eisenstein, D. J., et al. (2010). Baryon acoustic oscillations in the Sloan Digital Sky Survey Data Release 7 galaxy sample. *Monthly Notices of the RAS*, 401:2148–2168.

Perlmutter, S., Aldering, G., Goldhaber, G., et al. (1999). Measurements of Omega and Lambda from 42 High-Redshift Supernovae. *Astrophysical Journal*, 517:565–586.

Pieri, L., Lavalle, J., Bertone, G., and Branchini, E. (2011). Implications of high-resolution simulations on indirect dark matter searches. *Physical Review D*, 83(2):023518.

Planck Collaboration, Ade, P. A. R., Aghanim, N., et al. (2013). Planck 2013 results. I. Overview of products and scientific results. *ArXiv e-prints*. arXiv:astro-ph/1303.5062.

Puppi, G., Bridge, H., and Greisen, K. (1956). *Progress in Cosmic Ray Physics. Vol. 3. Edited by J. G. Wilson, Contributors: K. Greisen, H. S. Bridge, R. W. Thompson, G. Puppi*. North-Holland publishing Co.

Robertson, H. P. (1935). Kinematics and World-Structure. *Astrophysical Journal*, 82:284.

Robertson, H. P. (1936a). Kinematics and World-Structure II. *Astrophysical Journal*, 83:187.

Robertson, H. P. (1936b). Kinematics and World-Structure III. *Astrophysical Journal*, 83:257.

Rolke, W. A., López, A. M., and Conrad, J. (2005). Limits and confidence intervals in the presence of nuisance parameters. *Nuclear Instruments and Methods in Physics Research A*, 551:493–503.

Rowell, G. P. (2003). A new template background estimate for source searching in TeV gamma -ray astronomy. *Astronomy and Astrophysics*, 410:389–396.

Rubin, V. C. and Ford, Jr., W. K. (1970). Rotation of the Andromeda Nebula from a Spectroscopic Survey of Emission Regions. *Astrophysical Journal*, 159:379.

Rubin, V. C., Ford, W. K. J., and . Thonnard, N. (1980). Rotational properties of 21 SC galaxies with a large range of luminosities and radii, from NGC 4605 R = 4kpc to UGC 2885 R = 122 kpc. *Astrophysical Journal*, 238:471–487.

Schneider, P. (1996). Detection of (dark) matter concentrations via weak gravitational lensing. *Monthly Notices of the RAS*, 283:837–853.

Schramm, D. N. and Turner, M. S. (1998). Big-bang nucleosynthesis enters the precision era. *Reviews of Modern Physics*, 70:303–318.

Smoot, G. F., Bennett, C. L., Kogut, A., et al. (1992). Structure in the COBE differential microwave radiometer first-year maps. *Astrophysical Journal, Letters*, 396:L1–L5.

Springel, V., Frenk, C. S., and White, S. D. M. (2006). The large-scale structure of the Universe. *Nature*, 440:1137–1144.

Springel, V., Wang, J., Vogelsberger, M., et al. (2008a). The Aquarius Project: the subhaloes of galactic haloes. *Monthly Notices of the RAS*, 391:1685–1711.

Springel, V., White, S. D. M., Frenk, C. S., et al. (2008b). Prospects for detecting supersymmetric dark matter in the Galactic halo. *Nature*, 456:73–76.

Springel, V., White, S. D. M., Jenkins, A., et al. (2005). Simulations of the formation, evolution and clustering of galaxies and quasars. *Nature*, 435:629–636.

Tasitsiomi, A. and Olinto, A. V. (2002). Detectability of neutralino clumps via atmospheric Cherenkov telescopes. *Physical Review D*, 66(8):083006.

Tisserand, P., Le Guillou, L., Afonso, C., et al. (2007). Limits on the Macho content of the Galactic Halo from the EROS-2 Survey of the Magellanic Clouds. *Astronomy and Astrophysics*, 469:387–404.

Tsuchiya, K., Enomoto, R., Ksenofontov, L. T., et al. (2004). Detection of Sub-TeV Gamma Rays from the Galactic Center Direction by CANGAROO-II. *Astrophysical Journal, Letters*, 606:L115–L118.

Vincent, P., Denanca, J.-P., Huppert, J.-F., et al. (2003). Performance of the H.E.S.S. Cameras. In *International Cosmic Ray Conference*, volume 5 of *International Cosmic Ray Conference*, page 2887.

Walsh, D., Carswell, R. F., and Weymann, R. J. (1979). 0957 + 561 A, B - Twin quasistellar objects or gravitational lens. *Nature*, 279:381–384.

Wikipedia (2013). `http://en.wikipedia.org/wiki/Bilinear_interpolation`. visited in March 2013.

XENON (2013). `http://xenon.astro.columbia.edu/`. visited in January 2013.

Zwicky, F. (1933). Die Rotverschiebung von extragalaktischen Nebeln. *Helvetica Physica Acta*, 6:110–127.

Zwicky, F. (1937a). Nebulae as Gravitational Lenses. *Physical Review*, 51:290–290.

Zwicky, F. (1937b). On the Masses of Nebulae and of Clusters of Nebulae. *Astrophysical Journal*, 86:217.

Zwicky, F. (1937c). On the Probability of Detecting Nebulae Which Act as Gravitational Lenses. *Physical Review*, 51:679–679.

List of Figures

List of Tables

Acknowledgements / Danksagung

So viele Leute haben mir während meiner Promotion auf so unterschiedliche Weise geholfen. Euch allen bin ich sehr dankbar, auch wenn ich nicht alle von Euch im Folgenden namentlich nenne.

Ganz herzlich bedanken möchte ich mich bei:

- Frau Prof. Dr. Gisela Anton und Herrn Prof. Dr. Christian Stegmann, die mir die Promotion in der Erlanger H.E.S.S. Gruppe ermöglicht haben. Desweiteren bedanke ich mich für die Freiheit bei der Themenwahl meiner Arbeit und für die große Unterstützung bei der Bewerbung um Stipendien und bei meinem Auslandsaufenthalt in Stockholm.
- Kathrin Valerius und Ira Jung, die meine Arbeit gewissenhaft Korrektur gelesen, mit zahlreichen Anmerkungen sehr verbessert und mir bei Fragen weitergeholfen haben.
- Meinen treuen Bürokollegen Julia und Daniel, die mir mit Rat und Tat zur Seite standen. Danke vor allem auch für unsere vielen Gespräche!
- Allen Mitgliedern der Erlanger H.E.S.S. Gruppe (auch bei den ehemaligen), mit denen ich sooo viele schöne Kaffeepausen, Grillfeste und Dinnerabende verbracht habe.
- Den Kollegen am Oskar Klein Centre in Stockholm, die mich so nett aufgenommen haben.
- Meinen Freunden, die dafür gesorgt haben, dass ich die Arbeit auch mal vergessen konnte.
- Meinen Eltern und meiner Schwester, die immer für mich da waren.
- Meinem Anton für Alles!